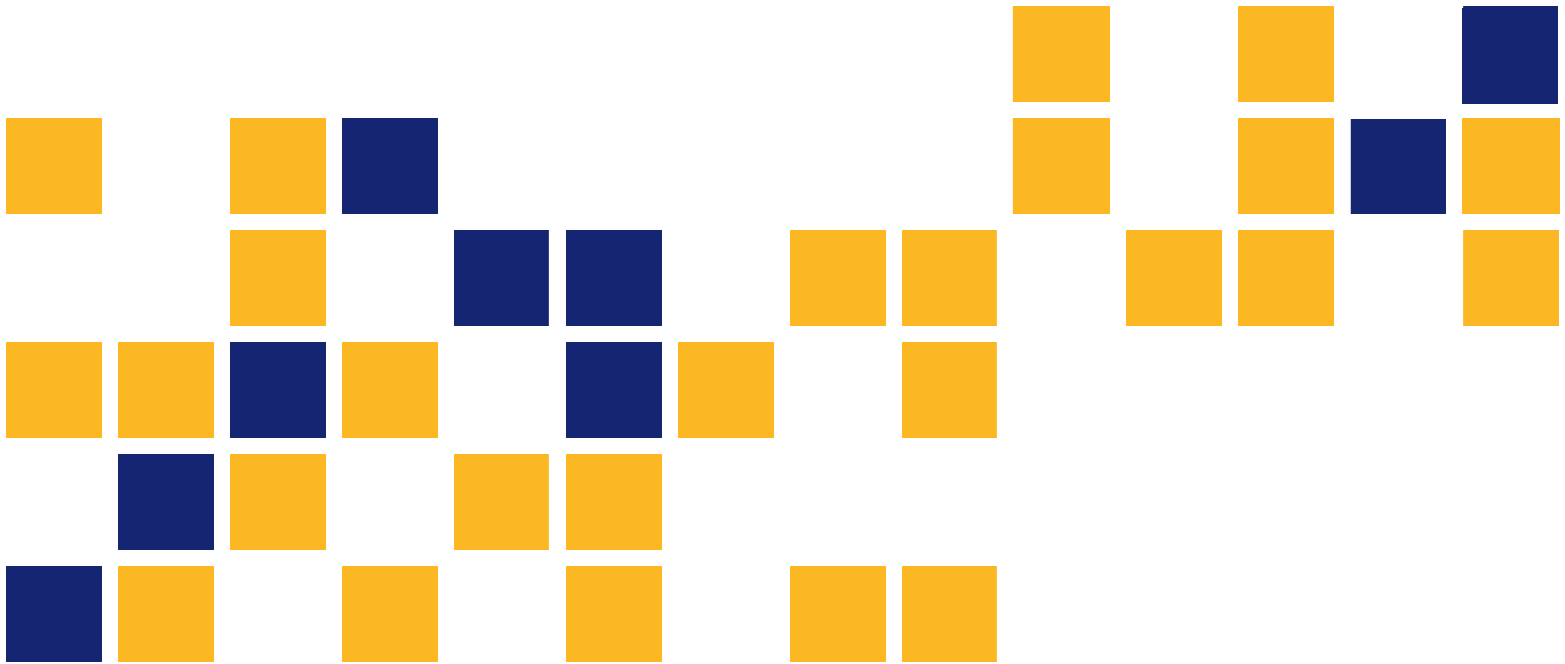


Establishing a Design Procedure for Buried Steel-Reinforced High- Density Polyethylene Pipes: A Field Study

Jie Han, Ph.D., P.E.
Fei Wang
Deep Kumar Khatri, Ph.D.
Robert L. Parsons, Ph.D., P.E.

The University of Kansas



1 Report No. K-TRAN: KU-14-4	2 Government Accession No.	3 Recipient Catalog No.	
4 Title and Subtitle Establishing a Design Procedure for Buried Steel-Reinforced High-Density Polyethylene Pipes: A Field Study		5 Report Date November 2015	6 Performing Organization Code
		7 Performing Organization Report No.	
7 Author(s) Jie Han, Ph.D., P.E., Fei Wang, Deep Kumar Khatri, Ph.D., Robert L. Parsons, Ph.D., P.E.		10 Work Unit No. (TRAIS)	
9 Performing Organization Name and Address The University of Kansas Department of Civil, Environmental and Architectural Engineering 1530 West 15th St Lawrence, Kansas 66045-7609		11 Contract or Grant No. C1969	
		13 Type of Report and Period Covered Final Report August 2013–August 2015	
12 Sponsoring Agency Name and Address Kansas Department of Transportation Bureau of Research 2300 SW Van Buren Topeka, Kansas 66611-1195		14 Sponsoring Agency Code RE-0635-01	
		15 Supplementary Notes For more information write to address in block 9. Phase I of this project was published in November 2013 as Report No. K-TRAN KU-11-6, <i>Establishing a Design Procedure for Buried Steel-Reinforced High Density Polyethylene (SRHDPE) Pipes.</i> Two field tests were conducted to investigate the field performance of steel-reinforced high-density polyethylene (SRHDPE) pipes during installation and under traffic loading. One test site was located on E 1000 road in Lawrence, KS, which is close to Clinton Lake. Three SRHDPE pipes with a diameter of 3 ft and a length of 24 ft were buried in a 6 ft wide trench with 2 ft thick soil cover. This test site had two test sections: one section was filled with Aggregate Base Class 3 aggregate (AB3) and the second section was filled with crushed stone. The second field study was conducted at a Kansas Department of Transportation (KDOT) storage yard in Kansas City, KS. Four 6 ft long SRHDPE pipes with a diameter of 2 ft were connected and buried in a trench with a dimension of 4.6 ft wide × 27.5 ft long × 4.2 ft deep. Two types of backfill material were also used in the trench, namely, AB3 aggregate and crushed stone. Earth pressures, pipe deflections, and pipe strains on plastic valley, plastic cover, and steel ribs were monitored during pipe installation and under static loading on both test sites. The test results from the pipe installation and static loading showed that (1) the vertical arching factor (VAF) on the top of the pipe was approximately 1.1 and the lateral earth pressure coefficient was approximately 0.65; (2) the peaking deflection was observed in both field tests in a range of 0.25 to 1.80% (the peaking deflection in the AB3 section was greater than that in the crushed stone section); (3) the maximum strain of the pipe occurred on the plastic valley in the longitudinal direction at the pipe crown, which was in a range of 0.4-0.6% and much lower than the strain limit of 5% suggested by the American Association of State Highway and Transportation Officials (AASHTO, 2012); and (4) the Giroud and Han (2004) method and the AASHTO (2012) method could reasonably estimate the earth pressure on the pipe under static loading, while the Iowa Formula could estimate the pipe deflection during installation and caused by static loading. The earth pressures, the pipe deflections, and the strains of the pipes in the Lawrence site were monitored for 680 days and all increased with time. Two empirical correlations were proposed to calculate the VAF and the pipe stiffness factor at a given time. The AASHTO (2012) design methods for metal pipes and high-density polyethylene (HDPE) pipes were modified for SRHDPE pipes based on the laboratory and field test results. A design procedure for SRHDPE pipes is proposed and illustrated by a design example.	
17 Key Words Steel-Reinforced High-Density Polyethylene Pipe, SRHDPE, Plastic Pipe, Buried Pipe, Culvert		18 Distribution Statement No restrictions. This document is available to the public through the National Technical Information Service www.ntis.gov .	
19 Security Classification (of this report) Unclassified	20 Security Classification (of this page) Unclassified	21 No. of pages 227	22 Price

This page intentionally left blank.

Establishing a Design Procedure for Buried Steel-Reinforced High-Density Polyethylene Pipes: A Field Study

Final Report

Prepared by

Jie Han, Ph.D., P.E.

Fei Wang

Deep Kumar Khatri, Ph.D.

Robert L. Parsons, Ph.D., P.E.

The University of Kansas

A Report on Research Sponsored by

THE KANSAS DEPARTMENT OF TRANSPORTATION
TOPEKA, KANSAS

and

THE UNIVERSITY OF KANSAS
LAWRENCE, KANSAS

November 2015

© Copyright 2015, **Kansas Department of Transportation**

PREFACE

The Kansas Department of Transportation's (KDOT) Kansas Transportation Research and New-Developments (K-TRAN) Research Program funded this research project. It is an ongoing, cooperative and comprehensive research program addressing transportation needs of the state of Kansas utilizing academic and research resources from KDOT, Kansas State University and the University of Kansas. Transportation professionals in KDOT and the universities jointly develop the projects included in the research program.

NOTICE

The authors and the state of Kansas do not endorse products or manufacturers. Trade and manufacturers names appear herein solely because they are considered essential to the object of this report.

This information is available in alternative accessible formats. To obtain an alternative format, contact the Office of Public Affairs, Kansas Department of Transportation, 700 SW Harrison, 2nd Floor – West Wing, Topeka, Kansas 66603-3745 or phone (785) 296-3585 (Voice) (TDD).

DISCLAIMER

The contents of this report reflect the views of the authors who are responsible for the facts and accuracy of the data presented herein. The contents do not necessarily reflect the views or the policies of the state of Kansas. This report does not constitute a standard, specification or regulation.

Abstract

Two field tests were conducted to investigate the field performance of steel-reinforced high-density polyethylene (SRHDPE) pipes during installation and under traffic loading. One test site was located on E 1000 road in Lawrence, KS, which is close to Clinton Lake. Three SRHDPE pipes with a diameter of 3 ft and a length of 24 ft were buried in a 6 ft wide trench with 2 ft thick soil cover. This test site had two test sections: one section was filled with Aggregate Base Class 3 aggregate (AB3) and the second section was filled with crushed stone. The second field study was conducted at a Kansas Department of Transportation (KDOT) storage yard in Kansas City, KS. Four 6 ft long SRHDPE pipes with a diameter of 2 ft were connected and buried in a trench with a dimension of 4.6 ft wide \times 27.5 ft long \times 4.2 ft deep. Two types of backfill material were also used in the trench, namely, AB3 aggregate and crushed stone. Earth pressures, pipe deflections, and pipe strains on plastic valley, plastic cover, and steel ribs were monitored during pipe installation and under static loading on both test sites. The test results from the pipe installation and static loading showed that (1) the vertical arching factor (VAF) on the top of the pipe was approximately 1.1 and the lateral earth pressure coefficient was approximately 0.65; (2) the peaking deflection was observed in both field tests in a range of 0.25 to 1.80% (the peaking deflection in the AB3 section was greater than that in the crushed stone section); (3) the maximum strain of the pipe occurred on the plastic valley in the longitudinal direction at the pipe crown, which was in a range of 0.4-0.6% and much lower than the strain limit of 5% suggested by the American Association of State Highway and Transportation Officials (AASHTO, 2012); and (4) the Giroud and Han (2004) method and the AASHTO (2012) method could reasonably estimate the earth pressure on the pipe under static loading, while the Iowa Formula could estimate the pipe deflection during installation and caused by static loading.

The earth pressures, the pipe deflections, and the strains of the pipes in the Lawrence site were monitored for 680 days and all increased with time. Two empirical correlations were proposed to calculate the VAF and the pipe stiffness factor at a given time.

The AASHTO (2012) design methods for metal pipes and high-density polyethylene (HDPE) pipes were modified for SRHDPE pipes based on the laboratory and field test results. A design procedure for SRHDPE pipes is proposed and illustrated by a design example.

Table of Contents

Abstract	v
Table of Contents	vi
List of Tables	ix
List of Figures	x
Chapter 1: Introduction	1
1.1 Background	1
1.2 Problem Statement	2
1.3 Objectives	3
1.4 Research Methodology	4
1.5 Organization of Report	4
Chapter 2: Literature Review	5
2.1 Introduction	5
2.2 Installation of Pipes	5
2.2.1 Trench Width and Soil Cover Thickness	5
2.2.2 Backfill Material	7
2.2.3 Compaction Techniques and Simulation Methods	9
2.3 Load Transfer Mechanism Above Buried Pipes	14
2.3.1 Loads and Deflections of Pipes During Installation	14
2.3.2 Load Transfer Mechanism of Buried Pipes in Service	17
2.4 Long-Term Behavior of HDPE Pipes	20
2.5 Previous Research on SRHDPE Pipes	21
2.6 Performance Limits	22
2.6.1 Wall Crushing (Primary Performance Limit for Rigid Pipes and Stiffer Flexible Pipes)	22
2.6.2 Wall Buckling	23
2.6.3 Buckling Check for the Pipe Installation	25
2.6.4 Over-Deflection	26
2.6.5 Strain Limit	26
2.6.6 Delamination	28
Chapter 3: Field Performance of the SRHDPE Pipes Field Test I	29
3.1 Introduction	29
3.2 Properties of the Backfill Material	30
3.3 Test Site, Test Pipes, and Instrumentation	34
3.3.1 Test Site Condition	34
3.3.2 Test Pipe	34
3.3.3 Instrumentations	36
3.4 Pipe Installation and Static Loading	42
3.4.1 Exhumation of the Corroded Corrugated Metal Pipe	42

3.4.2 Bedding	44
3.4.3 Placement of Pipe	45
3.4.4 Backfilling and Soil Cover	47
3.4.5 Loading	52
3.4.6 HMA Base and HMA Surface Preparation	54
3.4.7 Quality Control	57
3.5 Analysis of Test Results During Pipe Installation	59
3.5.1 Earth Pressure-Test Section A	59
3.5.2 Earth Pressure-Test Section B	64
3.5.3 Deflections-Test Section A	68
3.5.4 Deflections-Test Section B	71
3.5.5 Strains-Test Section A	75
3.5.6 Strains-Test Section B	78
3.6 Analysis of Test Results Under Static Loading	81
3.6.1 Earth Pressure-Test Section A	81
3.6.2 Earth Pressure-Test Section B	84
3.6.3 Deflections-Test Section A	89
3.6.4 Deflections-Test Section B	91
3.6.5 Strains-Test Section A	94
3.6.6 Strains-Test Section B	99
3.7 Conclusions	105
Chapter 4: Field Performance of the SRHDPE Pipes Field Test II	107
4.1 Introduction	107
4.2 Properties of Backfill Material	108
4.3 Test Site, Test Pipes, and Instrumentation	112
4.3.1 Test Site	112
4.3.2 Test Pipes	113
4.3.3 Instrumentation	115
4.4 Pipe Installation and Static Loading	120
4.4.1 Trench Excavation	120
4.4.2 Bedding	120
4.4.3 Placement of the Pipe	122
4.4.4 Backfilling of Sidefill and Soil Cover	124
4.4.5 Static Loading	125
4.4.6 Quality Control	126
4.4.7 Pipe Exhumation	128
4.5 Analysis of Test Results During Pipe Installation	129
4.5.1 Earth Pressure	129
4.5.2 Deflections	131
4.5.3 Strains	135
4.6 Analysis of Test Results Under Static Loading	141

4.6.1 Earth Pressure	141
4.6.2 Deflections	144
4.6.3 Strains	145
4.7 Observation of Exhumed Pipes	149
4.8 Conclusions	151
Chapter 5: Evaluation of the Long-Term Performance of the SRHDPE Pipe.....	153
5.1 Introduction	153
5.2 Brief Description of Pipe Monitoring	153
5.3 Data Analysis	154
5.3.1 Earth Pressure	154
5.3.2 Deflections	163
5.3.3 Strains	165
5.4 Long-Term Empirical Correlations	171
5.4.1 Vertical Soil Arching Factor	172
5.4.2 Pipe Stiffness	173
5.5 Conclusions	176
Chapter 6: Design Procedures for SRHDPE Pipes	177
6.1 Introduction	177
6.2 AASHTO Design Methods	177
6.2.1 Strength Limit State	178
6.2.2 Flexibility Factor Limit	178
6.2.3 Soil Envelop	179
6.2.4 Soil Cover Thickness	179
6.2.5 Pipe Spacing	179
6.2.6 Metal Pipe Design	179
6.2.7 HDPE Pipe Design	181
6.3 SRHDPE Pipe Design Considerations	191
6.4 Proposed SRHDPE Pipe Design Procedure	193
6.5 SRHDPE Pipe Design Example	194
6.5.1 Design Problem	194
6.5.2 Solution	194
Chapter 7: Conclusions and Recommendations	200
7.1 Conclusions	200
7.2 Recommendations	201
References	203

List of Tables

Table 1.1: Specifications for Different Types of Pipes.....	2
Table 2.1: Minimum Cover Over the Top of the Pipe.....	7
Table 2.2: Backfill Material Classifications for Thermoplastic Pipes.....	8
Table 2.3: Backfill Material Categories for Rigid Pipes.....	8
Table 2.4: Live Load Distribution Under the AASHTO H-25 Truck.....	19
Table 3.1: Comparison of the Earth Pressures (psi) Measured Around the Pipe in the Field Test	88
Table 3.2: Comparison of the Measured and Calculated Earth Pressures (psi) Around the Pipe in the Field Test Using Foster and Ahlvin (1954) Method.....	89
Table 3.3: Comparison of the Average Measured Crown Pressures (psi) with AASHTO (2012) and Giroud and Han (2004) Methods	89
Table 3.4: Comparison of the Deflections of the Pipe.....	93
Table 3.5: Comparison of the Calculated and Measured Strains of the Pipe in the Field	95
Table 4.1: Comparison of the Calculated and Measured Deflections Under Static Loading.....	144
Table 6.1: Flexibility Factor Limits.....	178
Table 6.2: Secant Constraint Modulus M_s of Backfill Based on Soil Type and Compaction Condition (Unit: ksi).....	184
Table 6.3: Shape Factors Based on Pipe Stiffness, Backfill, and Compaction Level.....	191

List of Figures

Figure 1.1: Schematic Representation of a Cross Section of the Corrugated SRHDPE Pipe	2
Figure 2.1: Basis Concept of the Hysteretic K_0 Method.....	11
Figure 2.2: Compaction Models for Buried Pipes by Applying Additional Pressure	13
Figure 2.3: Schematic of the Wall Crushing.....	23
Figure 3.1: Location of the First Test Site	29
Figure 3.2: Road Section in the Field Test	30
Figure 3.3: Grain Size Distribution of the Crushed Stone	31
Figure 3.4: Large Direct Shear Box Tests for the Crushed Stone	32
Figure 3.5: Grain Size Distribution of the AB3 Aggregate Used in the Lawrence Field Test	33
Figure 3.6: Standard Proctor Compaction Curve of the AB3 Aggregate Used in the Lawrence Field Test	33
Figure 3.7: Field Test Sections in the Lawrence Site	35
Figure 3.8: Test SRHDPE Pipes with Bell and Spigot Joints in the Field Test.....	36
Figure 3.9: Displacement Transducers Inside the Pipe Section in the Field	37
Figure 3.10: Strain Gages Fixed Outside of the Pipe in the Field	38
Figure 3.11: Symbols, Locations, and Orientations of the Strain Gages on the Pipe.....	38
Figure 3.11: Symbols, Locations, and Orientations of the Strain Gages on the Pipe (Continued)	39
Figure 3.11: Symbols, Locations, and Orientations of the Strain Gages on the Pipe (Continued)	40
Figure 3.12: Earth Pressure Cells Around the Pipe Section	41
Figure 3.13: The Corroded Corrugated Metal Pipe Before Replacement	42
Figure 3.14: Excavation of a Trench.....	43
Figure 3.15: Marking the Centerline Before the Placement of Bedding Materials	43
Figure 3.16: Placement of the Bedding Materials	44
Figure 3.17: Marking of the Locations of the Wheel Paths	45
Figure 3.18: An Earth Pressure Cell Installed at the Invert Of The Pipe.....	45
Figure 3.19: Galvanized Steel End Sections.....	46
Figure 3.20: Placement of a Pipe into the Trench.....	46
Figure 3.21: Fully-Instrumented Pipes in the Trench.....	47
Figure 3.22: Backfilling and Compaction with a Vibratory Plate Compactor and a Tamping Hammer.....	48
Figure 3.22: Backfilling and Compaction with a Vibratory Plate Compactor and a Tamping Hammer (Continued)	49
Figure 3.23: Backfilling up to the Springline	49
Figure 3.24: A Bobcat Used to Dump and Level Soils.....	50
Figure 3.25: The Compacted AB3 Surface Before the Placement of the HMA Base	50
Figure 3.26: Earth Pressure Cells, E_{s0} and E_{s18} Placed at the Springline and E_{C0} and E_{C12} at the Crown.....	51
Figure 3.27: Test Truck Used to Load the Pipe	52
Figure 3.28: Axle Load Configuration of the Test Truck.....	53

Figure 3.29: Application of Static Loads by the Test Truck.....	53
Figure 3.29: Application of Static Loads by the Test Truck (Continued)	54
Figure 3.30: Placement of HMA Material by Truck.....	55
Figure 3.31: Leveling of HMA Material Using a Bobcat.....	55
Figure 3.32: Compaction of the HMA Base by a Vibratory Roller.....	56
Figure 3.33: Construction and Instrumental Details of a Test Section in the Field Including the Soil Lifts and the Earth Pressure Cells	56
Figure 3.34: LWD Test on the Compacted AB3 Aggregate.....	57
Figure 3.35: CBR Profiles on the Western Test Section	58
Figure 3.36: A Test Box Used for Density Determination	59
Figure 3.37: Measured Earth Pressures Around the Pipe During Installation in Test Section A.	60
Figure 3.38: Comparison of Measured and Calculated Pressures at the Crown During Installation in Test Section A.....	61
Figure 3.39: Measured and Calculated Lateral Earth Pressures at the Springline in Test Section A	62
Figure 3.40: Lateral Earth Pressure Coefficients (K) at the Springline in Test Section A	63
Figure 3.41: Measured Earth Pressures Around the Pipe During Installation in Test Section B.	64
Figure 3.42: Comparison of Measured and Calculated Pressures at the Crown During Installation in Test Section B.....	65
Figure 3.43: Measured Lateral and Overburden Pressures at the Springline in Test Section B...	66
Figure 3.44: Lateral Earth Pressure Coefficients (K) at the Springline in Test Section B	67
Figure 3.45: Measured Deflections of the Pipe During the Installation in Test Section A	68
Figure 3.46: Relations Between the Measured Vertical and Horizontal Deflections During the Installation in Test Section A.....	69
Figure 3.47: Comparison of the Measured and Calculated Horizontal Deflections by the Iowa Formula in Test Section A	70
Figure 3.48: Deflections Produced by the Tamping Hammer During the Compaction at the Pipe Shoulder in Test Section A	71
Figure 3.49: Deflections Produced by the Smooth Wheel Vibratory Roller During the Compaction Before Placing the HMA Base in Test Section A	71
Figure 3.50: Measured Deflections of the Pipe During the Installation in Test Section B.....	73
Figure 3.51: Relations Between the Measured Vertical and Horizontal Deflections During the Installation in Test Section B.....	73
Figure 3.52: Comparison of the Measured and Calculated Horizontal Deflections by the Iowa Formula in Test Section B	74
Figure 3.53: Deflections Produced by the Vibratory Plate Compactor During the Compaction at the Pipe Shoulder in Test Section B	75
Figure 3.54: Deflections Produced by the Smooth Wheel Vibratory Roller During the Compaction Before the Placement of the HMA Base in Test Section B.....	75
Figure 3.55: Measured Strains on the Steel Surface During the Installation in Test Section A...	76
Figure 3.56: Measured Strains on the Plastic Ribs During the Installation in Test Section A	76

Figure 3.57: Measured Strains on the Plastic at Inside and Outside Pipe Walls During the Installation in Test Section A.....	77
Figure 3.58: Measured Strains on the Steel During the Installation in Test Section B	79
Figure 3.59: Measured Strains on the Plastic Ribs During the Installation in Test Section B	79
Figure 3.60: Measured Strains on the Plastic at Inside and Outside Pipe Walls During the Installation in Test Section B.....	80
Figure 3.61: Axle Loads on the Pipe in Test Section A.....	83
Figure 3.62: Measured Earth Pressures Around the Pipe Under Truck Loading on Test Section A	84
Figure 3.63: Axle Loads on the Pipe in Test Section B.....	86
Figure 3.64: Measured Earth Pressures Around the Pipe Under Truck Loading on Test Section B	87
Figure 3.65: Deflections of the Pipe Under the Truck Loading in Test Section A.....	91
Figure 3.66: Deflections of the Pipe Under the Truck Loading in Test Section B.....	92
Figure 3.67: Measured Strains on the Steel Ribs in Test Section A	95
Figure 3.68: Measured Strains on the Plastic at Ribs in Test Section A	96
Figure 3.69: Measured Strains on the Inside and Outside Plastic Walls of the Pipe in Test Section A.....	98
Figure 3.70: Measured Strains on the Inside and Outside Plastic Walls of the Pipe in Test Section A.....	99
Figure 3.71: Measured Strains on the Steel Ribs in Test Section B	100
Figure 3.72: Measured Strains on the Plastic at Ribs in Test Section B.....	101
Figure 3.73: Measured Strains on Inside and Outside Plastic Walls of the Pipe in Test Section B	103
Figure 3.74: Measured Strains on the Inside and Outside Plastic Walls of the Pipe in Test Section B.....	104
Figure 3.75: Comparison of the Strains Measured on the Steel and Plastic in the Field Test....	105
Figure 4.1: Location of the Second Field Test Site	107
Figure 4.2: Particle Size Distribution Curves of the AB3 Aggregate and the Crushed Stone....	109
Figure 4.3: The Compaction Curve of the AB3 Aggregate	109
Figure 4.4: Plate Loading Test Results of the AB3 Aggregate and the Crushed Stone	110
Figure 4.5: Stress-Strain Curves of the AB3 Aggregate from the Triaxial Compression Tests at Different Confining Pressures.....	110
Figure 4.6: Stress-Strain Curves of the Crushed Stone from the Triaxial Compression Tests at Different Confining Pressures.....	111
Figure 4.7: Mohr's Circles of the AB3 Aggregate and the Crushed Stone	111
Figure 4.7: Mohr's Circles of the AB3 Aggregate and the Crushed Stone (Continued)	112
Figure 4.8: Schematic of the Installation Plan (Not to Scale, Unit: Inches).....	113
Figure 4.9: Schematic of Cross-Section of the Corrugated SRHDPE Pipe (Unit: Inches, Not to Scale).....	114
Figure 4.10: Two Connected Pipes with a Soil-Tight Type Connector.....	114
Figure 4.11: Schematic of the Locations of Pressure Cells	116

Figure 4.12: Placement of a Pressure Cell	116
Figure 4.13: Schematic of the Locations of the Displacement Transducers.....	117
Figure 4.14: Installed Displacement Transducers Inside of the SRHDPE Pipe	118
Figure 4.15: Symbols, Locations, and Orientations of the Strain Gages on the Pipe.....	119
Figure 4.16: Excavation of a Trench.....	120
Figure 4.17: Compaction of the Bedding.....	121
Figure 4.18: LWD Test on the Bedding.....	122
Figure 4.19: Sand Cone Tests on the Bedding in the Crushed Stone Section	122
Figure 4.20: Placement of the Pipes	123
Figure 4.21: Pipes Placed on the Bedding	123
Figure 4.22: The Compaction of Difficult Zones Using the STANLEY TA45 Rammer.....	124
Figure 4.23: The John Deere 310G Loader Backhoe Above the Pipes	126
Figure 4.24: The CAT 953D Crawler Loader Above the Pipes	126
Figure 4.25: Leveling Measurements During the Pipe Installation	127
Figure 4.26: DCP Test Results of the AB3 Aggregate Section After Construction.....	127
Figure 4.27: Markers of the Rib Gaps Before Installation.....	128
Figure 4.28: An Exhumed Pipe.....	128
Figure 4.29: Development of Earth Pressures Around Pipes with Soil Thickness.....	130
Figure 4.30: Lateral Earth Pressure Coefficients at the Springline of the Pipe with Soil Thickness	131
Figure 4.31: Development of Deflections with Soil Thickness in Three Directions During Backfilling.....	133
Figure 4.31: Development of Deflections with Soil Thickness in Three Directions During Backfilling (Continued)	134
Figure 4.32: Strains of the Steel Ribs in Section A During the Pipe Installation.....	135
Figure 4.33: Strains of the Plastic Cover in Section A During the Pipe Installation.....	136
Figure 4.34: Strains of the Plastic Valley in Section A During the Pipe Installation.....	137
Figure 4.35: Strains of the Steel Ribs in Section B During the Pipe Installation	138
Figure 4.36: Strains of the Plastic Cover in the Crushed Stone Section During the Pipe Installation.....	139
Figure 4.37: Strains of the Plastic Valley in the Crushed Stone Section During the Pipe Installation.....	140
Figure 4.38: Comparison of the Measured Strains and Calculated Strains on the Plastic in Both Sections.....	141
Figure 4.39: The Measured Earth Pressures in Section A at the End of the Construction and Under Static Loading	142
Figure 4.40: The Measured Earth Pressures in Section B at the End of the Construction and Under Static Loading	142
Figure 4.41: Comparison of the Measured Earth Pressures at the Pipe Crown with the Calculated Ones Under Static Loading.....	143
Figure 4.42: Diameter Changes of the Pipes Under Static Loading	145
Figure 4.43: The Measured Strains of the Pipe in Section A.....	146

Figure 4.43: The Measured Strains of the Pipe in Section A (Continued)	147
Figure 4.44: The Measured Strains of the Pipe in Section B.....	148
Figure 4.44: The Measured Strains of the Pipe in Section B (Continued)	149
Figure 4.45: Displacements of Ribs at the Springline of Pipes in Two Sections	150
Figure 5.1: Measured Vertical Earth Pressure and Temperature at the Pipe Crown in the Crushed Stone Section at a Distance of 114 Inches	154
Figure 5.2: Corrected Vertical Earth Pressure at the Pipe Crown in Section A	156
Figure 5.3: Corrected Lateral Earth Pressure at the Pipe Springline in Section A	157
Figure 5.4: Corrected Vertical Earth Pressure at the Shoulder in Section A.....	158
Figure 5.5: Corrected Lateral Earth Pressure at the Trench Wall at the Pipe Springline Level in Section A.....	158
Figure 5.6: Corrected Vertical Earth Pressure at the Pipe Invert in the Section A.....	159
Figure 5.7: Corrected Vertical Earth Pressure at the Pipe Crown in Section B.....	160
Figure 5.8: Corrected Lateral Earth Pressure at the Pipe Springline in Section B	161
Figure 5.9: Corrected Vertical Earth Pressure at the Shoulder in Section B.....	161
Figure 5.10: Corrected Earth Pressure at the Trench Wall at the Pipe Springline Level in Section B.....	162
Figure 5.11: Corrected Vertical Earth Pressure at the Pipe Invert in Section B.....	163
Figure 5.12: Pipe Deflections with Time in Section A.....	164
Figure 5.13: Pipe Deflections with Time in Section B.....	164
Figure 5.14: Longitudinal Strains on the Plastic Valley at the Pipe Crown in Section A	165
Figure 5.15: Longitudinal Strains on the Plastic Valley at the Pipe Springline and Invert in Section A.....	166
Figure 5.16: Circumferential Strains of the Plastic Cover in Section A.....	167
Figure 5.17: Circumferential Strains of Steel Ribs in Section A.....	168
Figure 5.18: Longitudinal Strains on the Pipe Valley at the Pipe Crown in Section B	169
Figure 5.19: Longitudinal Strains on the Pipe Valley at the Pipe Springline and the Invert in Section B.....	169
Figure 5.20: Circumferential Strains of the Pipe Covers in Section B.....	170
Figure 5.21: Circumferential Strains of Steel Ribs in Section B	171
Figure 5.22: Variation of the VAFs With the Time.....	172
Figure 5.22: Variation of the VAFs With the Time (Continued)	173
Figure 5.23: Variation of the Pipe Stiffness Factor with Time for Sections A and B	175
Figure 6.1: Typical and Idealized Cross Sections of a Profile Wall Pipe.....	187
Figure 6.2: Schematic of Cross-Section of the Corrugated SRHDPE Pipe (Unit: Inches, Not to Scale).....	194

Chapter 1: Introduction

1.1 Background

High density polyethylene (HDPE) pipes have been widely used worldwide for several decades due to their light weight, low cost, and chemical resistance (Masada & Sargand, 2007). More than 54% of natural gas pipeline projects all over the world have used HDPE pipes. In the United States, this percentage is even higher than 90%. However, HDPE pipes also have some disadvantages, including low strength, limited pressure rating, and high potential buckling, which limit the usage of HDPE pipes in some specific working conditions.

Metal pipe is another popularly used pipe type in the practice, which has a high load carrying capacity for dead and live loads. However, corrosion is a major problem for metal pipes. The corroding process of metal pipes depends on the following factors: (1) the material properties of pipes; (2) the chemical properties of the soil surrounding the pipes; (3) the groundwater properties and conditions; and (4) the fluid transmitting in the pipes. Corrosion is a result of electrochemical electron exchanges between metals and solutions (Centers for Disease Control and Prevention, 2013).

Steel-reinforced high-density polyethylene (SRHDPE) pipes combine the advantages of metal and HDPE pipes to overcome their disadvantages (Khatri, Han, Parsons, et al., 2013; Corey, Han, Khatri, & Parsons, 2014; Wang et al., 2015). Figure 1.1 shows the schematic representation of an SRHDPE pipe section. The steel rib is used to enhance the load-carrying capacity of the pipe, and the plastic cover for the steel ribs prevents possible corrosion. Based on the document published by the American Concrete Pipe Association, SRHDPE pipe is being marketed nationwide for storm drainage systems (ACPA, 2009). The State of Kansas planned to spend \$9.8 million USD to replace and repair the pipeline system between 2013 and 2016 (KDOT, 2012). Due to the advantages of the SRHDPE pipes, they can be an alternative pipe type to be used for replacement of corroded pipes in the pipeline system. ASTM International published a specification for SRHDPE pipes to be used for non-pressure drainage and sewerage purposes. This specification covers the requirements and test methods for materials, dimensions,

workmanship, impact resistance, pipe stiffness, flattening, buckling tensile strength, shipment, and storage for SRHDPE pipes (ASTM F2562, 2008).

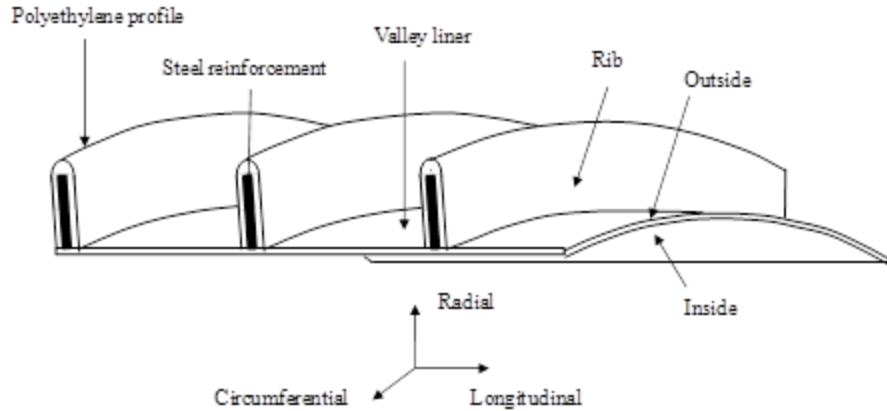


Figure 1.1: Schematic Representation of a Cross Section of the Corrugated SRHDPE Pipe
After ASTM F2562 (2008)

1.2 Problem Statement

Several national standards and specifications have been developed for design, installation, and materials for precast concrete pipe, corrugated metal pipes, and HDPE pipes. Table 1.1 lists the coverage of these standards and specifications. However, no nationally accepted installation standard or design method is available for SRHDPE pipes, which limits their usage. Even though ASTM F2562 (2008) provides the requirements for the SRHDPE pipe product, it does not provide engineers any guidance or instructions on how to design SRHDPE pipes during installation and under traffic loading.

Table 1.1: Specifications for Different Types of Pipes

Specifications	Material	Construction & Installation	Trench Width
Concrete Pipe	ASTM C78, AASHTO-M170, ASTM C14	ASTM C1479, AASHTO LRFD Bridge Construction Specifications (Sec. 27)	ASTM C1479, AASHTO Section 27
HDPE Pipe	ASTM F2306, AASHTO M294	ASTM D2321, AASHTO LRFD Bridge Construction Specifications (Sec. 30)	AASHTO Section 30
SRHDPE Pipe	ASTM F2562	Not Available	Not Available

Source: ACPA (2009)

Moser and Folkman (2008) summarized that flexible pipe design is mainly based on the following three parameters: (a) load; (b) soil stiffness in the pipe zone; and (c) pipe stiffness. Load transfer mechanism of buried pipes is attributed to trench width, soil cover depth, and backfill and its compaction degree. Soil stiffness in the pipe zone also depends on the backfill properties and the compaction and construction procedures. In addition, long-term reduction in HDPE pipe stiffness is always considered in HDPE pipe design due to the material relaxation and temperature effect. However, no existing method is available for the SRHDPE pipe installation design and long-term behavior evaluation. Therefore, lack of applicable specifications for the SRHDPE design has limited the usage of the SRHDPE pipe.

Laboratory research on the performance of the SRHDPE pipe was conducted in the previous research project (i.e., Phase I; Khatri, Han, Corey, & Parsons, 2013). A series of tests, including parallel plate load test, creep test, stub compression tests, and pipe bending test, were conducted to determine the mechanical properties of the SRHDPE pipe. Large-scale box tests were also conducted to investigate the mechanical behavior of the SRHDPE pipe under static and dynamic loadings. Some recommendations were provided based on the test results. Laboratory conditions are not necessarily the same as those in field due to possible boundary effect, moisture and temperature variations, different construction equipment, traffic loading, and time effect. Therefore, field tests are necessary to verify laboratory test results and establish a design procedure for the SRHDPE pipe.

1.3 Objectives

The objective of this research was to use the test data obtained from the field study to verify/improve the design procedure for the SRHDPE pipes during installation and traffic loading. This objective has been achieved by the following tasks:

- To develop compaction and installation parameters for design of SRHDPE pipes during installation;
- To investigate the load distribution around the SRHDPE pipe and develop a design procedure to calculate required parameters;

- To evaluate the field performance of the SRHDPE pipe with time and establish evaluation criteria for long-term performance of SRHDPE pipes in field.

1.4 Research Methodology

The research methodology adopted for this research includes: (1) a literature review on pipe installation, load transfer mechanism above buried pipes, and long-term behavior of HDPE pipes, (2) laboratory tests to determine the properties of the backfill materials (i.e., Aggregate Base Class 3 [AB3] and crushed stone) used in the field tests, (3) two field tests to investigate the performance of the SRHDPE pipes during installation and traffic loading, (4) long-time monitoring of pipes in one field test to investigate the long-term performance of the SRHDPE pipe, and (5) establishment of the design procedures through modification and improvement of the American Association of State Highway and Transportation Officials (AASHTO, 2012) design method.

1.5 Organization of Report

The research report includes eight chapters. Chapter 1 is the introduction and the background of this research. Chapter 2 focuses on the literature review. Chapter 3 presents the field installation test in Lawrence, KS. Chapter 4 presents the field installation test in a KDOT storage yard in Kansas City, KS. Chapter 5 discusses the evaluation of the long-term performance of the SRHDPE pipe based on the monitoring data of the tested pipes in the field. Chapter 6 presents the design procedures by modifying the AASHTO (2012) design method for buried pipes. Chapter 7 presents the conclusions and recommendations from this research.

Chapter 2: Literature Review

2.1 Introduction

Based on the objective of this research, the literature review includes the following sections: (a) installation of pipes; (b) load transfer mechanism above buried pipes; (c) long-term behavior of flexible pipe considering material relaxation and stiffness reduction; (d) existing research on the SRHDPE pipe; and (e) performance limits of buried pipes used in the pipe installation design.

2.2 Installation of Pipes

Researchers have investigated the following aspects of the pipe installation: (a) determination of the trench width and/or soil cover thickness (e.g., Katona, 1988; Moser & Folkman, 2008); (b) backfill material selection and compaction (e.g., Molin, 1981); and (c) stress and strain evaluation of the pipes after construction (Meyerhof & Baikie, 1963; Moser & Folkman, 2008). These investigations may be attributed to the following reasons: (1) trench width and soil cover thickness are related to the load transfer mechanism during pipe service and they are essential for buried pipe design and evaluation; (2) backfill material provides support for flexible pipes and is therefore important for their performance (compaction is mainly responsible for peaking deflection of a pipe and enhances its capacity to carry more loads); and (3) stresses and strains of a pipe after construction serve as the initial condition of the pipe before being subjected to service loading (the initial condition is essential to evaluate the pipe behavior during service loading, especially possible failure).

2.2.1 Trench Width and Soil Cover Thickness

Marston and Anderson (1913) proposed the following equation to calculate the load at the top of a rigid pipe in a ditch condition:

$$W_d = C_d \gamma B_c B_d$$

Equation 2.1

Where:

W_d = the load at the crown of the pipe

C_d = the load coefficient for ditch pipes

γ = the unit weight of backfill

B_c = the horizontal breadth of the pipe (i.e., the diameter of the pipe)

B_d = the horizontal width of the ditch at top of the pipe

Equation 2.1 shows that the vertical load on the top of the pipe is proportional to the width of the trench. It reflects the soil arching effect in the soil cover, i.e., the narrower trench can induce more reduction in the vertical load on the pipe top. Under this condition, the load on the rigid pipe would increase from the prism load due to the negative soil arching effect. They found that when the trench width is equal to or greater than a specific value, the ditch condition can be treated as the embankment condition. The trench width when the ditch condition turns into the embankment condition is referred to as the *transition width*.

ASTM C1479 (2013) and AASHTO (2012) required that the trench width for a rigid pipe should be equal to four-thirds of the pipe outside diameter. Space for compaction at both sides of the pipes should be adequate. ASTM D2321 (2014) suggests that the minimum width of the trench for a thermoplastic pipe should be not less than the greater of the pipe outside diameter plus 15.7 inches or pipe outside diameter times 1.25 plus 11.8 inches. AASHTO (2012) recommended that the trench width for an HDPE pipe should be 1.50 times the pipe outside diameter plus 11.8 inches.

Adequate soil cover thickness not only ensures the safety of the pipe subjected to compaction loads above the pipe but also limits the load distribution mechanism around the buried pipe. Based on Boussinesq's solution, Moser and Folkman (2008) concluded that the live load effect induced by an AASHTO H-20 truck above a buried pipe can be neglected when the soil cover thickness is greater than 8 ft. AASHTO (2012) suggested that the negligible depth of the live load caused by an H-25 truck is 10 ft. Katona (1988) proposed an empirical formula to determine of the minimum soil cover thickness for a pipe subjected to various standard

AASHTO truck loadings without considering the effect of the pavement. Table 2.1 summarizes the minimum soil cover thickness from the KDOT (2007) specification. ASTM D2321 (2014) provides the minimum soil cover thickness requirements for different types of backfill material. For a good soil (referred to as Class I), a soil cover thickness of 2 ft or equivalent to one diameter of the pipe is required before construction vehicles are allowed to pass, while for a Class III soil, the soil cover thickness should be at least 3 ft or one diameter of the pipe. A 4 ft thick soil cover should be placed before hydro-hammer compaction.

Table 2.1: Minimum Cover Over the Top of the Pipe

PE and PVC Diameter (ft)	Axle Load (kips)			
	18 to 50	50 to 75	75-110	110 to 150
	Required Soil Cover (ft)			
1 to 3	2	2.5	3	3
3.7 to 4	3	3	3	4.5
4.5 to 5	3	3	3.5	4.5

Source: KDOT (2007)

2.2.2 Backfill Material

Properties of backfill material are essential to the performance of flexible pipes. For flexible pipes, cohesionless backfill materials are strongly suggested. However, silty sand and clayey sand may be also acceptable for economic purposes for pipes under low to moderate loads (Molin, 1981). For cohesive soil, compaction should be operated at the optimum moisture content (Rogers, Fleming, Loeppky, & Faragher, 1995; ASTM A798, 2013; ASTM D2321, 2014).

Different types of soils are commonly classified based on the Unified Soil Classification System (USCS; see ASTM D2487, 2011). The soil types defined in the USCS are divided into five classes according to the thermoplastic pipe design (ASTM D2321, 2014). Table 2.2 lists the backfill material classifications for thermoplastic pipes.

Table 2.2: Backfill Material Classifications for Thermoplastic Pipes

Backfill class	I	II	III	IV	V
Soil Type Symbols	Manufactured Angular Granular Material	GW	GM	ML	OL
		GP	GC	CL	OH
		SW	SM	MH	PT
		SP	SC	CH	

Note: All symbols listed in this table follow the definitions in ASTM D2487 (2011).
Source: ASTM D2321 (2014)

ASTM C1479 (2013) defined the backfill categories for rigid pipe design. It combined the USCS system with the AASHTO soil classification system (AASHTO M145, 2003) and proposed four categories of backfill material for rigid pipes as shown in Table 2.3.

Table 2.3: Backfill Material Categories for Rigid Pipes

Soil category	USCS	AASHTO
I	SW, SP, GW, GP	A-1, A-3
II	GM, GC, SM, SC, CL, ML, CL-ML with 30% or more retained on #200 sieve	A-2-4, A-2-5, A-2-6, or A-4, or A-6 with 30% or more retained on #200 sieve
III	CL, ML, CL-ML with less than 30% retained on #200 sieve	A-2-7, or A-4, or A-6 with less than 30% retained on #200 sieve
IV	MH, CH, OL, OH, PT	A-5, A-7

Note: All symbols listed in the above table follow the definitions in ASTM D2487 (2011) and AASHTO M145 (2003).
Source: ASTM C1479 (2013)

The stiffness of a flexible pipe influences the compaction effect of backfill soil because more deflection of the pipe causes more stress relaxation in the pipe. The AASHTO (2012) requires a minimum pipe stiffness to minimize this distortion of flexible pipes during installation. Over-compacted soil could limit the lateral deformation of the pipe after construction so that it increased the possibility of pipe buckling at the pipe crown (Cameron, 2006). Initial peaking deflection of flexible pipes, if not excessive, is favorable (Webb, McGrath, & Selig, 1996). The non-symmetric backfilling at two sides of the pipe could cause distortion of the pipe (Rogers et al., 1995; Cameron, 2006). The clear spacing of the profile ribs for profile pipes should be smaller than 0.6 or larger than 2.6 times the maximum size of backfill soil to prevent potential

voids around the pipe (Sargand, Masada, & Hurd, 1996). The particle size of the bedding soil should be smaller than 1.25 inches (AASHTO, 2012).

Controlled Low Strength Material (CLSM), known as flowable fill, is also used as the backfill material in pipeline projects. Typical mix of CLSM uses sand, fly ash, and water; however, cement content is on the order of 50 – 100 lbs/yd³, which is extremely low relative to structural concrete mixes (Howard, 1996).

The trench width and backfill material are essential for buried pipe design. However, for SRHDPE pipes, no specification is available for design. It is necessary to investigate the width and backfill effects on the mechanical behavior of the SRHDPE pipes.

2.2.3 Compaction Techniques and Simulation Methods

Compaction is important for installation of buried pipes, especially for flexible pipes. Compaction has been recognized as the source for increasing the load carrying capacity of a flexible pipe due to its low stiffness (Katona, 1978). Vibratory plate compactor and rammer are two commonly used compactors in pipe installation. A rammer has a smaller size of foot and higher compaction pressure and is normally used for hunch zone compaction. Duncan, Williams, Sehn, and Seed (1991) proposed a method to estimate the earth pressure induced by compaction using different models of compactors from different manufactures.

Duncan et al. (1991) explained the mechanism of compaction as follows: (1) during compaction, both the vertical and horizontal stresses in soil increase due to the weight of the compactor and the dynamic force generated by the compactor; (2) when the compactor moves away, the increment of the vertical stress becomes zero; however, the horizontal earth pressure decrease to a certain value, which is referred to as the residual horizontal stress. Several investigators (e.g., Duncan & Seed, 1986; Seed & Duncan, 1986; Filz & Duncan, 1996; Chen & Fang, 2008; Yang, Han, Leshchinsky, & Parsons, 2012) developed different methods to simulate the compaction-induced stresses in different types of applications, for example, retaining walls and buried culverts. These methods can be grouped into two types and are briefly discussed below:

2.2.3.1 Hysteretic K_0 Method

The hysteretic K_0 method was originally proposed by Duncan and Seed (1986). They assumed the multiple cycles of loading and unloading happened under a K_0 -condition; in other words, the lateral stress increment is proportional to the vertical stress increment by a factor of K_0 . They treated the compaction-induced residual horizontal stress as an over-consolidation case, and the lateral earth pressure coefficient can be modified from K_0 considering the over-consolidation effect. Figure 2.1 presents the basic concept of the K_0 hysteretic method, which can be explained by the following stress path: (a) the initial stress condition in the soil can be represented as Point A in Figure 2.1 due to the overburden pressure caused by the placement of the backfill lift; (b) during the compaction, both the vertical and horizontal stresses increase to Point B following the K_0 line; (c) when the compaction load moves away, the stress condition moves to Point C following the K_p line; (4) the vertical stress continues to decrease following the K_p line to Point D at the same vertical pressure of Point A. During the compaction, the maximum increase of the horizontal stress is Δ , and the residual horizontal stress can be expressed as $\beta\Delta$, where β is fraction of Δ in fully reloading. They also proposed simplified steps which allow hand calculations by this method. These steps are briefly described as follows:

- Determine the maximum increase of the horizontal stress using Boussinesq's solution by the compaction load. A factor between zero and one should be multiplied by the maximum horizontal stress increase to obtain the residual horizontal stress increase;
- Calculate the residual horizontal stress as the summation of the residual horizontal stress increase and the horizontal stress at rest; and
- The near surface horizontal stress should be limited to the Rankine passive lateral earth pressure.

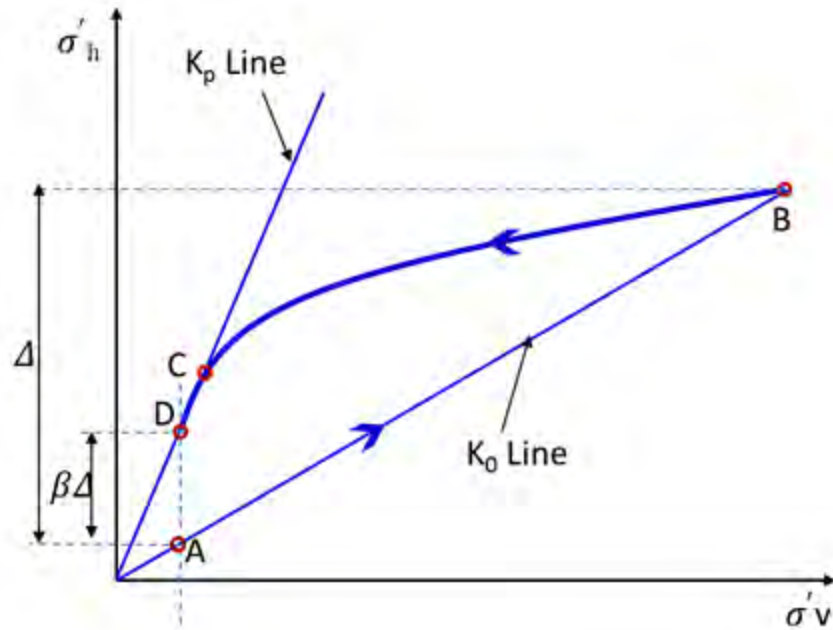


Figure 2.1: Basis Concept of the Hysteretic K_0 Method

Source: Duncan & Seed (1986)

Seed and Duncan (1986) incorporated the hysteretic K_0 method into the FE analysis to analyze the compaction effect in retaining walls and buried culverts. In their model, the compaction-induced horizontal stress was applied to the mesh to simulate the compaction. They ignored the relaxation of the residual horizontal stress due to the deformation of the mesh. This method was also evaluated by Filz and Duncan (1996) through laboratory and field tests. Chen and Fang (2008) developed a laboratory-scale model test to investigate the compaction effect on sand without any consideration of movement of the wall behind the sand. They compared the measured data, the Jaky at-rest earth pressure line, the Rankine active earth pressure line, and the Rankine passive earth pressure line. They concluded that in the compaction zone, the lateral stress could be calculated using the Rankine passive earth pressure theory, while below the compaction zone, the lateral stress was close to the Jaky at-rest earth pressure. Yang et al. (2012) modified the hysteretic K_0 method and allowed the stress path to cross the Rankine passive earth pressure line to consider the geocell reinforcement effect during the compaction.

The hysteretic K_0 method uses the concept of the over-consolidation ratio to consider the compaction-induced horizontal stress. In this method, the compaction effect is expressed by an

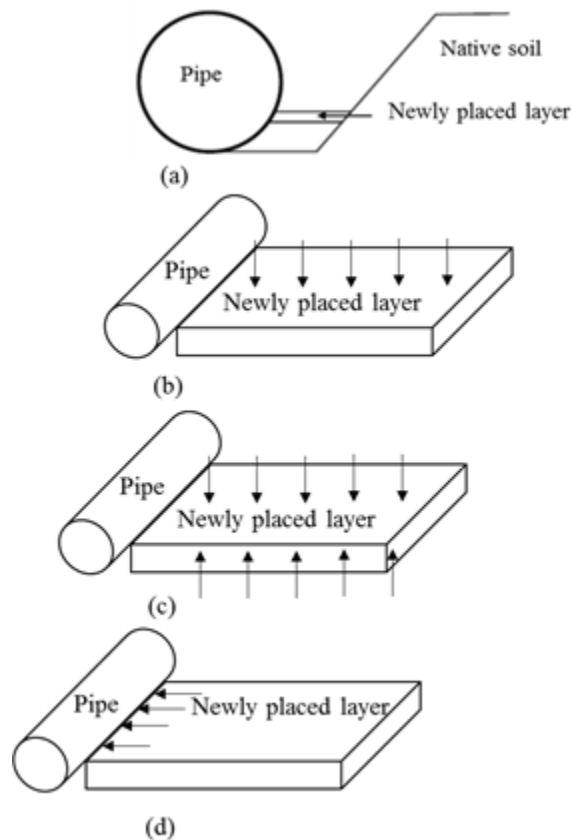
equivalent over-consolidation ratio. This method has proven difficult to analyze the elastic-plastic behavior of the soil during compaction (Elshimi & Moore, 2013).

2.2.3.2. Additional Surcharge Method

Additional surcharge method is a more straight forward method. One should apply additional surcharge load to the soil to simulate the compaction; however, the load has to be maintained all the way even after the completion of the compaction. Katona (1978) proposed to apply a temporary surcharge on the surface of the newly placed layer to simulate the compaction around the pipe. This surcharge remains after the compaction, which is not real in the engineering practice. In order to solve this problem, Katona suggested applying a pressure in the opposite direction on the placed layer before the placement of the next layer. This method was named as the “squeeze layer method.” However, the above two methods could not create a comparable lateral movement of soil during compaction because of the use of the elastic model. Furthermore, the additional load could not be removed; otherwise the residual deformation would become zero. The lateral earth pressure coefficient during the compaction is assumed as K_0 , which is not accurate because the soil moves towards the pipe. Taleb and Moore (1999) proposed to apply horizontal pressure directly on the soil to simulate the compaction. The magnitude of the earth pressure can be calculated as the vertical earth pressure times the passive lateral earth pressure coefficient. Elshimi and Moore (2013) considered the possible relaxation of the horizontal pressure caused by the deformation of the flexible pipe and suggested to use 2 as the lateral earth pressure coefficient. The applied horizontal load should be maintained after the completion of compaction. McGrath, Selig, Webb, and Zoladz (1999) summarized the above-mentioned techniques as shown in Figure 2.2 and assessed the advantages and disadvantages of each method. Katona (2015a, 2015b) modified the Duncan-Selig soil model to simulate the plastic-like behavior of soil during compaction and incorporated the modified model into the Culvert Analysis and DEsign (CANDE) software for different types of pipes to demonstrate the effectiveness of this model.

Even though the above methods can simulate the compaction-induced stresses, they cannot address the following three characteristics of compaction behavior:

- Applied load should be removed after the completion of the compaction for each layer;
- Residual horizontal stress and strain should remain after the compaction load is removed;
- Pipe interacts with soil during the compaction. In other words, the deformation of the pipe is induced by the lateral deformation of the surrounding soil.



(a) Placement of a new layer; (b) Applying vertical pressure method; (c) Squeeze layer method; and (d) Applying horizontal pressure method

Figure 2.2: Compaction Models for Buried Pipes by Applying Additional Pressure

Modified from McGrath et al. (1999)

2.3 Load Transfer Mechanism Above Buried Pipes

2.3.1 Loads and Deflections of Pipes During Installation

Several methods have been proposed to estimate the earth pressure at the top of pipes (Marston & Anderson, 1913; Spangler, 1941; McGrath et al., 1999; Sargand, Masada, & Schehl, 2001; Sargand et al., 2002; Sargand, Masada, Tarawneh, & Gruver, 2008; Corey et al., 2014). Marston and Anderson (1913) developed a theoretical solution for the vertical load transferred to the top of a pipe considering the friction between the soil above the pipe and the trench walls. Marston (1930) investigated the earth pressures on pipes buried in an embankment. He suggested that the embankment height could be increased by introducing a compressible layer over the pipe to enhance the soil arching effect. Spangler (1941) assumed a horizontal passive earth pressure distributed like a parabolic at the side of the flexible pipe, and the magnitude of this horizontal pressure was a function of the soil stiffness and the pipe horizontal deflection. Spangler (1962) considered the complete and incomplete projection conditions to calculate the earth pressures on the top of pipes buried in an embankment. However, the Marston-Spangler theory likely overestimates the earth pressure at the top of the pipe by the following reasons: (1) the backfill above the pipe was assumed at an active state, thus underestimating the friction between the trench wall and the backfill material, and (2) the cohesion of the backfill soil was neglected (Schofield, 1980; Moser & Folkman, 2008; McAfee & Valsangkar, 2008). In addition, the existing methods (Marston, 1930; Spangler, 1941, 1962) using the Marston-Spangler theory require 10 empirical parameters. Determination of each parameter includes uncertainty. Therefore, the uncertainty of earth pressure estimation could be enlarged (Moser & Folkman, 2008). Höeg (1968) investigated the pipe-soil interaction and found that the influence zone of the pipe-soil interaction was one to two times the rigid pipe diameter. Meyerhof and Adams (1968) developed a formula for the earth pressure on a buried rigid pipe similar to the Marston-Spangler theory. They assumed that the lateral earth pressure coefficient of the soil above the rigid pipe was 0.95. The American Water Works Association (Lischer, 1969) adopted a simplified approach based on the Marston-Spangler theory. In this method, the product of the settlement ratio (r_{sd}) and the projection ratio (p) was estimated as 0.75. The frustum calculation method (Matyas & Davis, 1983; Li, 2009) assumed the soil load on a buried rigid pipe was equal to the

weight of the soil column above the pipe. The China Association for Engineering Construction Standardization (CECS, 2004) simplified the earth pressure acting on the top of a buried flexible pipe as that equal to the geostatic stress of the overburden soil. AASHTO (2012) has widely been used in the design of buried pipes in the United States. This standard includes two methods to calculate the earth pressure on the top of the pipe: (1) the soil prism pressure, which is equal to the overburden stress at the top of the pipe level; and (2) the soil arch pressure, which is equal to the overburden stress multiplied by the vertical arching factor (VAF). The VAF can be calculated by an empirical method, which was originally proposed by McGrath (1998). The vertical load on the top of the pipe can be calculated as follows:

$$W = VAF \times W_{sp} \quad \text{Equation 2.2}$$

For a fully-bonded interface between pipe and soil (McGrath et al., 1999):

$$VAF = 1.06 - 0.96 \left(\frac{S_H - 0.7}{S_H + 1.75} \right) \quad \text{Equation 2.3}$$

For a free-slip interface between pipe and soil (McGrath et al., 1999; AASHTO, 2012):

$$VAF = 0.76 - 0.71 \left(\frac{S_H - 0.7}{S_H + 1.75} \right) \quad \text{Equation 2.4}$$

$$S_H = \frac{M_s}{EA/R} \quad \text{Equation 2.5}$$

Where:

W_{sp} = the soil prism load above a pipe

S_H = the hoop stiffness parameter

M_s = the constrained modulus of elasticity of soil

E = the Young's modulus of elasticity of the pipe material

A = the wall cross-sectional area of the pipe

R = the radius of the pipe.

The load on a pipe during installation can cause the deflection of the pipe. Spangler (1941) considered the following reasons for the ability of a flexible pipe to carry the load: (1) the redistribution of the load around the pipe, and (2) the passive pressure at sides of the pipe induced by the outward movement of the pipe against the trench walls. The pipe deflection results in the above two benefits. Spangler proposed the Iowa Formula to calculate the deflection of a flexible pipe as expressed in Equation 2.6.

$$\Delta X = \frac{D_L K W_c r^3}{EI + 0.061er^4} \quad \text{Equation 2.6}$$

Where:

D_L = the deflection lag factor

K = a bedding constant

W_c = Marston's load

r = the mean radius of a pipe

E = the modulus of elasticity of pipe material

I = the moment of inertia of pipe wall

e = the modulus of passive resistance of side fill

ΔX = the horizontal deflection or change in pipe diameter.

The modulus of passive resistance of the side fill e in Equation 2.6 was difficult to determine since it was not a soil property. Watkins and Spangler (1958) modified the Iowa Formula by introducing a new parameter referred to as the modulus of reaction instead of e . They also developed a test method to determine the modulus of reaction. However, great efforts have been made by researchers attempting to measure the modulus of reaction without much success. A more reliable method of estimating the modulus of soil reaction was proposed by Howard (1996) using the back-calculation method. The deflections, strains, buckling deformations, bending, and hoop stresses can be calculated and used as the design criteria for buried flexible pipes using the above methods (Spangler, 1941; Watkins & Spangler, 1958). However, these methods assumed the deformation of the pipe was only caused by the overburden pressure of the soil cover and the weight of a superstructure above the buried pipe. Design methods, including Spangler (1941), Watkins and Spangler (1958), CECS (2004), and

AASHTO (2012), do not consider the initial deformation of the pipe caused by the compaction during backfilling. The Spangler (1941) method assumed the pipe deformed like a horizontal ellipse; however, a vertical ellipse was observed once the installation effect was considered (Arockiasamy, Chaallal, Limpeteprakarn, 2006; Mai, Hoult, & Moore, 2014). Sargand et al. (1996), McGrath (1998), and Masada and Sargand (2007) pointed out that the flexible pipe deformed into a shape like a vertical ellipse when the backfilling and compaction were below the pipe crown level. The shape of the pipe gradually returned to be round when the backfilling was above the pipe crown level. This phenomenon was referred to as “peaking behavior,” which is beneficial for improving the load carrying capacity of the flexible pipe verified by field test results. Masada and Sargand (2007) proposed a theoretical formula to calculate the peaking deflection as shown in Equation 2.7:

$$\frac{\Delta y}{D} = \frac{4.7P_c + K_0 r \gamma}{3.874(PS)} \quad \text{Equation 2.7}$$

Where:

Δy = the vertical deflection of the pipe

D = the diameter of the pipe

K_0 = the lateral earth pressure coefficient at rest

r = the radius of the pipe

γ = the unit weight of the backfill material

PS = the pipe stiffness.

2.3.2 Load Transfer Mechanism of Buried Pipes in Service

Buried pipes have been commonly used for drainage in highway and railway projects, which are often subjected to traffic loading. Boussinesq’s solution is a basic formula commonly used to calculate the additional stress in the soil cover of the pipe at different depth. Hall and Newmark (1977) developed a load coefficient based on Boussinesq’s solution for calculating the concentrated load on a pipe:

$$W_{sc} = \frac{C_s P F'}{L}$$

Equation 2.8

Where:

W_{sc} = the load per length on the pipe

P = the concentrated load

L = the effective length of the pipe

C_s = a load coefficient, which is a function of the trench width and the soil cover thickness

F' = an impact factor (typically 1.0-1.5 for pipes under highways)

Antaki (1997) suggested that the pressure on the top of the pipe induced by the surface load can be calculated using the following equation:

$$p_p = \frac{3P_s}{2\pi H^2 \left[1 + \left(\frac{d_s}{H} \right)^2 \right]^{\frac{5}{2}}}$$

Equation 2.9

Where:

p_p = the pressure transmitted to the pipe

P_s = the concentrated load on the road surface

H = the soil cover thickness

d_s = the offset distance from the pipe to the line of the load application on the surface.

Moser and Folkman (2008) suggested that the total load on the pipe was the surface load plus the weight of the soil cover. Typically, the weight of the soil cover is ignored. The surface load transferred to the top of the pipe with a distribution angle of $\theta = 45^\circ - \phi/2$ (ϕ is the soil friction angle). In practice, the pressure on the pipe top can be simply calculated as follows with a friction angle of 27° :

$$P = \frac{W}{(B + H)(L + H)}$$

Equation 2.10

Where:

p = the pressure on the pipe top

W = the surface load

B = the width of the stress distribution area

H = the soil cover thickness

L = length of the stress distribution area

AASHTO (2012) suggested the live load transferred to the pipe with the distribution width based on the AASHTO H-25 truck load as shown in Table 2.4. The live load distribution coefficient was also suggested in AASHTO (2012) as the lesser of the ratio of the distribution width to the outside diameter of the pipe and one.

Table 2.4: Live Load Distribution Under the AASHTO H-25 Truck

Soil cover thickness (ft)	Live load transfer to pipe (psi)	Live load distribution width (ft)
1	15.6	2.3
2	7.0	4.0
3	5.2	5.5
4	3.5	7.2
5	2.2	8.8
6	1.7	10.3
7	1.6	12
8	0.9	13.6
10	negligible	N/A
12	negligible	N/A

Source: AASHTO (2012)

Giroud and Han (2004) suggested an approximate solution for the vertical pressure distribution angle from a base course to a subgrade based on Burmister's layered elastic solution as follows:

$$\tan \alpha_1 = \tan \alpha_o \left[1 + 0.204 \left(\frac{E_1}{E_2} - 1 \right) \right] \quad \text{Equation 2.11}$$

Where:

α_1 = the pressure distribution angle in the base coarse

α_o = the reference pressure distribution angle for a uniform medium defined by $E_1 = E_2$, E_1 = the modulus of elasticity of the base coarse, and E_2 = the modulus of elasticity of the subgrade

The reference distribution angle for a uniform medium can be taken as 27° (i.e., 2:1 distribution)

The above-mentioned methods are mainly based on elastic solutions. The compatibility of pipe and soil (i.e., the soil deformation and the pipe deflection) was not considered. In other words, if the deflection of the pipe is larger than the deformation of the surrounding soil, more load will transfer to the surrounding soil; if the deflection of the pipe is smaller than the deformation of the surrounding soil, the pipe will carry more load. These phenomena are referred to as the soil arching effect.

2.4 Long-Term Behavior of HDPE Pipes

AASHTO (2012) proposed a method to calculate the vertical load on the top of the pipe as shown in Equations 2.2 to 2.4. In Equation 2.4, the hoop stiffness depends on the elastic modulus of the pipe material. For HDPE pipes, the pipe material is polyethylene. The recommended short-term modulus of polyethylene is 110 ksi while its long-term modulus is only 22 ksi. Consequently, load would gradually transfer from the pipe to the surrounding soil considering the soil arching effect. However, it has to be pointed out that the soil arching effect may lose with elapsed time. In practice, the soil prism load is widely used as the design load for flexible pipes. The long-term behavior of HDPE pipe is more critical for the HDPE pipe design. A series of research was conducted by Hsuan and her co-workers for the Florida Department of Transportation (FDOT) on the long-term behavior of the HDPE pipe material (Hsuan & Zhang, 2005; Hsuan & McGrath, 2005). They used accelerated creep tests to simulate the HDPE pipe under different environments and temperatures. The recommended short-term and long-term

tensile strengths of the HDPE material are 3 and 0.9 ksi, respectively; while their short-term and long-term moduli are the same as those suggested by AASHTO (2012).

Khatri (2012) conducted a creep test on an SRHDPE pipe section in the air for 1 month under a constant temperature of 27°C. He found that the pipe stiffness decreased by 25% with time. No stiffness reduction factor is available for the current SRHDPE pipe design.

2.5 Previous Research on SRHDPE Pipes

Moser and Folkman (2008) buried SRHDPE pipes in the field with different pipe diameters, while the soil compacted was 87% of standard proctor density. The test results indicated that the SRHDPE pipes had a similar behavior with the low stiffness metal corrugated pipes. Moore (2009) performed stub compression and hoop compression tests on SRHDPE pipe samples or sections with diameters of 2 and 5 ft. He found that the helically-wounded steel ribs provided sufficient safety for the SRHDPE pipes at required buried depths. To evaluate the performance of a deeply buried pipe system, large-scale buried pipe tests were also conducted on 2 and 5 ft diameter pipes. The pipe deflected like a conventional buried metal culvert and the deflection was less than the limit of 5%. He concluded that the AASHTO method for the flexible steel pipe can be used to design the SRHDPE pipe to meet the deflection requirement.

One steel-reinforced pipe and one conventional HDPE pipe were installed with crushed stone as a backfill on the Manhead Road by the Utah Department of Transportation (UDOT; Folkman & Rowley, 2013). The diameter of both pipes was 2 ft. These two pipes were installed in parallel at clear spacing of 5 inches using the same installation method. The thickness of the soil cover over both pipes was approximately 3 ft. The vertical and horizontal deflections of the pipes were measured immediately after the installation and during the service life. The conventional HDPE pipe had larger deflections than the steel reinforced HDPE pipe. The maximum average vertical and horizontal deflections were -1.99% and 2.24%, respectively, for the SRHDPE pipe, while the conventional HDPE pipe had -4.24% vertical and 4.06% horizontal deflections after 1 month of installation. In addition, the maximum average vertical and horizontal deflections were -1.63% and 1.78%, respectively, for the SRHDPE pipe, while the HDPE pipe had -4.19% vertical and 3.97% horizontal deflections after 1 year of installation.

Three SRHDPE pipes with a diameter of 8 ft and a length of 100 ft were installed in Fort Benning, Georgia (Hardert, 2011). The thickness of the soil cover was 16.2 ft. The vertical and horizontal diameter changes in 1 year were 1.54 and 1.18 inches, respectively.

Research on SRHDPE pipes has also been conducted at the University of Kansas. Khatri (2012, 2014) did a series of laboratory tests to determine the mechanical properties of the SRHDPE pipe. Khatri, Han, Parsons, et al. (2013) conducted parallel plate load tests on the SRHDPE to determine the pipe stiffness. Corey et al. (2014) conducted large-scale box tests to evaluate the protection effect of the geogrid on the shallow buried SRHDPE pipes. Khatri, Han, Corey, Parsons, and Brennan (2015) investigated the installation effect of the SRHDPE pipe in a large test box.

2.6 Performance Limits

Buried pipes should first survive during installation. There are the performance limits for a pipe during installation, which are related to stress, strain, deflection, and buckling of the pipe. The following performance limits are usually considered in the buried pipe design (Moser & Folkman, 2008):

2.6.1 Wall Crushing (Primary Performance Limit for Rigid Pipes and Stiffer Flexible Pipes)

This performance limit describes the stress condition in the pipe reaches the yield stress or the ultimate stress of the pipe material. Wall crushing check can be easily conducted by comparing the compressive stress in the pipe with the yield strength of the pipe. The compressive stress in the pipe can be calculated as follows:

$$\sigma_{rc} = \frac{P_v D}{2A}$$

Equation 2.12

Where:

σ_{rc} = the compressive stress of the pipe

P_v = the vertical soil pressure as shown in Figure 2.3

D = the pipe diameter

A = the cross section area of the pipe wall per unit length.

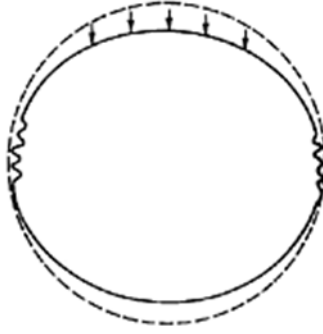


Figure 2.3: Schematic of the Wall Crushing

Source: Moser & Folkman (2008)

Wall crushing can also be influenced by the bending stress in the pipe wall. The bending stress is:

$$\sigma_b = \frac{Mt}{2I} \quad \text{Equation 2.13}$$

Where:

σ_b = the bending stress in the pipe

M = the bending moment per unit length

t = the thickness of the pipe wall

I = the moment of inertia of pipe wall per unit length

2.6.2 Wall Buckling

Wall buckling can occur when the pipe stiffness is not sufficient. Wall buckling may control the design when the buckling strain is greater than the strain limit of the pipe wall.

For a circular ring (without buried in a soil) in a plane stress condition subjected to uniform external pressure, its critical buckling pressure is:

$$P_{cr} = \frac{3EI}{R^3} \quad \text{Equation 2.14}$$

Where:

P_{cr} = the critical buckling pressure

E = the elastic modulus of the ring

I = the moment of inertia

R = the radius of the ring

For a long tube, its elastic modulus should be changed to:

$$E_L = \frac{E}{1-\nu^2} \quad \text{Equation 2.15}$$

Where:

E_L = the elastic modulus of the long tube

E = the elastic modulus of the tube material

ν = the Poisson's ratio of the long tube

The moment of inertia of the pipe is:

$$I = \frac{t^3}{12} \quad \text{Equation 2.16}$$

Where:

I = the moment of inertia of the pipe wall

t = the thickness of the pipe wall.

When Equations 2.15 and 2.16 are substituted into Equation 2.14, it becomes:

$$P_{cr} = \frac{Et^3}{4R^3(1-\nu^2)} \quad \text{Equation 2.17}$$

The limiting value of P_{cr} should be less than $\frac{Et^3}{4R^3}$ or $\frac{\sigma_y t}{R}$, where σ_y is the yield stress of the pipe material.

The above equation of the buckling pressure is only valid for the pipe submerged in water. For pipes buried in the soil, Meyerhof and Baikie (1963) developed the following equation:

$$P_{cr} = 2\sqrt{\frac{E'}{1-\nu^2} \left(\frac{EI}{R^3} \right)} \quad \text{Equation 2.18}$$

Where:

E' = the soil reaction modulus, which is equal to the soil constrained modulus

Equation 2.18 can also be rewritten as:

$$P_{cr} = 1.15 \sqrt{E'P_b}, \quad P_b = \frac{2E}{1-\nu^2} \left(\frac{t}{D} \right)^3 \quad \text{Equation 2.19}$$

Where:

D = the diameter of the pipe

Test results showed that the above equation worked well for steel pipes; however, it was conservative for plastic pipes (Moser & Folkman, 2008). The more exact approach for pipe buckling is:

$$q_a = \frac{1}{FS} \left(32R_w B' E' \frac{EI}{D^3} \right)^{1/2} \quad \text{Equation 2.20}$$

Where:

q_a = the allowable buckling pressure

FS = the design factor of safety, 2.5 ($h/D > 2$) and 3.0 ($h/D > 2$), in which h is the soil cover thickness and D is the pipe diameter

R_w = the water buoyancy factor, $R_w = 1 - 0.33 \left(\frac{h_w}{h} \right)$, in which h_w is the height

of the groundwater surface above the top of the pipe

$B' = \frac{4(h^2 + Dh)}{(1 + \nu)[(2h + D)^2 + D^2(1 - 2\nu)]}$, if the Poisson's ratio of soil is assumed

to be 0.5, it can be simplified as $B' = \frac{4(h^2 + Dh)}{1.5(2h + D)^2}$

2.6.3 Buckling Check for the Pipe Installation

If a live load is considered, the following equation should be required for pipe installation:

$$\gamma_w h_w + R_w \frac{W_c}{D} + \frac{W_L}{D} \leq q_a \quad \text{Equation 2.21}$$

Where:

W_c = the vertical soil load on the top of the pipe per length

W_L = the live load above the top of the pipe

Equation 2.21 is not valid for the condition when a large diameter pipe is buried shallowly below the groundwater surface.

2.6.4 Over-Deflection

Over-deflection was defined as the deflection larger than 7.5% at a factor of safety of 4. The design deflection limit is recommended as 5% in most standards considering a factor of safety of 4.

2.6.5 Strain Limit

Strain is related to the deflection of a pipe. Strain limit can be satisfied by controlling the deflection limit during installation. Brittle, composite pipe, or deeply buried pipe is often controlled by a strain limit.

The strain described in the strain limit is referred to as the total circumferential strain, which includes bending strain, ring compression strain, hoop strain due to internal pressure, and strain due to Poisson's ratio effect in the longitudinal direction. For gravity sewer pipes, the bending strain is typically the largest and other types of strain may be negligible.

2.6.5.1 Bending Strain

If a pipe is assumed to deform elliptically, the bending strain of the pipe can be calculated as:

$$\varepsilon = \pm \left(\frac{t}{D} \right) \left(\frac{3\Delta y/D}{1 - 2\Delta y/D} \right)$$

Equation 2.22

Where:

ε = the maximum strain in the pipe due to ring bending

t = the pipe wall thickness

Δy = the pipe diameter change in the vertical direction

D = the pipe diameter

For profile wall pipes, Equation 2.22 can be simplified into:

$$\varepsilon = \pm \left(6 \frac{t}{D} \right) \left(\frac{\Delta y}{D} \right) \quad \text{Equation 2.23}$$

In Equation 2.23, the ratio of the pipe deflection to the pipe diameter ($\frac{\Delta y}{D}$) is assumed as 0.25.

2.6.5.2 Compression Strain.

From Equation 2.12, the compression strain of the pipe is:

$$\varepsilon_{rc} = \frac{P_v D}{2AE} = \frac{P_v D}{2tE} \quad \text{Equation 2.24}$$

Where:

ε_{rc} = the compression strain

P_v = the vertical soil pressure as shown in Figure 2.3

D = the pipe diameter

t = the thickness of the pipe wall

A = the cross section area of the pipe wall per unit length

2.6.5.3 Circumferential Strain Due to Poisson's Ratio Effect

The circumferential strain can be calculated as follows:

$$\varepsilon_c = \nu \varepsilon_L \quad \text{Equation 2.25}$$

Where:

ε_c = the circumferential strain

ε_L = the longitudinal strain

ν = the Poisson's ratio of the pipe wall

2.6.6 Delamination

Reinforced pipes may experience delamination when subjected to a ring deflection due to the radial tension and inter-laminar shear. The radial tensile stress is given by:

$$\sigma_r = \frac{T}{t(R + y)}$$

Equation 2.26

Where:

$$T = \int_{-c}^y \sigma da$$

σ_r = the radial tensile stress

t = the pipe wall thickness

R = the pipe radius

y = the distance from the neutral axis to the point in question

$c = t/2$

σ = the stress in the tangential direction as function of the position in the pipe wall (My/I); $da = (dy) \times (\text{unit length})$

Chapter 3: Field Performance of the SRHDPE Pipes Field Test I

3.1 Introduction

To evaluate the field performance of the SRHDPE pipe, two field tests were conducted in this research. This chapter presents the first field test, which is located close to Clinton Lake in Lawrence, KS, as shown in Figure 3.1. This field test is referred to as the Lawrence field test. The pipes were installed on E 1000 Road. The E 1000 Road is a two-way single-lane and high-volume road. The test road section consisted of a 24-ft-wide roadway with 2% grade on each side, a 6-ft-wide shoulder with 4% grade on each side, and an embankment beyond the shoulder with 6:1 grade on each side (Figure 3.2). The SRHDPE pipes were installed to replace corroded steel pipes. To investigate field performance of the SRHDPE pipes during installation and service, the test section was instrumented with displacement transducers, earth pressure cells, and strain gauges, and has been monitored for almost two years.



Figure 3.1: Location of the First Test Site
Source: Google (n.d.)

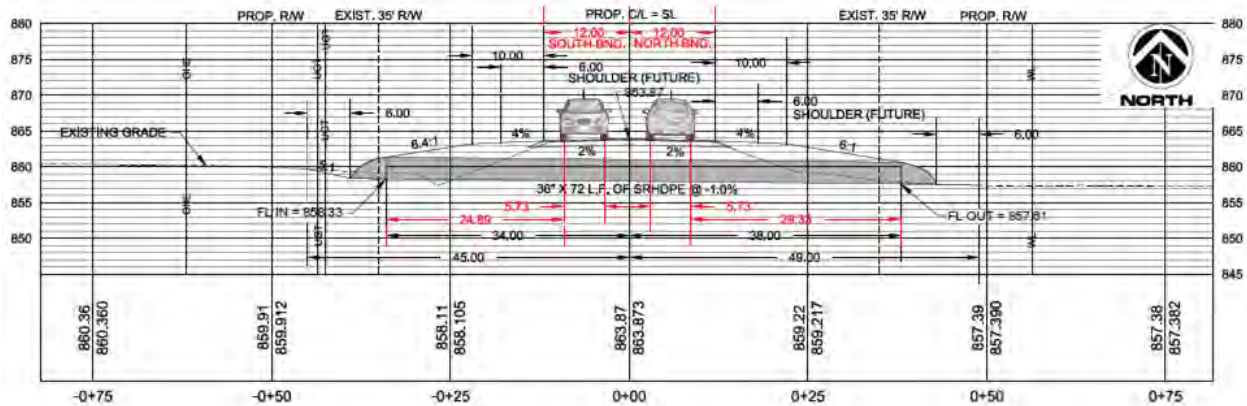


Figure 3.2: Road Section in the Field Test

3.2 Properties of the Backfill Material

The roadway section was divided into two test sections, in which crushed stone and AB3 aggregate were used, respectively. Crushed stone, used as bedding and backfill materials in one of the sections in the Lawrence field test, was poorly graded based on the USCS. Figure 3.3 shows the grain size distribution of the crushed stone. It had a mean size of 0.50 inches, a uniformity coefficient C_u of 1.28, and a curvature coefficient C_c of 0.95. The minimum and maximum unit weights of the crushed stone were 87 and 100 pcf, determined by conducting the minimum and maximum density tests (ASTM D4254, 2014; ASTM D4253, 2014). Plate loading tests were conducted on the fill material in a wooden box with a dimension of 32 inches long \times 32 inches wide \times 18 inches high to determine the modulus of the crushed stone. The modulus of the crushed stone compacted at the relative density of 79% was determined as 1,700 psi from the plate loading test. The peak friction angle of the crushed stone was 53° , obtained by large direct shear tests (ASTM D3080, 2011). The test results of the large direct shear test are shown in Figure 3.4.

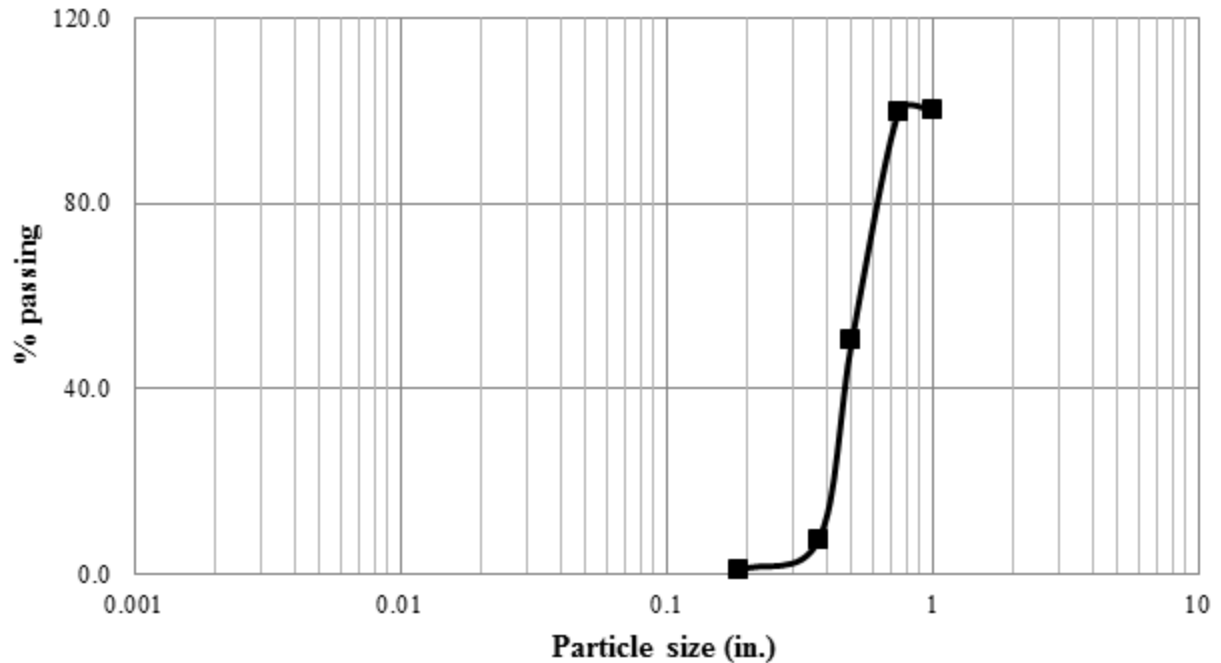
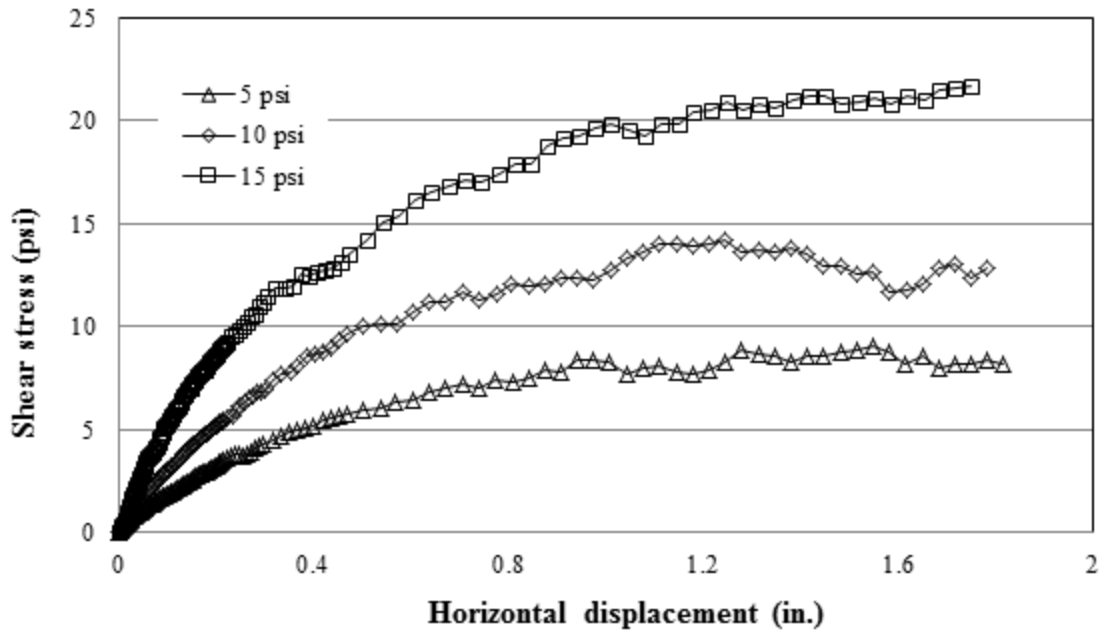
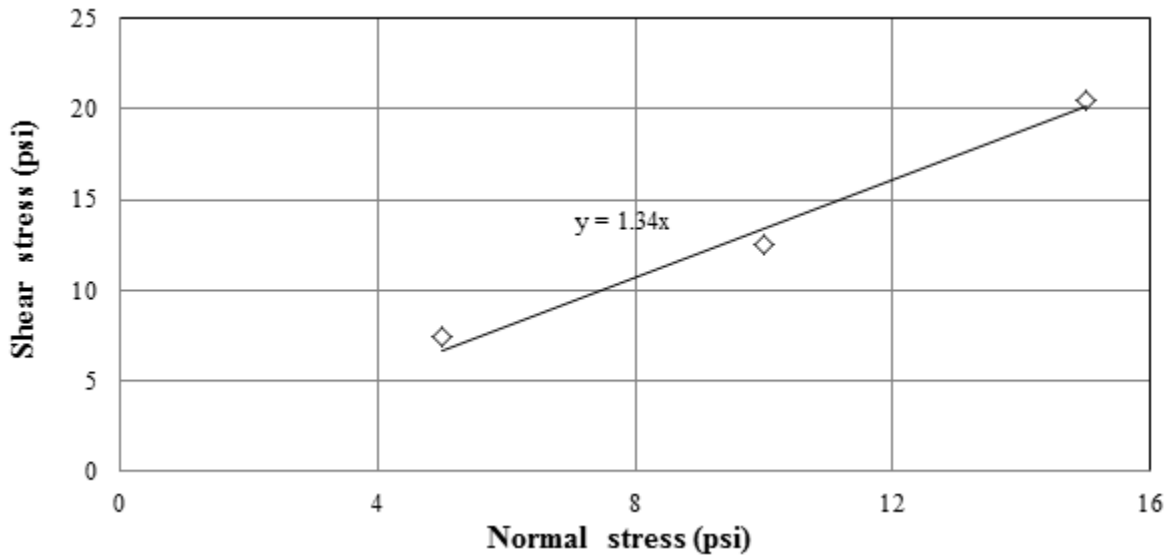


Figure 3.3: Grain Size Distribution of the Crushed Stone

AB3 aggregate were used as bedding and backfill materials in the second section in the Lawrence field test. The grain size distribution of the AB3 aggregate is shown in Figure 3.5. The AB3 aggregate was well-graded with a mean size of 0.1 inches, a uniformity coefficient C_u of 55, and a curvature coefficient C_c of 1.043. The fine particles of the AB3 aggregate had a liquid limit of 18. Figure 3.6 shows the compaction curve of the AB3 aggregate by the standard Proctor compaction tests per ASTM D698 (2012), which resulted in a maximum dry density of 141 pcf at the optimum moisture content of approximately 8%. The modulus of AB3 aggregate compacted at the optimum moisture content was 2,675 psi. The peak friction angle of the AB3 aggregate was 52.4° determined using large direct shear tests.



(a) Shear Stress vs. Displacement Curves



(b) Shear vs. Normal Stress

Figure 3.4: Large Direct Shear Box Tests for the Crushed Stone

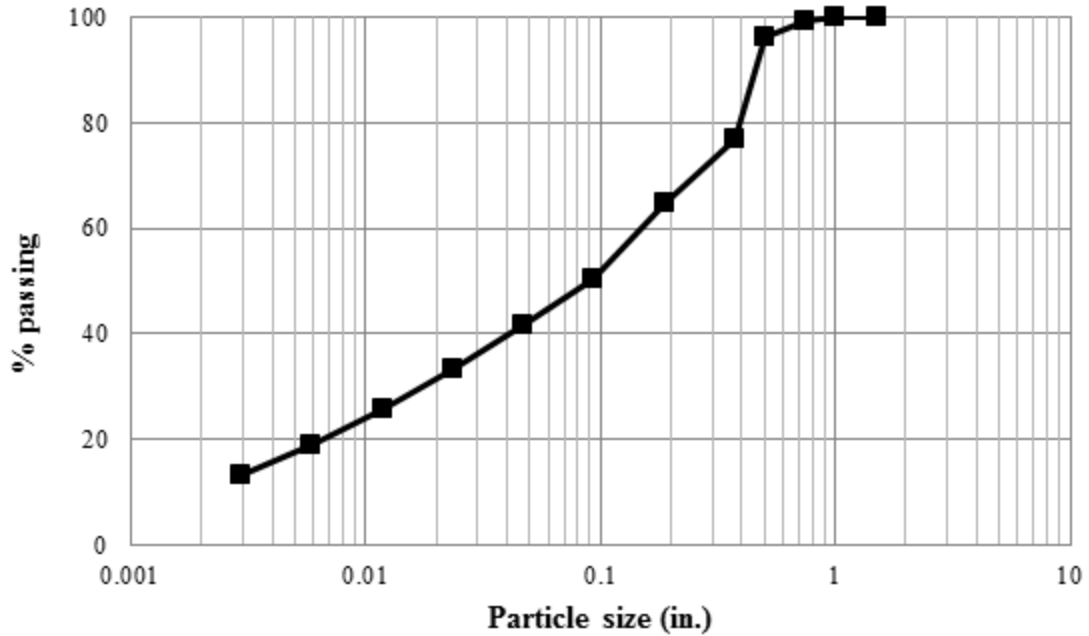


Figure 3.5: Grain Size Distribution of the AB3 Aggregate Used in the Lawrence Field Test

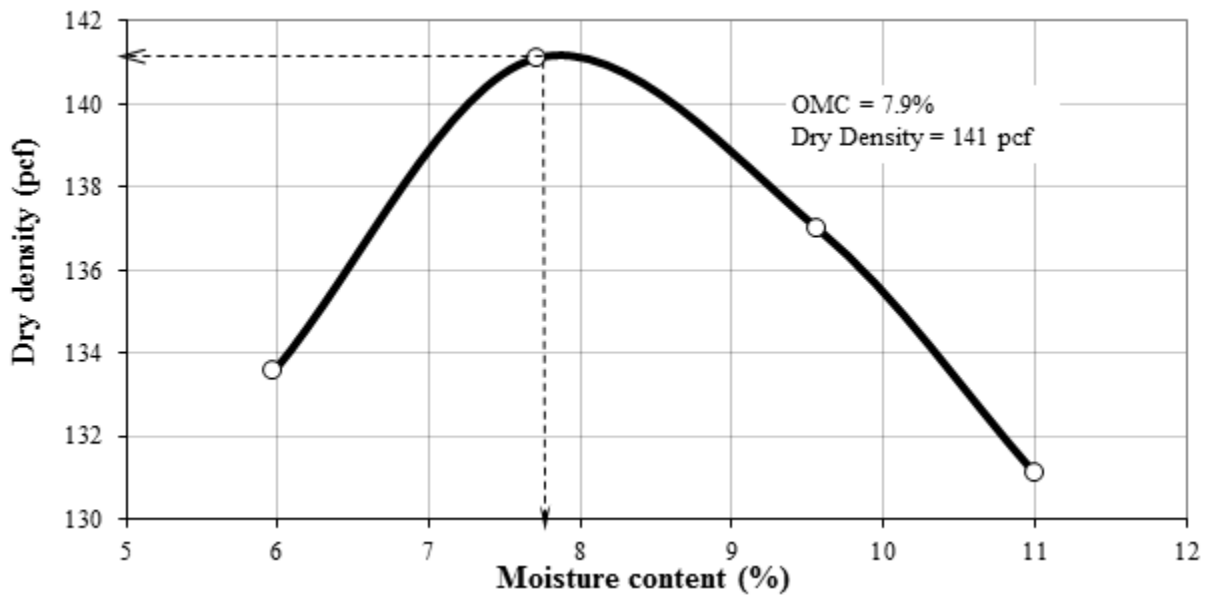


Figure 3.6: Standard Proctor Compaction Curve of the AB3 Aggregate Used in the Lawrence Field Test

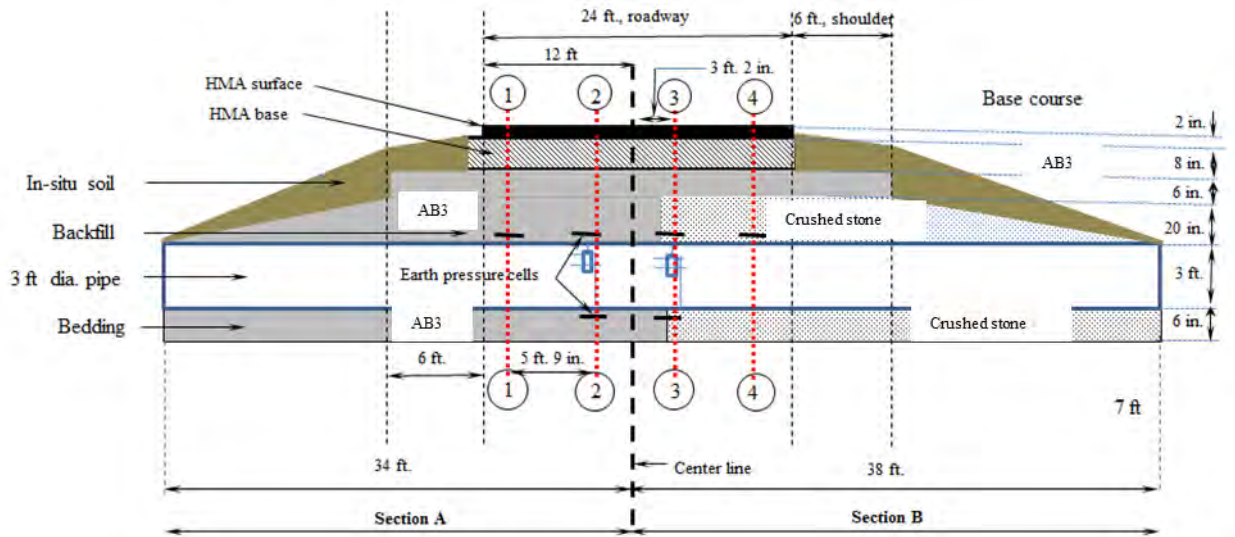
3.3 Test Site, Test Pipes, and Instrumentation

3.3.1 Test Site Condition

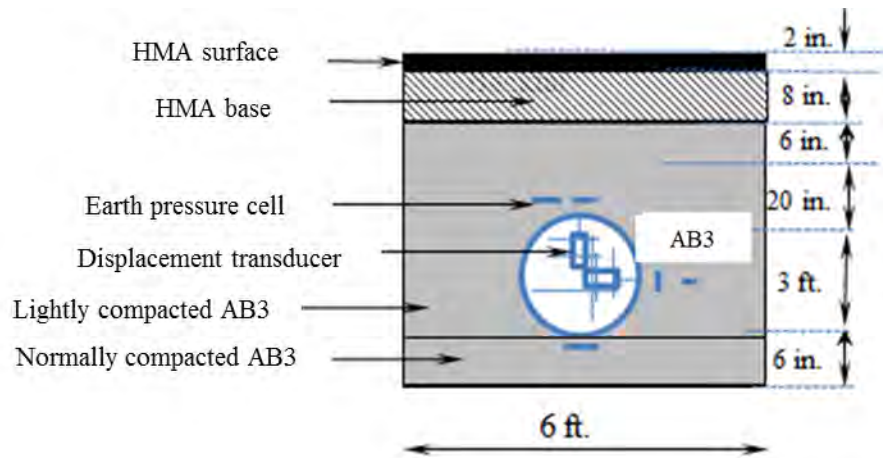
In the field test, the total run of the pipe was divided into two sections from the center of the roadway. Section A was backfilled with AB3 aggregate as both bedding and backfill materials on the western end, while Section B was with crushed stone as both bedding and backfill materials on the eastern end. Figure 3.7 shows the longitudinal and cross sections of the test. The test sections had a rectangular trench of 6 ft wide and 5 ft 8 inches deep in in-situ soil. The trench consisted of 6-inch-thick bedding material, 3 ft backfill, and 3 ft soil cover including a 9-inch-thick hot mix asphalt (HMA) base and a 2-inch-thick HMA surface. Three pipes with the length of 24 ft were installed in the trench. Section A had the AB3 aggregate as the backfill material up to the HMA base (Figure 3.7b); however, Section B had the same HMA base and surface and a 6 inch thick AB3 aggregate on the top of the crushed stone (Figure 3.7c).

3.3.2 Test Pipe

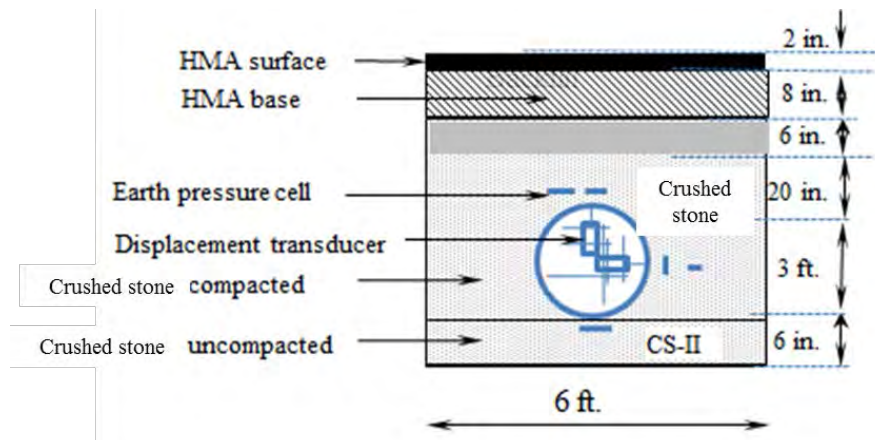
SRHDPE pipes of 36 inches in diameter were tested in the Lawrence field test. Three 24 ft long SRHDPE pipes with bell and spigot (with gasket) ends were provided by Contech Construction Products, Inc. Both the bell and spigot are reinforced with steel that is fully encased in stress-rated high-density polyethylene as shown in Figure 3.8. SRHDPE pipes were inspected and found that the pipes had glossy appearance, no chalking, no sticky or tacky materials, and no blisters, voids, or other defects.



(a) Longitudinal Section of the Test Section



(b) Section 2-2 (Section 2)



(c) Section 3-3 (Section 3)

Figure 3.7: Field Test Sections in the Lawrence Site



Figure 3.8: Test SRHDPE Pipes with Bell and Spigot Joints in the Field Test

3.3.3 Instrumentations

The instrumentation plan was developed to collect the data required to accurately characterize the structural performance of the pipe. The results from the laboratory tests in the first phase of this project indicated that the most significant pipe response would be near the crown and springline, thus the instrumentation was focused on these two positions. Figure 3.7a shows four different instrumented sections. For the Section A (i.e., the AB3 aggregate section), the pipe was instrumented as Sections 1 and 2, whereas for the Section B (i.e., the crushed stone section), the pipe was instrumented as Sections 3 and 4. Section 2 in the Section A and Section 3 in the Section B were instrumented under the traffic wheel paths close to the centerline of the roadway. Sections 2 and 3 were instrumented extensively to capture deflections using displacement transducers, strains on pipes using strain gages, and earth pressures around the pipe using vibrating wire type pressure cells. In addition, Sections 1 and 4, which were close to the shoulder, had only one vibrating wire pressure cell installed at the crown of the pipe under each path. Three SRHDPE pipes, each of 24 ft long, were used for the 72 ft pipe run. The middle pipe was laid under the roadway.

Four displacement transducers, two on each test section (Sections 2 and 3), were used to measure the changes in vertical and horizontal diameters during installation and service vehicles.

The displacement transducers were manufactured by Tokyo Sokki Kenkyujo, Co., Ltd, Japan. The holes were drilled through the pipe walls to fix the transducers on the pipes as shown in Figure 3.9.

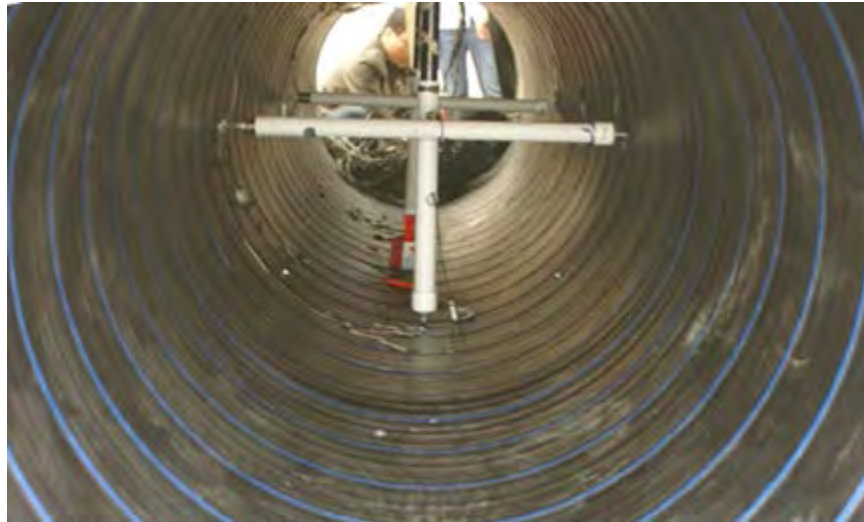
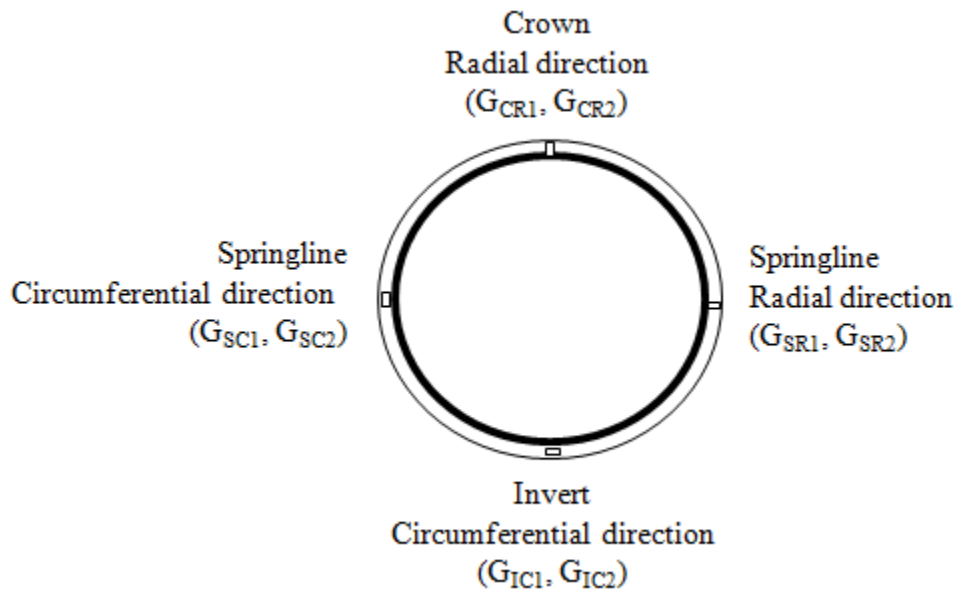


Figure 3.9: Displacement Transducers Inside the Pipe Section in the Field

Uniaxial foil-type electrical resistance (C2A-13-250 LW-120) strain gages, manufactured by the Vishay Precision Group, were used to measure the circumferential, radial, and longitudinal strains of the pipe at various locations as shown in Figure 3.10. For both pipe sections (Sections 2 and 3), the strain gages were installed outside and inside of the pipe on steel and plastic surfaces. The symbols, locations, and orientations of the strain gages were fixed on the pipe in the field test as shown in Figure 3.11a to d. In addition, six more strain gages on each section (Sections A and B) labeled with a double prime (") symbol were placed on the plastic, inside and outside of the pipe, between the ribs (i.e., valley) to measure the strains in the plastic at the pipe crown as shown in Figure 3.11e. These six strain gages were placed along the pipe run to the centerline of the roadway. For example, the strain gages notations (G''_{CL3} and G''_{CL4}) with a double prime symbol represent the strains at the pipe crown on plastic in the longitudinal direction from the instrumented section to the roadway centerline.

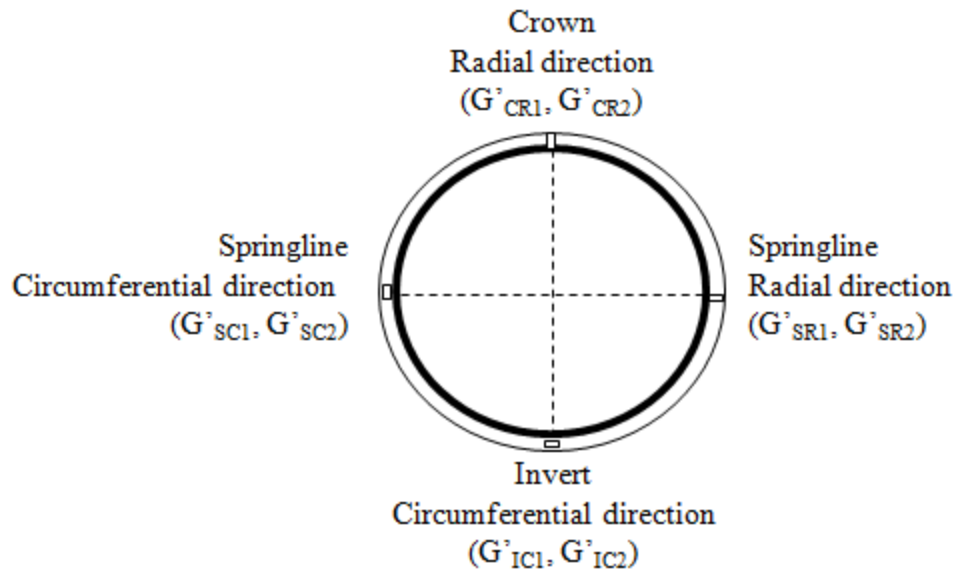


Figure 3.10: Strain Gages Fixed Outside of the Pipe in the Field

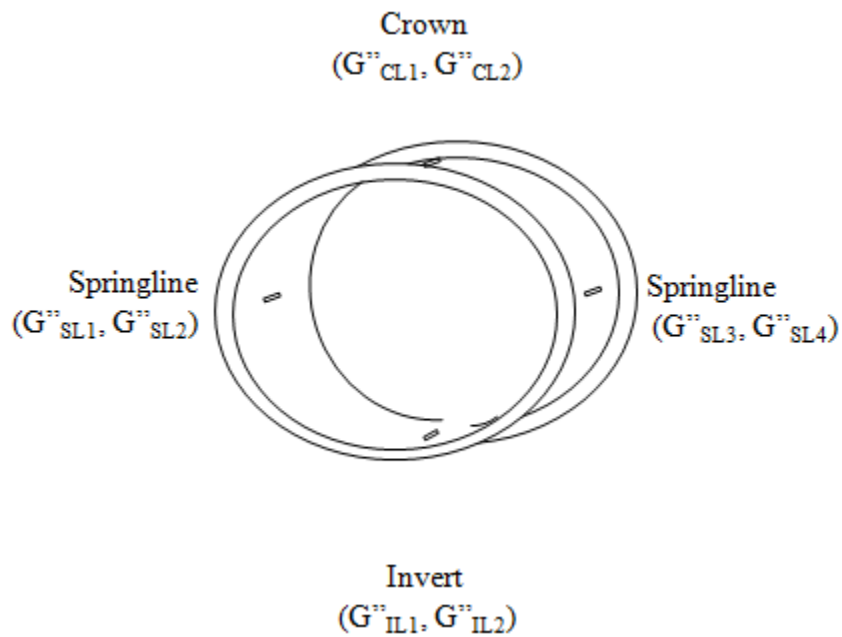


(a) On the Steel at Ribs

Figure 3.11: Symbols, Locations, and Orientations of the Strain Gages on the Pipe

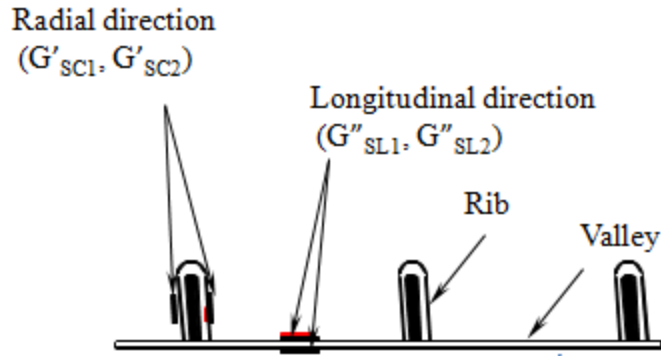


(b) On the Plastic at Ribs

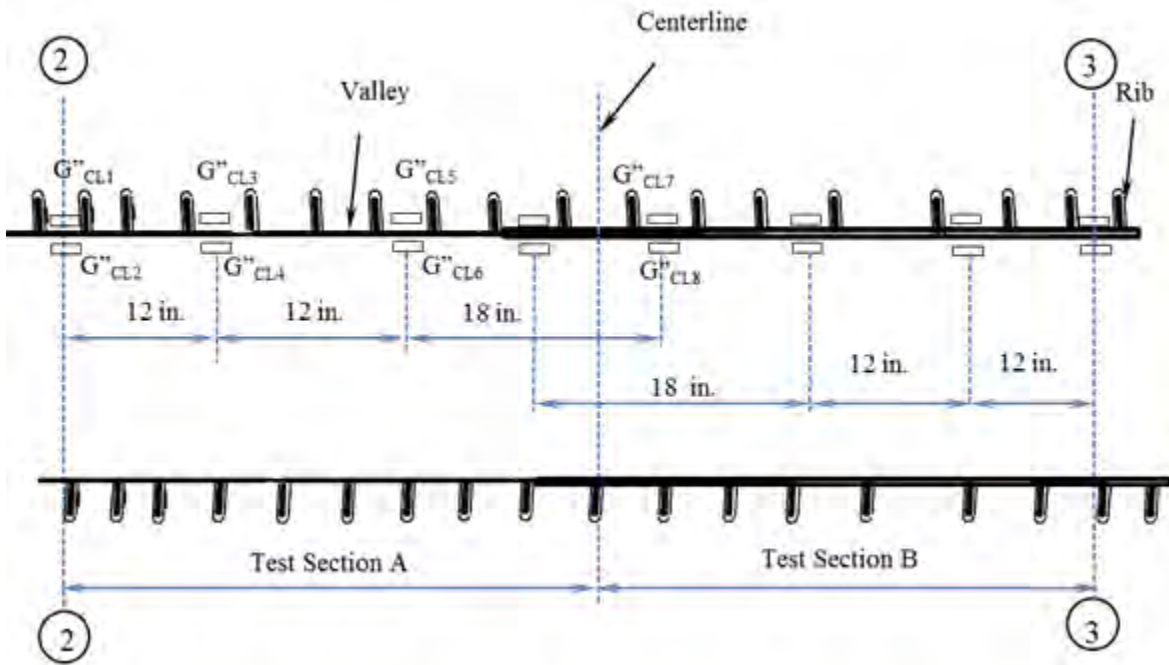


(c) In the Longitudinal Direction on the Plastic at Valley

Figure 3.11: Symbols, Locations, and Orientations of the Strain Gages on the Pipe (Continued)



(d) Strain Gages on the Plastic Surface



(e) On the Longitudinal Direction

Figure 3.11: Symbols, Locations, and Orientations of the Strain Gages on the Pipe (Continued)

Twelve vibrating wire pressure cells (model 4810), manufactured by Geokon with a capacity of 51 psi were installed around the pipe under the wheel paths of the vehicles. Sections 2 and 3 had five pressure cells each, whereas Sections 1 and 4 had one pressure cell each at the crown of the pipe. The notations, locations, and orientations of the pressure cells are presented in

Figure 3.12. The subscripts of the notations represent the positions at which the earth pressure cells were placed. The subscript letters I, S, W, and C stand for invert, springline, wall, and crown of the pipe, respectively, whereas the numerical value gives the horizontal distance from the position defined by the subscript letter. For example, the notations, E_{C0} and E_{C12} , represent earth pressure cells placed at the crown and at 12 inches horizontal distance from the crown towards the trench wall, respectively. Pressure cells, E'_{S0} , and E'_{S18} , labeled with a prime (') symbol, were installed for the horizontal earth pressure measurements, whereas the remaining pressure cells without the prime (') symbol were installed for the vertical earth pressure measurements.

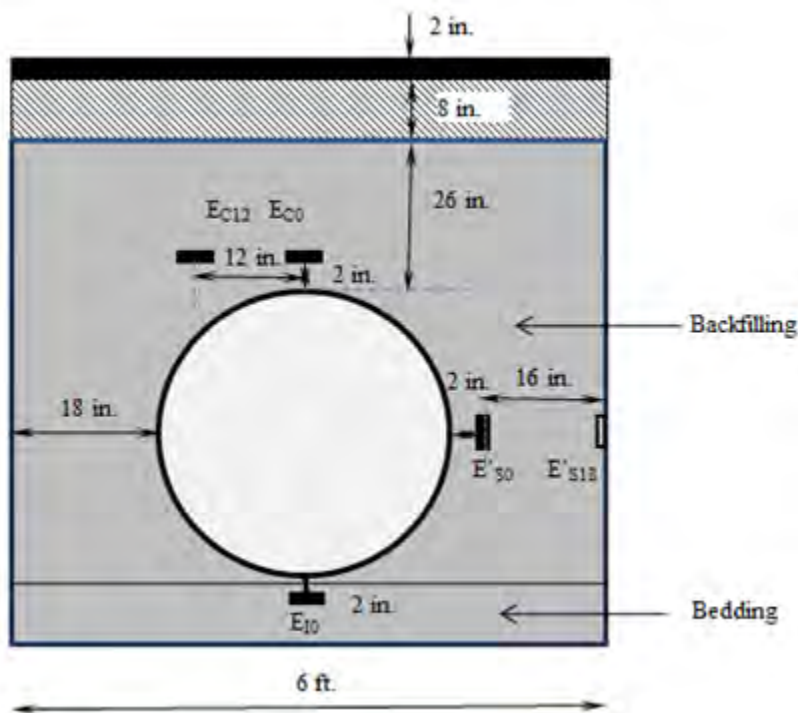


Figure 3.12: Earth Pressure Cells Around the Pipe Section

Two smart dynamic DC-204R data recorders were used to record data for four displacement transducers and four strain gauges. A CR1000 data logger produced by Campbell Scientific was used to measure earth pressures around the pipe from the vibrating wire pressure cells and strains at various locations on the steel and plastic. The power to the data recorders and computers was supplied using batteries and a generator.

3.4 Pipe Installation and Static Loading

3.4.1 Exhumation of the Corroded Corrugated Metal Pipe

An existing corrugated metal pipe of 24 inches diameter on the E 1000 Road at Lawrence, KS, because of the excessive corrosion was to be replaced with SRHDPE pipes of 36 inches in diameter. Figure 3.13 shows the corroded corrugated metal pipe before replacement. The existing metal pipe was found having lost most of its invert portions due to the corrosion. The test sections were constructed by the Douglas County Public Work.



Figure 3.13: The Corroded Corrugated Metal Pipe Before Replacement

A 2000 model Case 9030B excavator was used to dig out the existing HMA base and surface and the rectangular trench of 6 ft wide as shown in Figure 3.14. The width of the trench was chosen according to the KDOT (2007) specifications for pipe and culvert to provide sufficient working space for compaction equipment to properly and safely place and compact bedding, hunching, and backfill materials. A minimum trench width was maintained not to be less than the greater of either 1.5 times the pipe outside diameter plus 12 inches or the pipe

outside diameter plus 12 inches on each side suggested by ASTM D2321 (2014). The existing corrugated metal pipe was exhumed. The in-situ soil was found to be clayey soil at a moisture content of 24%. After the trench was excavated, the centerline of the roadway was marked as shown in Figure 3.15, and the placement of the bedding materials in both western and eastern sections (Sections A and B) was started.



Figure 3.14: Excavation of a Trench



Figure 3.15: Marking the Centerline Before the Placement of Bedding Materials

3.4.2 Bedding

AB3 aggregate and crushed stone were dumped from the height of approximately 5 to 6 ft into the trench using the excavator on the western and eastern test sections, respectively, and were leveled as shown in Figure 3.16. The bedding materials were not compacted on both test sections. The wheel paths on both sections were marked in order to locate the sections to be instrumented as shown in Figure 3.17. All earth pressure cells were connected to the data acquisition system. The earth pressure cells E_{10} were installed in the bedding materials on both test sections (Sections 2 and 3) under the wheel paths close to the centerline of the road at the invert of the pipe before the placement of the pipe in the trench as shown in Figure 3.18. Before each earth pressure installation, the trench bottom surface was leveled using sand and the pressure cell was placed, checked level with a spirit level, and then covered by the sand. The pressure cells were covered by sand to minimize the effect of non-uniform contacts of the backfill materials on the sensor surfaces of the pressure cells.



Figure 3.16: Placement of the Bedding Materials



Figure 3.17: Marking of the Locations of the Wheel Paths



Figure 3.18: An Earth Pressure Cell Installed at the Invert Of The Pipe

3.4.3 Placement of Pipe

After the placement of the bedding materials, galvanized steel end sections were connected to the ends of the pipes as shown in Figure 3.19. Each pipe was placed in the trench using the excavator (Figure 3.20). The pipes were connected to each other with the help of attached bell and spigot (with gasket) ends. The instrumented (middle) pipe was connected

carefully so that the displacement transducers fixed on the pipe inside to measure vertical deflections of the pipe oriented vertically. Figure 3.21 shows the pipes in the trench before backfilling. All the sensors, strain gages, and displacement transducers were connected to two separate DC-204R and the CR 1000 data acquisition system. The recorders were then adjusted and balanced to set all the initial values to zero.



Figure 3.19: Galvanized Steel End Sections

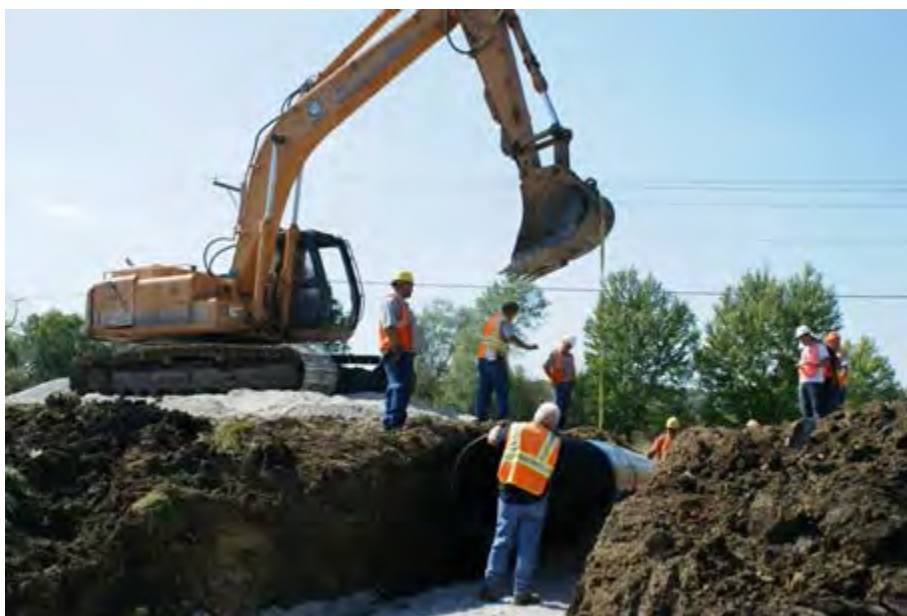


Figure 3.20: Placement of a Pipe into the Trench



Figure 3.21: Fully-Instrumented Pipes in the Trench

3.4.4 Backfilling and Soil Cover

AB3 aggregate and crushed stone were used as backfill materials. The backfilling was performed in layers of approximately 6 to 9 inches lift thick after compaction. A vibratory plate compactor, Wacker WP1550AW, was used for compaction of the crushed stone, whereas a tamping hammer, Multiequip MT65H, was used for compaction of the AB3 aggregate. The vibratory plate compactor, Wacker WP1550AW, consisted of a base plate of 23 inches \times 19.5 inches size with the operating weight of 194 lbs, vibrated at a frequency of 100 Hz. The tamping hammer, Multiequip MT65H, consisted of a shoe size of 11 inches \times 13 inches with the impact force of 2,450 to 2,900 lbs/blow, which can apply 590 to 695 blows in a minute. The vibratory plate compactor and the tamping hammer were used for the compaction of the backfills and the soil covers (up to a height of 26 inches above the crown of the pipe) as shown in Figure 3.22. For the AB3 aggregate backfill on the western test section (Section A), light compaction was used up to the springline to avoid excessive uplifting of the pipe. Compaction directly above the pipe surface was avoided to prevent possible damage of the pipe due to the compaction equipment. The backfilling was done in equal lifts on both sides of the pipe so as not to disturb the pipe alignment. Figure 3.23 shows the backfills placed up to the springline. To dump AB3 aggregate and crushed stone up to a height of 6 inches above the crown, the excavator was used. After that,

a Bobcat 2006 Model S300 was used to dump and level the soils as shown in Figure 3.24. The top 6 inches of AB3 aggregate was placed and compacted throughout the test section using the tamping hammer and then a smooth wheel vibratory roller, 2005 Model Hamm HD13. The vibratory roller, which has the operating weight of 8,741 lbs, compacts soils with the centrifugal force of 14 kips for a high amplitude and 9 kips for a low amplitude vibrating at a frequency of 60 to 51 Hz. Figure 3.25 shows the compacted AB3 aggregate surface before the placement of the HMA base. During the backfilling, the earth pressure cells were installed around the pipe for each test section as shown in Figure 3.26. The readings of the strain gages, displacement transducers, and earth pressure cells were taken using the data recorders after completion of each lift during backfilling.



(a) Eastern Test Section (Section B)

Figure 3.22: Backfilling and Compaction with a Vibratory Plate Compactor and a Tamping Hammer



(b) Western Test Section (Section A)

Figure 3.22: Backfilling and Compaction with a Vibratory Plate Compactor and a Tamping Hammer (Continued)



Figure 3.23: Backfilling up to the Springline



Figure 3.24: A Bobcat Used to Dump and Level Soils



Figure 3.25: The Compacted AB3 Surface Before the Placement of the HMA Base



(a) At the Pipe Springline



(b) At the Pipe Crown

Figure 3.26: Earth Pressure Cells, E_{s0} and E_{s18} Placed at the Springline and E_{C0} and E_{C12} at the Crown

3.4.5 Loading

After the compaction of the top 6-inch-thick AB3 aggregate, the wheel paths of vehicles were marked on the surface for each test section to apply a truck load on the pipe, as shown in Figure 3.27. A dump truck, 2004 International 7400 6x4, weighing 13.7 tons (empty) loaded with the HMA base course material of 15.2 tons, was used as the test truck (Figure 3.27) to apply the load on the pipe to monitor the effects of the construction vehicles on the pipe. The test truck consisted of two physical axles: a front steering axle and tandem axles at the end. Seventy-two percent of the total gross weight of 29 tons (sum of the weights of the empty truck and the loaded material) was carried by the rear axle, and the remaining 28% was shared by the front axle. The axle configuration and the load on each axle are shown in Figure 3.28. Based on the empty weight of 13.7 tons of the truck and the ground vehicle weight rating (GVWR) of around 28 tons, the maximum axle load capacities were 10 and 23 tons for front and rear axles, respectively.



Figure 3.27: Test Truck Used to Load the Pipe

The static truck load was applied on both the western and eastern test sections (Sections A and B) with the rear axle: a back axle at the center between the trench wall and the pipe crown, a back axle above the pipe crown, and a middle axle above the pipe crown, as shown in Figures 3.28 and 3.29. The contact area calculated for each rear wheel load of 5.25 tons at the axle

pressure of 120 psi was found to be 87.5 in². For each loading step, the truck was kept for a while until all readings from the displacement transducers were stable and recorded. After the truck static load, the truck was run over the pipe at a slow speed in order to capture the effect of the moving construction vehicle on the pipe.

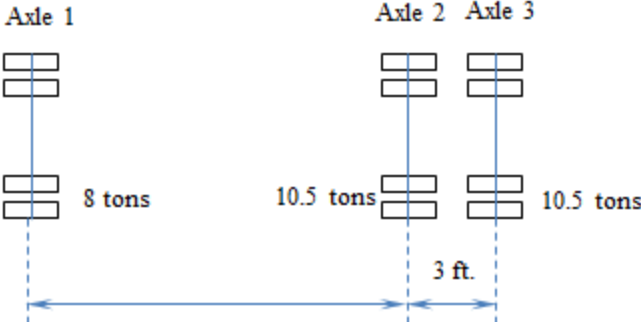
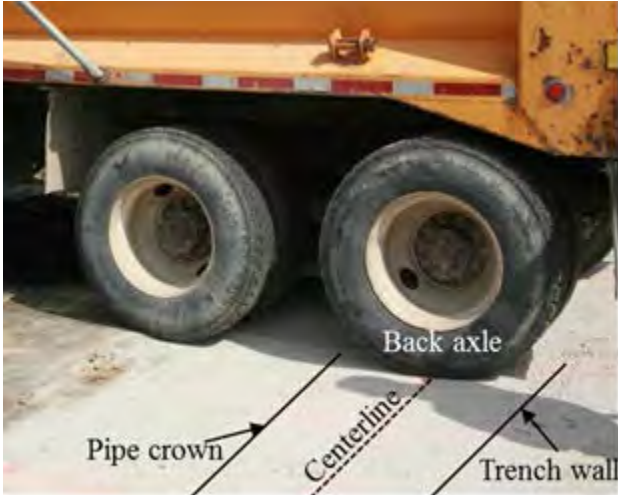


Figure 3.28: Axle Load Configuration of the Test Truck



(a) The Back Axle at the Center Between the Trench and the Crown

Figure 3.29: Application of Static Loads by the Test Truck



(b) The Back Axle Above the Crown



(c) The Middle Axle Above the Crown

Figure 3.29: Application of Static Loads by the Test Truck (Continued)

3.4.6 HMA Base and HMA Surface Preparation

After the truck load was applied on the unpaved road, an 8-inch-thick HMA base was placed using the dump truck (Figure 3.30), leveled using the Bobcat (Figure 3.31), and compacted uniformly in a single layer by the vibratory roller (Figure 3.32) for several passes.

After the HMA base, the HMA material was placed, leveled, and compacted to produce a 2-inch-thick surface course.



Figure 3.30: Placement of HMA Material by Truck



Figure 3.31: Leveling of HMA Material Using a Bobcat



Figure 3.32: Compaction of the HMA Base by a Vibratory Roller

A sketch of the cross section of the test section is shown in Figure 3.33, which presents the compaction schedule of the backfill and the base course, and also includes the locations of the earth pressure cells.

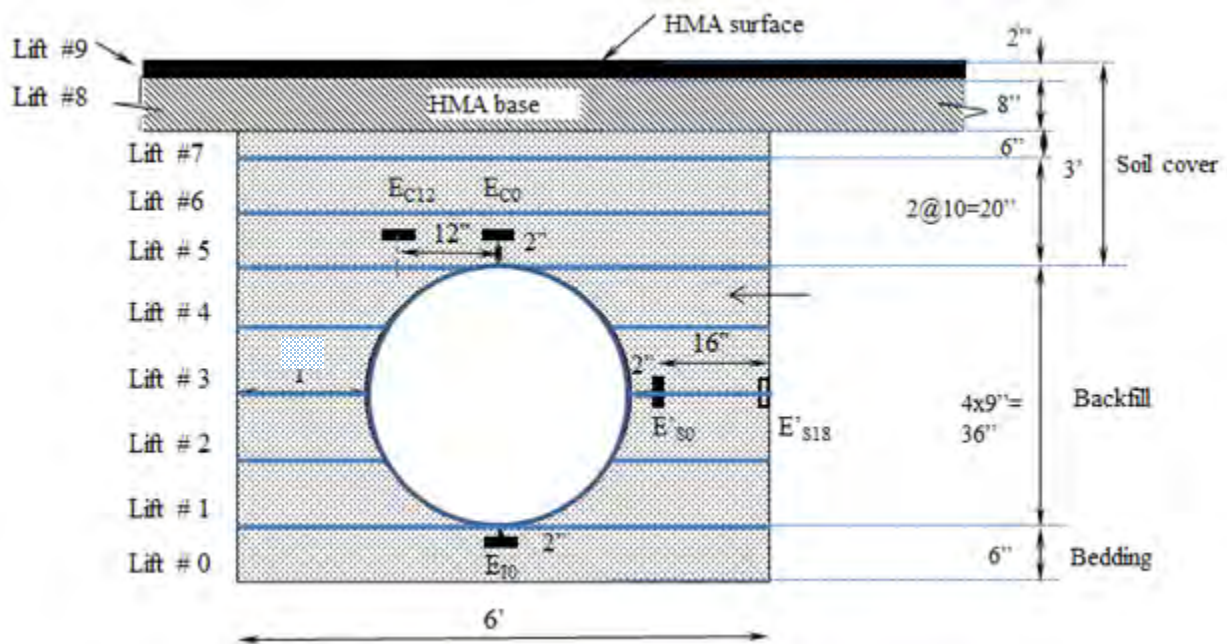


Figure 3.33: Construction and Instrumental Details of a Test Section in the Field Including the Soil Lifts and the Earth Pressure Cells

3.4.7 Quality Control

The installation of the pipe on this E1000 Road was planned to finish in two days. It was scheduled to open the road for traffic in the afternoon on the second day. This resulted in a very busy schedule for the installation of the pipe. To save the time, the installation of the strain gages and the displacement transducers on the pipes was done at a warehouse prior to the field work while the pressure cells were installed on the site. To control the quality of the construction, instead of slow and tedious field tests, non-destructive Light Weight Deflectometer (LWD) tests were conducted over the compacted crushed stone and the AB3 aggregate at various locations during the preparation of the test sections, as shown in Figure 3.34. The dynamic deformation moduli (E_{vd}) obtained from LWD tests (using a 1 ft diameter plate) were in a range of 2,700 to 3,700 psi with an average value of 3300 psi for the AB3 section, and 2,460 to 3,480 psi with an average value 2900 psi for the crushed stone section.



Figure 3.34: LWD Test on the Compacted AB3 Aggregate

In addition, Dynamic Cone Penetration (DCP) tests were carried out following the ASTM D6951 (2003) on both sides of the backfill next to the pipe on the western test section (Section A) after the compaction of the backfill up to the pipe haunch. The DCP tests were also conducted

before the placement of the HMA base at two different locations on the western test section (Section A) and at two locations on the eastern section (Section B). On the eastern test section (Section B), the DCP rod was penetrated to a depth of 6 inches to the crushed stone. The CBR profiles of the test section (Section A) obtained from the DCP tests are shown in Figure 3.35. The average CBR values of the compacted and light compacted AB3 aggregate, resulting from the DCP tests, were approximately 25% and 12%, respectively.

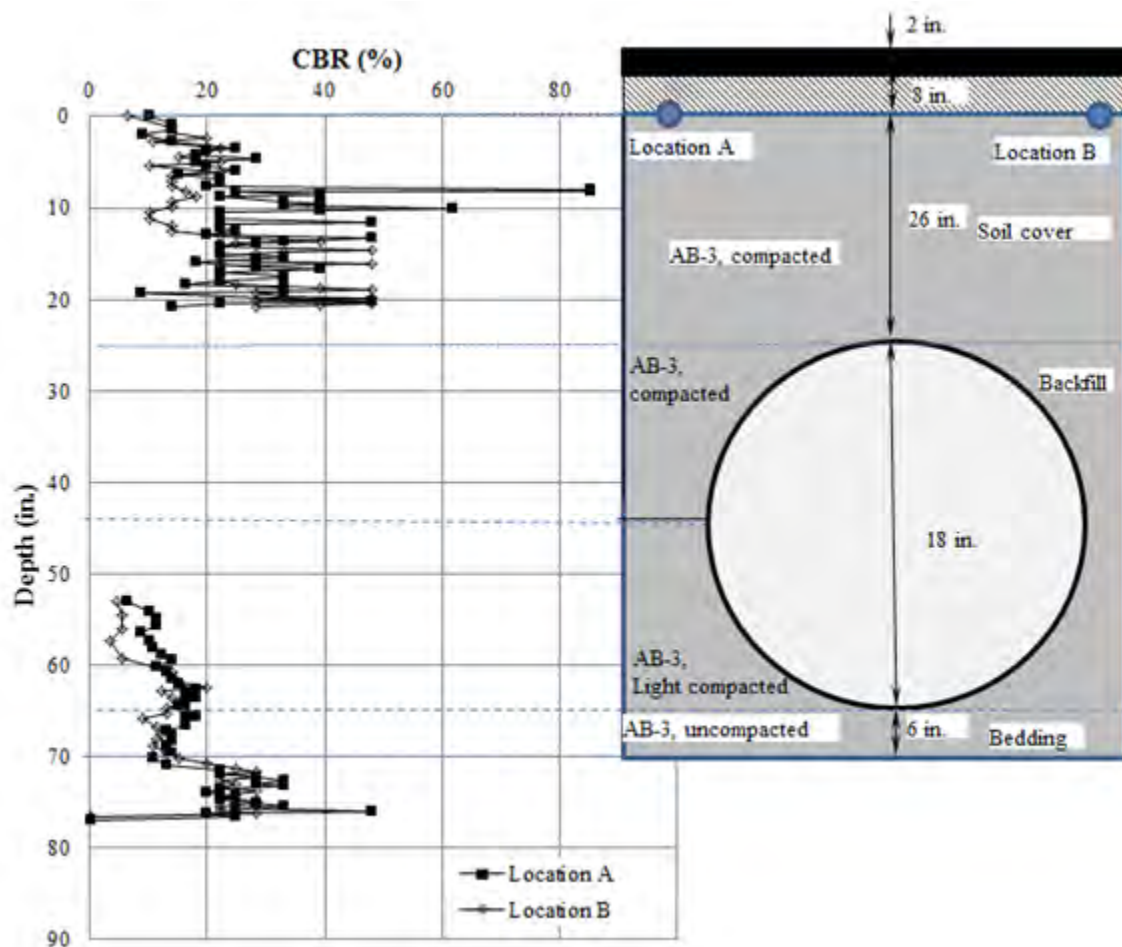


Figure 3.35: CBR Profiles on the Western Test Section

The densities of the AB3 aggregate compacted in the field were determined later by constructing test sections at the Big Spring Quarry at Lawrence, KS. A test section of compacted AB3 material was constructed by compacting the material using the vibratory plate compactor until the desired CBR values of 25% from the DCP tests and the dynamic deformation moduli

(E_{vd}) value (3,200 psi for the compacted AB3 section) from LWD tests were obtained. The densities of the compacted AB3 sections determined by the sand cone method following the ASTM D1556 (2007) were found to be 127 pcf at approximately 7% moisture content.

The densities of crushed stone compacted in the field were determined later in the laboratory at KU. A small box of 2 ft 7.5 inches long \times 2 ft 7.5 inches wide \times 3 ft high was used as shown in Figure 3.36. A 2 ft thick compacted crushed stone material was constructed by compaction using the vibratory plate compactor until the desired dynamic deformation moduli (E_{vd}) value of 2,900 psi from LWD tests were obtained. To determine the densities of uncompacted AB3 aggregate and crushed stone beddings, each material was dumped from the height of around 5 ft and leveled in the box. The densities of the uncompacted AB3 aggregate, uncompacted crushed stone, and compacted crushed stone materials determined by the weight-volume method were found to be 110, 94, and 97 pcf, respectively.



Figure 3.36: A Test Box Used for Density Determination

3.5 Analysis of Test Results During Pipe Installation

3.5.1 Earth Pressure-Test Section A

Figure 3.37 shows the measured earth pressures developing around the pipes against the levels of construction (labeled as 1 to 9, as shown in Figure 3.33). The pressures measured around the pipe in the field had similar trends to the pressures measured around the pipe in the

laboratory tests. The earth pressure cells, $1E_{C0}$, $2E_{C0}$, and $2E_{C12}$, fixed at the crown in Section 1, at the crown in Section 2, and at 12 inches away from the crown to the trench wall measured similar vertical earth pressures during the installation. The vertical earth pressures recorded by the pressure cell fixed at the invert (E_{I0}) were higher than the crown pressures.

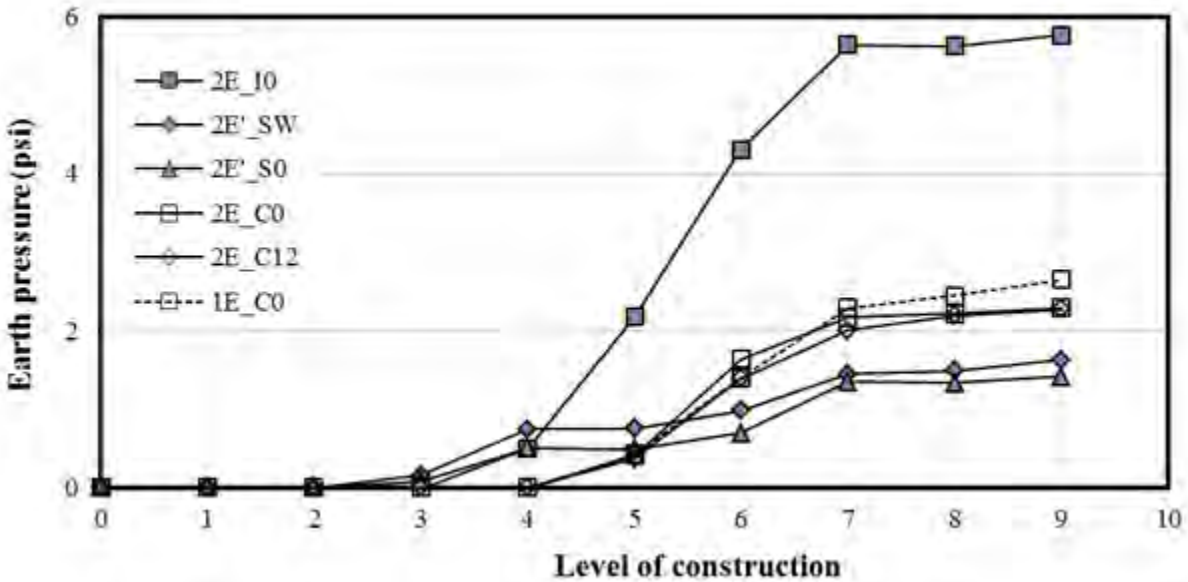


Figure 3.37: Measured Earth Pressures Around the Pipe During Installation in Test Section A

The overburden pressure $E_{C0, cal}$ (i.e., the unit weight of the soil $[\gamma_s] \times$ the thickness of the soil from the crown $[H]$) was calculated at the crown of the pipe. The vertical earth pressures measured at the crown by the earth pressure cells ($1E_{C0}$ and $2E_{C0}$) were then compared with the calculated overburden pressures as shown in Figure 3.38. The vertical arching factors (VAFs), calculated as the ratio of the measured pressure to the overburden pressure at the crown, are shown in Figure 3.38. The VAFs varied from 1.0 to 1.41 with an average value of 1.20. Based on the vertical arching factor and the hoop stiffness described by McGrath (1998), the SRHDPE pipe behaved similarly to a corrugated steel pipe. In addition, the vertical arching factors calculated using the Burns and Richard no-slip and full-slip solutions resulted in VAFs of 1.39 and 1.01, respectively. In this calculation, the hoop stiffness needed for the Burns and Richard solutions was estimated based on the constrained modulus ($M_s = 3,900$ psi) of the backfill (i.e.,

the AB3 aggregate), the radius of the pipe (36 inches), the area of the steel reinforcement (0.056 in.²/ft), and the modulus of elasticity of the steel reinforcement (29,000 ksi). The constrained modulus, M_s , of the AB3 aggregate was back-calculated from the modulus of elasticity of the AB3 aggregate determined from the small plate loading test in the laboratory. The vertical arching factors (VAFs) from the measurement of the earth pressures on the crown were in between the vertical arching factors obtained from the Burns and Richard solutions for the no-slip and full-slip cases, as shown in Figure 3.38. Therefore, the SRHDPE pipe should be designed based on a no-slip condition to be conservative for the VAF value.

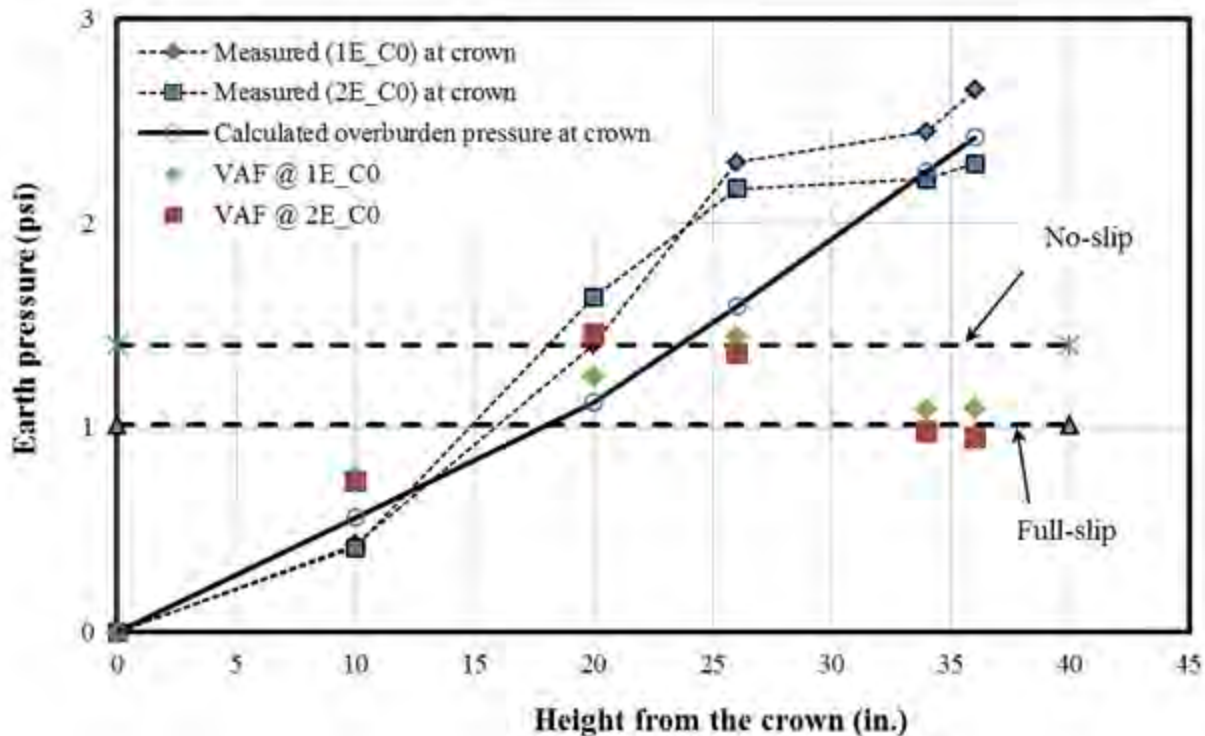


Figure 3.38: Comparison of Measured and Calculated Pressures at the Crown During Installation in Test Section A

Figure 3.39 shows the measured lateral pressures, E'_{s0} and E'_{sw} , at the springline near the pipe surface and at the trench wall and the calculated overburden pressures at the springline. Figure 3.40a shows the coefficients of lateral earth pressure (K) at the springline, calculated as the ratio of the measured lateral pressures to the calculated overburden pressures. The lateral earth pressure coefficients were higher at the level of construction 4 (i.e., at the pipe crown) and

decreased with the increased fill height. After the level of construction 6, the lateral pressure coefficients were constant. This type of behavior was also observed in the laboratory test results in the first phase of this project. Figure 3.40b compares the measured coefficients at the springline with the lateral earth pressure coefficient (K_p), calculated using the friction angle and the cohesion of the AB3 aggregate. The friction angle of 52.4° and the AB3 aggregate reported by Yang (2010) was used for the calculation of the passive earth pressure coefficient using the Rankine pressure coefficient with cohesion. The measured coefficients (K) were found to be much lower than the Rankine passive pressure coefficient (K_p).

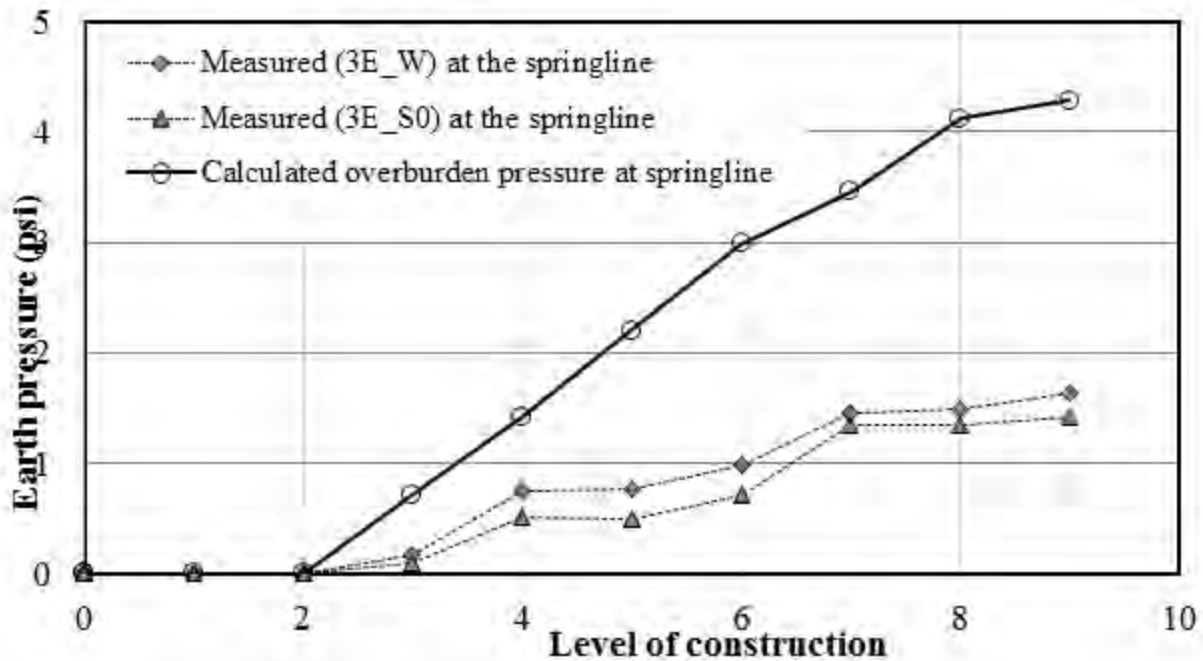
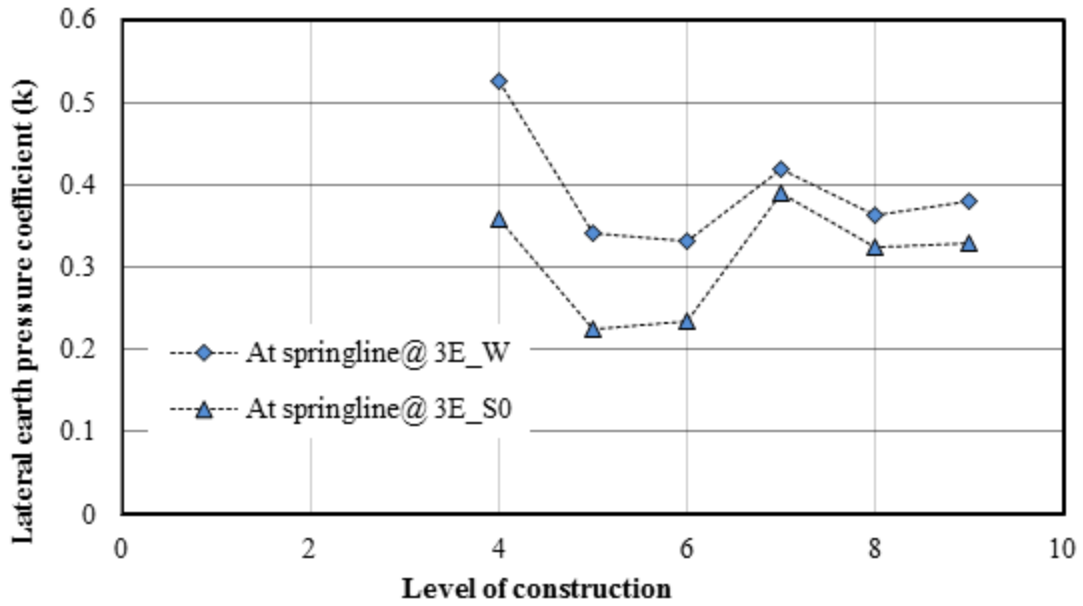
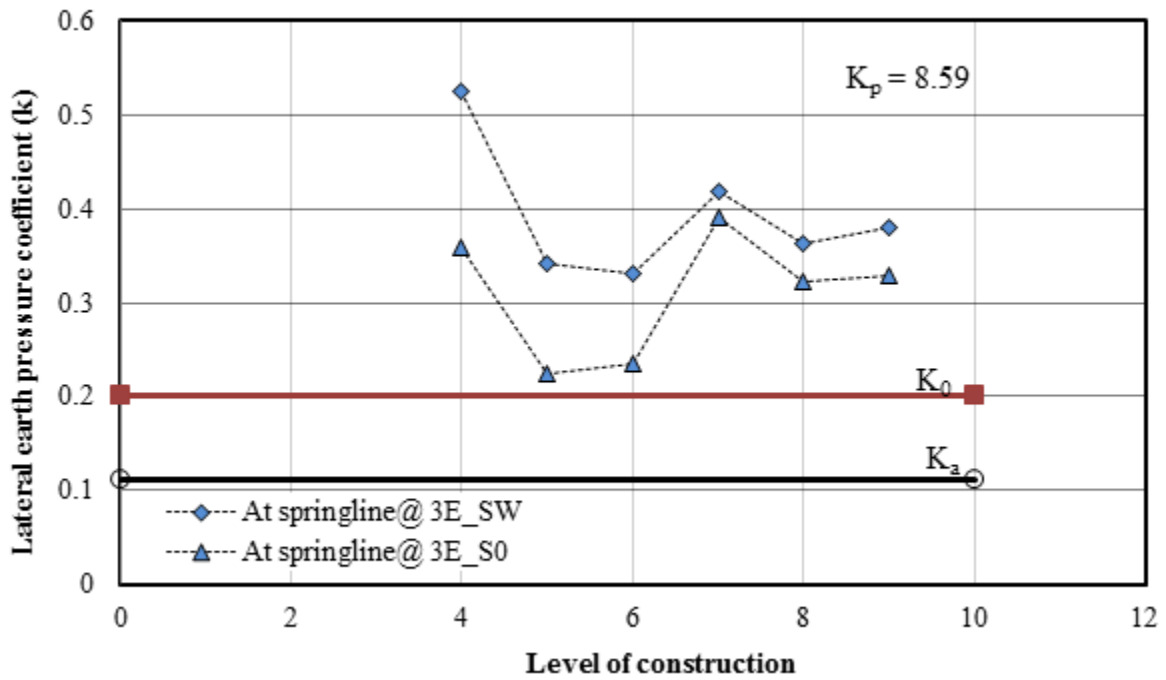


Figure 3.39: Measured and Calculated Lateral Earth Pressures at the Springline in Test Section A



(a) Lateral Earth Pressure Coefficients at the Springline



(b) Comparison to the Passive Lateral Earth Pressure Coefficients (K_p)

Figure 3.40: Lateral Earth Pressure Coefficients (K) at the Springline in Test Section A

3.5.2 Earth Pressure-Test Section B

Figure 3.41 shows the earth pressures developing around the pipes against the levels of construction. The earth pressure cells, E_{C0} and E_{C12} , fixed at the crown and 12 inches away from the crown, measured similar earth pressures during the installation. The vertical pressure recorded by the pressure cell fixed at the invert (E_{I0}) was lower than the pressure measured at the pipe crown.

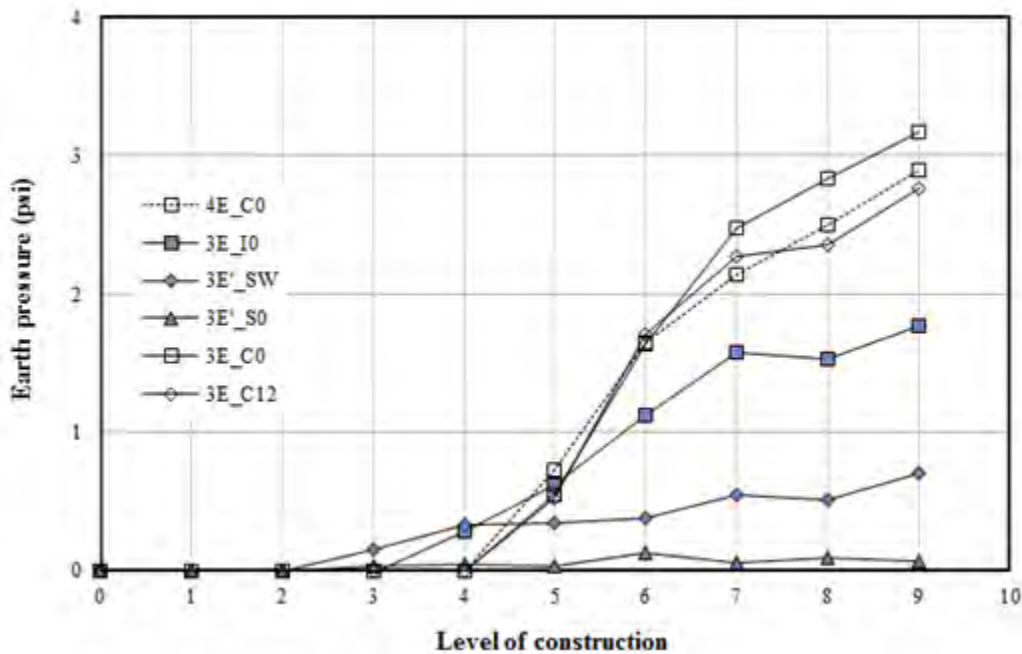


Figure 3.41: Measured Earth Pressures Around the Pipe During Installation in Test Section B

The overburden pressure $E_{C0, cal}$ (i.e., the unit weight of the soil $[\gamma_s] \times$ the thickness of the soil from the crown $[H]$) was calculated at the crown of the pipe. The vertical earth pressures measured at the crown by the earth pressure cells ($1E_{C0}$ and $2E_{C0}$) were then compared with the calculated overburden vertical pressures, as shown in Figure 3.42. The vertical arching factors (VAFs), calculated as the ratio of the measured pressure to the calculated pressure at the crown, are shown in Figure 3.42. The VAFs varied from 0.97 to 1.21 with average value of 1.1. Based on the vertical arching factor and the hoop stiffness described by McGrath (1998), the SRHDPE pipe behaved similarly to a corrugated steel pipe. In addition, the vertical arching factors calculated using the Burns and Richard no-slip and full-slip resulted in VAFs of 1.41 and 1.02,

respectively. In this calculation, the hoop stiffness needed for the Burns and Richard solutions was estimated based on the constrained modulus ($M_s = 2,520$ psi) of the backfill (i.e., the crushed stone), the radius of the pipe (36 inches), the area of the steel reinforcement (0.3575 in²/ft), and the modulus of elasticity of the steel reinforcement (29,000 ksi). The constrained modulus, M_s , of the crushed stone was back-calculated from the modulus of elasticity determined from the small plate loading test in the laboratory. The vertical arching factors (VAFs) from the measurement of the earth pressures on the crown were in between the vertical arching factors obtained from the Burns and Richard solutions for the no-slip and full slip cases, as shown in Figure 3.42. Therefore, the SRHDPE pipe should be designed based on a no-slip condition to be conservative for the VAF value.

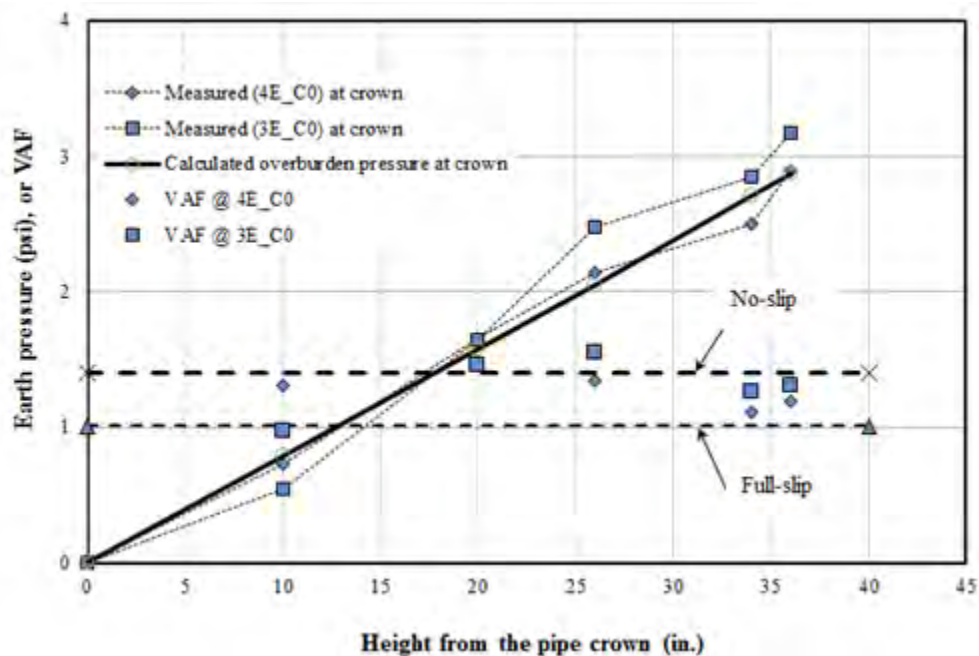


Figure 3.42: Comparison of Measured and Calculated Pressures at the Crown During Installation in Test Section B

Figure 3.43 shows the measured lateral pressures, E'_{s0} and E'_{sw} , near the pipe surface and at the trench wall and the calculated overburden pressures at the springline of the pipes. Figure 3.44a shows the coefficients of lateral earth pressure (K) at the springline calculated as the ratio of the measured lateral pressures to the overburden pressures. Figure 3.44b compares

the measured coefficients at the springline with the lateral earth pressure coefficients, K_a , K_o , and K_p , calculated using the friction angle of the crushed stone of 53° .

The measured coefficients (K) were found to be close to K_o . The coefficient (K) was the highest at level 4 (i.e., when the fill height reached the crown of the pipe) and then decreased to a value close to the coefficient K_o . The higher values of the coefficients (K), when the construction levels were close to the pipe, might be due to the higher effect of the compaction on the pipe.

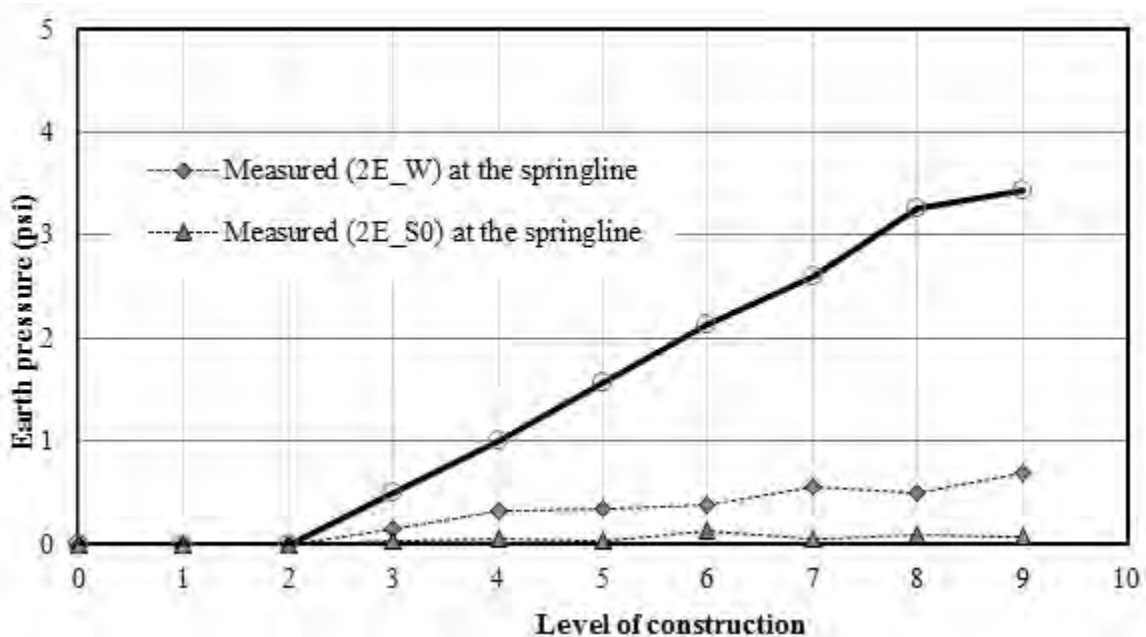
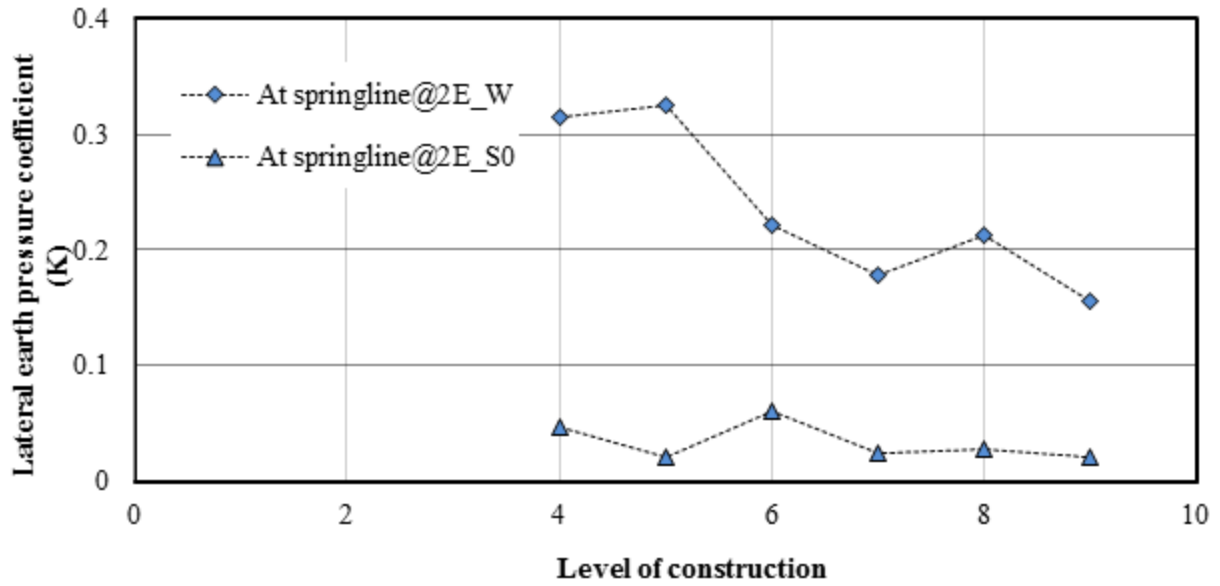
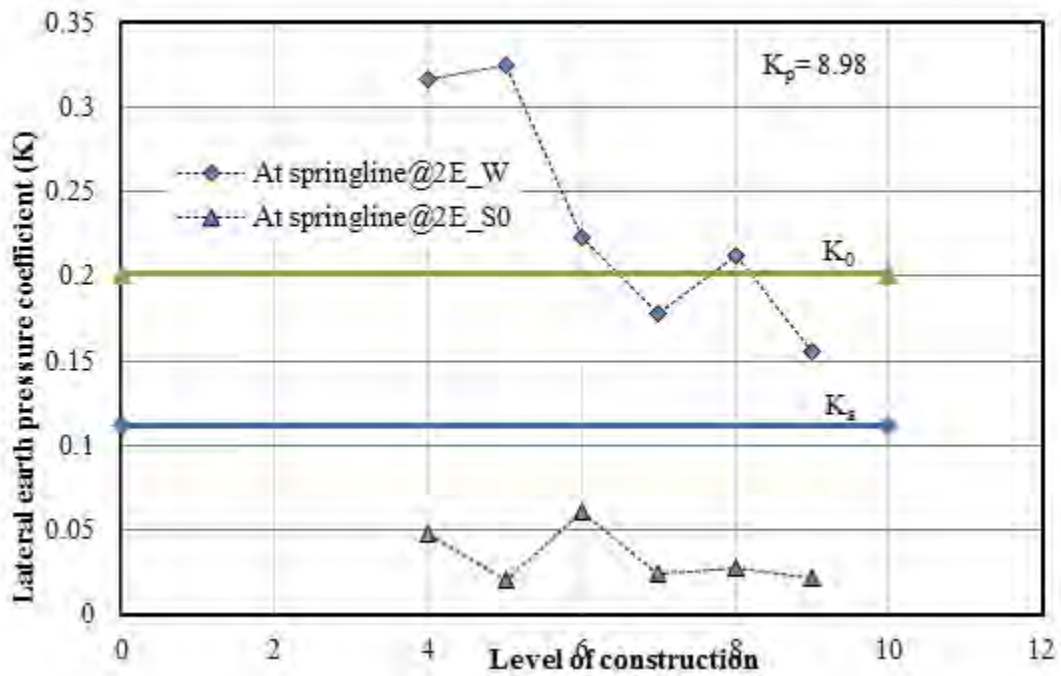


Figure 3.43: Measured Lateral and Overburden Pressures at the Springline in Test Section B



(a) Lateral Earth Pressure Coefficient at the Springline



(b) Comparison to the Active, At Rest, and Passive Lateral Earth Pressure Coefficients

Figure 3.44: Lateral Earth Pressure Coefficients (K) at the Springline in Test Section B

3.5.3 Deflections-Test Section A

The deflections of the pipe (or the changes in the inside diameters) against the levels of construction in Test Section A of the field test had similar behavior to the deflections of the pipes in the laboratory tests. The pipe exhibited peaking deflections during the backfilling, as shown in Figure 3.45. When the backfill height was at the same elevation as the pipe crown, the vertical diameter (ΔD_{VC}) was increased by an average of 0.15 inches (0.41%) while the horizontal diameter (ΔD_{HC}) was reduced by an average of 0.20 inches (-0.56%). When the compaction of the lifts was above the pipe crown level, the vertical diameter (ΔD_{VC}) started decreasing and the horizontal diameter (ΔD_{HC}) started increasing as the compaction commenced further. At the end of the construction of the test section, the net decreases in the vertical and horizontal diameters (ΔD_{VC} and ΔD_{HC}) were 0.0015 inches (-0.0044%) and 0.095 inches (0.269%), respectively. The vertical deflection of the pipe (ΔD_{VC}) was approximately equal to the horizontal deflection (ΔD_{HC}) during the backfilling up to the pipe crown, as shown in Figure 3.46.

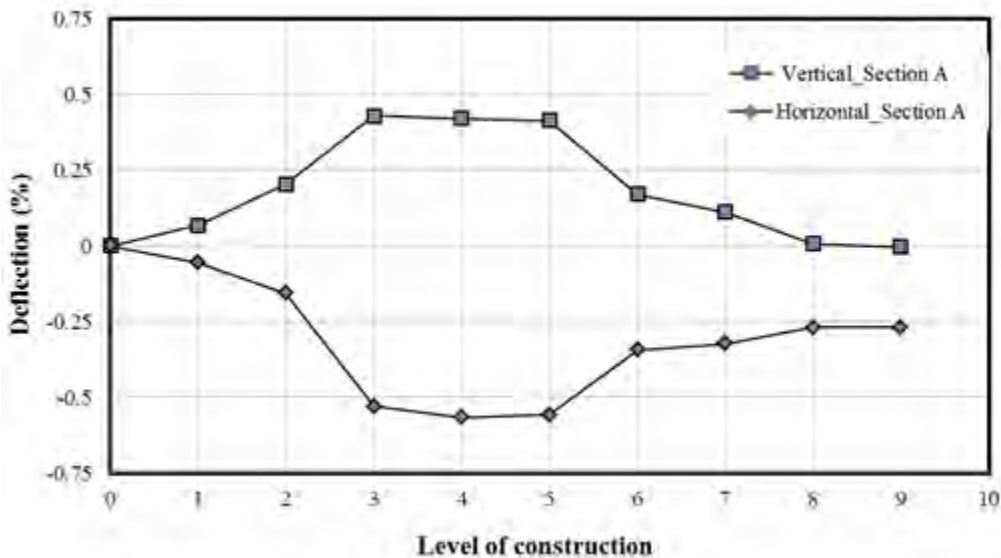


Figure 3.45: Measured Deflections of the Pipe During the Installation in Test Section A

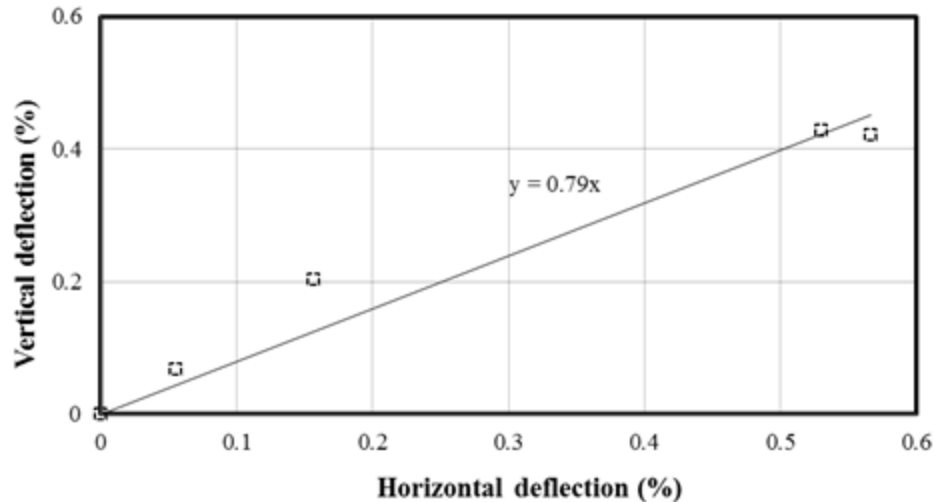


Figure 3.46: Relations Between the Measured Vertical and Horizontal Deflections During the Installation in Test Section A

The peaking deflection calculated using the method proposed by Masada and Sargand (2007) was 1.37%, which was higher than the measured peaking deflection (0.43%). The lateral pressure (P_c) generated by the rammer compaction for the sand backfill as 0.39 psi/in. was selected for the AB3 aggregate section to calculate the peaking deflection. The contribution of the backfill cohesion to the peaking deflection was neglected. The horizontal deflection of the pipe (ΔDHC) measured during the backfilling was also compared with the horizontal deflection calculated using the Iowa Formula as shown in Figure 3.47. The bedding constant (k) of 0.1, the VAF of 1.20, the unit weight of the AB3 aggregate (136 pcf), and the modulus of elasticity of 2,675 psi were used to calculate the horizontal deflection (ΔDHC). In the horizontal deflection calculation, the effect of the compaction effort on the pipe during the installation was ignored because of the unknown pressure increase caused by the compaction equipment during the installation of the pipe. The measured horizontal deflections (ΔDHC) were higher than the calculated ones. The higher horizontal deflections might not include the effect of the compaction effort (i.e., neglecting the peaking behavior) during the installation in the horizontal deflection calculation.

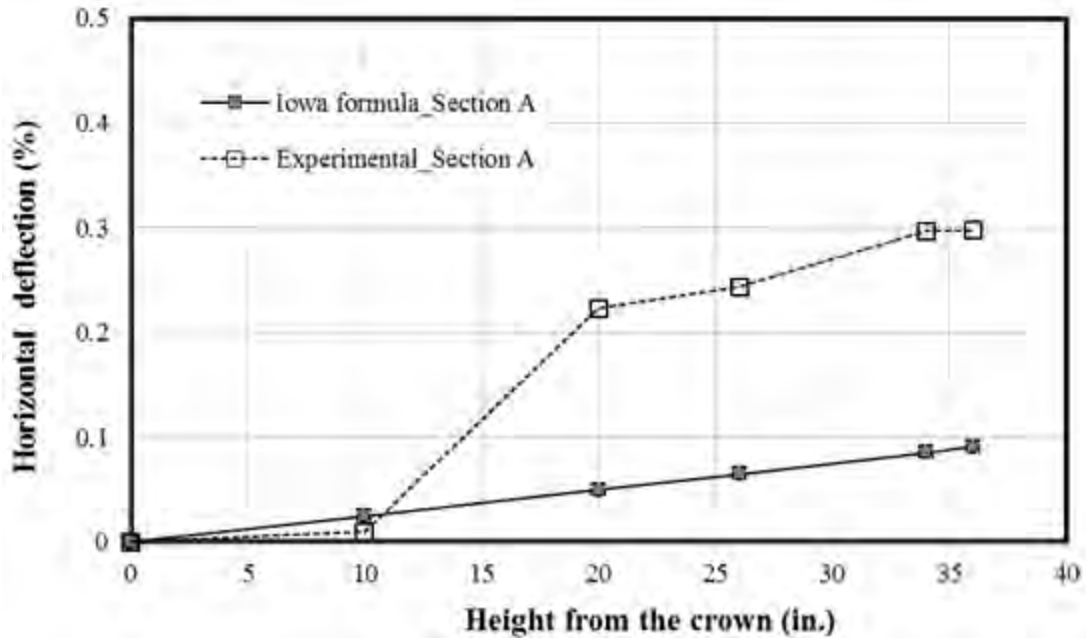


Figure 3.47: Comparison of the Measured and Calculated Horizontal Deflections by the Iowa Formula in Test Section A

To investigate the impact caused by the compactors and construction vehicles to the pipe, the data were continuously recorded once the pipe was placed in the trench. The displacement transducers which were instrumented to measure the deflections of the pipe were selected to collect the response of the pipe during the construction of the test sections. The data sample interval of 10 msec was set on the transducers to read the immediate response of the pipe. The responses of the pipe measured using other sensors, such as the pressure cells and the strain gages, were collected at 1 minute intervals. During the installation of the pipe, the maximum deflections of the pipe caused by the tamping hammer, Multiequip MT65H, were noticed during the backfill compaction at the shoulder, as shown in Figure 3.48, and during the compaction of the soil cover above the crown of the pipe. Figure 3.48 shows that the tamping hammer produced an immediate decrease in the horizontal diameter of around 0.23% and an increase in the vertical diameter of 0.19%. The deformation response of the pipe was also collected when the smooth wheel vibratory roller, 2005 Model Hamm HD13, was run above the top of the pipe before the placement of the HMA base, as shown in Figure 3.49. The maximum immediate decrease in the vertical diameter of 0.08% was measured.

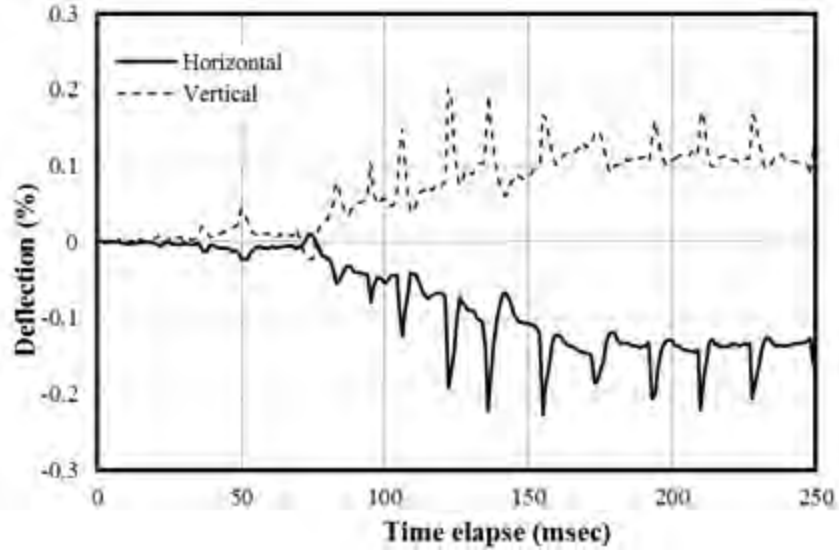


Figure 3.48: Deflections Produced by the Tamping Hammer During the Compaction at the Pipe Shoulder in Test Section A

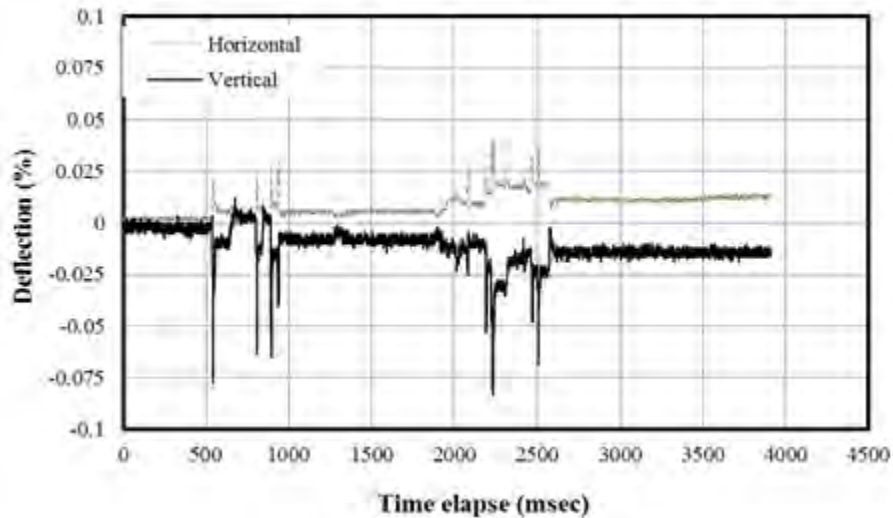


Figure 3.49: Deflections Produced by the Smooth Wheel Vibratory Roller During the Compaction Before Placing the HMA Base in Test Section A

3.5.4 Deflections-Test Section B

The pipe during the backfilling exhibited peaking deflections similar to those in both laboratory and field tests discussed above, as shown in Figure 3.50. When the backfill height was at the same elevation with the pipe crown, the vertical diameter (ΔD_{VC}) was increased by an average of 0.3 inches (0.85%), while the horizontal diameter (ΔD_{HC}) was reduced by an average of 0.30 inches (-0.87%). When the compaction of the lifts was above the pipe crown, the vertical

diameter (ΔD_{VC}) started decreasing and the horizontal diameter (ΔD_{HC}) started increasing as the compaction commenced further. At the end of the construction of the test section, the net increase in the vertical diameter and the decrease in the horizontal diameter (ΔD_{VC} and ΔD_{HC}) were 0.11 inches (0.30%) and 0.13 inches (-0.89%), respectively. The vertical deflection of the pipe (ΔD_{VC}) was approximately equal to the horizontal deflection (ΔD_{HC}) during the installation of the pipe, as shown in Figure 3.51.

The peaking deflection calculated using the method proposed by Masada and Sargand (2007) was 0.37%, which was lower than the measured peaking deflection (0.87%). The lateral pressure (P_c) generated by the vibratory plate compactor for the crushed stone backfill was selected as 0.06 psi/in. to calculate the peaking deflection. The lateral earth pressure coefficient at rest (K_o) was calculated as $K_o = 1 - \sin \phi$, where ϕ is the friction angle of 52.4°. The horizontal deflection (ΔD_{HC}) of the pipe measured during the backfilling was also compared with the horizontal deflection using the Iowa Formula, as shown in Figure 3.52. The bedding constant (k) of 0.1, the VAF of 1.10, the unit weight of the crushed stone (97 pcf), and the modulus of subgrade reaction of 3,780 psi were used to calculate the horizontal deflection (ΔD_{HC}). In the horizontal deflection calculation, the effect of the compaction effort on the pipe during the installation was ignored because of the unknown pressure increase caused by the compaction equipment during the installation of the pipe. The measured horizontal deflections (ΔD_{HC}) were higher than the calculated. The higher calculated horizontal deflections might not include the effect of the compaction effort during the installation of the pipe.

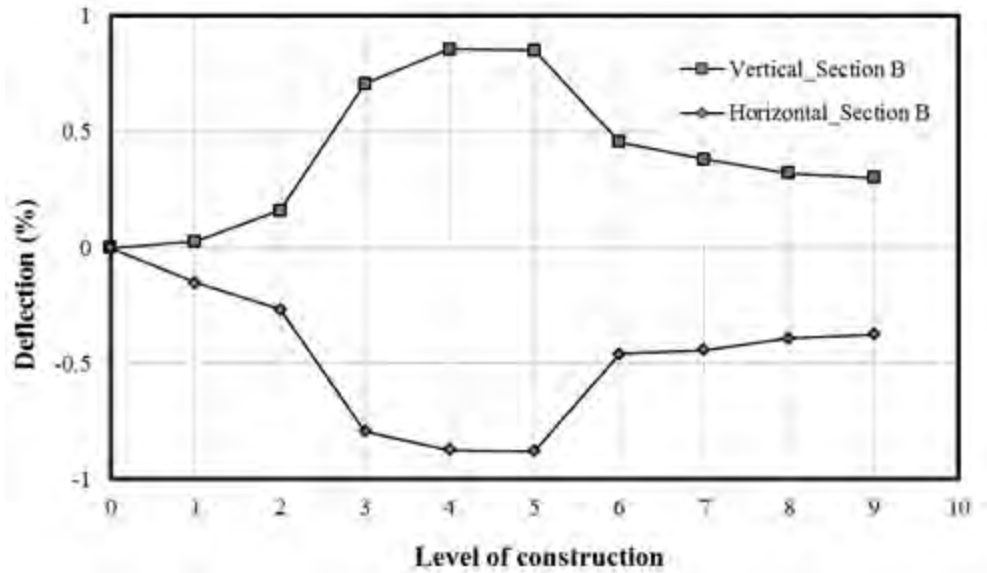


Figure 3.50: Measured Deflections of the Pipe During the Installation in Test Section B

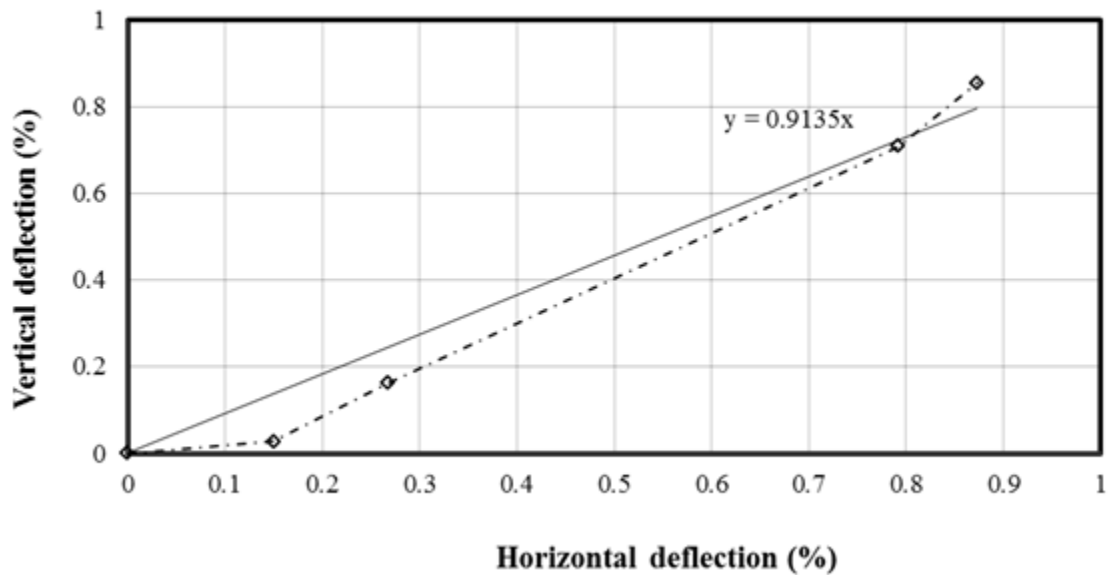


Figure 3.51: Relations Between the Measured Vertical and Horizontal Deflections During the Installation in Test Section B

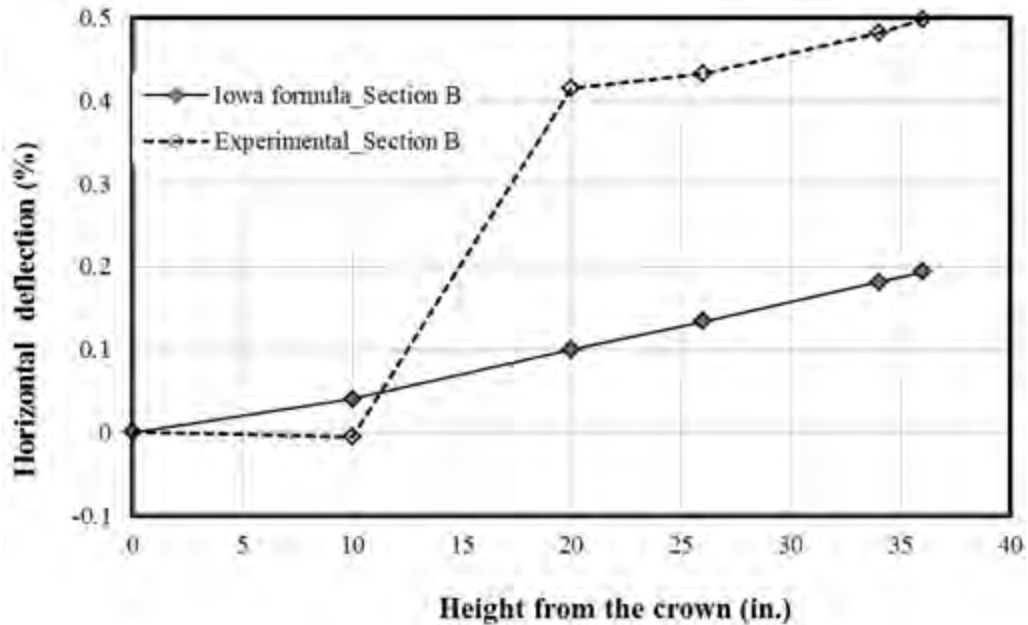


Figure 3.52: Comparison of the Measured and Calculated Horizontal Deflections by the Iowa Formula in Test Section B

To investigate the impact caused by the compactors and construction vehicles to the pipe in Test Section B, the data were continuously recorded as described above for Test Section A. During the installation of the pipe, the maximum deflections of the pipe caused by the vibratory plate compactor, Wacker WP1550AW, were also noticed during the backfill compaction at the shoulder, as shown in Figure 3.53, and during the compaction of the soil cover above the crown of the pipe as discussed earlier. Figure 3.53 shows that the deflection produced by the vibratory plate compactor in Test Section B was less than that produced by the tamping hammer in Test Section A. This result indicates that the vibratory plate compactor was less severe to the pipe as compared with the tamping hammer. The deformation response of the pipe was also collected when the smooth wheel vibratory roller, 2005 Model Hamm HD13, was run above the top of the pipe before the placement of the HMA base, as shown in Figure 3.54. The maximum immediate decrease in the vertical diameter of 0.083% was measured during the compaction using the smooth wheel vibratory roller.

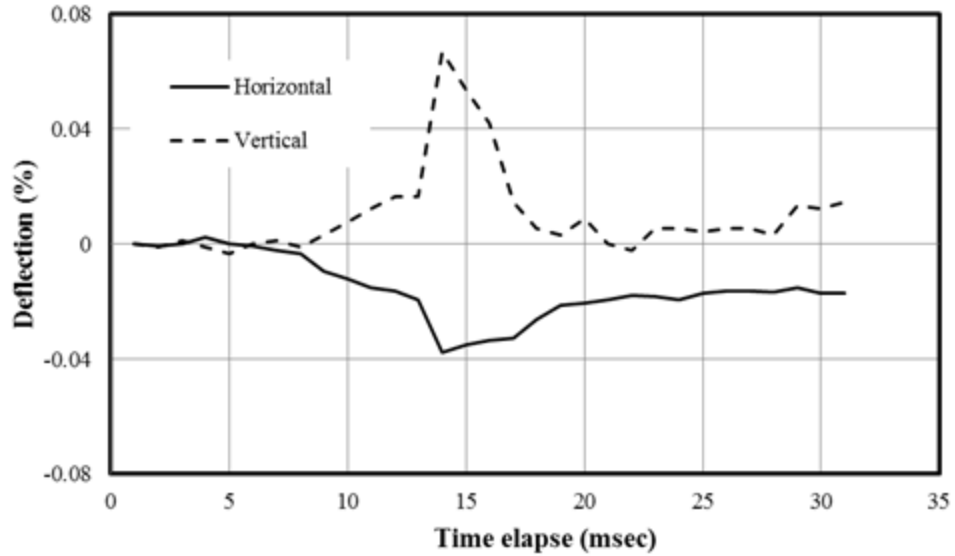


Figure 3.53: Deflections Produced by the Vibratory Plate Compactor During the Compaction at the Pipe Shoulder in Test Section B

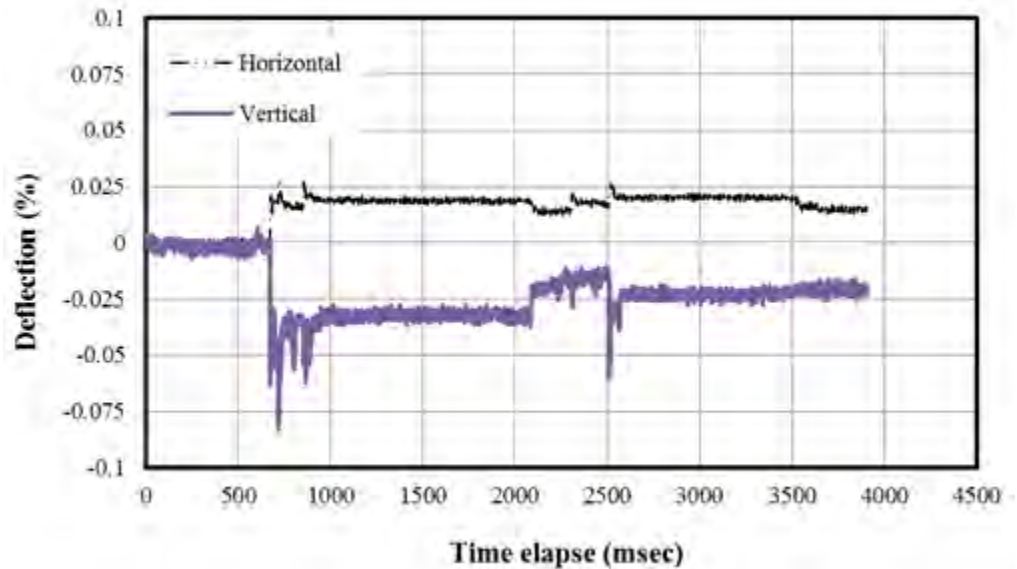


Figure 3.54: Deflections Produced by the Smooth Wheel Vibratory Roller During the Compaction Before the Placement of the HMA Base in Test Section B

3.5.5 Strains-Test Section A

Most strain gages (47 out of 52 strain gages) used in this test performed well during the installation of the pipe, except the strain gages G_{SR2} , G''_{SL1} , G''_{CL5} , and G''_{SL1} , fixed in Test Section A, and the strain gage G_{SR1} , fixed in Test Section B. All strain gages which did not work

during the installation of the pipe were fixed later and started working for the long-term monitoring of the pipe. The long-term performance data will be presented in Chapter 6.

The adjusted strains according to Brachman, Moore, and Munro (2008) are plotted against the levels of construction in Figures 3.55 to 3.57.

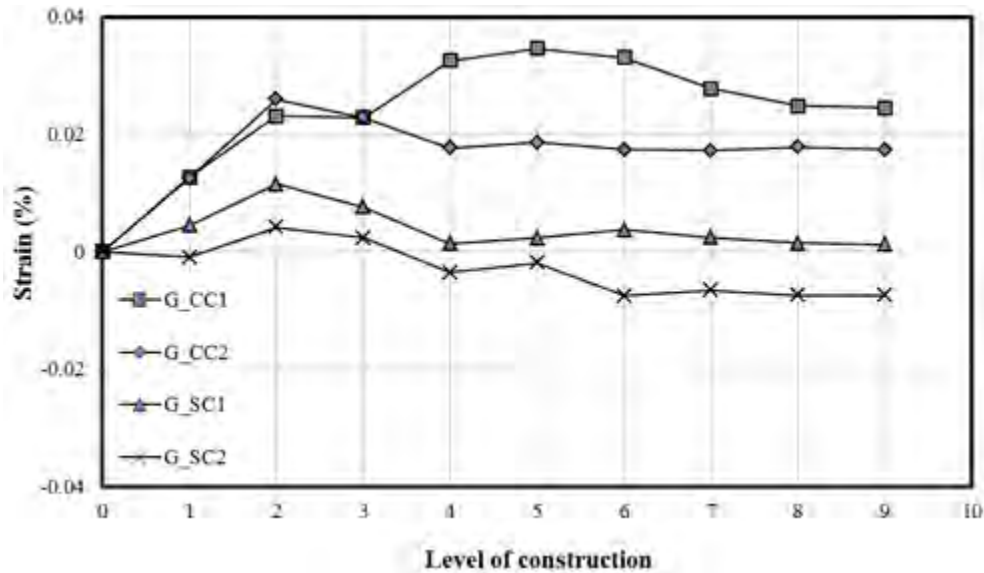


Figure 3.55: Measured Strains on the Steel Surface During the Installation in Test Section A

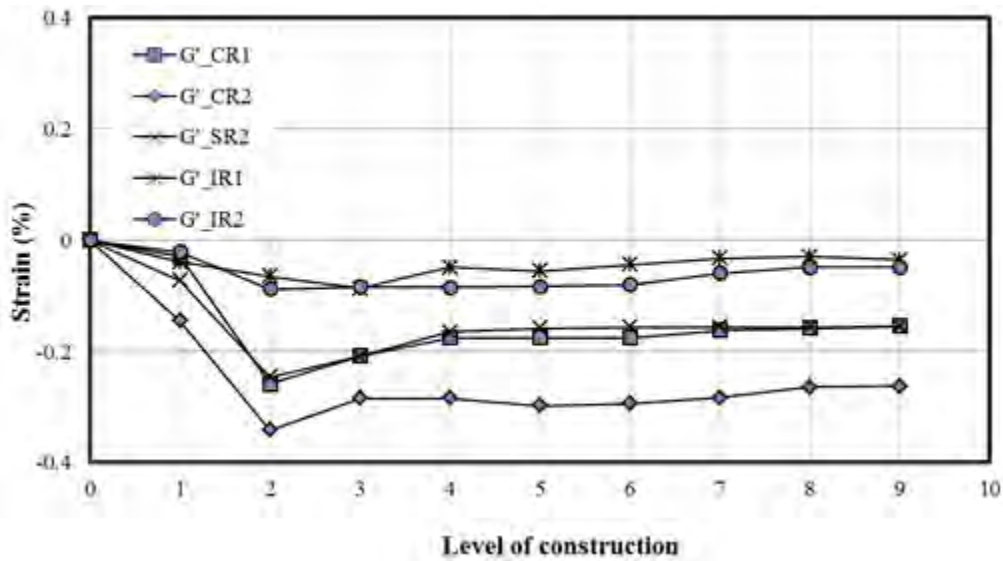
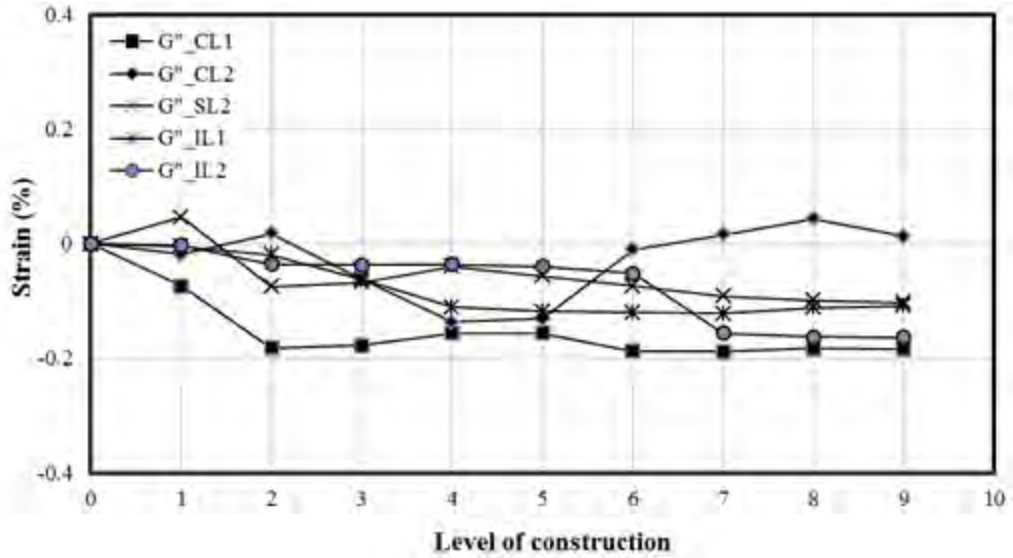
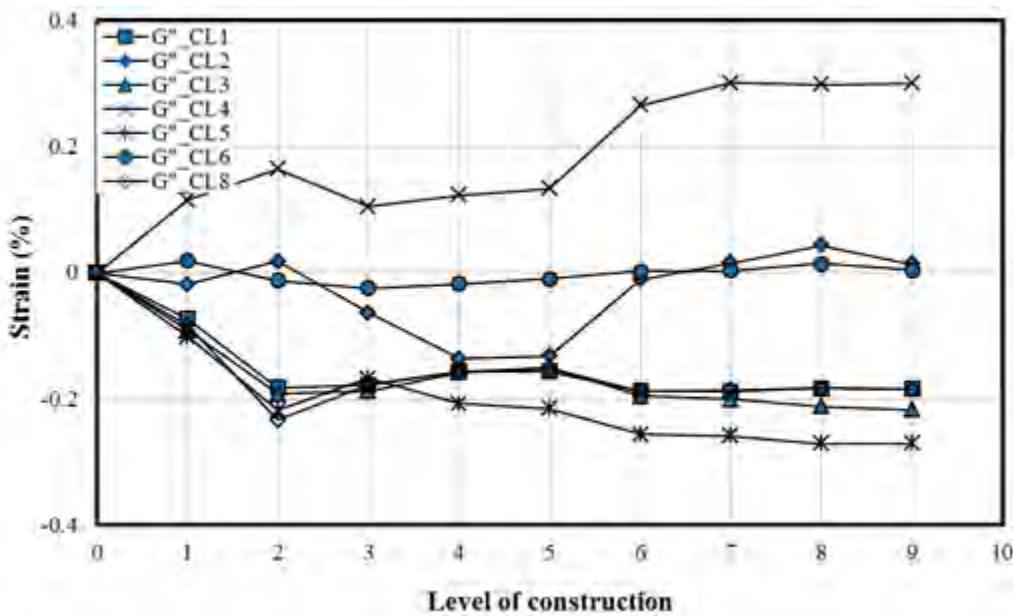


Figure 3.56: Measured Strains on the Plastic Ribs During the Installation in Test Section A



(a) Strains on Plastic Beneath the Wheel Path



(b) Strains on Plastic Away From the Wheel Path to Centerline of the Roadway

Figure 3.57: Measured Strains on the Plastic at Inside and Outside Pipe Walls During the Installation in Test Section A

The circumferential strains (Figure 3.55) developing on the steel of the pipe in the field in Test Section A had similar values to the strains on the steel in the laboratory tests. The strain gages, G_{SC1} and G_{SC2} at the springline and G_{CC1} and G_{CC2} at the crown, showed an increase in tensile strains until the backfill reached the pipe springline (i.e., Level 2 of construction). All

strain gages (except G_{CC1}) showed an increase in compressive strains with the increase in soil lifts. Strain gage G_{CC1} showed the increase in tensile strains up to Level 5 of construction. After that, strain gage G_{CC1} indicated the increase in the compressive strains. The maximum circumferential strain of 0.034% (G_{CC1} , tensile strain) and the maximum circumferential strain of 0.007% (G_{SC2} , compressive strain) developed during the installation. The strain gages fixed on both sides of a steel rib at any particular location (for example, G_{SC1} and G_{SC2} at the springline at the rib), gave similar values (i.e. there was no sudden change in strain values). This result indicates that the out-of-plane buckling of the steel ribs observed during the parallel plate load tests at a high level of load in the laboratory did not occur during the installation of the pipe in the field.

Figure 3.56 shows the radial strains on the plastic at the ribs against the levels of construction. The strains developing on the plastic were higher in magnitude than the strains on the steel. All strain gages showed an increase in compressive strains until the backfill was at the springline (i.e., Level 2 of construction) and started increasing in tensile strains with the increase in soil lifts. A maximum compressive strain of 0.34% was recorded during the installation.

The strains measured by the strain gages on the plastic wall inside and outside are shown in Figure 3.57. Figure 3.57a shows the strains at the crown, springline, and invert of the pipe under the wheel path, whereas Figure 3.57b shows the strains at the pipe crown at various locations from the pipe crown to the centerline of the roadway. Most strain gages fixed on the pipe outside experienced the increase in compressive strains, whereas most strain gages on the pipe inside experienced the increase in tensile strains after the backfill was at the springline (i.e., Level 2 of construction). The strain gages affixed on the pipe inside walls experienced more tensile strains than those on the outside walls. The magnitudes of the strains on the pipe walls were higher than the strains on the steel and higher than or close to the plastic at the ribs. The maximum tensile strain of 0.3% (G''_{CL4}) was recorded on the pipe wall during the installation.

3.5.6 Strains-Test Section B

The adjusted strains according to Brachman et al. (2008) are plotted against the levels of construction in Figures 3.58 to 3.60.

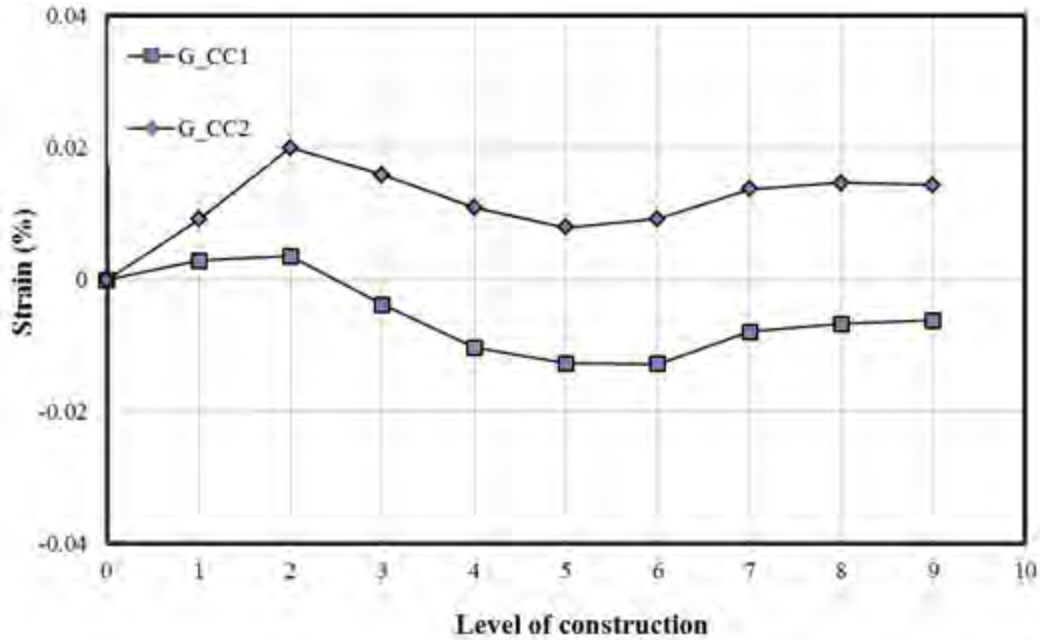


Figure 3.58: Measured Strains on the Steel During the Installation in Test Section B

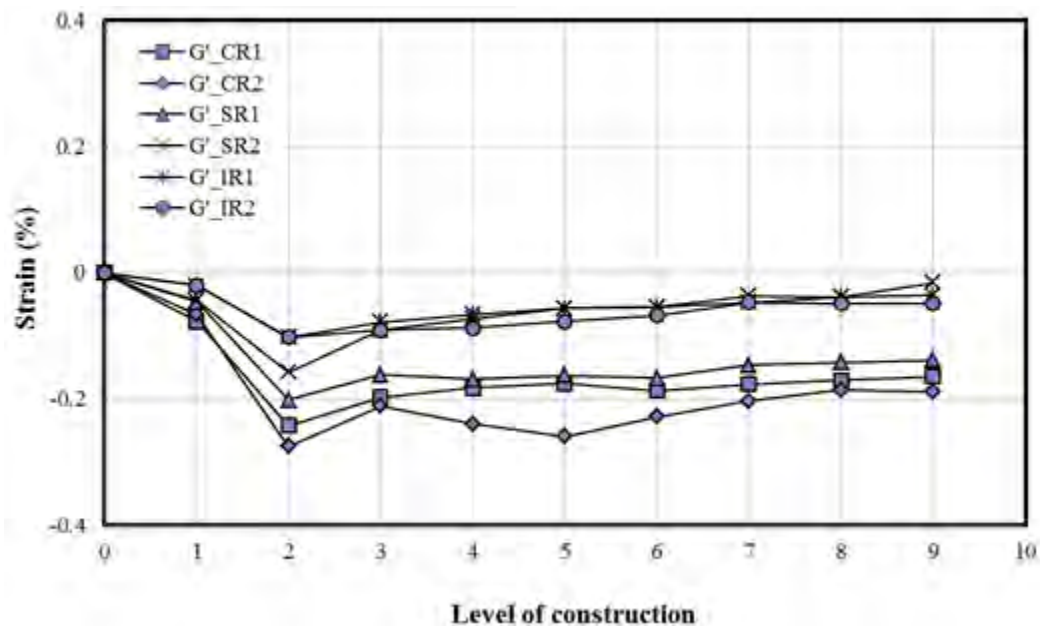
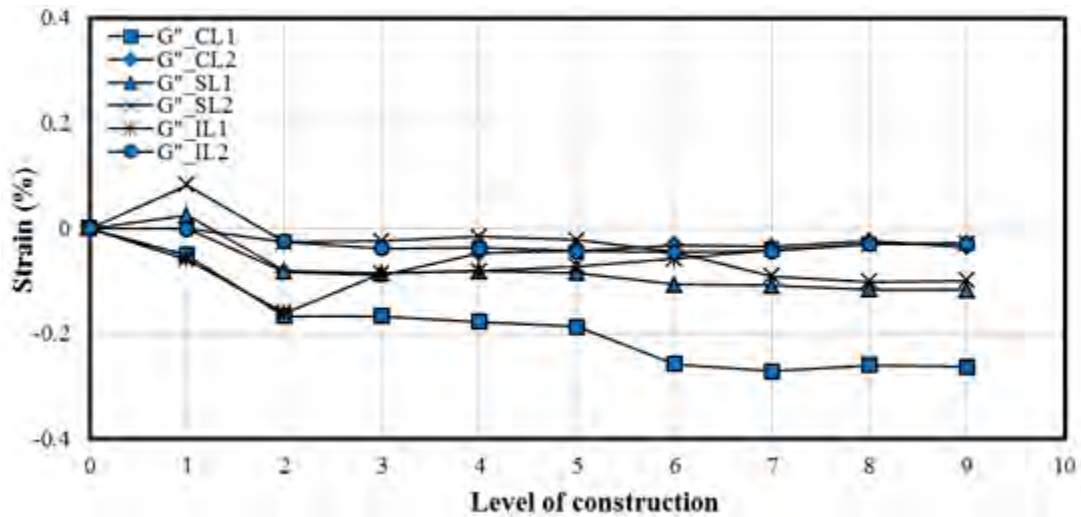


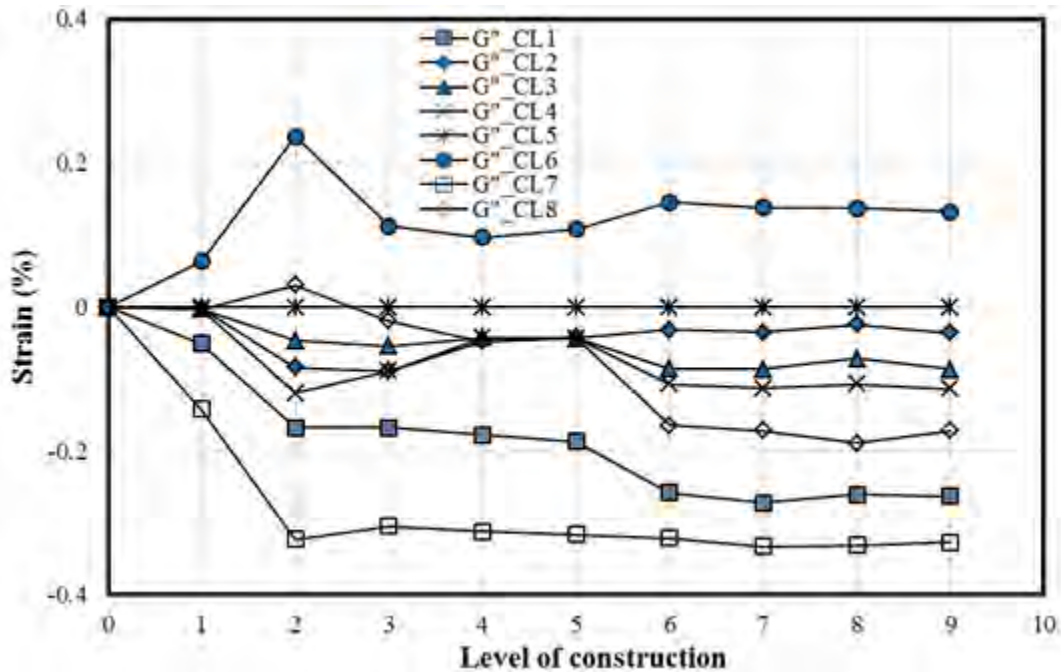
Figure 3.59: Measured Strains on the Plastic Ribs During the Installation in Test Section B

The circumferential strains (Figure 3.58) developing on the steel of the pipe in the field in Test Section B had similar values to the strains on the steel in the laboratory and field (Test Section A) tests. The strain gages, G_{CC1} and G_{CC2} at the crown, showed an increase in tensile strains until the backfill reached the pipe springline (i.e., Level 2 of construction). All strain

gages showed a decrease in compressive strains up to the top of the pipe and an increase in tensile strains with soil lifts as the construction commenced further. The maximum circumferential strain of 0.02% (G_{CC2} , tensile strain) and the maximum circumferential strain of 0.012% (G_{CC1} , compressive strain) developed during the installation.



(a) Strains on Plastic Beneath the Wheel Path



(b) Strains on Plastic Away From the Wheel Path to Centerline of the Road Way

Figure 3.60: Measured Strains on the Plastic at Inside and Outside Pipe Walls During the Installation in Test Section B

Figure 3.59 shows the radial strains on the plastic at the ribs against the levels of construction, and the strains were similar to the strains obtained on the plastic ribs in the laboratory and field (Test Section A) tests. The strains developing on the plastic were higher in magnitude than the strains on the steel. All strain gages showed an increase in compressive strains until the backfill was at the springline (i.e., Level 2 of construction) and started increasing in tensile strains with the increase in soil lifts. A maximum compressive strain G'_{CR2} of 0.27% was recorded during the installation.

The strains measured by the strain gages on the plastic wall inside and outside are shown in Figure 3.60. Figure 3.60a shows the strains at the crown, springline, and invert of the pipe under the wheel path, whereas Figure 3.60b shows the strains at the pipe crown at various locations from the pipe crown to the centerline of the roadway. Most strain gages affixed on the pipe outside experienced an increase in compressive strains, whereas most strain gages on the pipe inside experienced an increase in tensile strains after the backfill was at the springline (i.e., Level 2 of construction). The strain gages affixed on the pipe inside walls experienced more tensile strains than those on the outside walls. The magnitudes of the strains on the pipe walls were higher than the strains on the steel and higher than or close to the plastic at the ribs. The maximum strain of 0.32% (G''_{CL7} , tensile strain) was recorded on the pipe wall during the pipe installation.

3.6 Analysis of Test Results Under Static Loading

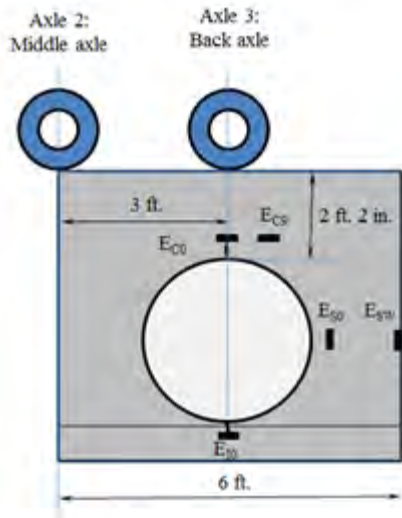
3.6.1 Earth Pressure-Test Section A

Before the placement of the HMA base material, the dump truck of 13.72 tons (empty) loaded with HMA base course material of 15.2 tons was used as the test truck. The contact area calculated for each rear wheel load of 5.25 tons with the tire pressure of 120 psi was found to be 87.5 in². The static truck load was applied on both the western and eastern test sections (Sections A and B) with three different loading configurations: (a) back axle above the pipe crown, (b) back axle at the center between the pipe crown and the trench wall, and (c) middle axle above the pipe crown. For each loading step, the truck was kept for a while until all readings from the

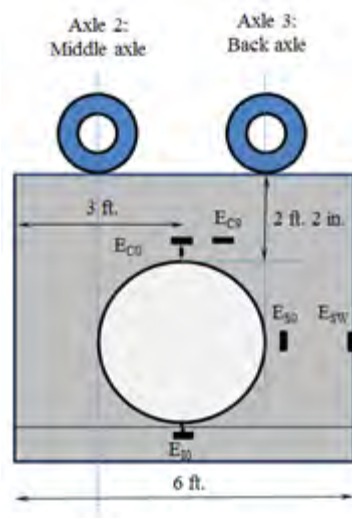
displacement transducers that were attached inside the pipe to measure the changes in the diameter of the pipe became stable.

Figure 3.61 shows the positions of the truck wheels when the truck loads were applied on Test Section A. Figure 3.62 shows the measured earth pressures around the pipe against the time elapsed both in Test Sections A and B with the truck loadings on Test Section A. Since Test Sections A and B were next each other, the load applied on Test Section A had some influence on Test Section B. When the truck load was applied directly above the instrumented section (Section 2) close to the centerline on Test Section A, there were no or little change in the earth pressures around the pipe at the instrumented section (Section 3) of the pipe in Test Section B. It is shown that the truck load applied above the instrumented section close to the centerline of the roadway (Section 2) in Test Section A had no or negligible effect on the instrumented section (Section 3) close to the centerline of the roadway in Test Section B.

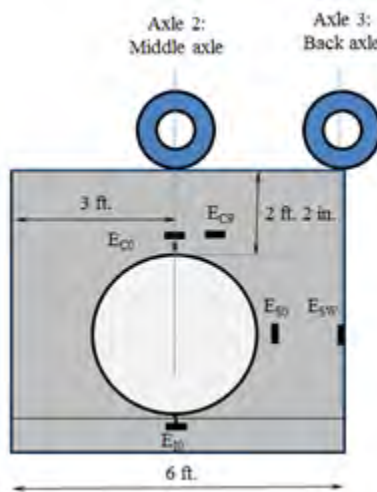
When the back axle was placed above the crown (Figure 3.61a), the pressure cells at the crown, $1E_{C0}$ and $2E_{C0}$, in Sections 1 and 2 on the western test section (Section A) recorded the equal highest vertical earth pressures of 10.03 psi. The vertical earth pressure at 12 inches away from the center ($2E_{C12}$) was 3.71 psi, which was 0.37 times the pressure at the pipe crown ($2E_{C0}$). The horizontal pressure at the pipe springline ($2E'_{s0}$) was 0.16 times the vertical earth pressure at the crown ($2E_{C0}$). The ratio of the horizontal pressure at the springline ($2E'_{s0}$) to that at the trench wall ($2E'_{sw}$) was 1.32. The vertical earth pressure at the invert ($2E_{I0}$) was 1.51 psi, which was 0.15 times the pressure at the pipe crown ($2E_{C0}$). When the back axle between the pipe crown and trench wall (Figure 3.61b) and the middle axle above the pipe crown (Figure 3.61c) were applied, there was not much variation (little higher) in the earth pressures measured around the pipe as compared with those measured with the back axle above the pipe crown (Figure 3.61a) as shown in Figure 3.62.



(a) Back Axle Over the Crown



(b) Back Axle in Between the Crown and Trench Wall



(c) Middle Axle Over the Crown

Figure 3.61: Axle Loads on the Pipe in Test Section A

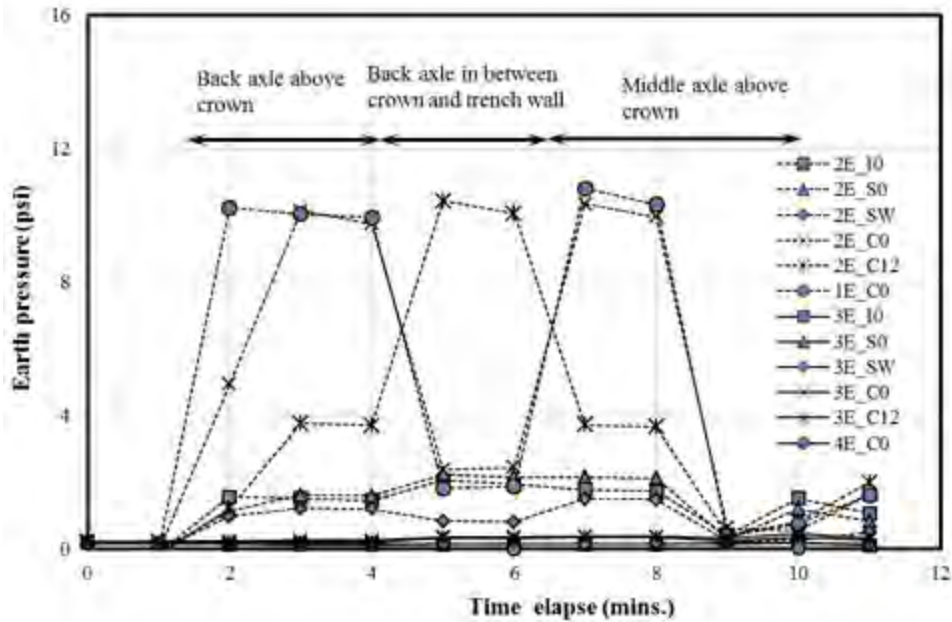


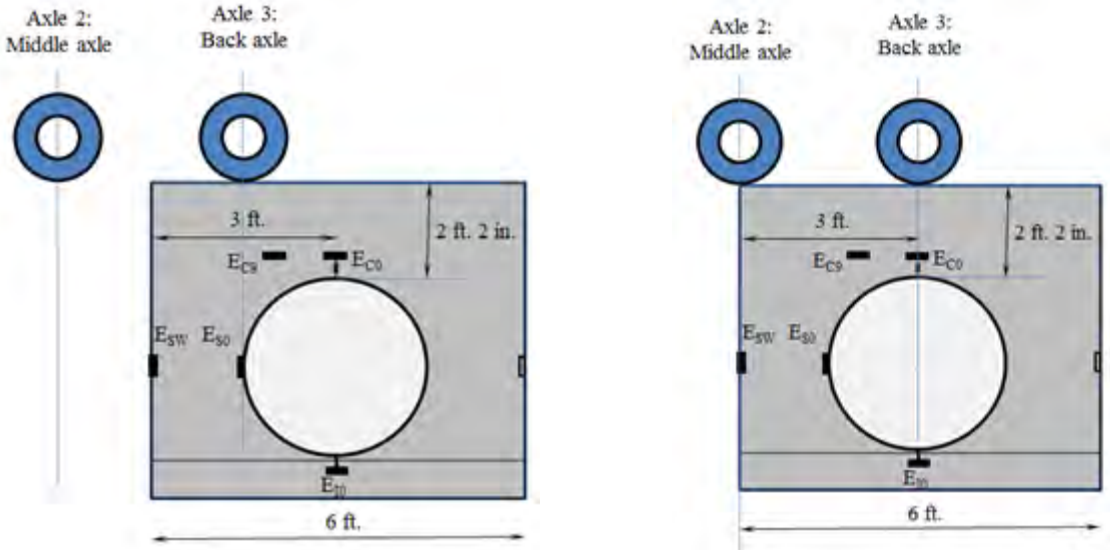
Figure 3.62: Measured Earth Pressures Around the Pipe Under Truck Loading on Test Section A

3.6.2 Earth Pressure-Test Section B

Figure 3.63 shows the positions of the wheels when the truck loads were applied on Test Section B. In Test Section B, when the back axle was applied between the pipe crown and the trench wall (Figure 3.63a) the middle axle was on the surrounding soil, whereas in Test Section A, the middle axle was on the trench (Figure 3.63b). This loading configuration in Test Section B was different from that in Test Section A when the back axle was applied between the pipe crown and the trench wall. Figure 3.64 shows the measured earth pressures around the pipe against the time elapsed in both Test Sections A and B with the truck loadings. When the truck load was applied on Test Section B, there was no or little change in the pressures measured around the pipe at the instrumented section (Section 2) of the pipe in Test Section A. It is shown that the truck load applied on Test Section B had no or negligible effects on the pipe in Test Section A.

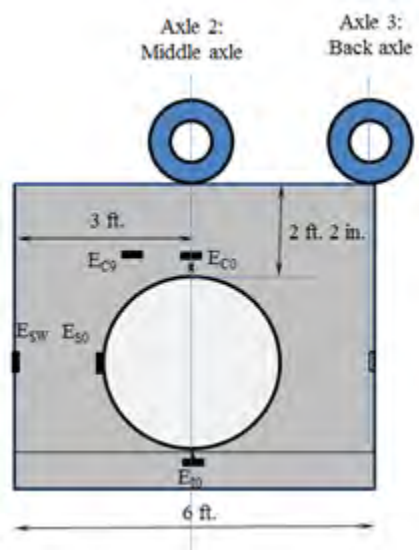
When the back axle was placed between the pipe crown and the trench wall (Figure 3.63a), the pressure cell 3E_{C12} placed at 12 inches away from the pipe crown in Section 3 in Test

Section B recorded the highest vertical earth pressures of 8.18 psi. The vertical earth pressure at the pipe crown $3E_{C0}$ showed 0.97 psi. When the back axle was placed above the crown (Figure 3.63b), the earth pressures measured around the pipe in Test Section B were similar to those obtained with the back axle above the crown in Test Section A. The pressure cells placed at the crown, $4E_{C0}$ and $3E_{C0}$, in Sections 4 and 3 on the eastern test section (Section B) recorded the highest pressures of 8.91 and 8.35 psi, respectively. The vertical earth pressure at 12 inches away from the center ($3E_{C12}$) was 5.01 psi, which was 0.6 times the pressure on the pipe crown ($3E_{C0}$). The horizontal earth pressure at the pipe springline ($3E'_{s0}$) was 0.11 times the vertical earth pressure on the crown ($3E_{C0}$). The ratio of the horizontal pressure at the springline ($3E'_{s0}$) to that at the trench wall ($3E'_{sw}$) was 1.16. The vertical earth pressure at the invert ($3E_{I0}$) was 1.04 psi, which was 0.12 times the pressure on the pipe crown ($3E_{C0}$). For the middle axle above the pipe crown (Figure 3.63c), the earth pressure distribution around the pipe was similar to that for the back axle applied above the crown (Figure 3.63b).



(a) Back Axle Between the Crown and Trench Wall

(b) Back Axle Over the Crown



(c) Middle Axle Over the Crown

Figure 3.63: Axle Loads on the Pipe in Test Section B

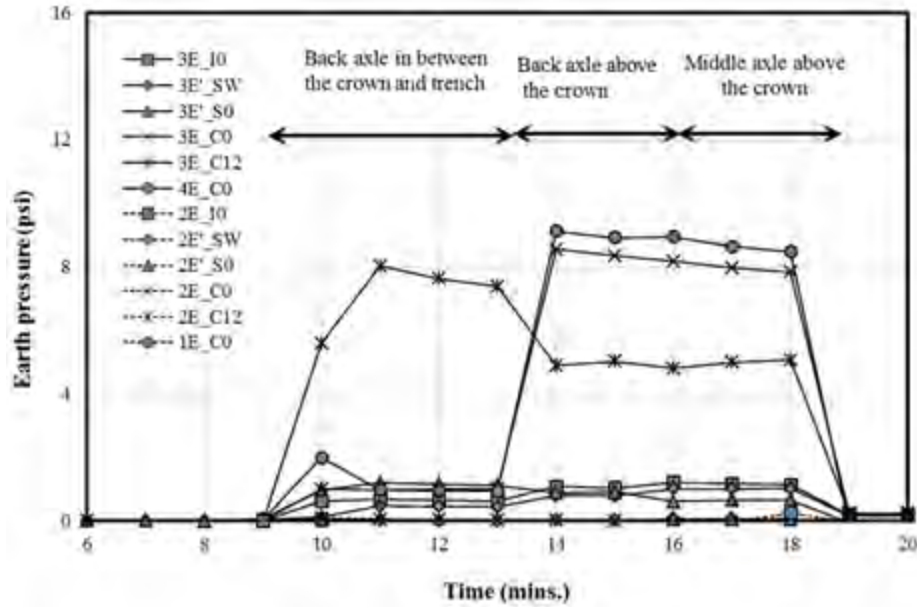


Figure 3.64: Measured Earth Pressures Around the Pipe Under Truck Loading on Test Section B

Table 3.1 shows the comparison of the earth pressure distributions around the pipe in Test Section A (with the AB3 aggregate as backfill) and Test Section B (with the crushed stone as backfill). When the truck load was applied with the back and middle axles over the pipe crown in Test Sections A and B, the measured earth pressures around the pipe in Test Section A were higher than those in Test Section B, except the earth pressure at 12 inches away from the pipe ($3E_{C12}$). For example, the earth pressures at the crown ($3E_{C0}$) in Test Section B were lower than those in Test Section A, whereas the earth pressures at 12 inches from the crown of the pipe ($3E_{C0}$) in Test Section A were higher than those in Test Section B. The possible reason is the side fill of the pipe in Test Section A is stiffer than that in Test Section B, and thus the side fill in Test Section A can provide more support to the pipe in the horizontal direction which results in stiffer pipe in Test Section A. Therefore, the earth pressure at the pipe crown in Test Section A is higher than that in Test Section B. When the back axle was applied between the crown and the trench wall, the earth pressure distributions around the pipe were not directly comparable between Test Section A and Test Section B because of the different loading configurations.

Table 3.1: Comparison of the Earth Pressures (psi) Measured Around the Pipe in the Field Test

Sections	Positions	Symbols	Back axle at the crown	Back axle between the crown and trench wall	Middle axle at the crown
Section A	Crown	1E _{C0}	9.95	1.87	10.33
		2E _{C0}	9.75	2.45	9.95
		2E _{C12}	3.72	10.06	3.66
	Springline	2E _{SW}	1.20	0.82	1.48
		2E _{S0}	1.60	2.16	2.13
	Invert	2E _{I0}	1.47	1.95	1.74
Section B	Crown	4E _{C0}	8.91	0.96	8.64
		3E _{C0}	8.35	0.99	7.96
		3E _{C12}	5.02	7.63	4.99
	Springline	3E _{SW}	0.79	0.45	1.02
		3E _{S0}	0.91	1.15	0.66
	Invert	3E _{I0}	1.04	0.64	1.17

The vertical earth pressures on the top of the pipe under the applied truck load with back and middle axles above the crown in each test were also calculated using two approximate methods: the simplified distribution methods in AASHTO (2012) and proposed by Giroud and Han (2004). The moduli of elasticity of the AB3 aggregate needed by the Giroud and Han method for the calculation of the earth pressures was determined from the small plate loading test. When the truck axle load was applied directly above the pipe crown, the pressure induced by the second axle load (at 3 ft distance apart) on the top of the pipe was found to be very small using the Foster and Ahlvin (1954) method under a uniformly loaded circular area. For example, when the back axle was applied above the pipe crown, the pressure on the pipe crown due to the middle axle load was found to be 0.24 psi, which was considered small or negligible. Therefore, in the calculation of the earth pressures on the top of the pipe using the approximate methods, the effect of the second axle load was neglected. The calculated earth pressures are then compared with the average earth pressures of E_{C0} and E_{C12} measured on the top of the pipe in Table 3.3. The measured pressures at the crown of the pipe were lower than those calculated using the

Giroud and Han (2004) method as well as the AASHTO (2012) method. In other words, the Giroud and Han method and the AASHTO method are conservative in estimating the distributed pressure on the pipe crown by the applied load on the surface.

Table 3.2: Comparison of the Measured and Calculated Earth Pressures (psi) Around the Pipe in the Field Test Using Foster and Ahlvin (1954) Method

Section	Location	Back Axle at the Crown		Back Axle between the Crown and the Trench Wall		Middle Axle at the Crown	
		Measured	Calculated	Measured	Calculated	Measured	Calculated
Section A	1E _{C0}	9.95	8.82	1.87	4.16	10.33	8.82
	2E _{C0}	9.75	8.82	2.45	4.16	9.95	8.82
	2E _{C12}	3.72	4.8	10.06	9.08	3.66	5.82
Section B	4E _{C0}	8.91	8.82	0.96	2.08	8.64	8.82
	3E _{C0}	8.35	8.82	0.99	2.08	7.96	8.82
	3E _{C12}	5.02	5.82	7.63	8.58	4.99	4.8

Table 3.3: Comparison of the Average Measured Crown Pressures (psi) with AASHTO (2012) and Giroud and Han (2004) Methods

Section	Measured	AASHTO (2012)	Giroud and Han (2004)
	Back Axle at the Crown		
Section A	6.7	9.2	8.9
Section B	6.7	9.2	9.2
Middle Axle at the Crown			
Section A	6.8	9.2	8.9
Section B	6.5	9.2	9.2

3.6.3 Deflections-Test Section A

The deflections of the pipe (or the changes of the inside diameters) with truck axle loadings against the time elapsed both in Test Sections A and B are shown in Figure 3.65. When the truck load was applied directly above the instrumented section (Section 2) close to the centerline on Test Section A, there were no or little changes in the diameter of the pipe in the

instrumented section (Section 3) of the pipe in Test Section B. It is shown that the truck load applied above the instrumented section close to the centerline of the roadway (Section 2) in Test Section A had no or negligible effects on the instrumented section (Section 3) close to the centerline of the roadway in Test Section B.

When the truck load was applied above the pipe, the vertical diameter of the pipe (ΔD_V) decreased while the horizontal diameter of the pipe (ΔD_H) increased. Figure 3.65 also shows that the horizontal deflection of the pipe (ΔD_H) was less than the vertical deflection (ΔD_V). The maximum deformation of the pipe was pronounced when the middle axle load was applied above the pipe crown. The deflections of the pipe which occurred with the middle axle above the pipe crown were slightly higher or close to those occurring when the back axle was above the pipe crown. The back axle placed between the pipe crown and the trench wall induced smaller deflections of the pipe than those under the back and middle axles above the pipe crown. When the middle axle was placed above the pipe crown, the decrease in the vertical diameter and the increase in the horizontal diameter of the pipe in Test Section A (ΔD_V and ΔD_H) were 0.071 inches (0.20% of the initial diameter) and 0.028 inches (0.08% of the initial diameter), respectively. The vertical deflections of the pipe (ΔD_V) were 2.53 times the horizontal deflections of the pipe (ΔD_H). After the completion of the static loading, the truck was run over the pipe at a slow speed and the deflections of the pipe were even higher than those at the static truck loading, as shown in Figure 3.65. The decrease in the vertical diameter and the increase in the horizontal diameter of the pipe in Test Section A (ΔD_V and ΔD_H) were 0.088 inches (0.24% of the initial diameter) and 0.039 inches (0.11% of the initial diameter) when the truck was run at the slow speed, respectively.

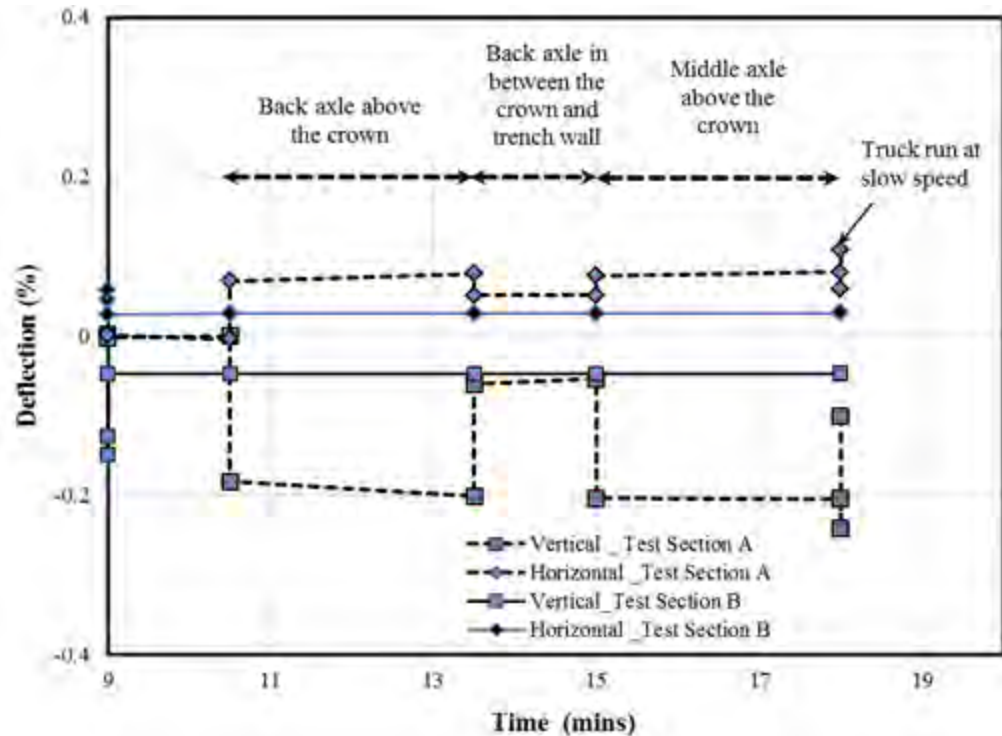


Figure 3.65: Deflections of the Pipe Under the Truck Loading in Test Section A

3.6.4 Deflections-Test Section B

The deflections of the pipe (or the changes of the inside diameters) with the truck axle loadings against the time elapsed both in Test Sections A and B are shown in Figure 3.66. The deflection of the pipe in Test Section B was similar to that in Test Section A. When the truck load was applied on Test Section B, there were no or little changes in the diameter of the pipe in Test Section A.

The maximum deflection of the pipe was pronounced when the back axle was placed above the pipe crown. The deflection of the pipe occurring with the back axle above the crown was slightly higher or close to that when the middle axle was above the pipe crown. The back axle placed between the pipe crown and the trench wall induced smaller deflections of the pipe than those under the back and middle axles above the pipe crown. When the back axle was placed above the pipe crown, the decrease in the vertical diameter and the increase in the horizontal diameter of the pipe in Test Section B (ΔD_V and ΔD_H) were 0.05 inches (0.14% of the initial diameter) and 0.016 inches (0.045% of the initial diameter), respectively. The vertical

deflections of the pipe (ΔD_V) were 3.22 times the horizontal deflections at the center of the pipe (ΔD_{HC}). After the completion of the static loading, the truck was run over the pipe at a slow speed and the deflections of the pipe were even slightly higher than those at the static truck loading, as shown in Figure 3.66. The decrease in the vertical diameter and the increase in the horizontal diameter of the pipe in Test Section A (ΔD_{VC} and ΔD_{HC}) were 0.053 inches (0.15% of the initial diameter) and 0.02 inches (0.057% of the initial diameter) when the truck was run at the slow speed, respectively.

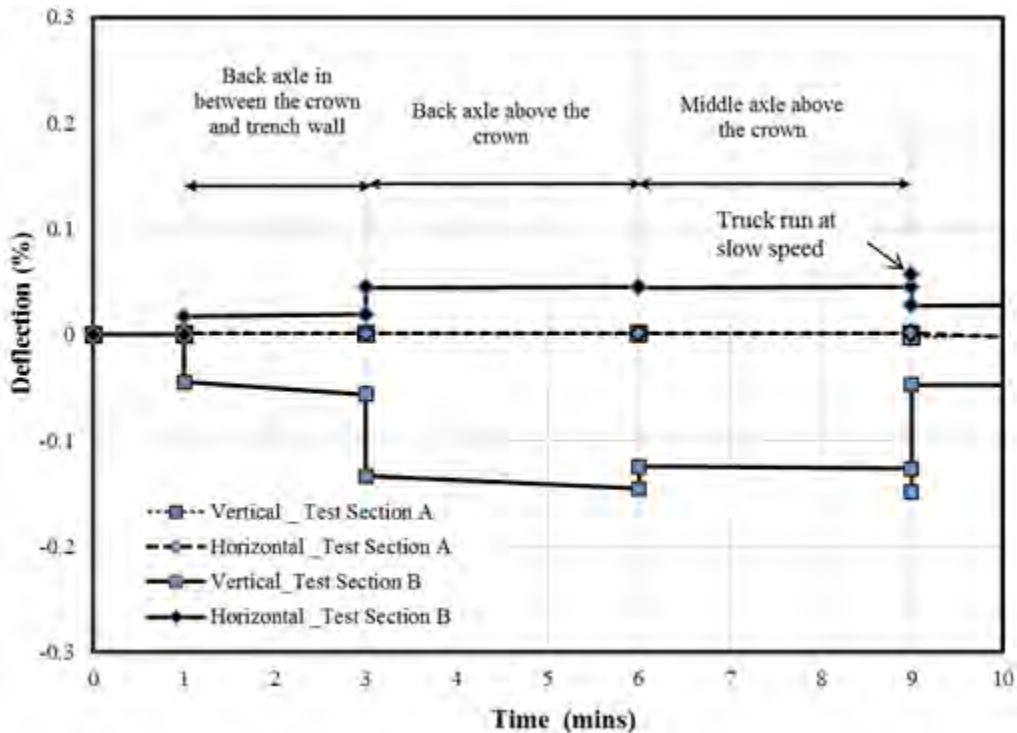


Figure 3.66: Deflections of the Pipe Under the Truck Loading in Test Section B

Table 3.4 shows the comparison of the deflections of the pipe in Test Section A (with the AB3 aggregate as the backfill) and Test Section B (with the crushed stone as the backfill). For the truck load applied with the back or middle axle over the pipe crown, the measured deflections of the pipe in Test Section A were larger than those in Test Section B. These differences might result from more stress concentration on the pipe crown in Test Section A. When the back axle was applied between the crown and the trench wall, the deflections of the pipe were not directly comparable between Test Section A and Test Section B because of the

different loading. The vertical to horizontal deflection ratios ($\Delta D_V/\Delta D_H$) for the pipe varied from 2.55 to 3.22 when the back and middle axles were placed above the pipe, and are presented in Table 3.4.

Table 3.4: Comparison of the Deflections of the Pipe

Sections	Symbols (unit)	Back Axle at the Crown	Back Axle in between the Crown and Trench Wall	Middle Axle at the Crown	Moving Truck Load
Section A	ΔD_V (in.)	0.201	0.053	0.204	0.244
	ΔD_H (in.)	0.078	0.051	0.080	0.173
	Ratio	2.570	1.030	2.550	1.410
	ΔD_H (in.) (calculated)	0.191	0.169	0.1936	-
Section B	ΔD_V (in.)	0.145	0.056	0.126	0.148
	ΔD_H (in.)	0.045	0.019	0.045	0.057
	Ratio	3.220	2.940	2.800	2.590
	ΔD_H (calculated)	0.375	0.332	0.379	-

Table 3.4 also shows the calculated horizontal deflections (ΔD_H) using the Iowa Formula. The calculated horizontal deflections (ΔD_H) of the pipe under the truck load in Test Sections A and B were based on the bedding constant (k) of 0.1, the earth pressure on the crown (i.e., under the applied truck load), and the moduli of subgrade reaction of 5,950 psi for the compacted AB3 aggregate and 3,700 psi for the compacted crushed stone. The moduli of the subgrade reaction for the AB3 aggregate and the crushed stone were determined based on the LWD test. The average values of the measured earth pressures on the crown (E_{C0}) and at 12 inches away from the crown (E_{C12}) were calculated (Table 3.3) and used for the deflection calculation. It is shown that the Iowa Formula over-predicted the deflections of the pipe during all applied truck loadings.

3.6.5 Strains-Test Section A

The measured strains on steel ribs and the adjusted strains on plastic according to Brachman et al. (2008) are plotted against the time elapsed, as shown in Figures 3.67 to 3.69, when the truck load was applied.

Since the maximum strains at the steel ribs recorded in the laboratory tests were in the circumferential direction at the pipe crown and the springline, the strain gages were only placed in the circumferential direction at the pipe crown and the springline in the field test. The strains measured on the steel at the ribs are shown in Figure 3.67. All strain gages, G_{SC1} and G_{SC2} at the springline and G_{CC1} and G_{CC2} at the crown in the circumferential direction, showed an increase in the compression strains under the applied truck load. The maximum circumferential strain of 0.0115% (G_{CC1} , compressive strain) was recorded at the steel rib in the pipe crown when the middle axle was placed above the pipe crown. The strain gages at the steel rib in the springline showed the maximum circumferential strain of 0.00416% (G_{SC2} , compressive strain) when the middle axle was above the pipe crown. For the back axle placed above the pipe crown, the measured strains were close to or slightly lower than those recorded for the middle axle placed above the pipe crown. The strain gages fixed on both sides of the steel rib at any particular location gave similar values (i.e., there were no sudden changes in the strain values). This result indicates that the out-of-plane buckling of the steel ribs did not occur during the truck loading. The maximum strains, which were observed at the springline in the circumferential direction, are compared with the calculated values in Table 3.5. The strains on the steel were calculated assuming the pipe carried all the applied loads on the top of the pipe (i.e., neglecting the side resistance from the fill at the springline). The calculated strains were higher than the measured strains.

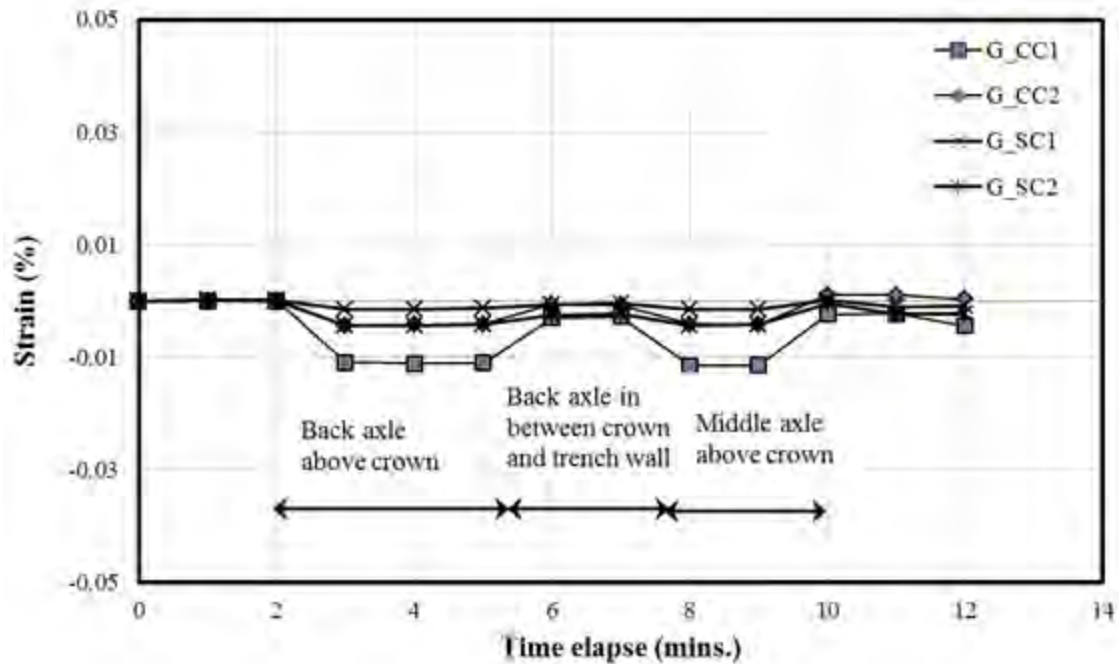


Figure 3.67: Measured Strains on the Steel Ribs in Test Section A

Table 3.5: Comparison of the Calculated and Measured Strains of the Pipe in the Field

Sections	Symbols		Back Axle at the Crown	Back Axle in between the Crown and Trench Wall	Middle Axle at the Crown
Section A	G_SC	Calculated	-0.01093	-0.0096	-0.01106
		Measured	-0.004360	0.0025	0.00416
	G'_CR	Calculated	0.03960	0.0351	0.04010
		Measured	0.032100	0.0124	0.03800
Section B	G_SC	Calculated	-0.010800	-0.00693	-0.010500
		Measured	N/A	N/A	N/A
	G'_CR	Calculated	0.039440	0.02530	0.038200
		Measured	0.03800	0.033	0.037100

Figure 3.68 shows the radial strains on the plastic cover at the ribs against the applied truck load. The strains developing on the plastic were higher in magnitude than the strains on the steel. Most of the strain gages showed an increase in tensile strains. The maximum radial strain on the plastic surface at the rib occurred at the pipe crown under the truck loadings. The maximum radial strain of 0.0369% (G'_{CR1} , tensile strain) was recorded at the plastic rib at the

pipe crown when the middle axle was placed above the pipe crown. The strain gages on the plastic at the plastic rib in the pipe springline and invert showed the maximum radial strains of 0.0195% (G'_{SR1} , tensile strain) and 0.0143% (G'_{IR1} , tensile strain), respectively, when the middle axle was above the pipe crown. For the back axle placed above the pipe crown, the measured strains were close to or slightly lower than those recorded for the middle axle placed above the pipe crown. The strain gages fixed on both sides of the steel rib at any particular location gave similar values (i.e., there were no sudden changes in the strain values). This result indicates that the out-of-plane buckling of the steel ribs did not occur during the truck loading.

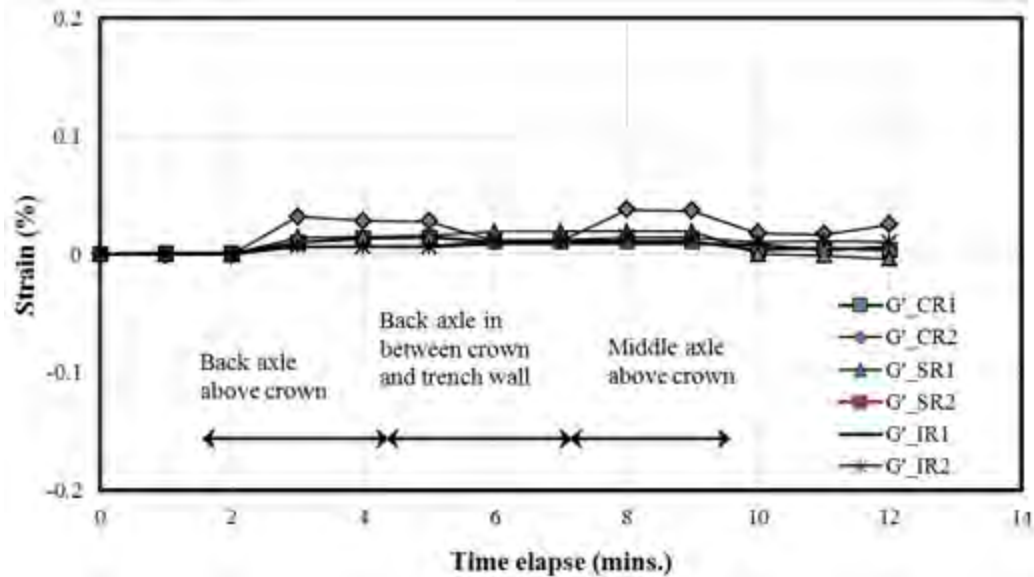
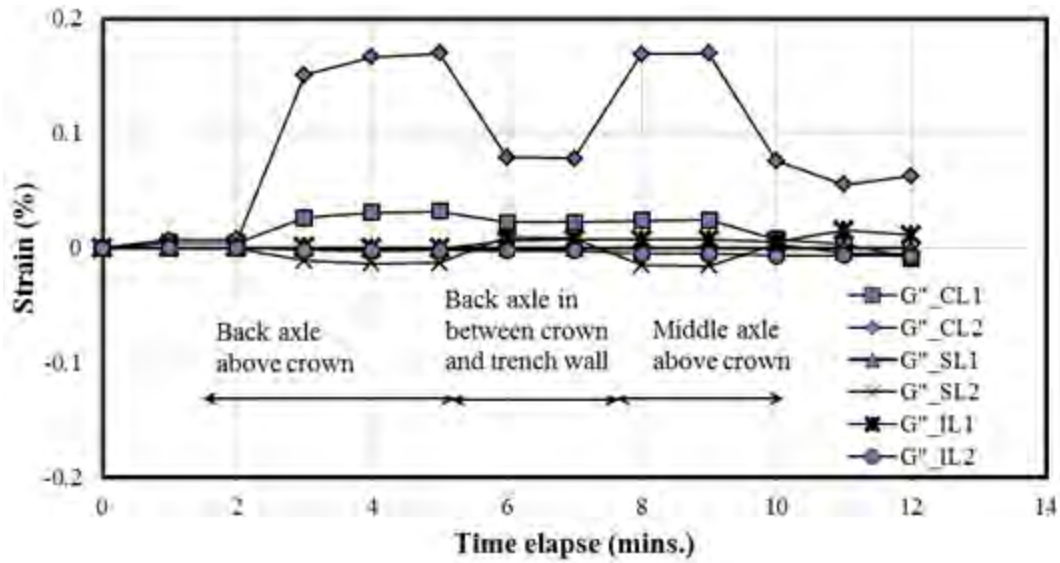


Figure 3.68: Measured Strains on the Plastic at Ribs in Test Section A

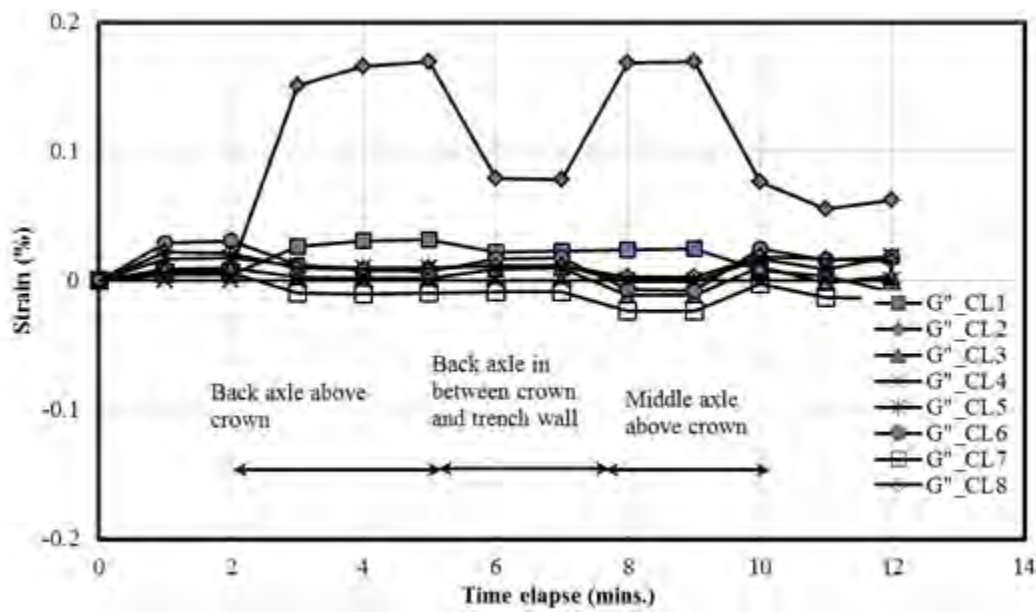
Since the maximum earth pressures and the strains (on the plastic) during the truck loading were observed on the top of the pipe at the crown, the strains on the plastic cover at the ribs in the radial direction at the pipe crown were calculated and compared with the measured strains. The comparison between the measured and calculated strains in the plastic cover on the rib at the pipe crown is presented in Table 3.5. The calculated strains were close to the measured strains when the back or middle axle was applied above the pipe crown. The measured strains at the plastic cover at the plastic rib in the crown were lower than the calculated strains for the back axle between the crown and the trench wall.

Figure 3.69 shows the strains measured by the strain gages on the plastic wall inside and outside the pipe. The magnitudes of the strains on the pipe walls were higher than the strains on the steel and the plastic at the ribs. Figure 3.69a shows the strains measured by the strain gages at the instrumented section (Section 2) close to the centerline of the roadway beneath the truck wheel path. The maximum strains were recorded at the pipe crown. At the pipe crown, both strain gages placed on the plastic inside and outside the pipe showed the tensile strain. This indicates that the plastic pipe wall behaved as the membrane element. However, the strain gage affixed on the plastic inside showed the higher tensile strain than the strain recorded by the strain gage on the plastic outside. This also indicates that the plastic wall between the ribs behaves as a beam element. Therefore, from the above two findings it is clear that the plastic pipe wall had the combined action of bended beam and tensioned membrane. The strains on the plastic wall at the invert and the springline were small as compared with those recorded on the pipe crown. The maximum tensile strain of 0.169% was recorded by the strain gage G''_{CL2} under the back axle load above the pipe crown. A numerical model is needed to investigate the load transfer mechanism of the plastic wall (i.e., the valley) further.

Figure 3.70 shows the strains measured by the strain gages on the plastic wall inside and outside at the crown against the distance of the strain gages from the instrumented section (Section 2) in Test Section A. The strains measured along the longitudinal direction of the pipe at different distances from the instrumented section showed the similar behavior for all three configurations of the truck loading. The maximum strains at the pipe wall were recorded at the instrumented section beneath the applied truck axle. These maximum strains might be due to the concentration of the truck axle load on the pipe crown beneath the point of application of the axle load. The strains measured on the outside plastic wall along the pipe run were lower than those measured inside on the plastic wall to a distance of approximately 36 inches from the instrumented section. After the distance of 36 inches along the pipe run, the strains on the outside wall were measured higher than those on the inside wall. The maximum strains of 0.125% (G''_{CL2} , tensile strain) and 0.024% (G'_{CL2} , tensile strain) were recorded during the truck loadings.



(a) Strains on Plastic Beneath the Wheel Path



(b) Strains on Plastic Away From the Wheel Path to the Centerline of the Roadway

Figure 3.69: Measured Strains on the Inside and Outside Plastic Walls of the Pipe in Test Section A

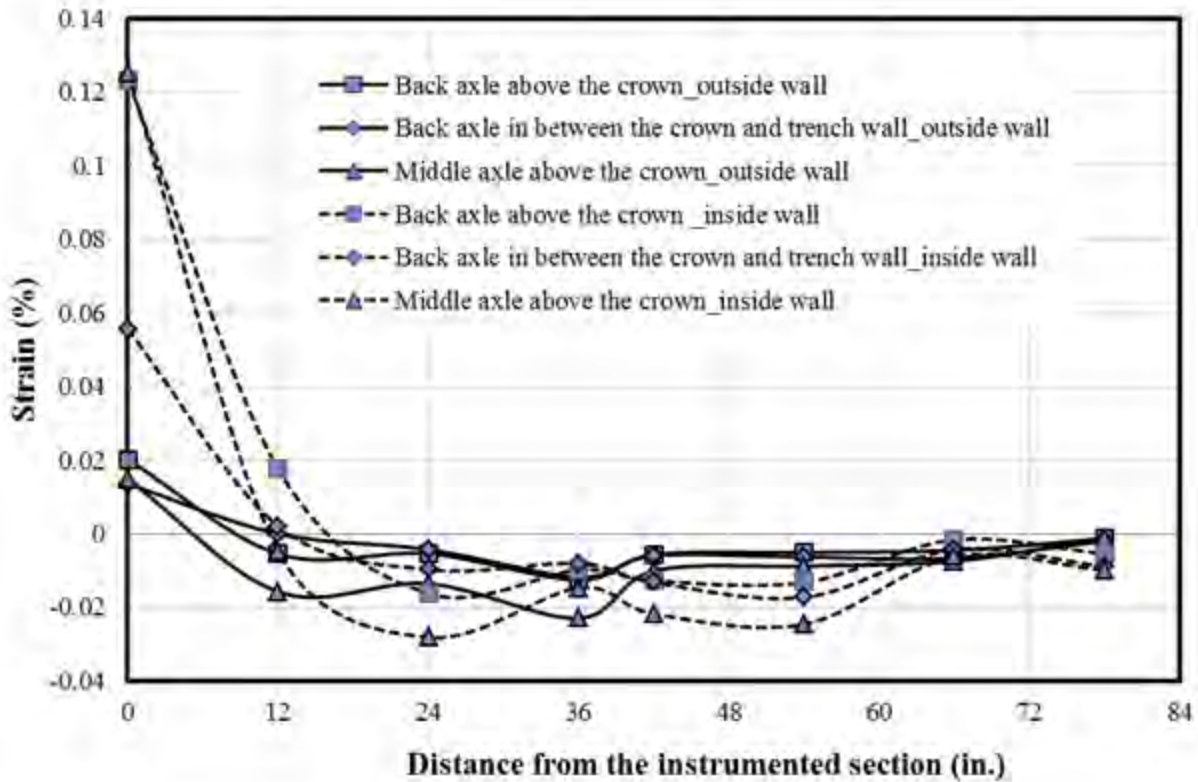


Figure 3.70: Measured Strains on the Inside and Outside Plastic Walls of the Pipe in Test Section A

3.6.6 Strains-Test Section B

The measured strains from the strain gages attached on the plastic surface of the pipe at the instrumented section (Section 3) of Test Section B were adjusted according to Brachman et al. (2008) and are plotted against the time elapsed during the truck loading as shown in Figures 3.70 to 3.71.

Two strain gages attached on the steel at the pipe springline did not work during the installation of the pipe. Two strain gages, G_{CC1} and G_{CC2} at the crown in the circumferential direction, showed an increase in the compression strain under the applied truck load, as shown in Figure 3.71. The maximum circumferential strain of 0.00378% (G_{CC1} , compressive strain) was recorded at the steel rib at the pipe crown when the back axle was placed above the pipe crown. For the middle axle placed above the pipe crown, the measured strains were close or slightly lower than those recorded for the back axle placed above the pipe crown. The strain gages fixed

on both sides of the steel rib at any particular location gave similar values (i.e., there were no sudden changes in the strain values). The calculated strains at the springline in the circumferential direction are presented in Table 3.5.

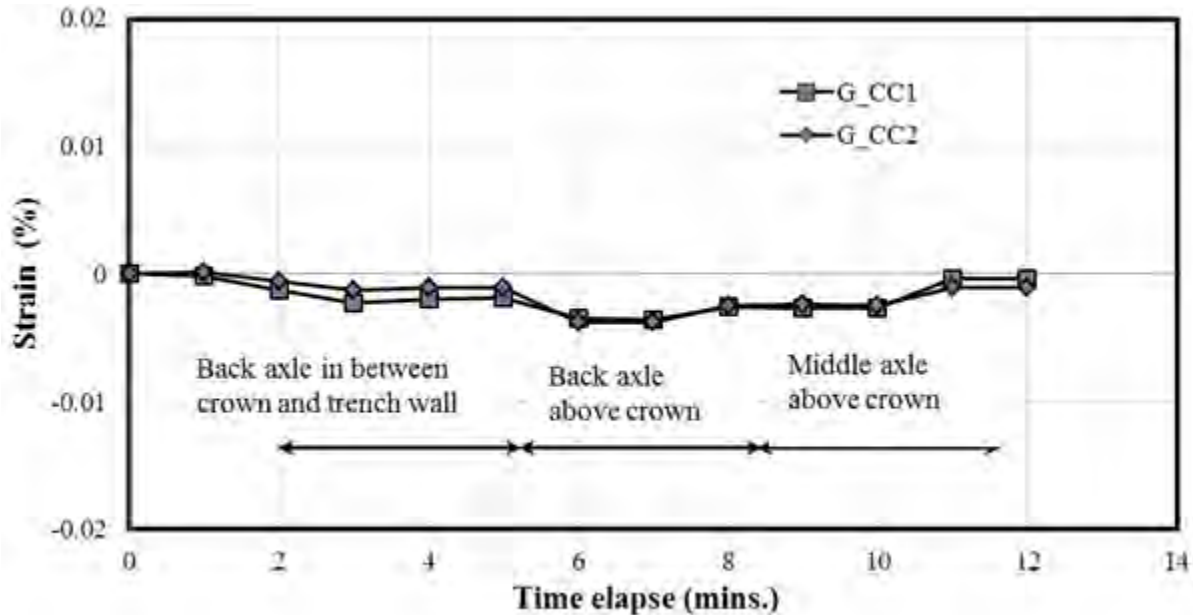


Figure 3.71: Measured Strains on the Steel Ribs in Test Section B

Figure 3.72 shows the radial strains on the plastic cover at the ribs against the applied truck load. The strains developing on the plastic were higher in magnitude than the strains on the steel. Most of the strain gages showed an increase in tensile strains except the strain gage G'_{IR2} at the pipe invert. The maximum radial strains on the plastic cover at the ribs occurred at the pipe crown under the truck loadings. The maximum radial strain of 0.037% (G'_{CR2} , tensile strain) was recorded on the plastic cover at the rib at the pipe crown when the middle axle was placed above the pipe crown. The strain gages on the plastic cover at the rib at the pipe springline and invert showed the maximum radial strains of 0.0113% (G'_{SR2} , tensile strain) and 0.0168% (G'_{IR1} , tensile strain), respectively, when the middle axle was above the pipe crown. For the back axle placed above the pipe crown, all measured strains were close or slightly lower than those recorded for the middle axle placed above the pipe crown. The strain gages fixed on both sides of

the steel rib at any particular location gave similar values (i.e., there were no sudden changes in the strain values).

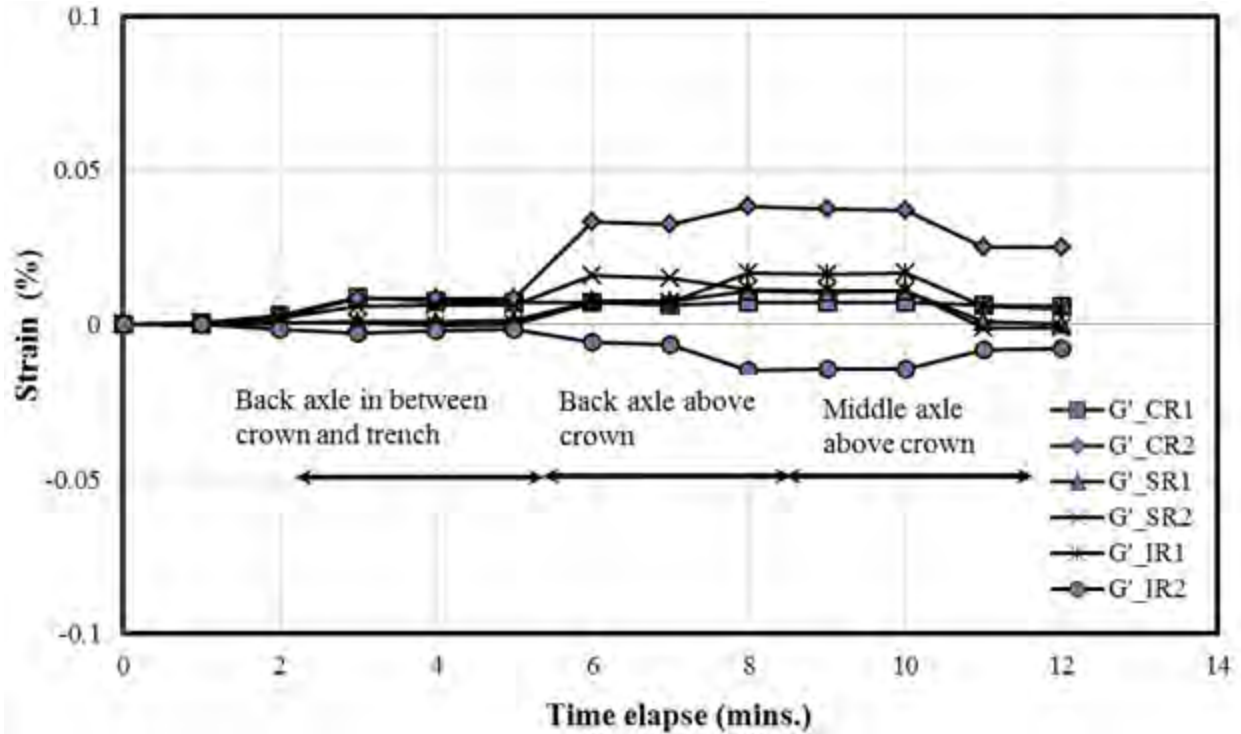


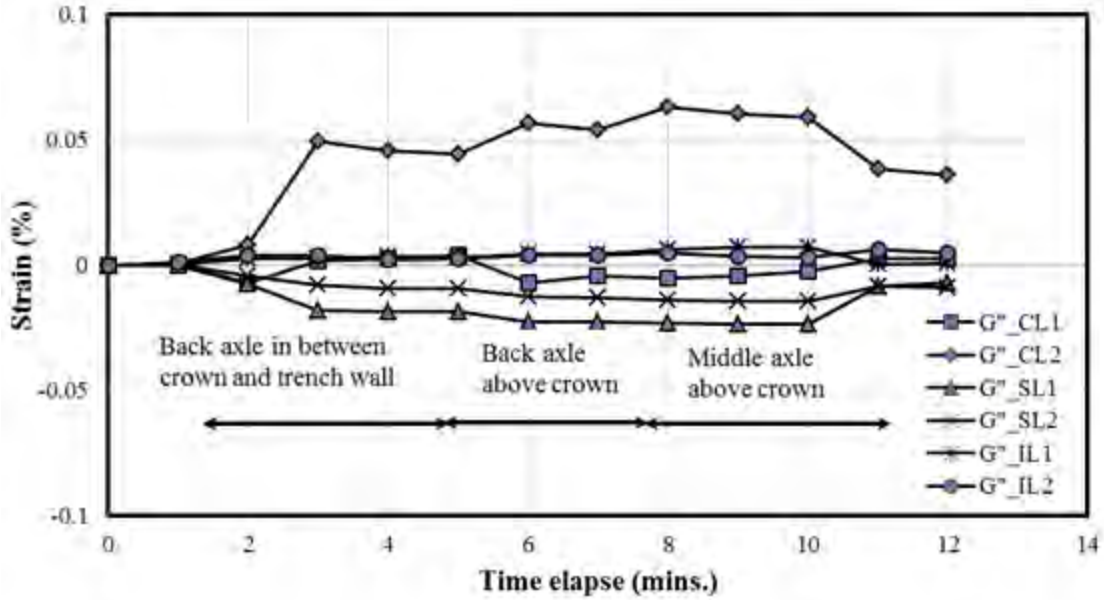
Figure 3.72: Measured Strains on the Plastic at Ribs in Test Section B

The maximum earth pressures and the strains (on the plastic) during the truck loading were observed on the top of the pipe at the crown. Therefore, the strains on the plastic cover at the ribs in the radial direction at the pipe crown were calculated and compared with the measured strains as provided in Table 3.5. The calculated strains were close to the measured strains when the back or middle axle was applied above the pipe crown. The measured strains were lower than the calculated strains at the plastic cover at the rib on the crown for the back axle between the crown and the trench wall.

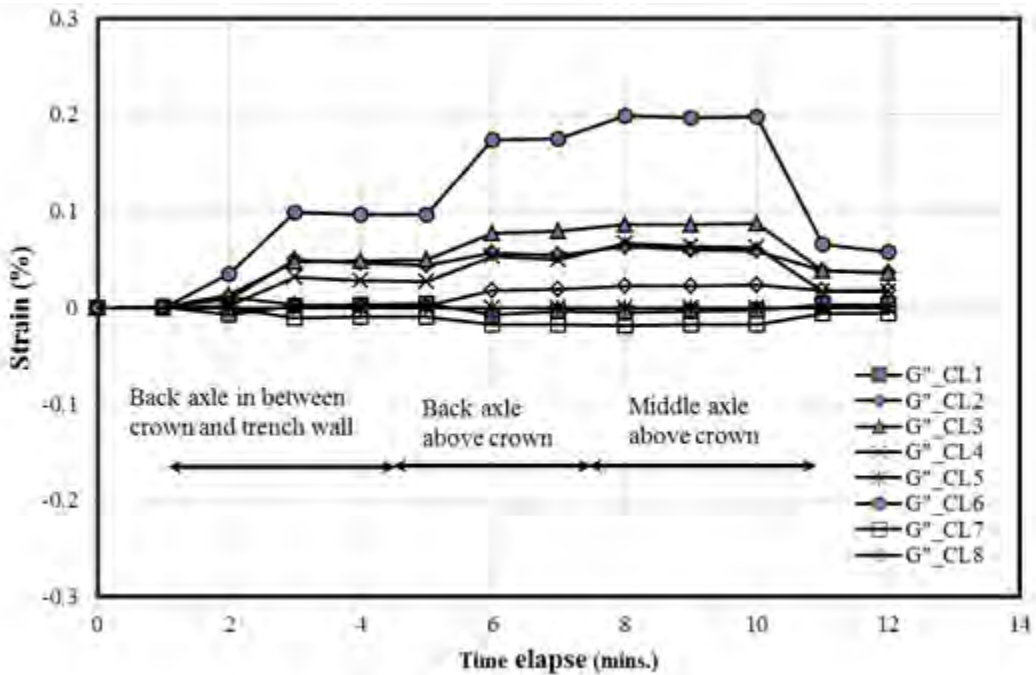
Figure 3.73 shows the strains measured by the strain gages on the plastic walls inside and outside the pipe. The magnitudes of the strains on the pipe walls were higher than the strains on the steel and plastic at the ribs. Figure 3.73a shows the strains measured by the strain gages at the instrumented section (Section 3) close to the centerline of the roadway beneath the truck wheel path in Test Section B. The maximum strains were recorded at the pipe crown. The strains on the

plastic wall at the invert and springline were small as compared with those recorded on the pipe crown. The maximum tensile strain of 0.063% was recorded by the strain gage G''_{CL2} under the middle axle load above the pipe crown. At the pipe crown, the strain gages placed on the plastic inside showed the tensile strains, whereas the strain gages placed outside the pipe showed the compressive strains under the truck loadings. However, the magnitudes of the strains were higher in the strain gages attached on the pipe outside than those on the pipe inside. Most strain gages placed on the plastic wall between the ribs showed the similar behavior to the strain gages attached at the pipe crown beneath the applied truck loadings, as shown in Figure 3.73. This result indicates that the plastic pipe wall had the combined beam and tensioned membrane effect.

Figure 3.74 shows the strains measured by the strain gages on the plastic walls inside and outside at the crown against the distance of the strain gages from the instrumented section (Section 3) in Test Section B. The strains measured along the longitudinal direction of the pipe run at different distances from the instrumented section showed similar behavior for all three configurations of the truck loading. The strains of the plastic walls measured by the strain gages in Test Section B showed the maximum strains were not close to the instrumented section below the point of application of the axle load (as recorded in Test Section A), but were approximately 24 inches away from the instrumented section. The measured strains were uniform near the instrumented section. Similar to Test Section A, the measured strains were higher on the inside pipe wall than those on the outside to a distance of approximately 36 inches. After the distance of approximately 36 inches, the higher strains were measured on the outside pipe wall than those on the inside pipe wall. These may result from the concentration of the truck axle load at the pipe crown beneath the point of application of the axle load. The strains measured on the outside plastic wall along the pipe run were lower than those measured inside on the plastic wall to a distance of approximately 36 inches from the instrumented section. After the distance of 36 inches along the pipe run, the strains on the outside wall were measured higher than those on the inside wall. The maximum strains of 0.153% (G''_{CL6} , tensile strain) and 0.037% (G''_{CL6} , compressive strain) were recorded during the truck loadings.



(a) Strains on Plastic Wall (i.e., Valley) Beneath the Wheel Path



(b) Strains on Plastic Wall (i.e., Valley) Away From the Wheel Path to Centerline of the Roadway

Figure 3.73: Measured Strains on Inside and Outside Plastic Walls of the Pipe in Test Section B

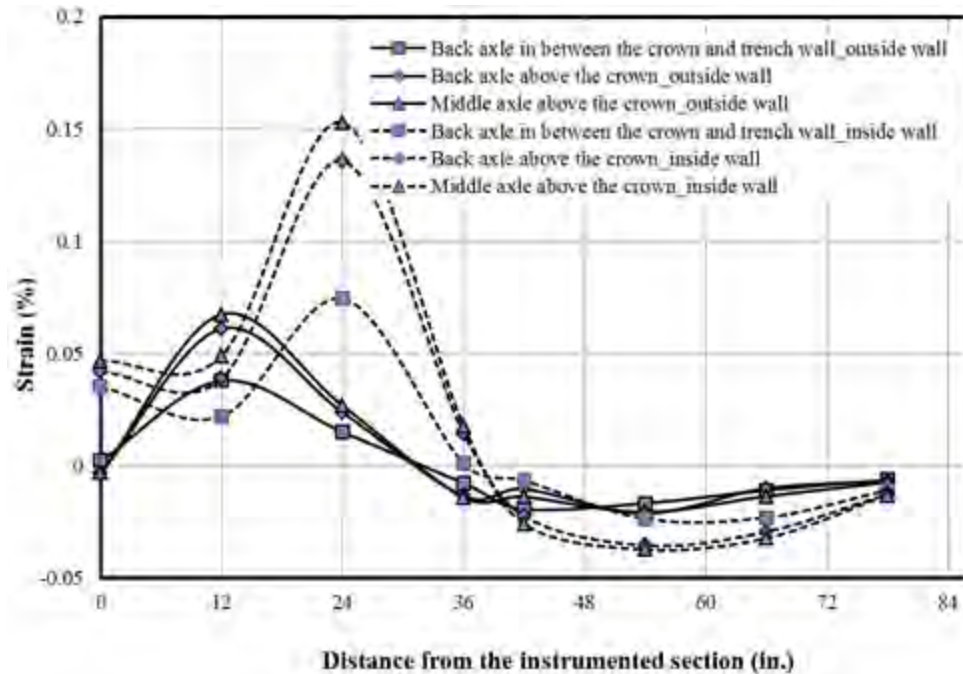


Figure 3.74: Measured Strains on the Inside and Outside Plastic Walls of the Pipe in Test Section B

Figure 3.75 shows the comparison of the strains measured in the field test on the steel at the springline and on the plastic cover at the ribs and pipe walls at the pipe crown in Test Section A (with the AB3 backfill and base course) and in Test Section B (with the crushed stone backfill and the top 6 inches AB3 aggregate). The measured strains on the steel and plastic cover in the field test had the same trends as those obtained on the measured strains in the laboratory tests. The strains measured in the field test were much lower than the permissible values for both steel and plastic of the pipe.

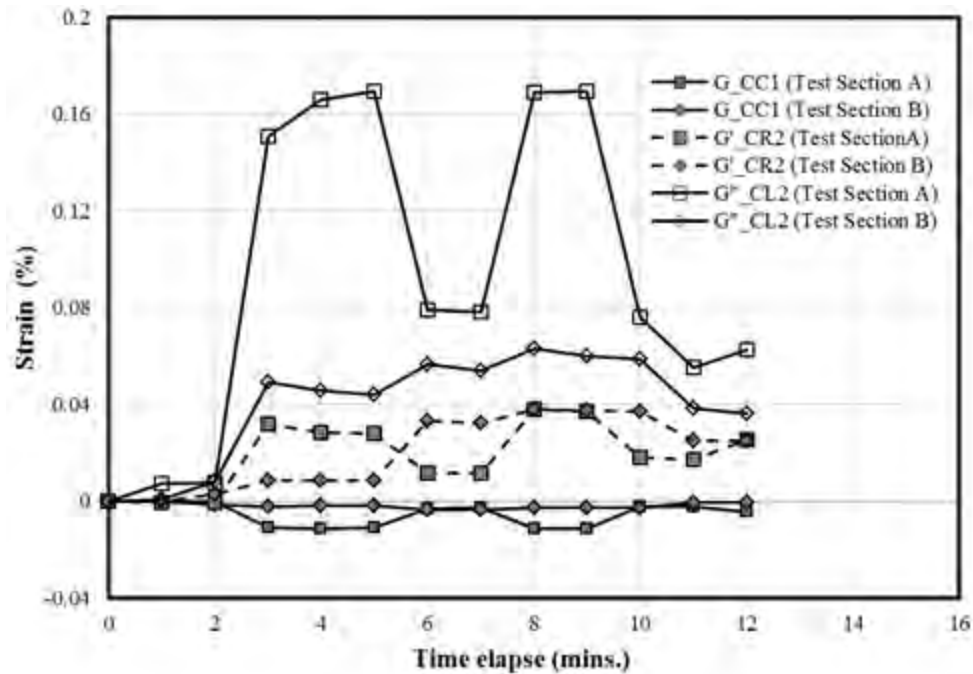


Figure 3.75: Comparison of the Strains Measured on the Steel and Plastic in the Field Test

3.7 Conclusions

Three SRHDPE pipes with a diameter of 36 inches and a total length of 72 ft were installed on 1000 E Road close to Clinton Lake in Lawrence, KS, to investigate the field performance of SRHDPE pipes. The test site was equally divided into four sections. The AB3 aggregate was used as the backfill material in two sections, while the crushed stone was filled in the other two sections. Earth pressures, deflections, and strains of pipes were monitored during the pipe installation and the static loading applied by a construction truck after the completion of the construction. Based on the test results, the conclusions can be drawn as follows:

1. Based on the earth pressure measurement around the pipes, the vertical arching factor (VAF), defined as the ratio of the measured load to the soil prism load on the top of the pipe, varied from 0.97 to 1.46. The average value was 1.15 in this field test. Based on the recommendation by McGrath (1998), the SRHDPE pipe behaved as a metal pipe. This finding is consistent with that from the laboratory tests in the first phase of the project.

2. The lateral earth pressure coefficients at the springline of the pipe were found between the lateral earth pressure coefficient at rest (i.e., K_0) and the passive earth pressure coefficient (i.e., K_p).
3. The peaking behavior induced by the side fill compaction was found both in the AB3 section and the crushed stone section. In the AB3 section, the measured peaking deflection was 0.43% of the pipe diameter, which was smaller than the calculated one of 1.37% using the Masada and Sargand (2007) method. In the crushed stone section, the measured peaking deflection was 0.87% of the pipe diameter, which was larger than the calculated one of 0.37%. The final deflections of the pipes in both sections after installation were smaller than 0.5% in vertical and horizontal directions, which were much smaller than the deflection limit of 5% for thermoplastic pipes suggested by AASHTO (2012).
4. The maximum strain observed during the pipe installation of 0.32% occurred on the pipe plastic wall, which was lower than the long-term service strain limit of 5% for flexible pipes suggested by AASHTO (2012).
5. The maximum earth pressure induced by the static loading occurred at the pipe crown. The Foster and Ahlvin (1954) method reasonably calculated the earth pressure on the crown as compared with the measured earth pressure. However, the Foster and Ahlvin method is not always conservative. The calculated earth pressures by the AASHTO (2012) method and the Giroud and Han (2004) method were slightly higher than the measured; therefore, they can be used to predict the earth pressures on the crown of the SRHDPE pipe under static loading with a certain factor of safety.
6. The maximum deflection of the pipe induced by the truck loading was 0.67% the pipe diameter. The vertical deflection of the pipe was 2 to 3 times the horizontal deflection during the truck loading. The maximum strain of 0.153% was recorded on the plastic wall in the longitudinal direction under the truck loadings.

Chapter 4: Field Performance of the SRHDPE Pipes Field Test II

4.1 Introduction

In the last chapter, a field test was conducted in Lawrence, KS, to investigate the SRHDPE pipe with a diameter of 36 inches during the installation. It is hard to know whether any damage to the pipes was caused by the installation since these pipes are in service. The second field test was conducted in Kansas City, KS, to evaluate possible damage to the pipes during installation as well as the field performance of the SRHDPE pipe. The diameter of the pipes used in this field test was 24 inches, which is the same as that used in the laboratory tests in Phase I, but different from that used in the first field test. Figure 4.1 shows the location of the second field test site, which is located at the right side of the Interstate Highway I-635 towards the Missouri River, close to the state line of Kansas and Missouri. This test site was a KDOT storage yard, which is referred to as the Kansas City field test in this report. This site was relatively flat and no groundwater was observed during the trench excavation.



Figure 4.1: Location of the Second Field Test Site

Source: Google (n.d.)

4.2 Properties of Backfill Material

Two types of backfill material were also used in the Kansas City field test: AB3 aggregate and crushed stone. Figure 4.2 presents the particle size distribution curves of these two backfill materials. The coefficients of uniformity for the AB3 aggregate and the crushed stone were 15.0 and 1.9, respectively while the coefficients of curvature for the AB3 aggregate and the crushed stone were 1.03 and 1.32, respectively. The liquid limit and the plasticity index of the particles passing the No. 40 sieve size in the AB3 aggregate were 20 and 13, respectively; therefore, it can be classified as CL-ML based on the Unified Soil Classification System (USCS) plasticity chart. Based on the ASTM D2487 (2011), the AB3 aggregate can be classified as well-graded gravel (GW-GC), while the crushed stone can be classified as poorly-graded gravel (GP). Figure 4.2 clearly shows that the AB3 aggregate had a much wider range of particle sizes than the crushed stone. The maximum dry density of the AB3 aggregate was determined as 136.5 pcf, and its optimum moisture content was 7.2% using the modified Proctor tests per ASTM D1557 (2012). Figure 4.3 shows the compaction curve of the AB3 aggregate. The maximum density of the crushed stone was 99.2 pcf following ASTM D4253 (2014). Plate loading tests were conducted on the fill material in a wooden box with a dimension of 32 inches long \times 32 inches wide \times 18 inches deep to determine their moduli of the subgrade reaction. The loading plate was a circular plate with a diameter of 6 inches. Figure 4.4 shows the load-settlement curves obtained in the plate loading tests. From Figure 4.4, the moduli of the AB3 aggregate and the crushed stone can be calculated as 3,414 and 2,842 psi, respectively. In other words, the moduli of the AB3 aggregate was higher than that of the crushed stone because the AB3 aggregate had a wide range of particle sizes, which could form a denser state. Triaxial compression tests were used to determine the shear strength parameters at three confining pressures of 5, 10, and 20 psi. The height of the samples was 8 inches, while the diameter of the samples was 4 inches. The samples for the AB3 aggregate were prepared at the optimum moisture content (i.e., 7.2%), while the crushed stone samples were tested in dry condition. Figures 4.5 and 4.6 show the stress-strain curves of the AB3 aggregate and the crushed stone, respectively. Figure 4.7 shows the Mohr circles of the AB3 aggregate and the crushed stone, respectively. The friction angle of both materials was 45° .

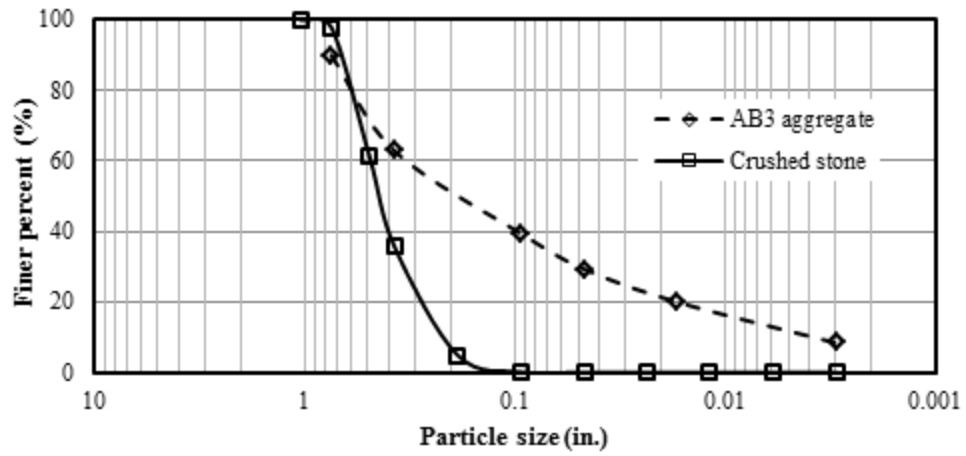


Figure 4.2: Particle Size Distribution Curves of the AB3 Aggregate and the Crushed Stone

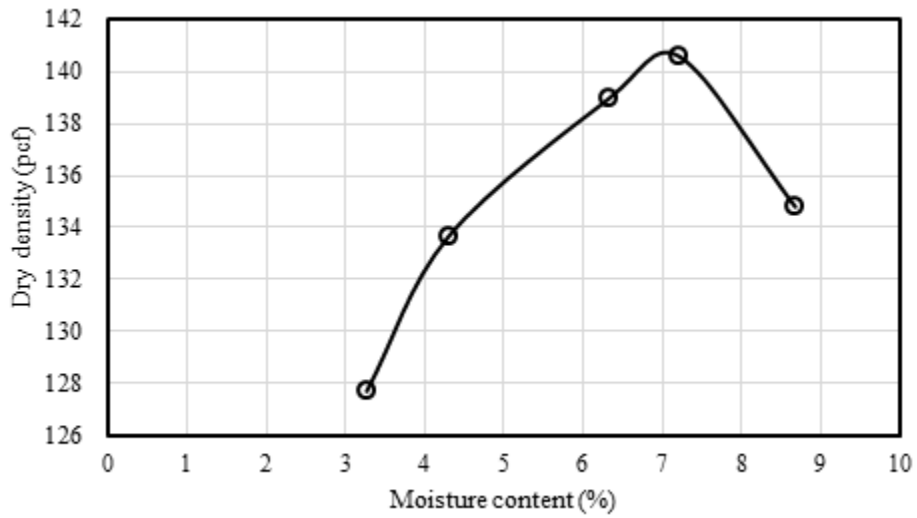


Figure 4.3: The Compaction Curve of the AB3 Aggregate

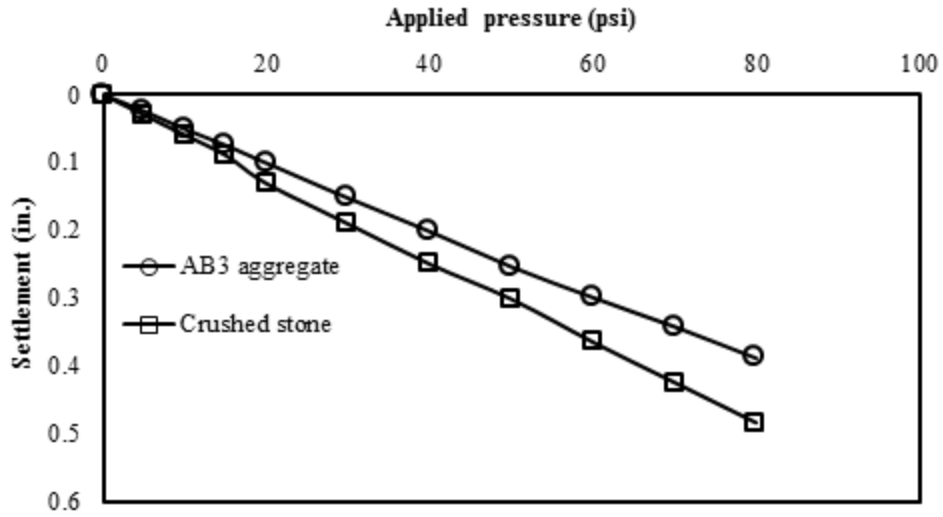


Figure 4.4: Plate Loading Test Results of the AB3 Aggregate and the Crushed Stone

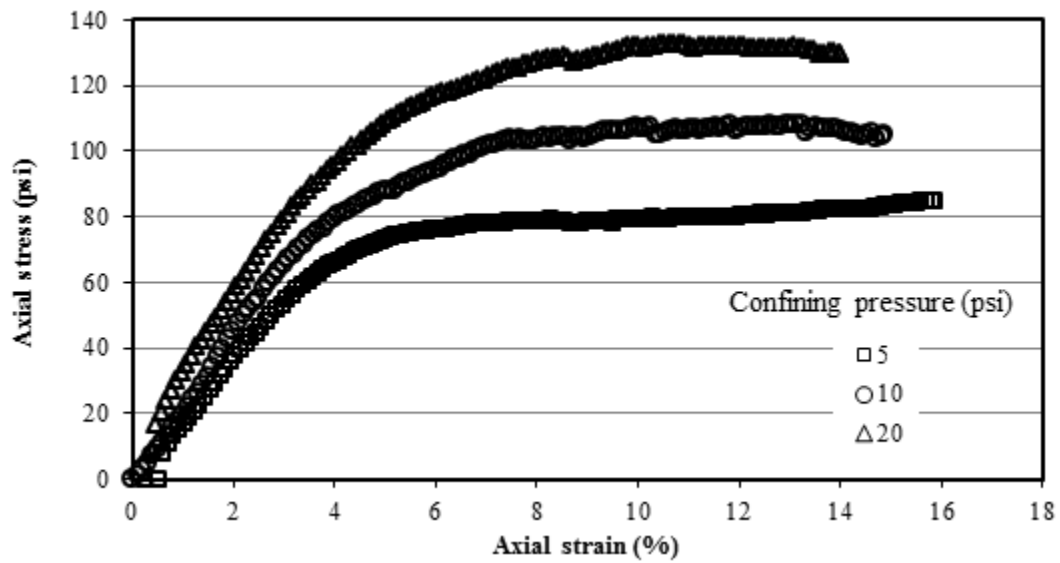


Figure 4.5: Stress-Strain Curves of the AB3 Aggregate from the Triaxial Compression Tests at Different Confining Pressures

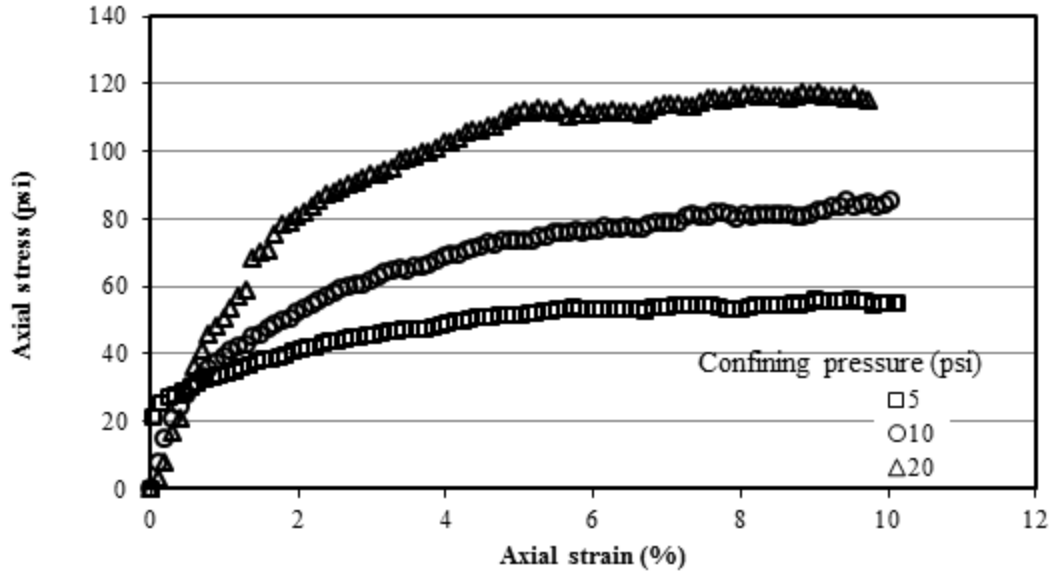
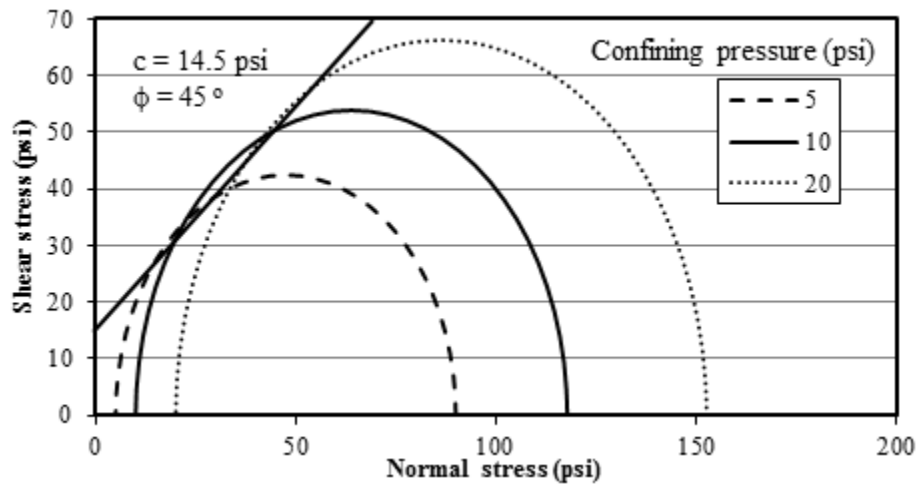


Figure 4.6: Stress-Strain Curves of the Crushed Stone from the Triaxial Compression Tests at Different Confining Pressures



(a) AB3 Aggregate

Figure 4.7: Mohr's Circles of the AB3 Aggregate and the Crushed Stone

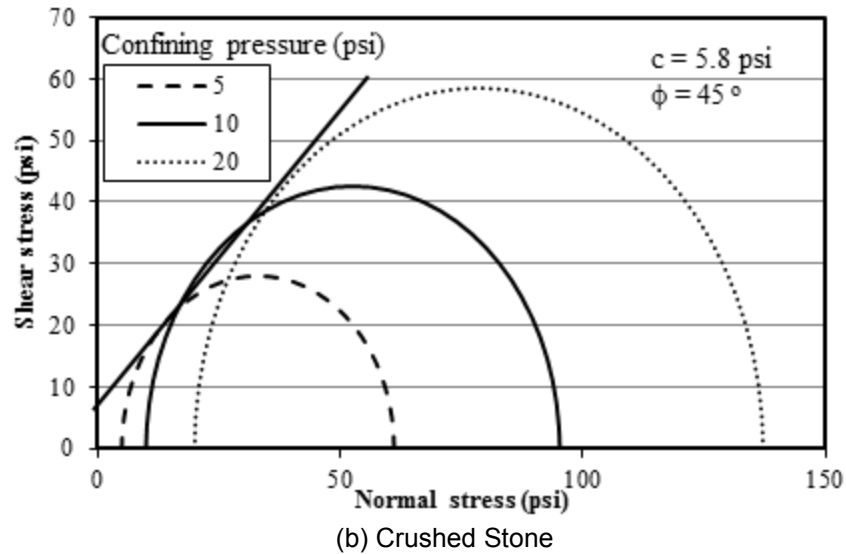


Figure 4.7: Mohr's Circles of the AB3 Aggregate and the Crushed Stone (Continued)

4.3 Test Site, Test Pipes, and Instrumentation

4.3.1 Test Site

A 4.6 ft wide × 27.5 ft long × 4.2 ft deep trench was excavated on the site. The bottom of the trench was leveled before backfilling. The side walls of the trench were vertical during and after the excavation. Figure 4.8 presents the installation plan of the SRHDPE pipes in Sections A and B. Two pipes were buried in the AB3 aggregate in Section A, while the other two pipes were installed in the crushed stone in Section B. The following procedure was followed for the installation: (1) before the installation of the pipe in the trench, Zone I was filled and compacted to form a 6 inch thick bedding layer both in Sections A and B; (2) the connected SRHDPE pipes were placed into the trench and Zone II was filled and compacted to reach the springline level of the pipe (the thickness of Zone II was 11.8 inches); (3) Zone III was filled and compacted with a thickness of 11.8 inches to reach the top of the pipe level; (4) Zone IV was filled and compacted with a lift thickness of 13.3 inches; and (5) Zone V was filled and compacted with a lift thickness of 11.8 inches. Section A was filled with the AB3 aggregate, while Section B was filled with the crushed stone in Zones I to IV. Zone V in both sections was filled with the AB3 aggregate as a base course layer. Two instrumented rings are shown in Figure 4.8b.

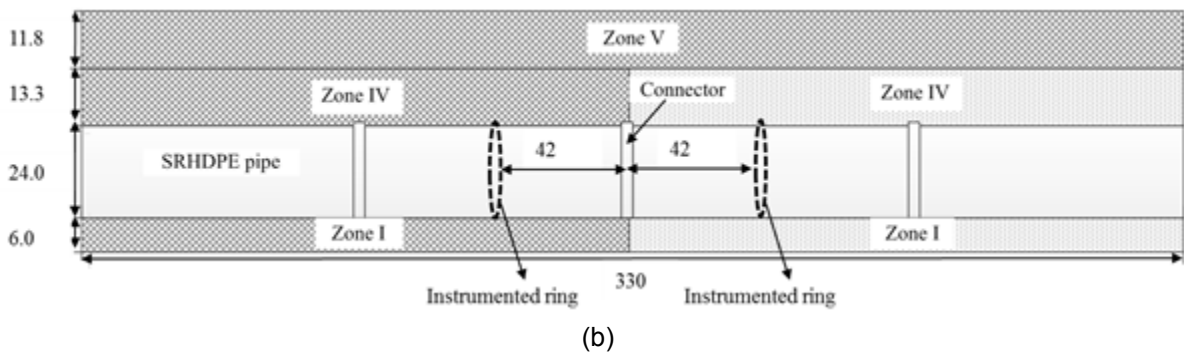
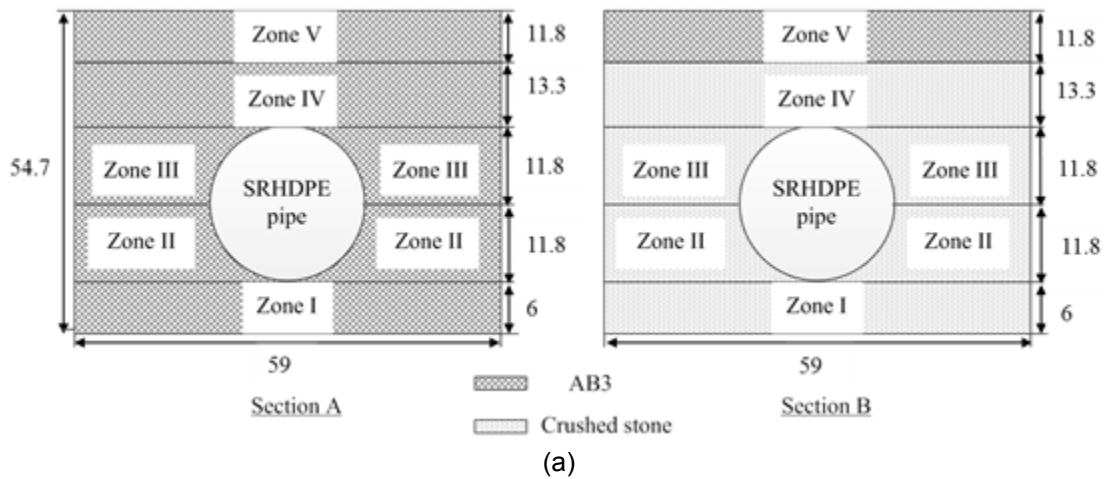


Figure 4.8: Schematic of the Installation Plan (Not to Scale, Unit: Inches)

4.3.2 Test Pipes

Figure 4.9 shows the schematic cross section of the corrugated SRHDPE pipe. This pipe consisted of steel spiral ribs for load carrying and stiffness and high-density polyethylene cover and liner for corrosion resistance. The width of the rib including the steel reinforcement and the plastic cover was 0.09 inches and the height was 0.67 inches. Steel reinforcement with a thickness of 0.06 inches was covered by the plastic material to form the rib, and the center to center spacing of the ribs was 1 inch. The diameter of the pipe used in the test was 24 inches and the thickness of the valley liner was 0.08 inches. Khatri, Han, Parsons, et al. (2013) reported the stiffness of the same SRHDPE pipe from the parallel plate load tests, which was 42.6 psi based

on the ASTM D2412 (2011). This SRHDPE pipe is the same as that used in the laboratory study by Khatri et al. (2015).

Soil-tight pipe metal connectors with a dimension of 13 inches wide \times 82.5 inches long \times 0.04 inches thick were used to connect the pipes. Before the installation of the connector, a rubber band was used to cover the pipe to keep the pipe and the connector tight. Expanding foam was filled in the corrugations of the pipe to seal the possible gap between the rubber band and the pipe. Each connector was wrapped around the pipe, and two bolts (8.1 inches long and 0.4 inches in diameter) attached on the connector were tightened to finish the connection. Figure 4.10 shows two connected pipes using the soil-tight type connector.

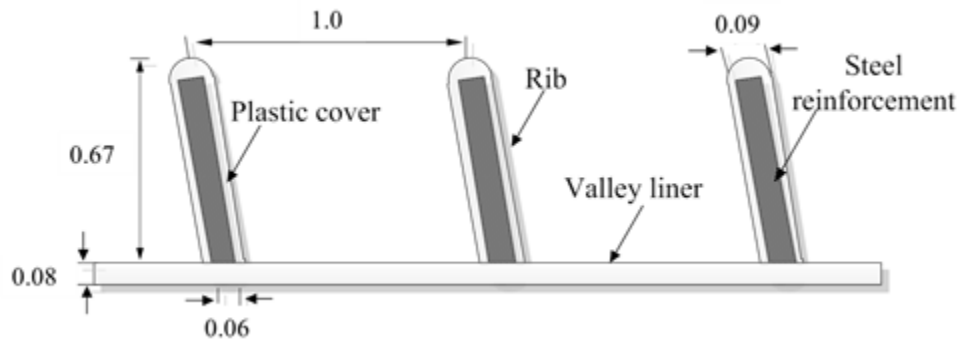


Figure 4.9: Schematic of Cross-Section of the Corrugated SRHDPE Pipe (Unit: Inches, Not to Scale)



Figure 4.10: Two Connected Pipes with a Soil-Tight Type Connector

4.3.3 Instrumentation

Figure 4.11 shows the locations of earth pressure cells. KDE-500KPA pressure cells with the maximum capacity of 72.5 psi were used in the field test in this study. These pressure cells had an outside diameter of 2 inches, a sensing surface diameter of 1.8 inches, and a thickness of 0.4 inches. Four pressure cells were installed in the instrumented rings in each section as shown in Figure 4.8b, and they are labeled as E1, E2, E3, and E4. E1 and E4 were used to measure the vertical pressures at the springline and the crown of the pipe, while E2 and E3 were installed to monitor the lateral earth pressures at the springline and 6 inches above the springline of the pipe. The locations of the pressure cells were determined with the following reasons: (1) E1 and E4 could be used to analyze the soil arching effect during backfilling and under static loading; (2) E2 and E3 could be used to examine the assumption made by Masada and Sargand (2007) that the pressure induced by compaction of backfill material is constant with the buried depth of the pipe (recognized as the reason for the peaking behavior); and (3) E1 and E2 could be used to calculate the coefficient of lateral earth pressure. Figure 4.12 shows the installation of pressure cells. The base of the pressure cell was leveled using the Kansas River sand to ensure the leveling of the pressure cell during the pipe installation. Then the pressure cell was placed and the wires of the pressure cells were covered by a plastic tube with a diameter of 2 inches to protect the wires during compaction. Self-made sand bags, which were a geotextile bag filled with sand, were placed on the top of the pressure cells to protect the pressure cells during the compaction.

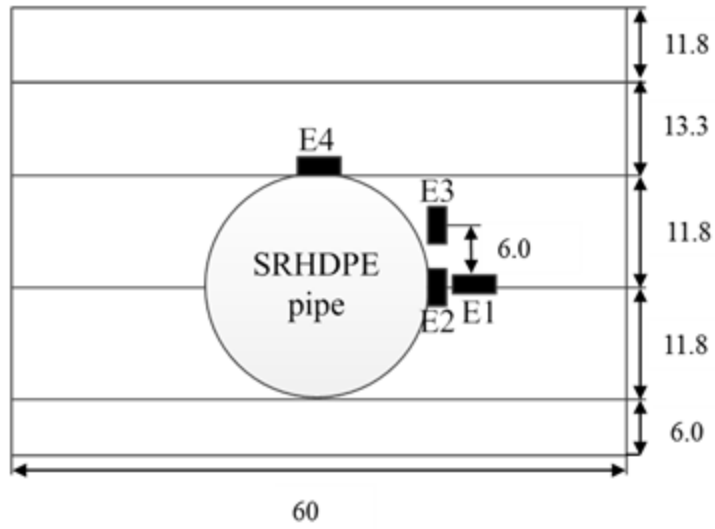


Figure 4.11: Schematic of the Locations of Pressure Cells



Figure 4.12: Placement of a Pressure Cell

Figure 4.13 shows the positions of displacement transducers. Four displacement transducers, labeled as L1, L2, L3, and L3', were installed in the instrumented rings in each section as shown in Figure 4.8b. L1 was used to measure the diameter change in the horizontal direction and L2 was installed to monitor the deformation of the pipe at 45° from the pipe crown. L3 and L3' were used to evaluate the vertical deflections of the pipe. Between these two transducers, L3 was positioned at the valley liner profile, while L3' was positioned at the steel reinforcement profile to investigate a possible deflection difference between the pipe wall and the steel reinforcement ribs. Figure 4.14 shows the installed displacement transducers inside of the pipe. Four small holes with a diameter of 0.5 inches were drilled in the instrumented pipe at the displacement transducer locations, as shown in Figure 4.13. Four steel bars with a diameter of 0.5 inches and length of 20 inches were fixed in the pipe through those four holes with nuts and washers. Displacement transducers were banded with the steel bars using clamps.

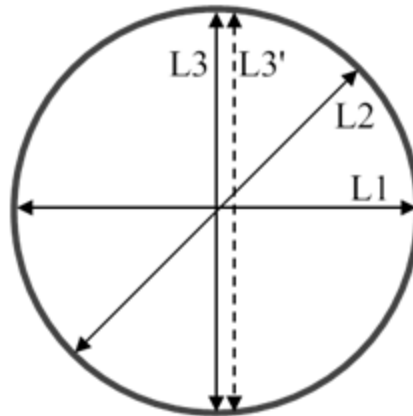
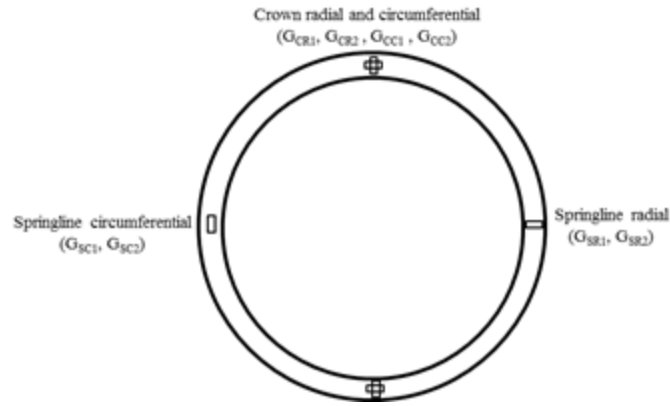


Figure 4.13: Schematic of the Locations of the Displacement Transducers

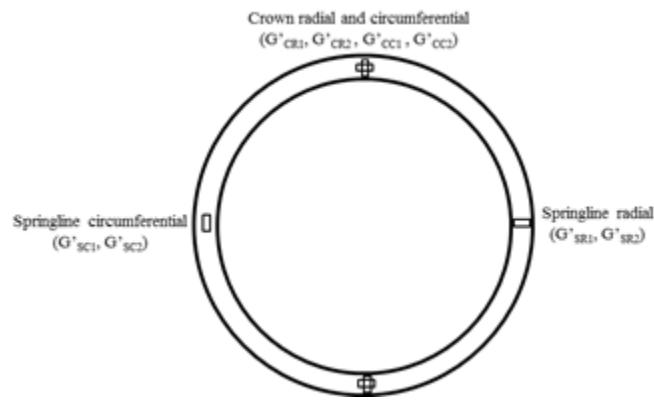


Figure 4.14: Installed Displacement Transducers Inside of the SRHDPE Pipe

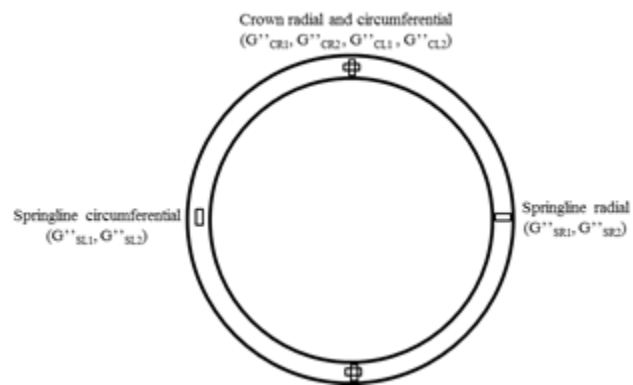
Uniaxial foil-type electrical resistance (C2A-13-250 LW-120) strain gages, manufactured by the Vishay Precision Group, were used to measure the circumferential and radial strains of the pipe at various locations as shown in Figure 4.15. The strain gages were installed at three elements, namely, the steel ribs, the plastic cover of ribs, and the plastic valley. For each element, 12 strain gages were installed at both sides, including four at the pipe crown, four at the invert, and four at the springline. Strain gages on the steel rib were labeled as G, while those at the plastic cover and plastic valley were named as G' and G'', respectively. "C" following G, G' and G'' denotes the crown. "R" means the strain gage in the radial direction, the second "C" means in the circumferential direction, and "L" represents the longitudinal direction (i.e., along the pipe). "1" and "2" illustrate the strain gages attached at two sides of the element. For example, G_{CR1} is the strain gage attached in the radial direction on one side of the steel rib at the pipe crown. In total, 24 strain gages were installed at each instrumented ring.



(a) On steel ribs



(b) On plastic cover of ribs



(c) At plastic valley

Figure 4.15: Symbols, Locations, and Orientations of the Strain Gages on the Pipe

4.4 Pipe Installation and Static Loading

4.4.1 Trench Excavation

A John Deere 310G Loader Backhoe was used to excavate the trench, as shown in Figure 4.16. The model of the machine was 4045D, and the net and gross power were 73 and 78 hp, respectively. The width of the trench was chosen according to the KDOT (2007) pipe and culvert specifications so as to provide sufficient working space for compaction equipment in order to properly and safely place and compact bedding, hunching, and backfill materials. A minimum trench width was maintained so as not to be less than greater of either 1.5 times the pipe outside diameter plus 12 inches or the pipe outside diameter plus 16 inches, as suggested by ASTM D2321 (2014). Considering the size of the excavator, the trench width was determined as 4.6 ft. The average moisture content of the native soil was 21.2%.



Figure 4.16: Excavation of a Trench

4.4.2 Bedding

The AB3 aggregate and the crushed stone were dumped into the trench by the Loader Backhoe in two sections. The length for each section was 165 inches (i.e., half the length of the trench), and then both sections were compacted by a vibratory compactor SFA 3500 with a 3,500

lbs eccentric force, as shown in Figure 4.17. The compaction pressure was 7 psi. The compacted thickness of the bedding was 2.5 inches based on the specification from ASTM D2321 (2014). Figure 4.18 shows the LWD test conducted on the bedding after the compaction to ensure the construction quality. Three tests were conducted in each section. The average modulus of the AB3 aggregate section was 1,845 psi, while that of the crushed stone section was 1,768 psi. Figure 4.19 presents the sand cone test used to determine the field density. Sand cone tests were conducted at three locations in each section. Considering that the gap between particles may influence the result in the crushed stone section, sand cone tests in this section were done for three times in each location and the average value was used. The average compaction degrees of the AB3 aggregate and the crushed stone sections were 88.3% and 85.5%, respectively.



Figure 4.17: Compaction of the Bedding



Figure 4.18: LWD Test on the Bedding



Figure 4.19: Sand Cone Tests on the Bedding in the Crushed Stone Section

4.4.3 Placement of the Pipe

After the quality control tests of the bedding were finished, four pipes were lifted up by an ALTEC crane and placed into the trench as shown in Figure 4.20. The pipes were lifted up at two connectors, which could make the lift force evenly and avoid the bending of the pipes. During the placement of the pipes, the wires of the sensors were collected together to prevent the

damage of the sensors by the pipe lifting. Figure 4.21 shows the pipes after the placement into the trench. Then, all sensors were connected with the data acquisition system and set the initial to zero.



Figure 4.20: Placement of the Pipes

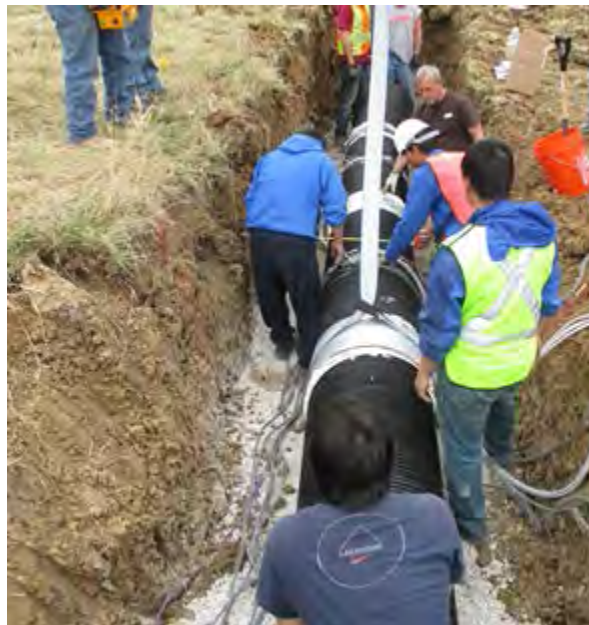


Figure 4.21: Pipes Placed on the Bedding

4.4.4 Backfilling of Sidfill and Soil Cover

As shown in Figure 4.8, the sidefill and the soil cover were placed and compacted in four lifts. The first lift (i.e., zone II in Figure 4.8) was up to the pipe springline. The AB3 aggregate section was filled first and then the crushed stone section. Subsequently, two sections were compacted together. A vibratory compactor SFA 3500 was used for the compaction of the main zone and a STANLEY TA45 rammer with a working pressure of 1,500 psi was used to compact the difficult zones near the pipe and the trench as shown in Figure 4.22. No pipe lift was observed during the compaction process. The average elastic moduli determined using the LWD tests for the AB3 aggregate section and the crushed stone section were 1,178 and 1,323 psi, respectively. The compaction degrees for the AB3 aggregate section and the crushed stone section from sand cone tests were 90.8% and 85.5%, respectively.



Figure 4.22: The Compaction of Difficult Zones Using the STANLEY TA45 Rammer

The second lift of the backfill was up to the level of the pipe top (i.e., zone III in Figure 4.8). The construction procedures and the quality control were the same with the first lift. The top of the pipe was not compacted. The average elastic moduli determined using LWD tests for the AB3 aggregate section and the crushed stone section were 1,318 and 1,439 psi, respectively. The compaction degrees for the AB3 aggregate section and the crushed stone section from sand

cone tests were 88.4% and 84.3%, respectively. The third lift was up to the bottom of the base course layer (i.e., zone IV in Figure 4.8). The construction procedures and the quality control were the same with the first two lifts. The average elastic moduli determined using the LWD tests for the AB3 aggregate section and the crushed stone section were 2,657 and 2,911 psi, respectively. The compaction degrees for the AB3 aggregate section and the crushed stone section from sand cone tests were 91.2% and 90.3%, respectively. The base course layer (i.e., zone V in Figure 4.8) in both sections was backfilled with the AB3 aggregate. Three lines were marked on the ground after the compaction to locate the positions of the pipes for the static loadings. The average elastic moduli determined using the LWD tests for the AB3 aggregate in Sections A and B were 2,318 and 2,515 psi, respectively. The compaction degrees for the AB3 aggregate section and the crushed stone section from sand cone tests were 89.8% and 90.5%, respectively.

4.4.5 Static Loading

To investigate the performance of pipes under the static loading, two static loads were applied on the ground surface above the pipe after the completion of the pipe installation. First, the back axle of the Loader Backhoe was stopped above the pipe for two minutes, as shown in Figure 4.23. The weight of the back axle was 12,800 lbs. The diameter of the rear tire was 52.7 inches, while the width of the rear tire was 10 inches. The contact area of the rear tire with the ground surface was 400 in². The contact pressure was 32 psi. Then, a CAT 953D crawler loader stopped at the ground surface above the pipes and moved over the pipes at a slow speed, as shown in Figure 4.24. The operating weight of the CAT 953D was 34,209 lbs. The track shoe width was 18.9 inches, and the ground contact area was 3,565 in². The contact pressure was 9.5 psi.



Figure 4.23: The John Deere 310G Loader Backhoe Above the Pipes



Figure 4.24: The CAT 953D Crawler Loader Above the Pipes

4.4.6 Quality Control

To ensure the quality of construction, the following tests were conducted during the compaction of each lift: (1) LWD test; (2) sand cone test; (3) leveling measurement; and (4) DCP test. LWD and sand cone tests were described in the construction section. A WILD N3 leveling device was used for the leveling measurement to ensure the leveling and thickness of each lift, as shown in Figure 4.25. Two DCP tests were conducted after the construction in the AB3

aggregate section to evaluate the CBR value of the AB3 aggregate after the construction. Figure 4.26 shows the DCP test results of the AB3 aggregate after the construction. The CBR values at two locations were almost consistent in a range of 10 to 20, with the exception of #2 at the depth of 30 inches, which was much higher. At that depth, the DCP cone might penetrate on a big aggregate particle. The rib gaps were marked before the installation on both instrumented pipes as shown in Figure 4.27 to investigate the gap change during the pipe installation.



Figure 4.25: Leveling Measurements During the Pipe Installation

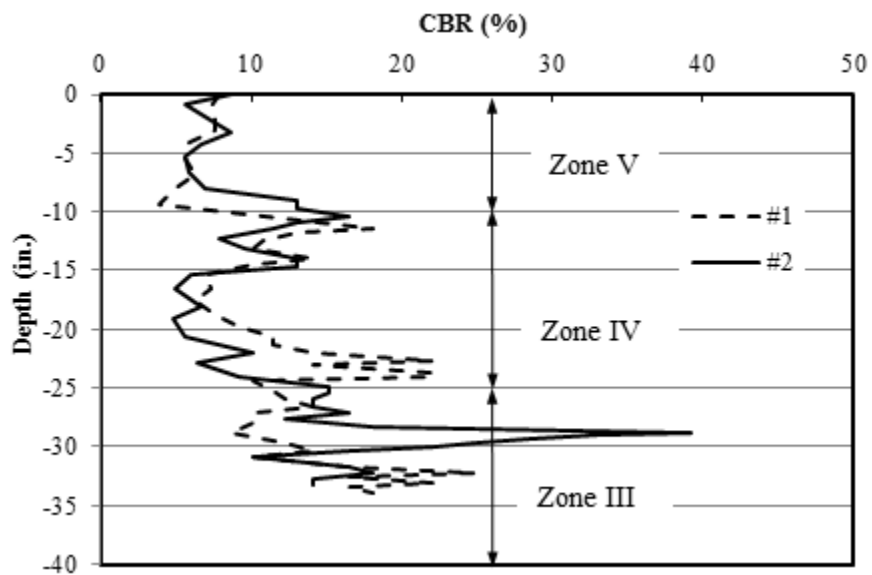


Figure 4.26: DCP Test Results of the AB3 Aggregate Section After Construction



Figure 4.27: Markers of the Rib Gaps Before Installation

4.4.7 Pipe Exhumation

The pipes were exhumed on the second day of the installation to observe any possible damage of the pipes during installation. Figure 4.28 shows an exhumed pipe.



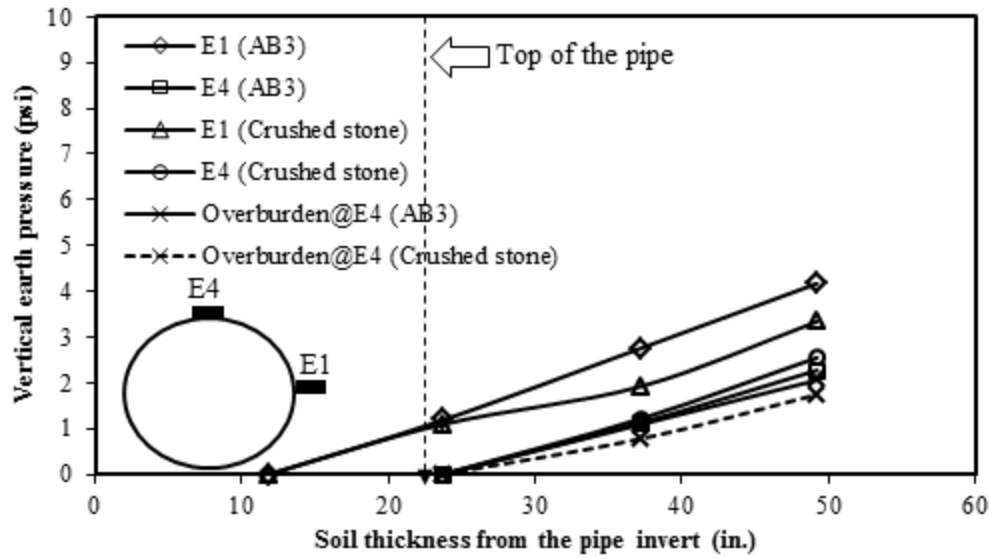
Figure 4.28: An Exhumed Pipe

4.5 Analysis of Test Results During Pipe Installation

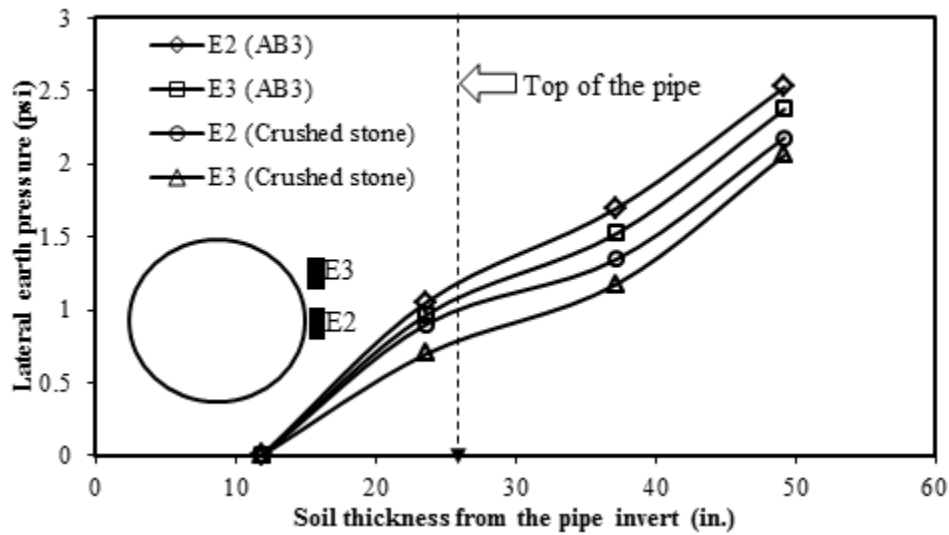
4.5.1 Earth Pressure

Figure 4.29a shows the vertical earth pressures at the springline and on the top of the pipes in both sections. The measured vertical pressure in Section A was higher than that in Section B. The vertical pressure at the top of the pipe increased with the increase of the soil cover thickness after the backfill reached the top of the pipe. The soil arching factors, VAF, defined as the ratio of the measured vertical pressure (σ_v) at the top of the pipe to the overburden stress (γh), were calculated as 1.10 and 1.47 for Sections A and B at the end of backfilling, respectively ($\sigma_v = 2.2$ psi, $\gamma h = 136.7 \times 1.97 / 144 = 1.9$ psi for Section A and $\sigma_v = 2.5$ psi, $\gamma h = (99.2 \times 1.1 + 136.7 \times 1) / 144 = 1.7$ psi for Section B). The soil arching factors in both sections demonstrated that some overburden stress of the soil cover was transferred from the surrounding soil to the pipe due to the negative soil arching effect (i.e., VAF is greater than 1). Figure 4.29b shows the lateral earth pressure at the springline and 6 inches above the springline of the pipe. From Figure 4.29 the lateral earth pressure coefficient at the springline of the pipe was calculated and is shown in Figure 4.30. It illustrates that the lateral earth pressure coefficient decreased with the increase of the soil thickness. This finding is the same as that from the laboratory study by Khatri et al. (2015). The lateral earth pressure coefficient for the AB3 aggregate was higher than that for the crushed stone; however, their difference decreased with the increase of the soil thickness and they were approximately equal at the ending of backfilling. The lateral earth pressure coefficients in both sections were lower than the passive earth pressure coefficients but higher than the earth pressure coefficients at rest. The measured lateral earth pressures at E2 and E3 in Section A with the backfilling at the top of the pipe were 1.13 and 0.97 psi, respectively; their difference was 0.16 psi. The difference induced by the soil overburden stress (i.e., 5.9 inches [distance between two pressure cells] \times 136.7 pcf [unit weight of AB3] \times 0.29 [lateral earth pressure coefficient at rest] = 0.15 psi). Therefore, the lateral earth pressures caused by the compaction were approximately equal at the positions of E2 and E3. Similarly, for Section B, the difference between E2 and E3 was 0.14 psi, which is also close to the difference induced by the soil overburden stress (i.e., 5.9 inches \times 99.2 pcf \times 0.29 = 0.10 psi). This analysis demonstrates

that the lateral earth pressure induced by the compactor was constant within the range of 40° to 140° from the pipe crown as suggested by Masada and Sargand (2007).



(a) Vertical Earth Pressure



(b) Lateral Earth Pressure

Figure 4.29: Development of Earth Pressures Around Pipes with Soil Thickness

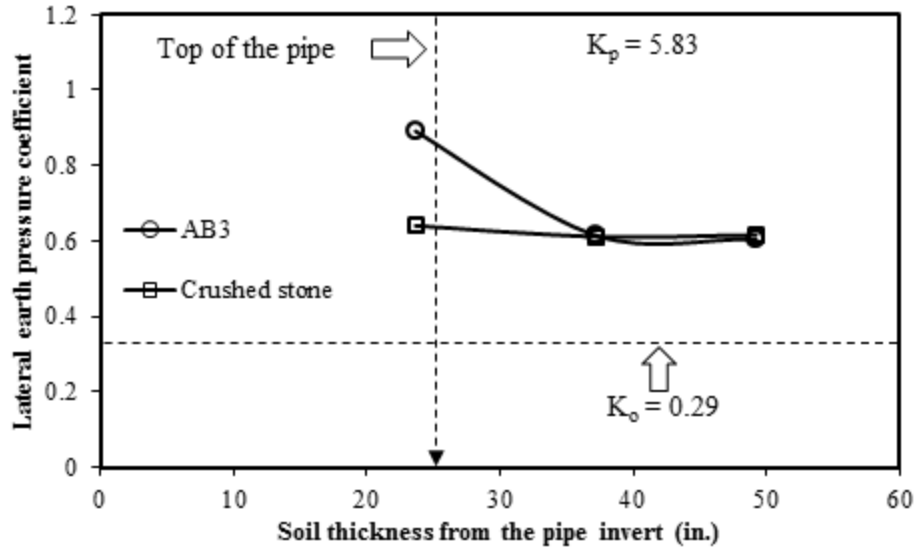


Figure 4.30: Lateral Earth Pressure Coefficients at the Springline of the Pipe with Soil Thickness

4.5.2 Deflections

In this field study, the increase of the pipe diameter as compared with that of the undeformed pipe in all three directions (i.e., vertical, 45°, and horizontal) was defined as positive. Figure 4.31a presents the vertical deflections at the valley liner and the steel reinforcement in both sections. It is obvious that the vertical diameter was increased before the backfill reached the top of the pipe, i.e., the peaking behavior, followed by the decrease of the vertical diameter. The peaking deflection of the pipe in Section A (i.e., the AB3 aggregate section) was approximately 0.06 inches, while that in Section B (i.e., the crushed stone section) was 0.04 inches. Masada and Sargand (2007) proposed the following equation to calculate the peaking deflection:

$$\frac{\Delta y}{D} = \frac{4.7 p_c + K_0 r \gamma}{3.874(PS)}$$

Equation 4.1

Where:

Δy = the vertical deflection

D = the diameter of an undeformed pipe

p_c = the lateral pressure induced by compaction

K_0 = the lateral earth pressure coefficient at rest

r = the radius of the undeformed pipe

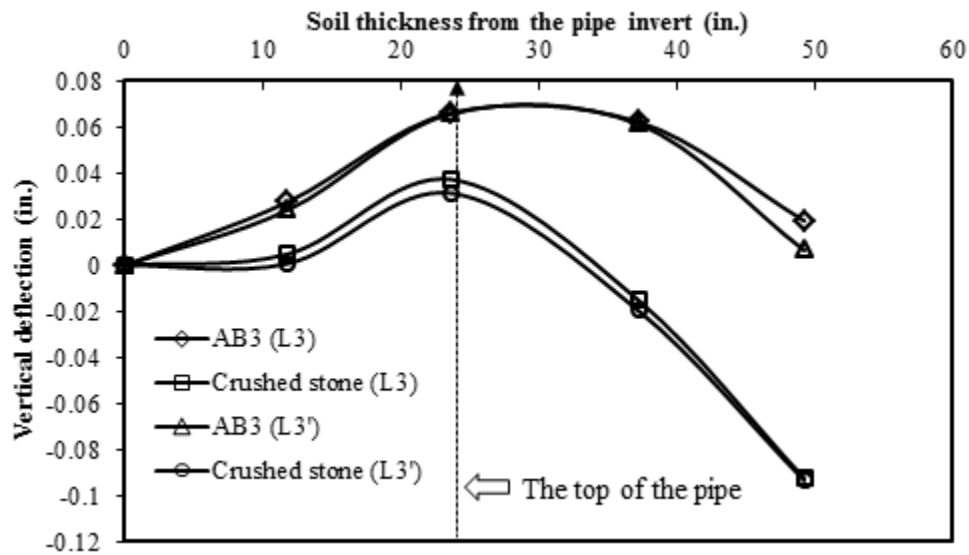
γ = the unit weight of backfill material

PS = the pipe stiffness

Equation 4.1 shows that the vertical deflection increases with the density of the backfill material considering the same friction angles of the AB3 aggregate (i.e., 45°) and the crushed stone (i.e., 45°). Since the densities for the AB3 aggregate and the crushed stone were 136.7 and 99.2 pcf, respectively, the vertical deflection in Section A should be larger than that in Section B. The calculated peaking deflections using Equation 4.1 are 0.05 and 0.04 inches, respectively, for Sections A and B using the following parameters: $p_c = 0.207$ psi as suggested by McGrath et al. (1999) for a vibratory plate compactor; $K_0 = 0.29$ (i.e., $K_0 = 1 - \sin 45^\circ = 0.29$) for the AB3 aggregate and 0.29 (i.e., $K_0 = 1 - \sin 45^\circ = 0.29$) for the crushed stone; $PS = 42.6$ psi; $\gamma = 136.7$ pcf for the AB3 aggregate and 99.2 pcf for the crushed stone; $r = 11.8$ inches. The measured peaking deflections are close to the calculated ones in both sections.

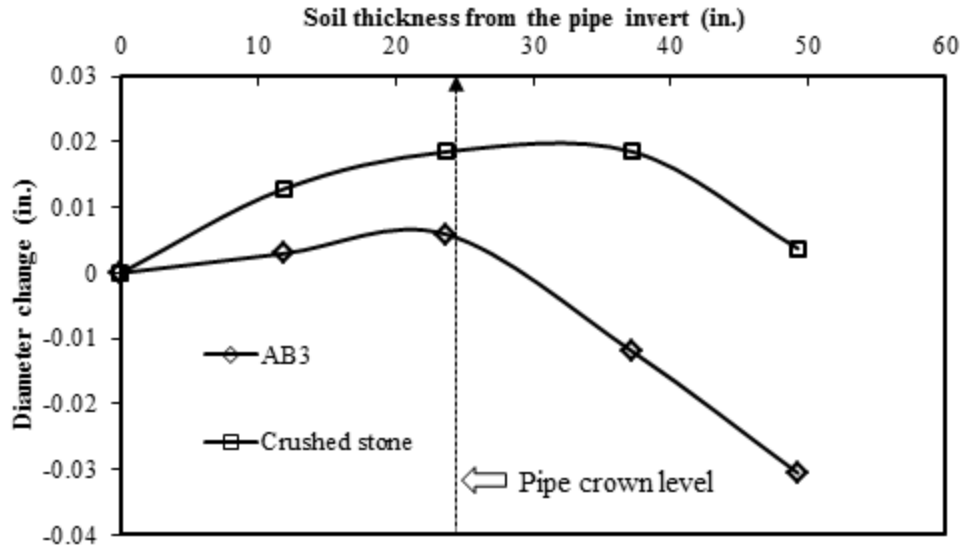
The vertical deflection at the valley liner was slightly larger than that at the steel reinforcement rib. The vertical diameter was reduced by 0.04 inches from the peaked vertical diameter in Section A at the end of backfilling, while that in Section B was reduced by 0.14 inches from the peaked vertical diameter. The larger reduction of the vertical deflection in Section B might be attributed to the fact that the crushed stone had a lower modulus of subgrade reaction and stress on the surrounding soil due to soil arching. The soil arching effect will be further discussed in the “Earth Pressure” section. Figure 4.31b presents the diameter change of the pipe at 45° from the pipe crown. It was observed that the diameter at 45° from the pipe crown first increased with backfilling (i.e., Zones II and III) in both sections and then decreased with

the increase of the soil cover thickness (i.e., Zones IV and V). The test results also show that the diameter change in the crushed stone was larger than that in the AB3 aggregate. Figure 4.31d shows that the comparison between the horizontal deflection at the valley liner was opposite to the vertical one. In other words, when the vertical deflection increased, the horizontal deflection decreased, and vice versa. In three directions (i.e., vertical, 45° from the pipe crown, and horizontal), the maximum deflections in both sections were 0.1 inches (i.e., 0.4% of the pipe diameter), which was much smaller than the typical deflection limit of 5% for the steel and HDPE pipes suggested by AASHTO (1998, 2010).

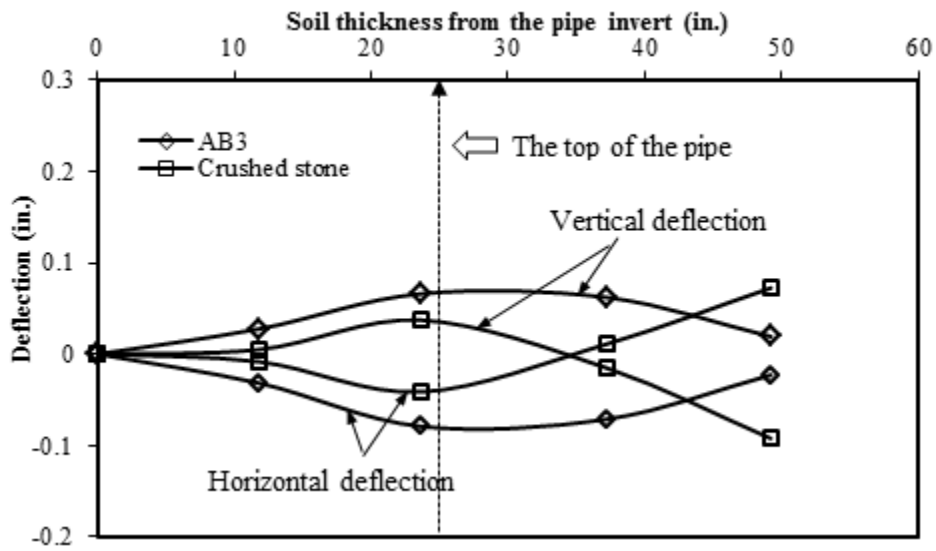


(a) Vertical Deflection (L3=deflection at the valley liner; L3'=deflection at the steel reinforcement)

Figure 4.31: Development of Deflections with Soil Thickness in Three Directions During Backfilling



(b) Diameter Change at 45° from the Pipe Crown



(c) Comparison of Vertical and Horizontal Deflections at the Valley Liner

Figure 4.31: Development of Deflections with Soil Thickness in Three Directions During Backfilling (Continued)

4.5.3 Strains

4.5.3.1 Test Section A

Figure 4.32 shows the strains on the steel ribs during the backfilling. “Crown_R” and “Crown_C” represent the strains at the crown in the radial and the circumferential directions, respectively. “Springline_R” and “Springline_C” denote the strains at the springline in the radial and the circumferential directions, respectively. Figure 4.32 illustrates that all the strains at the steel ribs increased with an increase of the soil thickness. The magnitude of the strain increase at the crown was greater than that at the springline in both the radial and circumferential directions. The compaction was directly above the pipe when the backfill above the pipe top level which would cause the strain increase at the pipe crown. However, the strain increase at the springline was induced by the lateral earth pressure increase, which should be lower than the vertical earth pressure increase at the pipe crown. It is worth noting that the maximum strain on the steel ribs (i.e., 0.0046%) was much smaller than the typical steel strain at the yield strain of 0.5% (Mamlouk & Zaniewski, 2011). It can be concluded that the compaction in Section A did not fail the steel ribs.

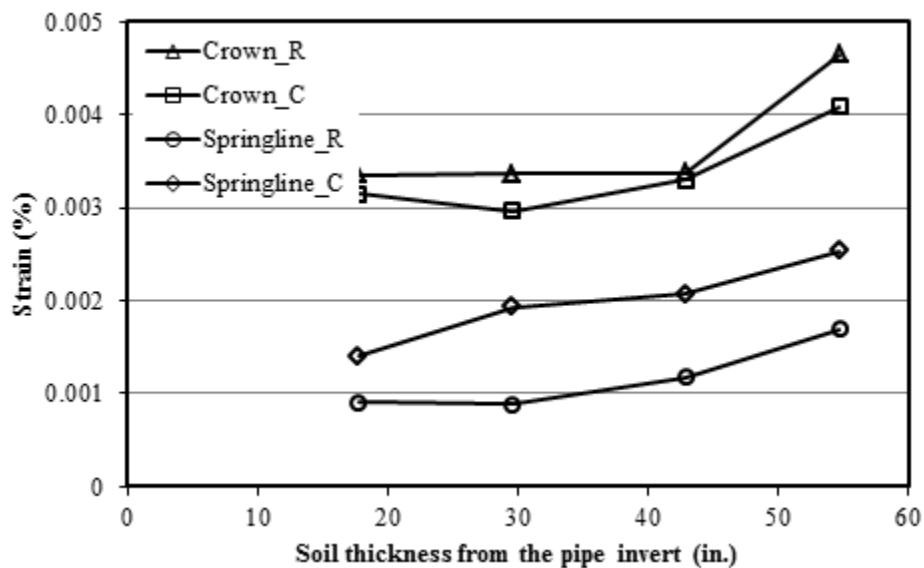


Figure 4.32: Strains of the Steel Ribs in Section A During the Pipe Installation

The strains at the plastic covers and valleys were adjusted by multiplying a factor of 1.29 according to Brachman et al. (2008). Figure 4.33 shows the strains on the plastic cover of the steel ribs. The strains in the radial direction both at the crown and the springline increased slightly; however, the strains in the circumferential direction at both locations increased significantly. In other words, the perimeter of the pipe increased with the backfilling and no local buckling occurred. The maximum strain of the plastic cover was 0.05% at the pipe springline, which was much lower than the long-term strain limit of the thermoplastic pipes of 5% suggested by AASHTO (2012).

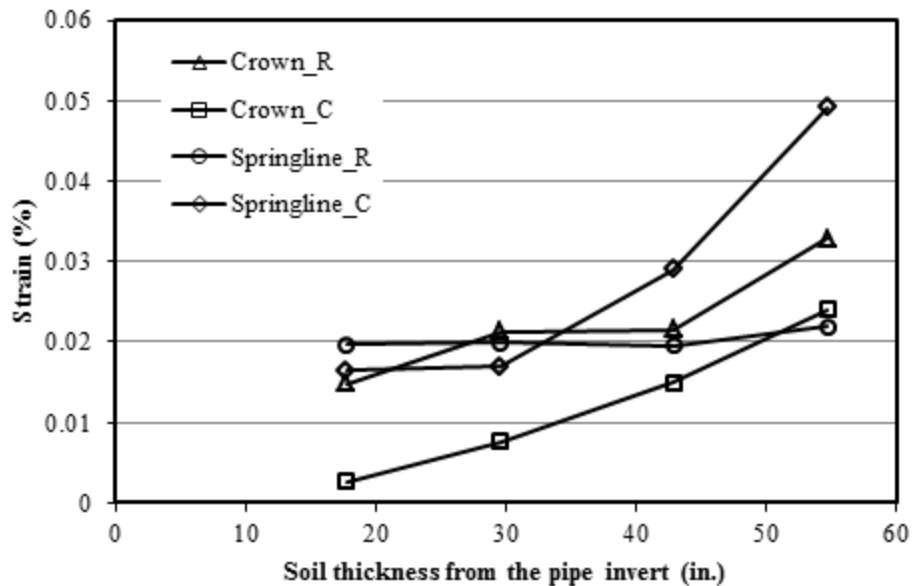


Figure 4.33: Strains of the Plastic Cover in Section A During the Pipe Installation

Figure 4.34 presents the strains of the plastic valley. “Crown_L” and “Springline_L” represent the strain in the longitudinal direction at the crown and the springline, respectively. The strain gages were fixed on the plastic valley in two directions, namely, the hoop direction and the longitudinal direction. This figure shows the strains of the plastic valley increased with an increase of the soil thickness. The strains in the longitudinal direction at both the pipe crown and the pipe springline were higher than the strains in the hoop direction. The possible explanation is that the pipe is reinforced in the hoop direction and the steel ribs can limit the development of the strain; however, the pipe in the longitudinal direction is only an HDPE liner, which has a low

elastic modulus. The measured maximum strain of the plastic valley was 0.14%, which was much higher than the strains of the plastic cover and the steel ribs. The strains of the plastic valley were also lower than the 5% long-term strain limit suggested by AASHTO (2012).

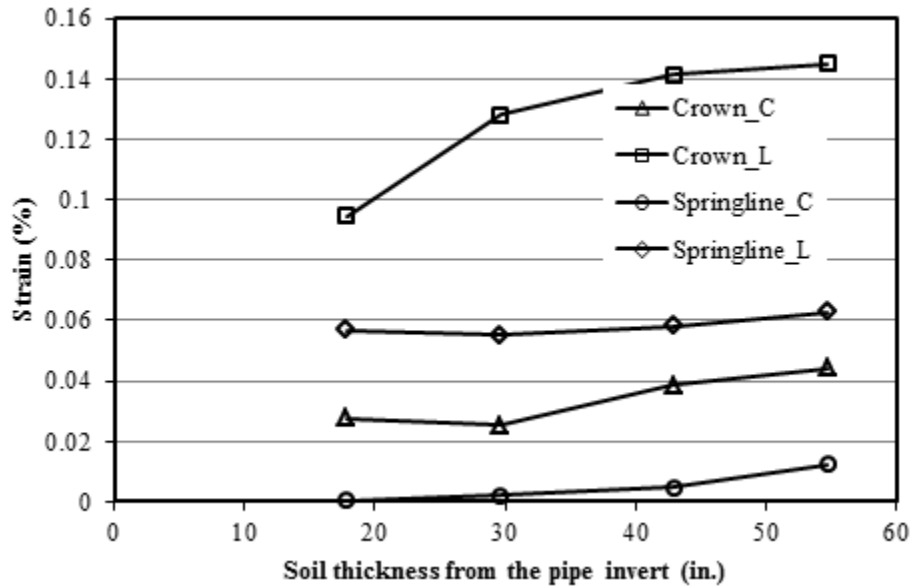


Figure 4.34: Strains of the Plastic Valley in Section A During the Pipe Installation

The strains of the pipe in the Section A (i.e., the AB3 aggregate section) all increased with an increase of the soil cover thickness. The maximum strains on the steel ribs and the plastic valley occurred at the pipe crown, while the maximum strain on the plastic cover was located at the pipe springline. The strains of the plastic valley were higher than those of the steel ribs and the plastic covers; however, they were much lower than the strain limit. The strains of the steel ribs were also much lower than the yield strain of the steel (0.5%). In summary, the tested SRHDPE pipes in the AB3 section did not have any strain problem during the pipe installation.

4.5.3.2 Test Section B

Figure 4.35 shows the strains of the steel ribs in the crushed stone section during the pipe installation. The strains at the springline changed slightly; however, the strains at the pipe crown changed significantly with the pipe installation. These strains are consistent with the strains of the steel ribs in Section A. The compaction of the soil cover should be responsible for the increase of the strains at the pipe crown. The strains of the steel ribs in the crushed stone were 2

to 4 times those in the AB3 section. The possible reason is that the vertical deflection of the pipes in the crushed stone (0.09 inches) was larger than that in the AB3 section (0.007 inches) when the backfilling was above the level of the pipe top.

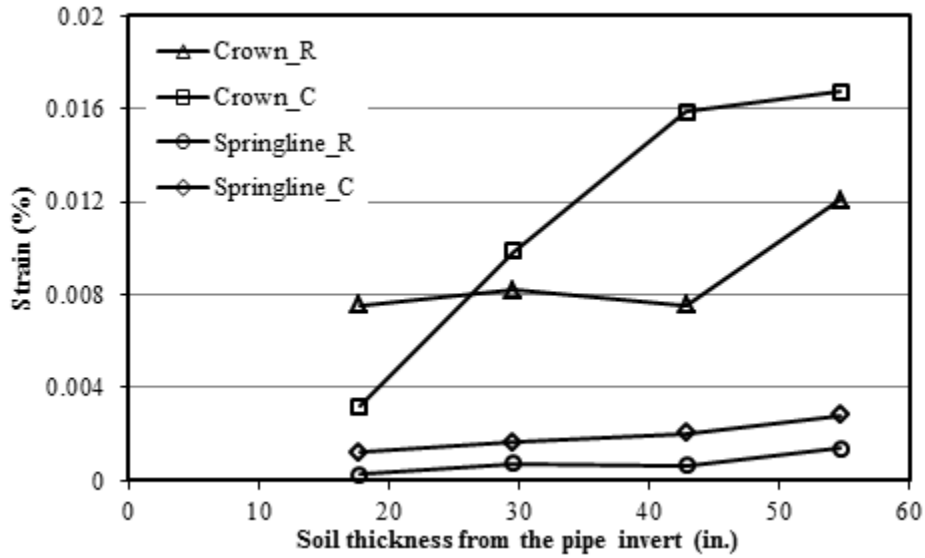


Figure 4.35: Strains of the Steel Ribs in Section B During the Pipe Installation

Figure 4.36 presents the strains of the plastic cover in the crushed stone section during the pipe installation. The strains of the plastic cover in both directions at the pipe springline increased slightly, while those at the pipe crown increased significantly. This finding was opposite to that in the AB3 aggregate section. The modulus of the crushed stone was relatively lower than that of the AB3 aggregate section based on the plate loading tests and the LWD tests. In the crushed stone section, the side fill could provide less support than that in the AB3 aggregate section to the pipe, which resulted in the lower modulus of the pipe buried in the backfill material. Therefore, the earth pressure at the pipe top in the crushed stone section was lower than that in the AB3 section. The maximum value of the strain was 0.062%, which was approximately 1.5 times that in the AB3 aggregate section, but much lower than the long-term strain limit of 5% suggested by AASHTO (2012).

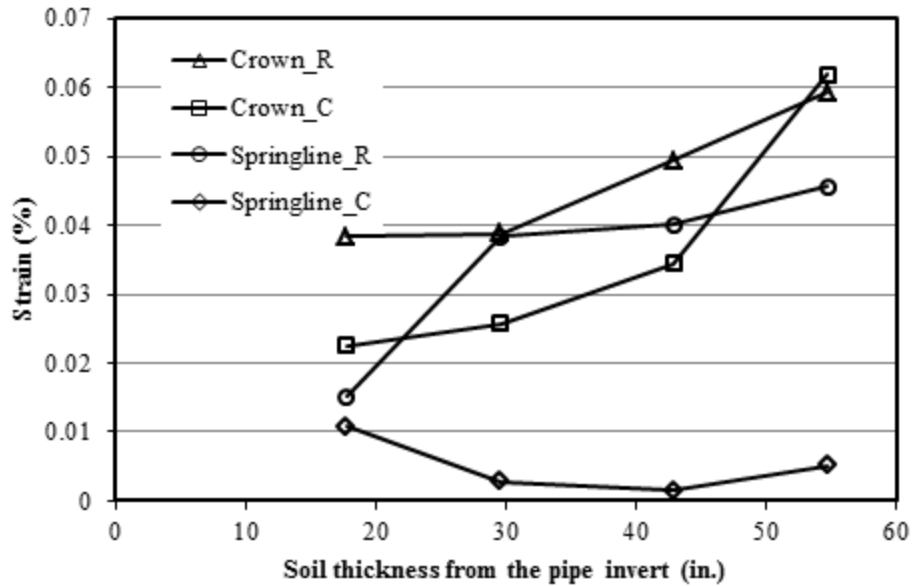


Figure 4.36: Strains of the Plastic Cover in the Crushed Stone Section During the Pipe Installation

Figure 4.37 shows the strains of the plastic valley in the crushed stone section during the pipe installation. The strains of the plastic valley were measured in two directions, namely, the hoop direction and the longitudinal direction (i.e., along the pipe). The test results demonstrate that the strain in the hoop direction increased slightly; however, the strain in the longitudinal direction increased significantly. This finding is the same as that in the AB3 section. The maximum strain of the plastic valley in the crushed stone section was 0.19%, which was approximately 1.5 times that in the AB3 section. However, the strain of the plastic valley was much smaller than the strain limit of 5%.

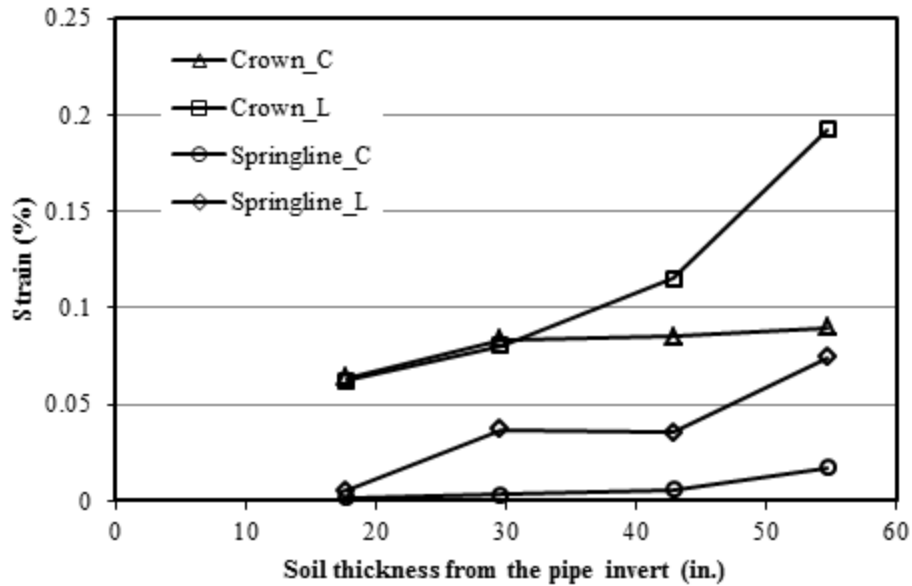


Figure 4.37: Strains of the Plastic Valley in the Crushed Stone Section During the Pipe Installation

The strains of the pipe in the Section B (i.e., the crushed stone section) at different locations increased with the construction. The maximum strains on the steel ribs, the plastic covers, and the plastic valley all occurred at the pipe crown. The strains of the plastic valley were higher than those of the steel ribs and the plastic covers; however, they were much smaller than the strain limit of 5%. The maximum strain of the steel ribs (i.e., 0.02%) was also much smaller than the yield strain of steel (0.5%). Even though the strains in the crushed stone section were all higher than those in the AB3 section at the same position, no failure happened to any elements in the crushed stone section during the pipe installation.

Figure 4.38 shows the comparison of the measured maximum strains on the plastic in the longitudinal and the circumferential directions and the calculated strains in the circumferential direction in both sections. Equations 2.23 and 2.24 were used to calculate the strain based on the deflection and the load above the pipe. In both sections, the measured strains were larger than the calculated ones. The calculated strains are the maximum strain of the plastic in the circumferential direction, which is typically recognized as the design criteria. The longitudinal strain is often neglected in most pipe design. However, for the SRHDPE pipe, the stiffness in the longitudinal direction is much lower than that in the hoop direction. This is why the measured

strains in the longitudinal direction were higher than those in other directions in this field test. In other words, the longitudinal strain is more critical for the SRHDPE pipe.

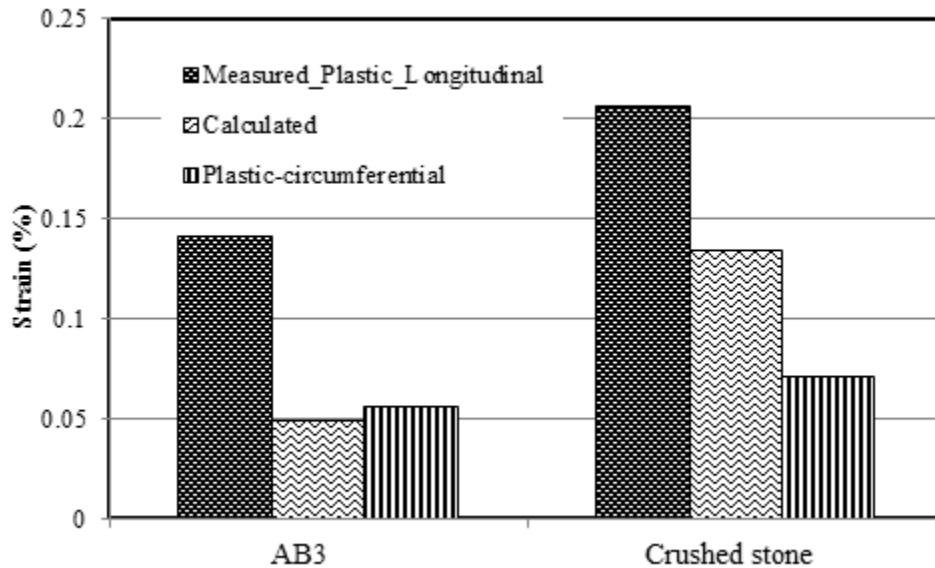


Figure 4.38: Comparison of the Measured Strains and Calculated Strains on the Plastic in Both Sections

4.6 Analysis of Test Results Under Static Loading

4.6.1 Earth Pressure

Figure 4.39 shows the earth pressure around the pipe at the end of the construction and under the static loading in Section A. Two types of static loading were applied above the pipe, namely, the use of the loader backhoe and the use of the crawler loader. The earth pressures at the pipe springline and the shoulder increased 2 to 4 psi under static loading from those at the end of construction, while the earth pressures at the pipe crown increased 11 and 9 psi under the loading of the loader backhoe and the crawler loader, respectively. Figure 4.39 indicates that static loading increased the earth pressure at the pipe crown up to 4 times that at the end of the construction.

Figure 4.40 presents the earth pressures around the pipe at the end of construction and under static loading in Section B. Static loading increased the earth pressures at the springline and the shoulder by 2 to 4 psi from those at the end of construction. This result is the same as that for Section A. The earth pressures at the pipe crown were 9.13 and 7.53 psi under the

loading of the loader backhoe and the crawler loader, respectively, which are 3.6 and 3 times those at the end of the construction. The magnitude of the earth pressure increase by static loading in the crushed stone section was lower than that in the AB3 aggregate section. The sidefill in Section A could provide support to the pipe due to the high stiffness which could make the pipe stiffer than that in Section B, which resulted in the higher earth pressure on the pipe top in Section A.

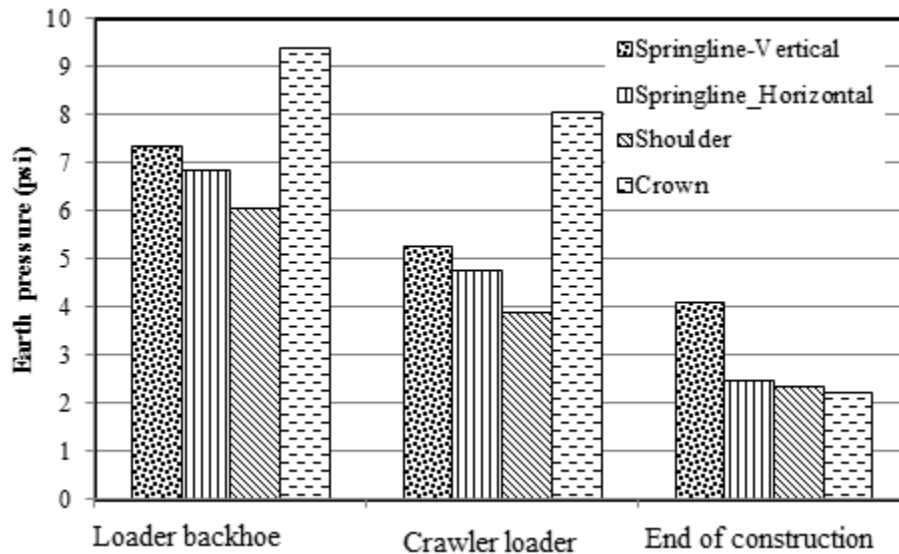


Figure 4.39: The Measured Earth Pressures in Section A at the End of the Construction and Under Static Loading

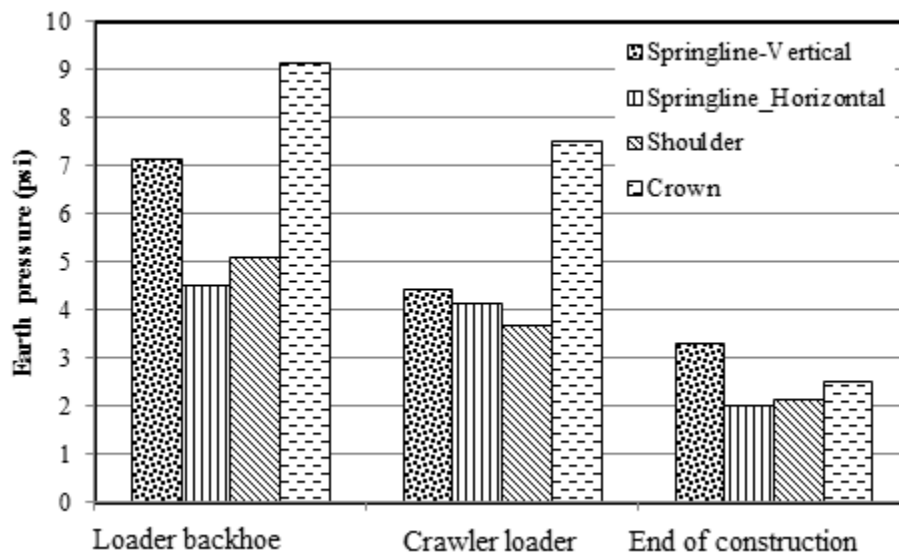
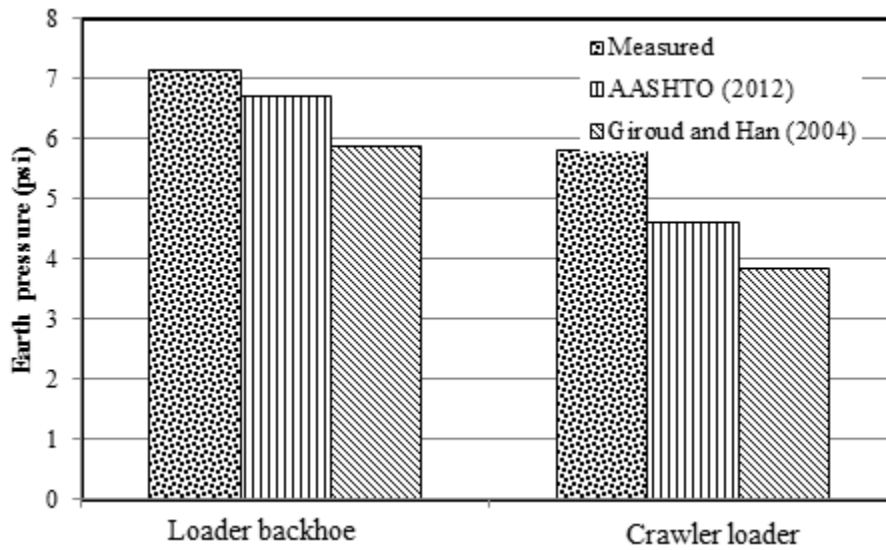
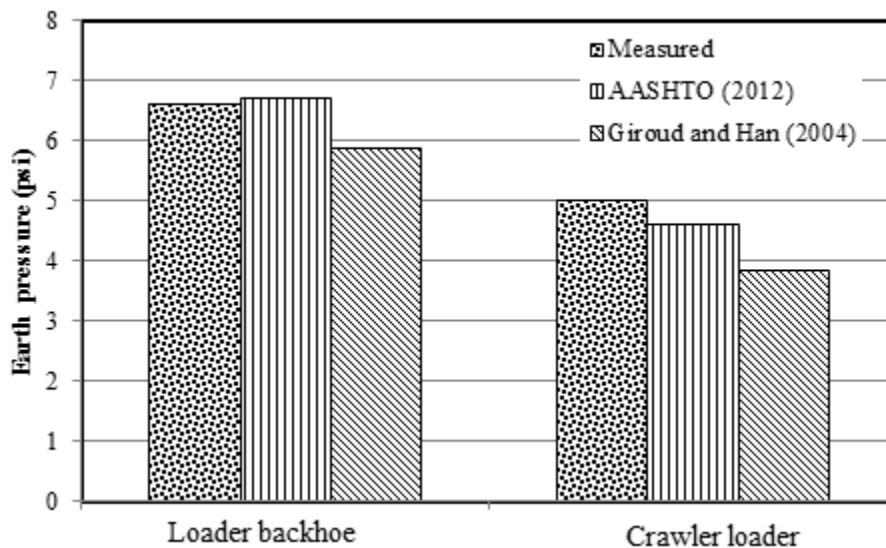


Figure 4.40: The Measured Earth Pressures in Section B at the End of the Construction and Under Static Loading

Figure 4.41 shows the comparison of the measured earth pressures at the pipe crown with the calculated earth pressures in both sections. This figure indicates the calculated pressures in both sections by the AASHTO (2012) method are higher than those by the Giroud and Han (2004) method. However, the calculated pressures by both methods were close to the measured ones. It can be concluded that both methods can be used to predict the earth pressures induced by static loading above the SRHDPE pipe.



(a) Section A



(b) Section B

Figure 4.41: Comparison of the Measured Earth Pressures at the Pipe Crown with the Calculated Ones Under Static Loading

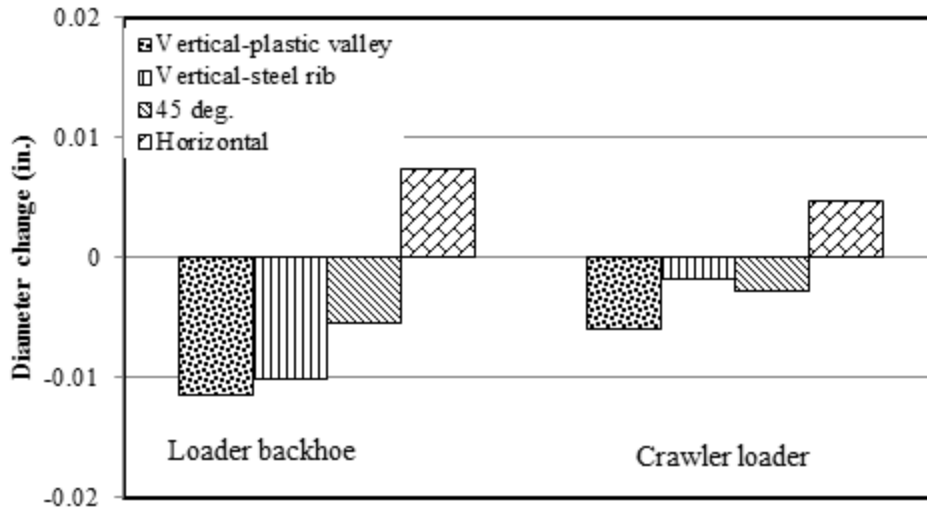
4.6.2 Deflections

Figure 4.42 presents the diameter change of the pipes under static loading in both sections. The maximum diameter changes occurred at the plastic valley. The vertical deflections were 0.011 and 0.009 inches in the Sections A and B, respectively. The deflections at the steel ribs were smaller but close to the deflections at the plastic valley. The horizontal deflections were close to the vertical deflections at the plastic valley with an exception of the horizontal deflection in Section B, which was 0.02 inches and two times the vertical deflection. In both sections, the deflection at the same position under the loading by the loader backhoe was larger than that induced by the crawler loader due to their different load magnitudes. The deflections of the pipes under static loading in Section A were larger than those in Section B. The possible reason is that more load was carried by the pipe in Section A than that in Section B.

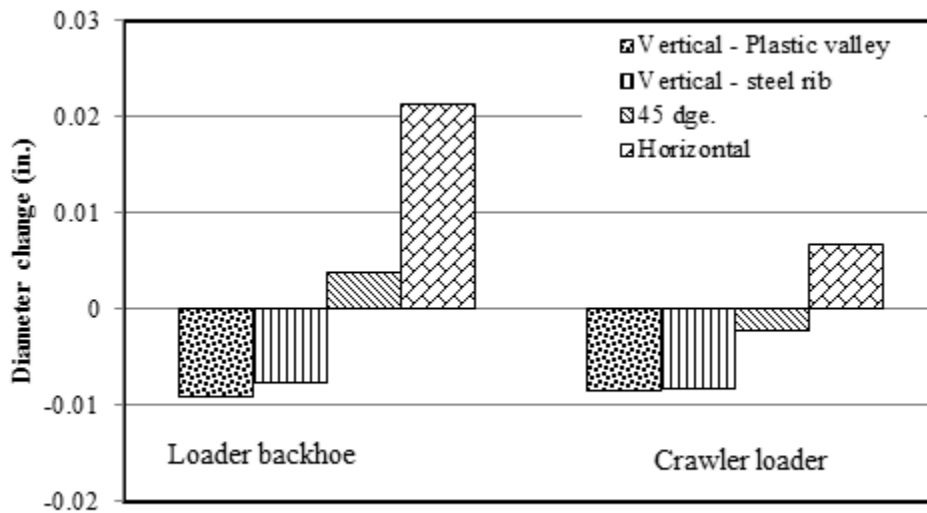
Equation 2.6 (i.e., the Iowa Formula) was used to calculate the deflection caused by static loading. The loads on the pipe top used in the calculation were the measured earth pressures reported in the earlier section. The deflection lag factor was determined as 1 since the short duration of the test. The bedding factor was 0.11 based on the suggestion by Moser and Folkman (2008). The pipe stiffness was 46.2 psi based on the parallel plate load tests in Phase I of this project. The constrained moduli were 3,414 and 2,842 psi for the AB3 aggregate and the crushed stone determined from the plate load tests, respectively. Table 4.1 compares the calculated deflections using the Iowa Formula and the measured ones. This table illustrates that the calculated results are close to the measured ones. This comparison confirms that the Iowa Formula can be used to estimate the deflection of the SRHDPE pipe induced by static loading.

Table 4.1: Comparison of the Calculated and Measured Deflections Under Static Loading

Section	Loading type	Measured (in.)	Calculated (in.)
A	Loader backhoe	-0.011	-0.007
	Crawler loader	-0.006	-0.007
B	Loader backhoe	-0.009	-0.008
	Crawler loader	-0.008	-0.006



(a) Section A



(b) Section B

Figure 4.42: Diameter Changes of the Pipes Under Static Loading

4.6.3 Strains

The strains at the plastic cover and the plastic valley in this section were also adjusted using a factor of 1.29 according to Brachman et al. (2008). Figure 4.43 shows the measured strains of the pipe in Section A caused by static loading. The strain changes of the steel ribs at the pipe crown were almost three times those at the pipe springline. The maximum strain on the

steel ribs at the pipe crown was 0.004%, which is only one-fiftieth of the steel yield strain limit of 0.5%. The strains of the plastic cover induced by static loading ranged from 0.015% to 0.045%, which are much smaller than the plastic strain limit of 5%. The strains at the pipe crown in both the circumferential and the radial directions were larger than the strain in the circumferential direction at the springline but close to the strain in the radial direction at the springline. The strains of the plastic valley in the longitudinal direction at the pipe crown were larger than the strains in the same direction at other locations under both static loadings. The maximum strain of the plastic valley in the longitudinal direction was approximately 0.13%, which is much smaller than the plastic strain limit of 5%.

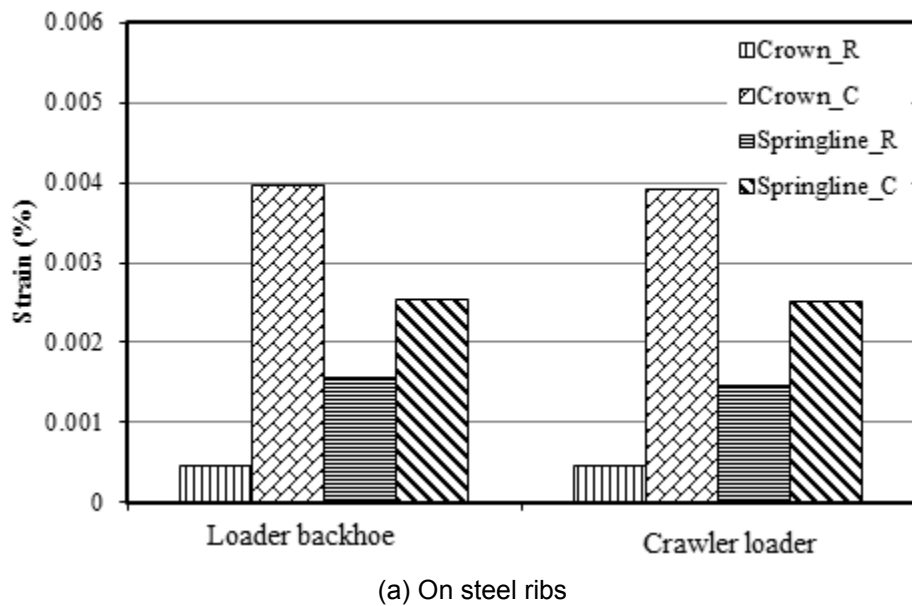
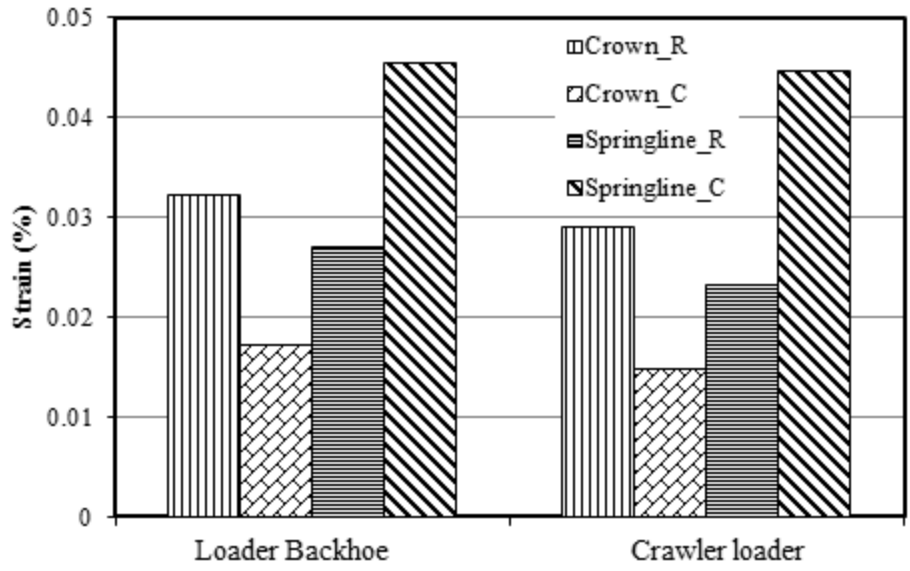
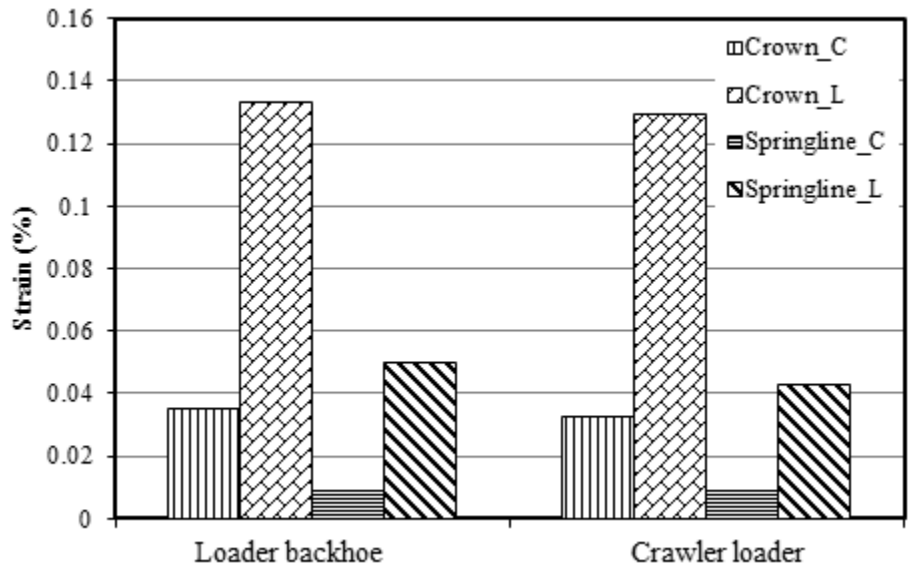


Figure 4.43: The Measured Strains of the Pipe in Section A



(b) On Plastic Cover



(c) On Plastic Valley

Figure 4.43: The Measured Strains of the Pipe in Section A (Continued)

Figure 4.44 shows the measured strains of the pipe in Section B caused by static loading. Similar to Section A, the strains of the steel ribs at the pipe crown were larger than those at the pipe springline. The maximum strain on the steel ribs at the pipe crown was 0.007%, which is only one-third of the steel yield strain limit of 0.5%. The strains of the plastic cover caused by

static loading ranged from 0.015% to 0.035%, which are much smaller than the plastic strain limit of 5%. The strains at the pipe crown in both the circumferential and the radial directions were higher than the strain in the hoop direction at the pipe springline but close to the strain in the radial direction at the springline. The strains of the plastic valley in the longitudinal direction were larger than the strains of steel ribs and plastic covers, which was caused by the lower stiffness of the pipe in the longitudinal direction. The maximum strain of the plastic valley was approximately 0.15%, which is much smaller than the plastic strain limit of 5%.

In summary, the strains induced by the loader backhoe at all positions in both sections were slightly larger than those caused by the track loader due to their pressure difference. All the strains of the pipes induced by static loadings were smaller than their strain limits; therefore, it can be concluded that the pipes were safe under these two types of static loadings in this field test.

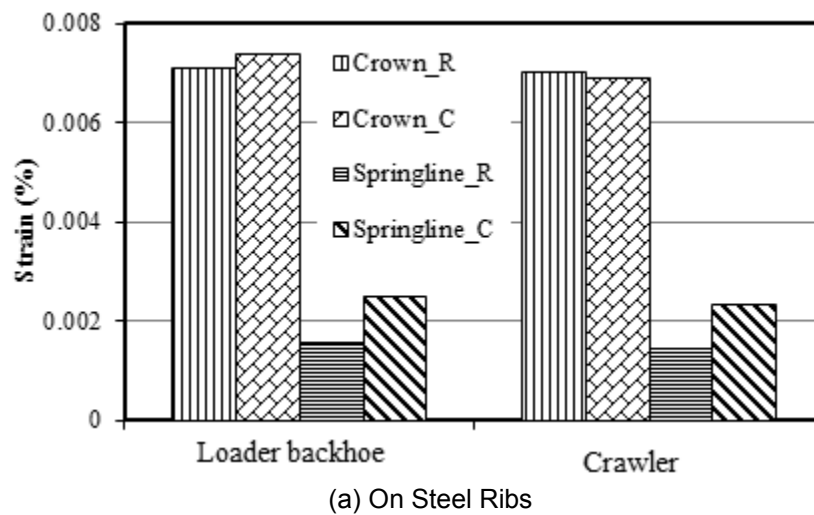


Figure 4.44: The Measured Strains of the Pipe in Section B

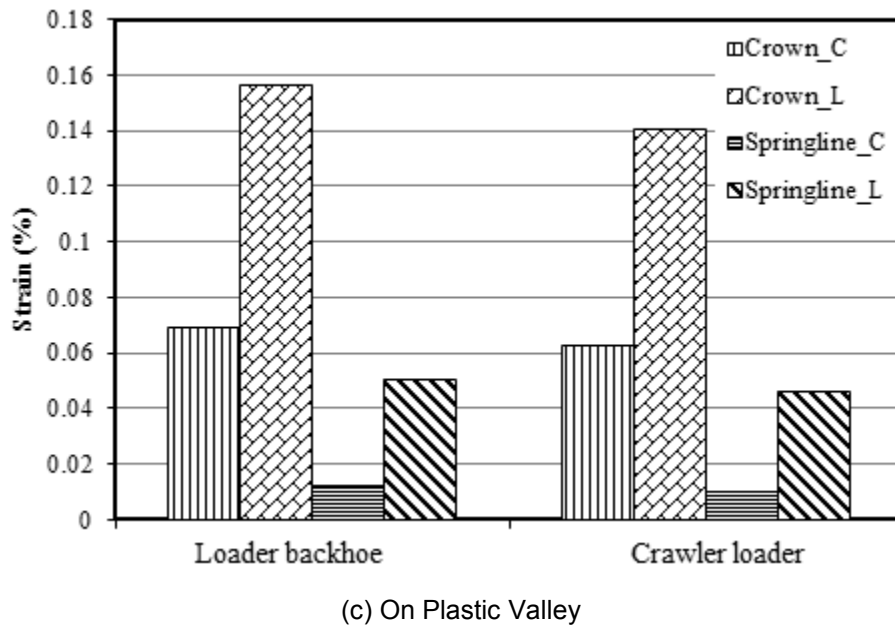
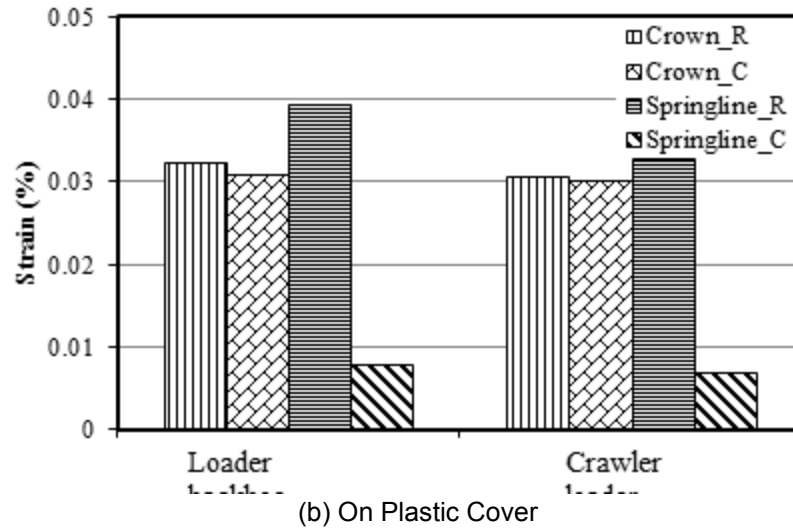
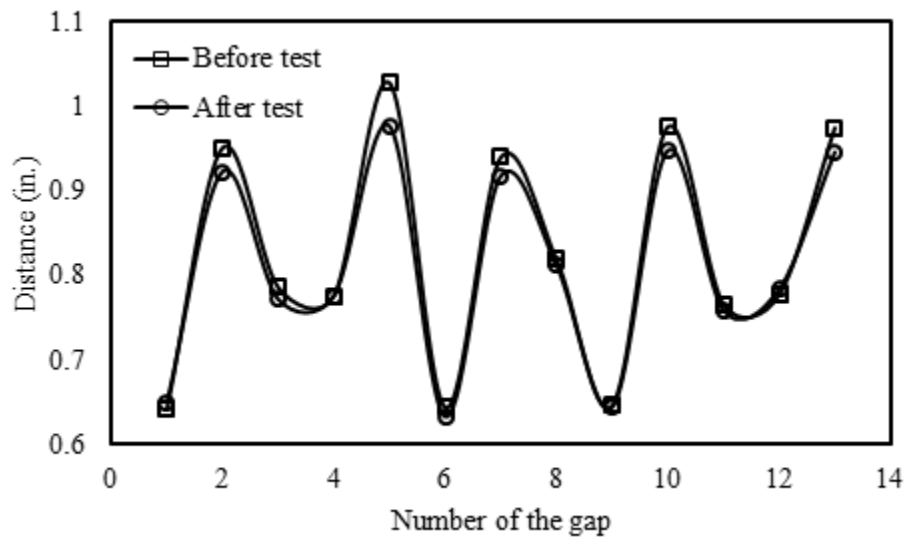


Figure 4.44: The Measured Strains of the Pipe in Section B (Continued)

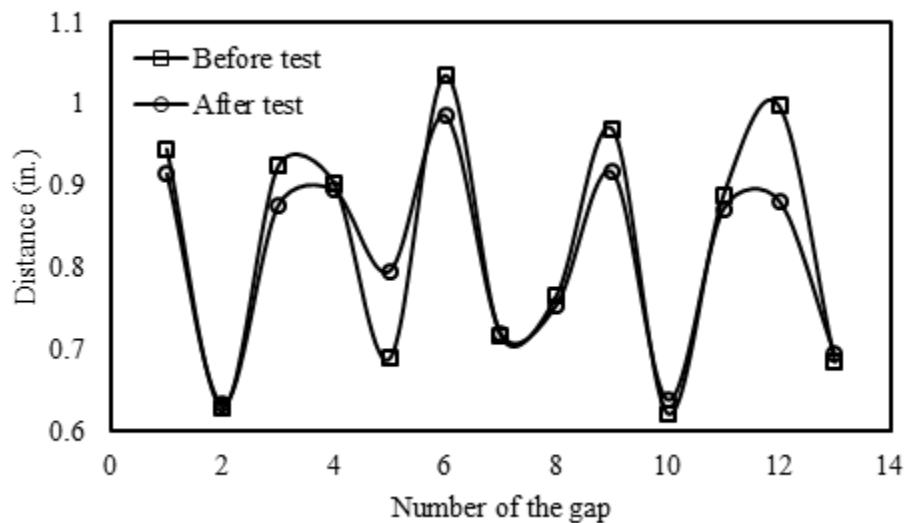
4.7 Observation of Exhumed Pipes

The buried pipes were exhumed for visual observations after the installation. No obvious damage to the ribs and liners of the pipes was observed. To investigate the deformations of ribs during installation, the displacements of ribs at the springline in both sections were monitored. Before the installation, 14 ribs at the springline of each of the middle two pipes were marked and

the gap distances (i.e., 13 gaps) between two adjacent ribs were measured and recorded. After field testing, the gap distances were measured again to evaluate possible distortions of the ribs during the installation. Figure 4.45 shows the gap distances before and after the installation in both sections. Generally, the gap distance changes in Section B were larger than those in Section A. The possible reason is that more large stone particles were pushed into the gaps in Section B by compaction than those in Section A.



(a) Section A



(b) Section B

Figure 4.45: Displacements of Ribs at the Springline of Pipes in Two Sections

4.8 Conclusions

A full-scale field test was conducted to investigate the installation effect on the SRHDPE pipes in the AB3 aggregate and the crushed stone with the soil cover thickness of 0.26 inches in both sections. The diameter of the pipe was 24 inches. The deflections and strains of the pipes and the earth pressures in the backfills were monitored during backfilling and under two types of static loadings. The following conclusions can be made from the analysis of the test results:

1. Based on the measured earth pressures around the pipes, the vertical arching factor (VAF), defined as the ratio of the measured load to the soil prism load on the top of the pipe, were 1.10 and 1.47 in the AB3 aggregate section and the crushed stone section, respectively. This finding was similar to that from the Lawrence field test and the laboratory tests in Phase I of this project.
2. The lateral earth pressure coefficients at the springline of the pipe were approximately 0.65, which is between the lateral earth pressure coefficient at rest (i.e., $K_0 = 0.29$) and the passive earth pressure coefficient (i.e., $K_p = 5.83$).
3. The peaking deflection of the pipe in the AB3 aggregate section was 1.5 times that in the crushed stone section. However, the vertical diameter of the pipe in the crushed stone section decreased by 3.5 times that in the AB3 aggregate section at the final level of the backfill. The vertical deflection of the pipe at the valley liner was slightly larger than that at the steel ribs. The diameter change of the pipe at 45° at the pipe crown in the crushed stone section was larger than that in the AB3 aggregate section. The horizontal deflection of the pipe during backfilling was opposite to the vertical deflection. The maximum deflections of the pipe in the AB3 aggregate section and the crushed stone section were both much smaller than the 5% deflection limit for the steel and HDPE pipes suggested by the AASHTO standards.

4. During the pipe installation, the maximum strain of 0.15% occurred on the pipe plastic valley, which was smaller than the long-term service strain limit of 5% for flexible pipes suggested by AASHTO (2012).
5. The maximum earth pressure induced by static loading occurred at the pipe crown. The measured earth pressures were close to the calculated ones by the methods proposed by AASHTO (2012) and Giroud and Han (2004). Both methods can be used to predict the vertical earth pressure above the SRHDPE pipe caused by static loading. The maximum deflection of the pipe induced by static loading was 0.02 inches (0.08%) in the crushed stone section, while that in the AB3 section was 0.01 inches. The maximum pipe strain of 0.1% was recorded under static loadings.
6. The SRHDPE pipe performed well in the AB3 aggregate and the crushed stone during the installation. The displacements of ribs at the springline of the pipe in the crushed stone section were larger than those in the AB3 section based on the observations of the exhumed pipes.

Chapter 5: Evaluation of the Long-Term Performance of the SRHDPE Pipe

5.1 Introduction

As discussed in Chapter 2, the long-term behavior of the HDPE pipe is different from that in the short-term due to the creep and degradation of the pipe material with time. The reduction of the stiffness of the pipe material in a long-term condition has been included in the calculation of the pipe deflection (AASHTO, 2012). Even though most of the load above the SRHDPE pipe is carried by the steel ribs, the plastic valley of the pipe shares some load, which may control the design. Therefore, the creep and degradation of the HDPE material may influence the long-term performance of the SRHDPE pipe. It is necessary to investigate the SRHDPE pipe performance in a long-term condition. The pipes installed in the Lawrence field test were monitored continuously for 22 months (starting from October 1st, 2013). The observation data include the earth pressures around the pipe, the pipe deflections, and the strains of the steel ribs, the plastic cover, and the plastic valley. This chapter evaluates the changes of the pipe stiffness, the load above the pipe, and the strains of the pipe with time.

5.2 Brief Description of Pipe Monitoring

The instrumentation of the earth pressures, and the deflections and strains of the pipes are the same as that during the pipe installation as described in Chapter 3. Three pipes were divided into two sections: Section A and Section B, which are the same as those discussed in Chapter 3. The AB3 aggregate was used as the backfill material in Section A, while the crushed stone was used in Section B. In each section, two pressure cells were installed at the pipe crown and another four pressure cells were located at the springline, the shoulder, the invert, and the trench wall, respectively. The strains of the pipes were measured at the plastic valley, the plastic cover, and the steel rib. More details about the instrumentation plan of the earth pressures and the strains can be found in Figures 3.11 and 3.12. The deflections of the pipes in both sections were measured in horizontal and vertical directions during the pipe installation. Two more measurements of the pipe deflections using a high precision laser tape Leica D210 (accuracy 3.9×10^{-3} inches) were added in each section for the long-term monitoring at 45° from the pipe

crowns in clockwise and anticlockwise directions. The soil temperature was measured by the temperature sensor included in the earth pressure cell to investigate the temperature effect on the pipe performance. The measurements were taken more often right after the construction. The frequency of measurements decreased to approximately once one month later. So far a total of 29 readings were collected for each sensor.

5.3 Data Analysis

5.3.1 Earth Pressure

5.3.1.1 Temperature Correction Procedures of the Measured Earth Pressure

Figure 5.1 shows the vertical earth pressures at the pipe crown in the crushed stone section at a distance of 114 inches from the roadway centerline. This figure shows that the earth pressure varied with the temperature. To eliminate temperature effect on the variations of earth pressures with time, the earth pressures should be presented at the same temperature. Therefore, all the measured earth pressure must be corrected.

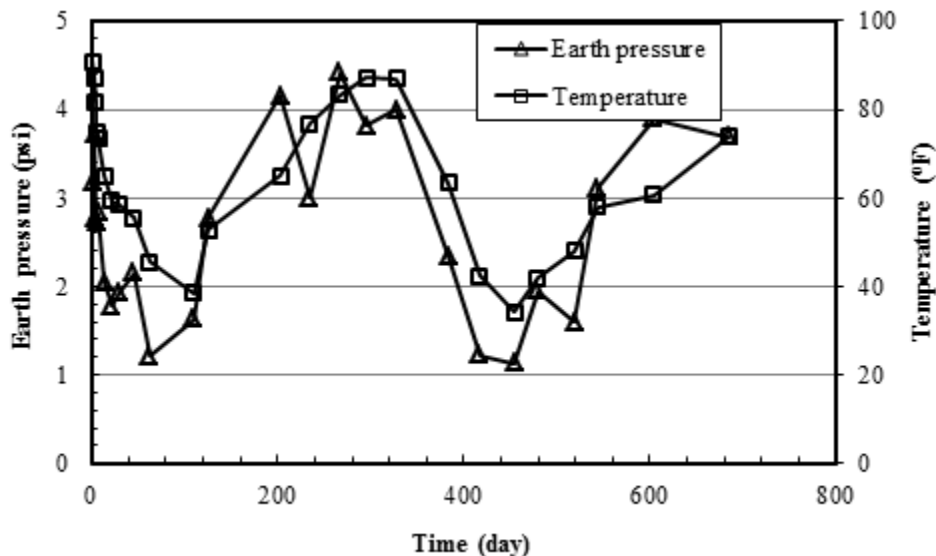


Figure 5.1: Measured Vertical Earth Pressure and Temperature at the Pipe Crown in the Crushed Stone Section at a Distance of 114 Inches

As mentioned in Chapter 3, Geokon total pressure cells 4810-350KPA were used in the field test to measure the earth pressures around the pipes. The manufacturer provided the temperature correction method as follows (Geokon, 2011):

$$\sigma_C = \sigma_M + C(T - T_0) \quad \text{Equation 5.1}$$

Where:

σ_C = the corrected earth pressure

σ_M = the measured earth pressure

C = the temperature correction factor, which can be determined by Equation 5.2

T = the temperature

T_0 = the initial temperature

$$C = \frac{3EKD}{R} \quad \text{Equation 5.2}$$

Where:

E = the elastic modulus of the surrounding medium (3,700 psi for the AB3 aggregate and 3,480 psi for the crushed stone)

K = the thermal expansion coefficient of the oil film in the pressure cell (0.00044/F°)

D = the thickness of the oil film in the pressure cell (0.06 inches for the Geokon total pressure cell)

R = the radius of the pressure cell (4.5 inches for the Geokon total pressure cell).

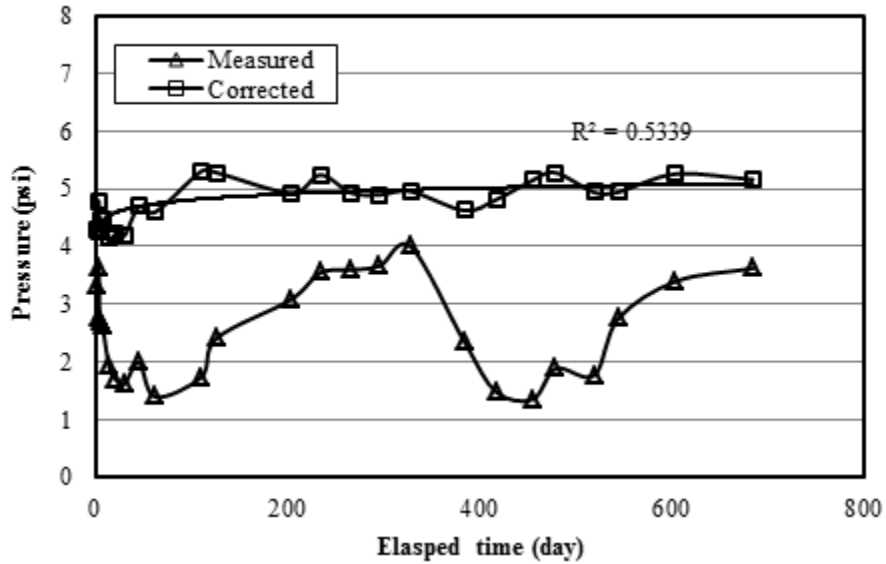
Based on Equation 5.2, the temperature correction factor C for the AB3 aggregate is 0.63 and that for the crushed stone is 0.58.

Based on the correction method provided by the manufacturer, all measured earth pressures presented in this chapter were corrected with respect to the temperature at which the pressure cells were installed.

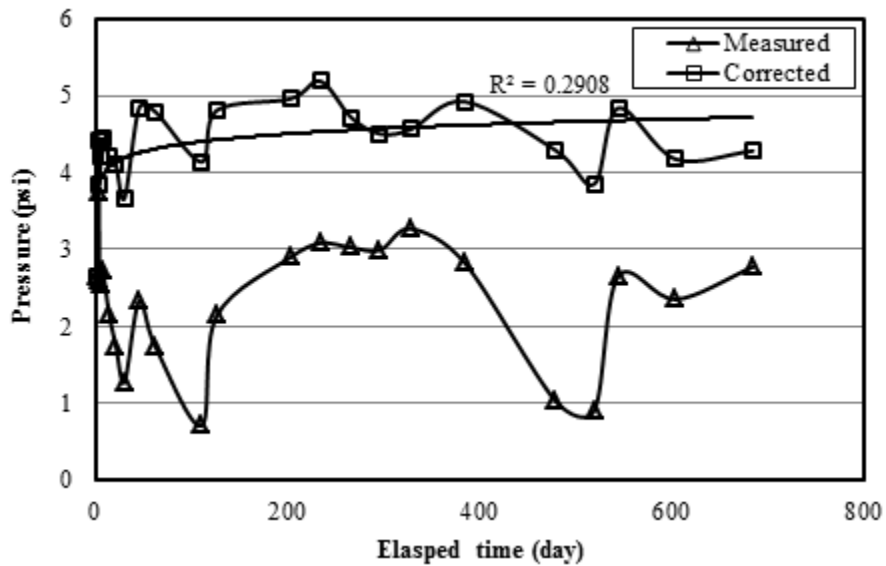
5.3.1.2 Test Section A

Figure 5.2 shows the measured and corrected vertical earth pressure with time at the pipe crown in Section A. The vertical earth pressure at the pipe crown in Section A slightly increased

with the time. The vertical earth pressure after 680 days of the construction was approximately 5.0 psi. The vertical soil arching factor (VAF) was approximately 1.72 (overburden stress = $141 \text{ pcf} \times 36 \text{ inches} / 12 / 144 = 2.9 \text{ psi}$).



(a) 38 Inches from the Roadway Centerline



(b) 114 Inches from the Roadway Centerline

Figure 5.2: Corrected Vertical Earth Pressure at the Pipe Crown in Section A

Figure 5.3 shows the measured and corrected lateral earth pressures at the pipe springline in Section A. The lateral earth pressure at the pipe springline increased to 3 psi within 680 days after the construction. Since there is no measured vertical earth pressure at the pipe springline, the lateral earth pressure coefficient was calculated as 0.75 using the theoretical overburden stress at the springline ($K = 3 / (50 \text{ inches} \times 141 \text{ pcf} / 12 / 144) = 0.75$). The lateral earth pressure coefficient at the pipe springline in Section A was higher than K_0 (i.e., 0.209).

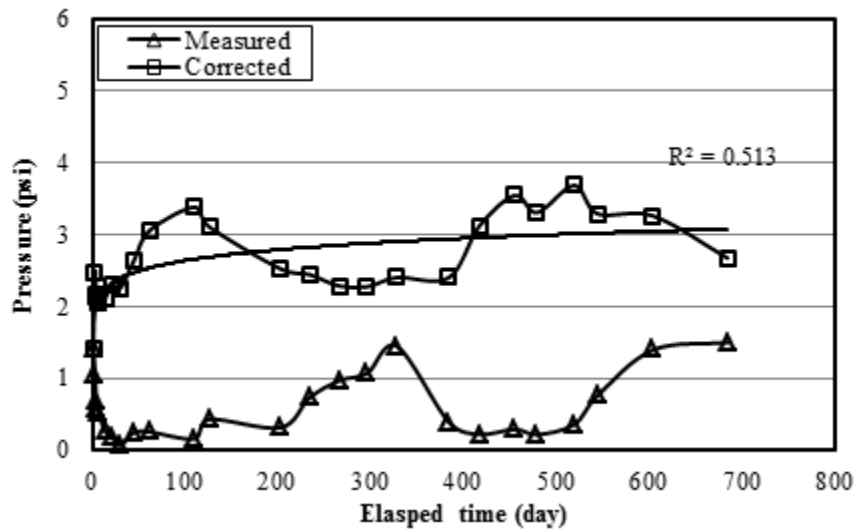


Figure 5.3: Corrected Lateral Earth Pressure at the Pipe Springline in Section A

Figure 5.4 shows the measured and corrected vertical earth pressures at the shoulder in Section A. This figure also shows that the corrected vertical earth pressure at the shoulder increased with the time and was approximately 4.6 psi at within 680 days, i.e., the VAF at the shoulder was equal to 1.84.

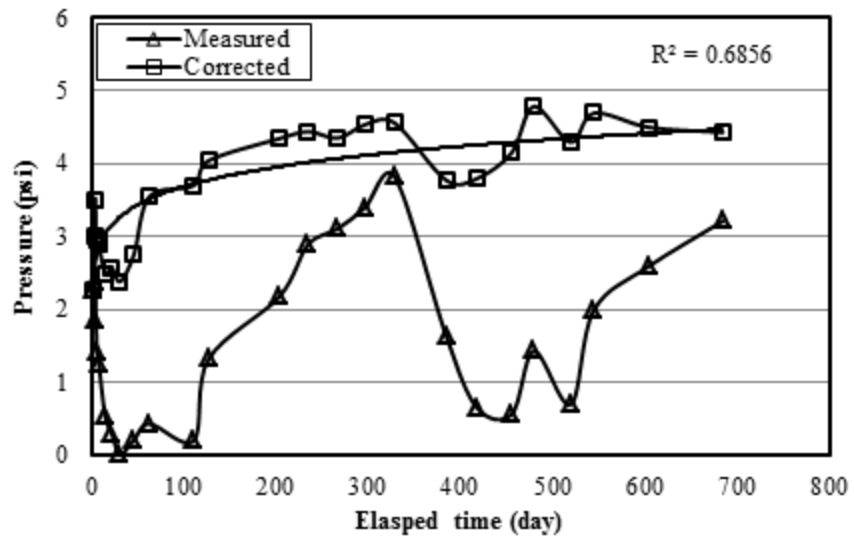


Figure 5.4: Corrected Vertical Earth Pressure at the Shoulder in Section A

Figure 5.5 shows the measured and corrected lateral earth pressures at the trench wall. The corrected lateral earth pressure at the trench wall was almost constant at 3.0 psi, indicating the long-term effect on the trench wall was insignificant.

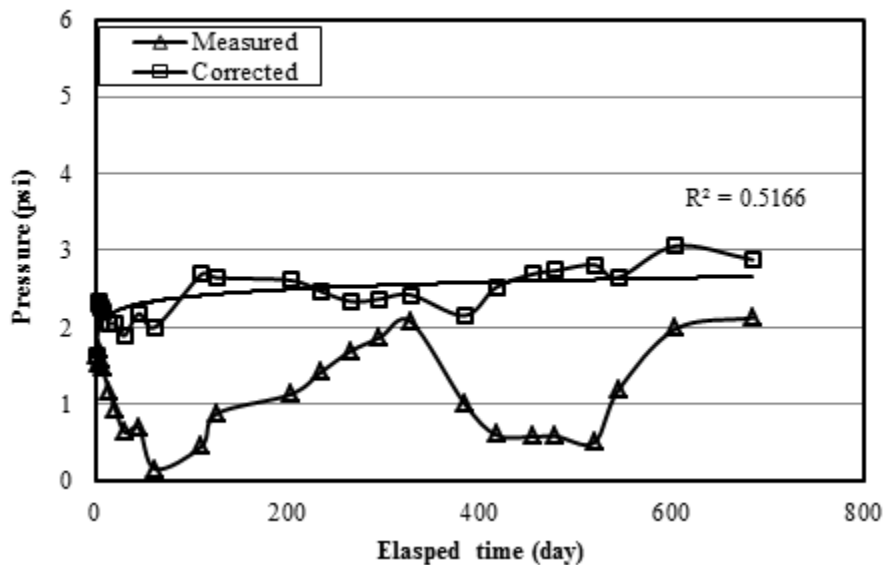


Figure 5.5: Corrected Lateral Earth Pressure at the Trench Wall at the Pipe Springline Level in Section A

Figure 5.6 shows the vertical earth pressures at the pipe invert. The corrected vertical earth pressure was approximately 4.7 psi at the end of monitoring.

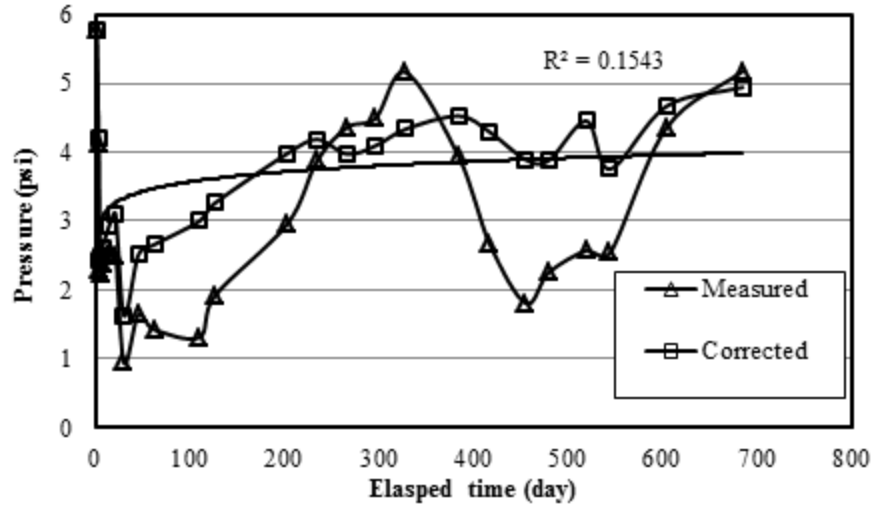
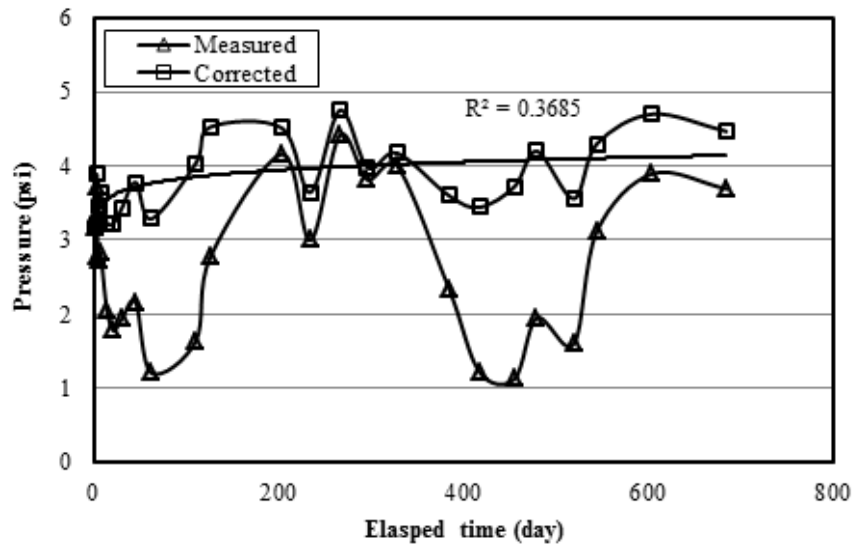


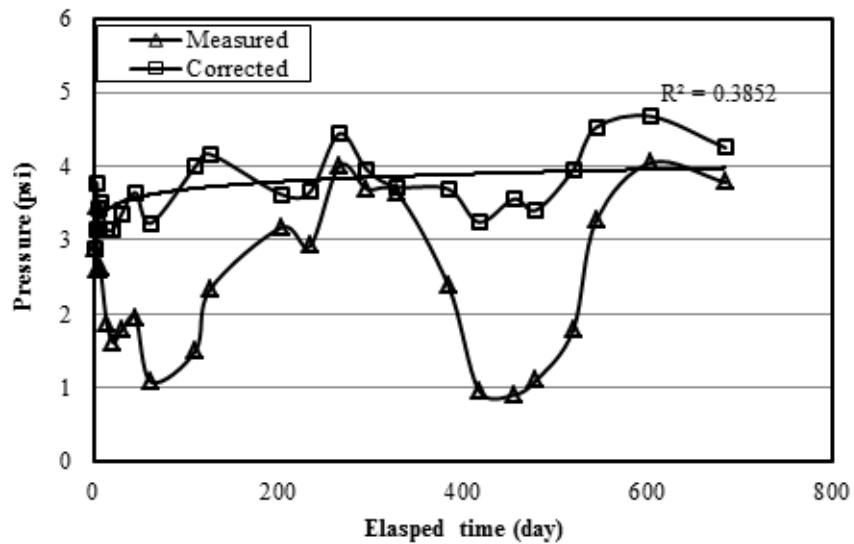
Figure 5.6: Corrected Vertical Earth Pressure at the Pipe Invert in the Section A

5.3.1.3 Test Section B

Figure 5.7 shows the measured and corrected earth pressures with the time at the pipe crown in Section B. The earth pressure at the pipe crown increased with time. The earth pressure after 680 days of the construction was approximately 4.5 psi. The VAF was approximately 2.18 (overburden stress = $99.2 \text{ pcf} \times 36 \text{ inches} / 12 / 144 = 2.06 \text{ psi}$). The VAF in Section A was lower than that in Section B. The load carried by the pipe in Section A (the AB3 aggregate section) was higher than that in Section B (the crushed stone section) due to the higher unit weight of the AB3 aggregate than the crushed stone.



(a) 38 Inches from the Roadway Centerline



(b) 114 Inches from the Roadway Centerline

Figure 5.7: Corrected Vertical Earth Pressure at the Pipe Crown in Section B

Figure 5.8 shows the measured and corrected lateral earth pressures at the pipe springline in Section B. The corrected lateral earth pressure at the pipe springline increased to approximately 4 psi at 680 days after the construction. Since there was no measured vertical earth pressure at the pipe springline, the lateral earth pressure coefficient was calculated as 1.38 based on the theoretical overburden stress at the springline ($K = 4 / (50 \text{ inches} \times 99.2 \text{ pcf} / 12 / 144) = 1.38$).

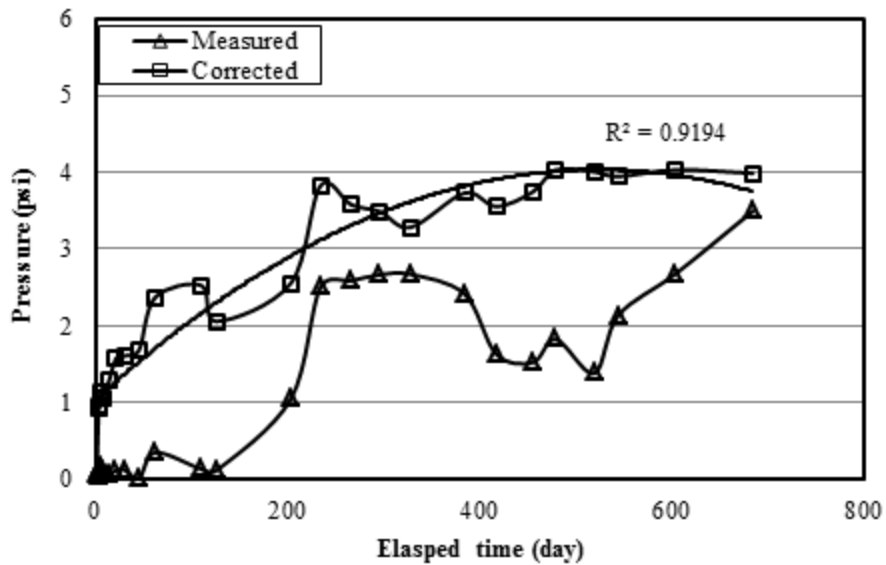


Figure 5.8: Corrected Lateral Earth Pressure at the Pipe Springline in Section B

Figure 5.9 shows the measured and corrected vertical earth pressures at the shoulder in Section B. This figure also shows that the corrected earth pressure at the shoulder generally increased with time and was around 5 psi at 680 days. The VAF at the shoulder was 2.43.

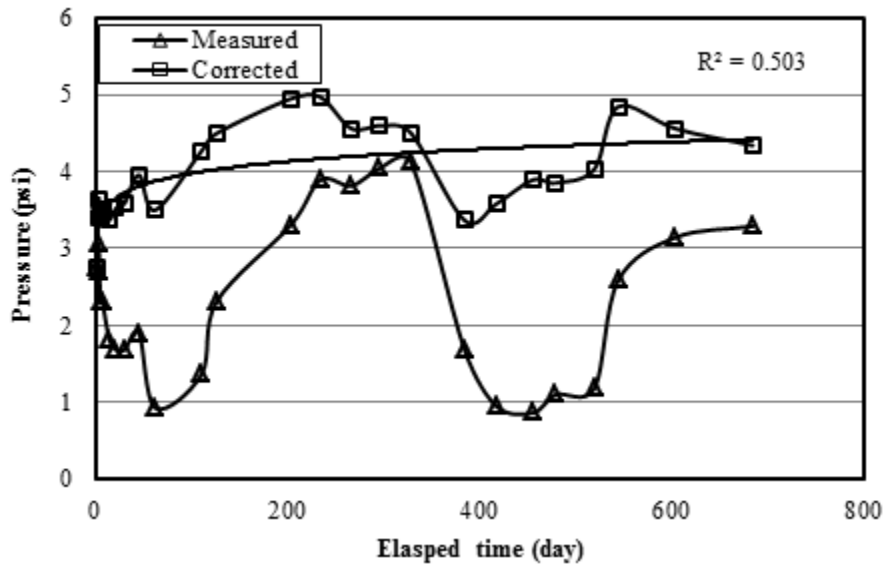


Figure 5.9: Corrected Vertical Earth Pressure at the Shoulder in Section B

Figure 5.10 shows the measured and corrected lateral earth pressures with time at the trench wall. The earth pressure at the trench wall generally increased with time and was approximately 3.0 psi, which is lower than that next to the pipe at the same level. The earth pressure cell next to the pipe was subjected to additional lateral pressure from the pipe.

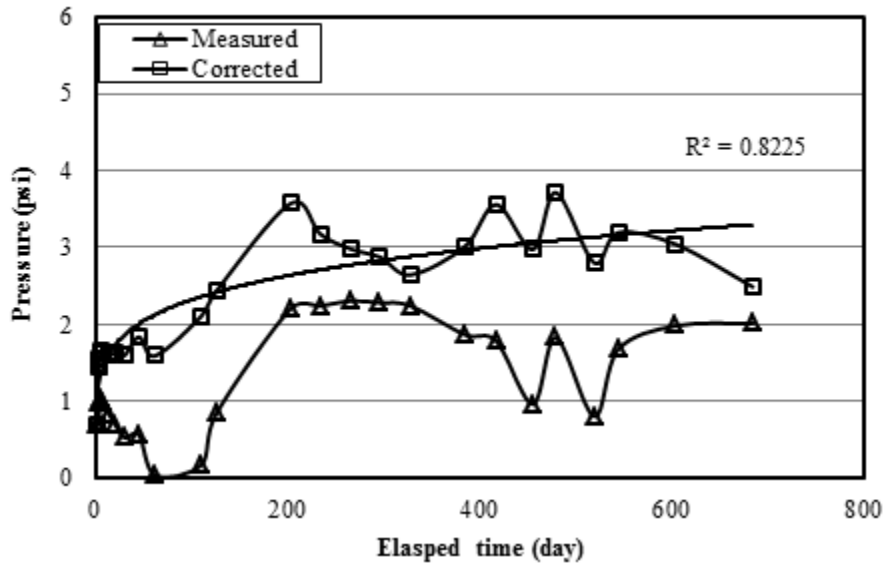


Figure 5.10: Corrected Earth Pressure at the Trench Wall at the Pipe Springline Level in Section B

Figure 5.11 shows the measured and corrected vertical earth pressures at the pipe invert. The readings after the construction to 300 days were not reliable due to the wire connection problem; therefore, they are not provided. After the problem was fixed, the earth pressure was almost constant at 3.2 psi.

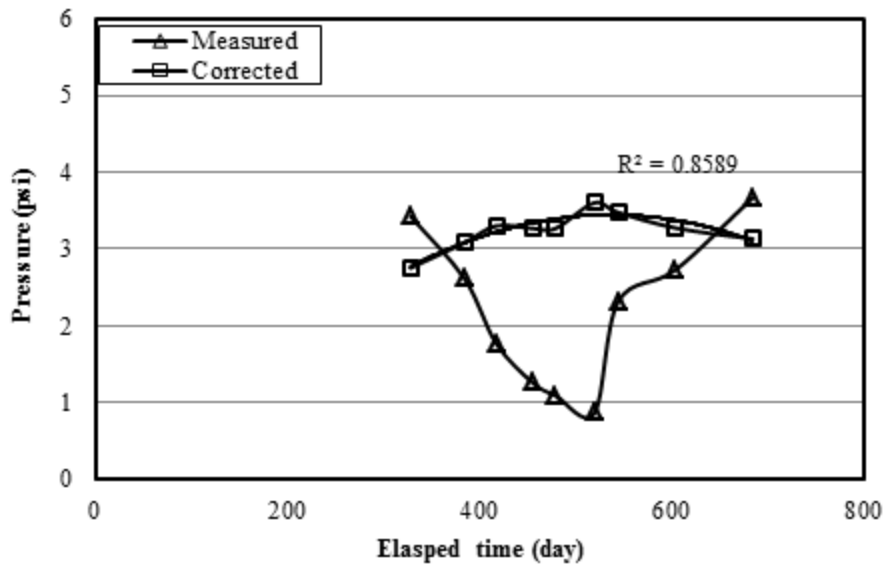


Figure 5.11: Corrected Vertical Earth Pressure at the Pipe Invert in Section B

5.3.2 Deflections

Figure 5.12 shows the pipe deflection with the time in Section A. The pipe deflection in the horizontal direction increased up to approximately 0.6%, while that in the vertical direction was 0.4% at 680 days. The diameter change at an angle of 45° from the pipe crown decreased slightly with the time. These changes indicate that the pipe returned to a round shape after the installation due to the traffic loading and the creep of the pipe material.

Figure 5.13 shows the pipe deflection with time in Section B. The pipe deflections in the vertical and horizontal directions increased with the time and reached approximately 0.8% of the pipe diameter in 680 days. This deflection increase can be attributed to the increase of the vertical earth pressure on the crown and the pipe creep deformation, which will be discussed in the next section. The diameter change at an angle of 45° from the pipe crown decreased slightly with time.

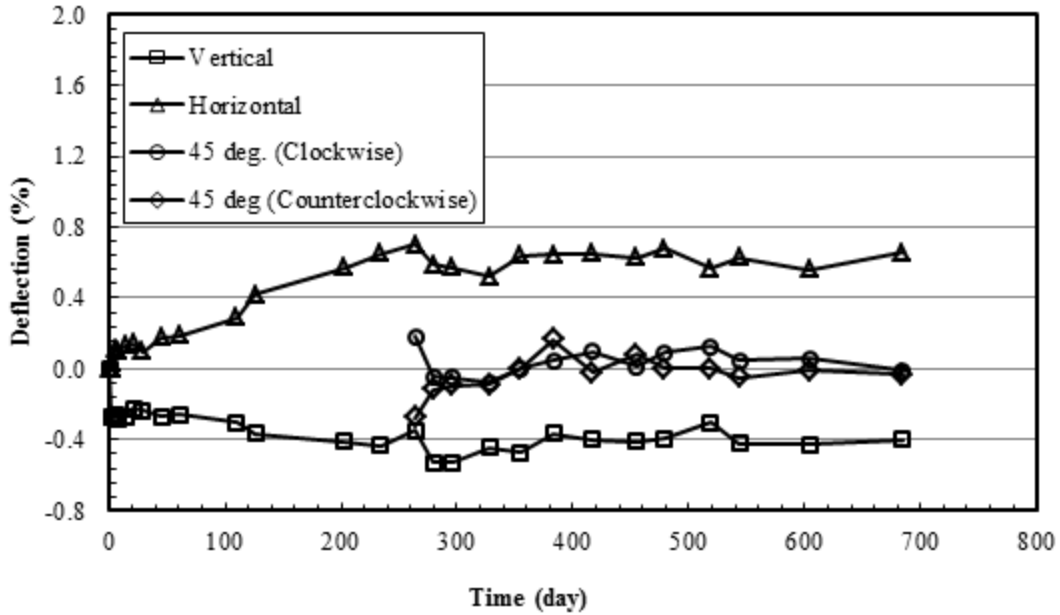


Figure 5.12: Pipe Deflections with Time in Section A

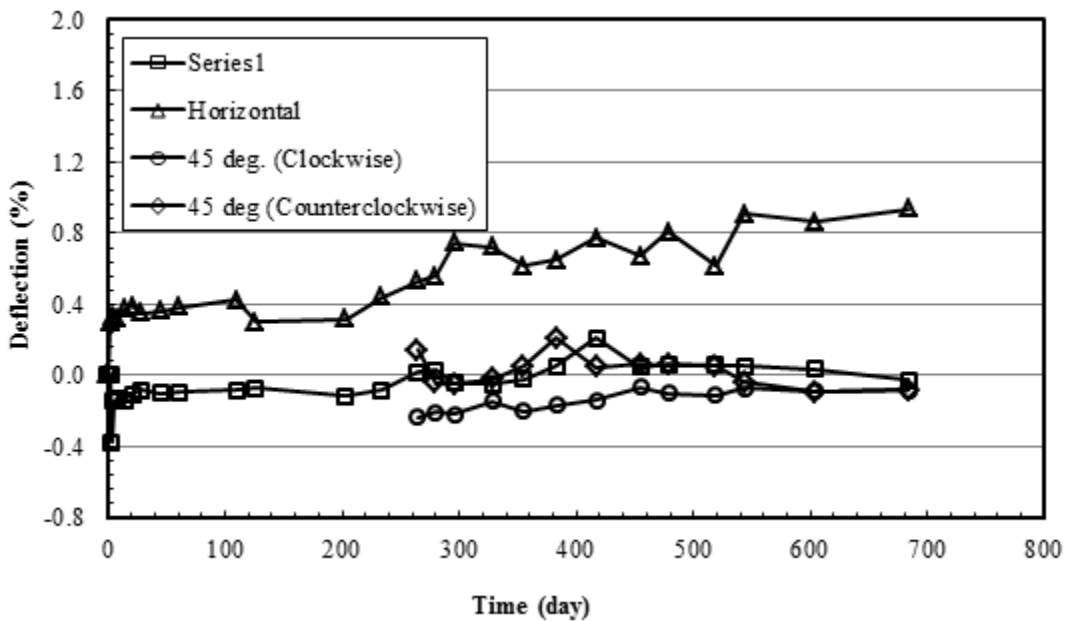


Figure 5.13: Pipe Deflections with Time in Section B

The deflections in the vertical and horizontal directions in Section A were smaller than those in Section B. The reason for this difference is that the AB3 aggregate in Section A had a higher modulus than the crushed stone in Section B and provided more lateral support for the pipe.

5.3.3 Strains

5.3.3.1 Test Section A

Four pairs of strain gages (outside and inside of the pipe) were attached on the plastic valley at the pipe crown in the longitudinal direction. Their distances to the roadway centerline were 33, 21, 9, and 3 inches, respectively. They are labeled as “L1, L2, L3, and L4” from the farthest point to the closest point to the centerline. Strains at the plastic valley and the plastic cover in this section were also adjusted using a factor of 1.29 according to Brachman et al. (2008). Figure 5.14 shows the longitudinal strains on the plastic valley at the pipe crown in Section A. Compared with the temperature curve, the longitudinal strains of the plastic valley at the pipe crown were not apparently affected by the temperature. As compared with the temperature curve, the longitudinal strains of the plastic valley at the pipe crown were not apparently affected by the temperature. For a clear presentation, the variation of the temperature is not included in later figures except for the case with an apparent temperature effect. The general trend is that the strains increased slightly with the time. The magnitude of the strains decreased with an increase of the distance to the centerline. The maximum longitudinal strain on the plastic valley at the pipe crown was approximately 0.3% at 3 inches from the roadway centerline.

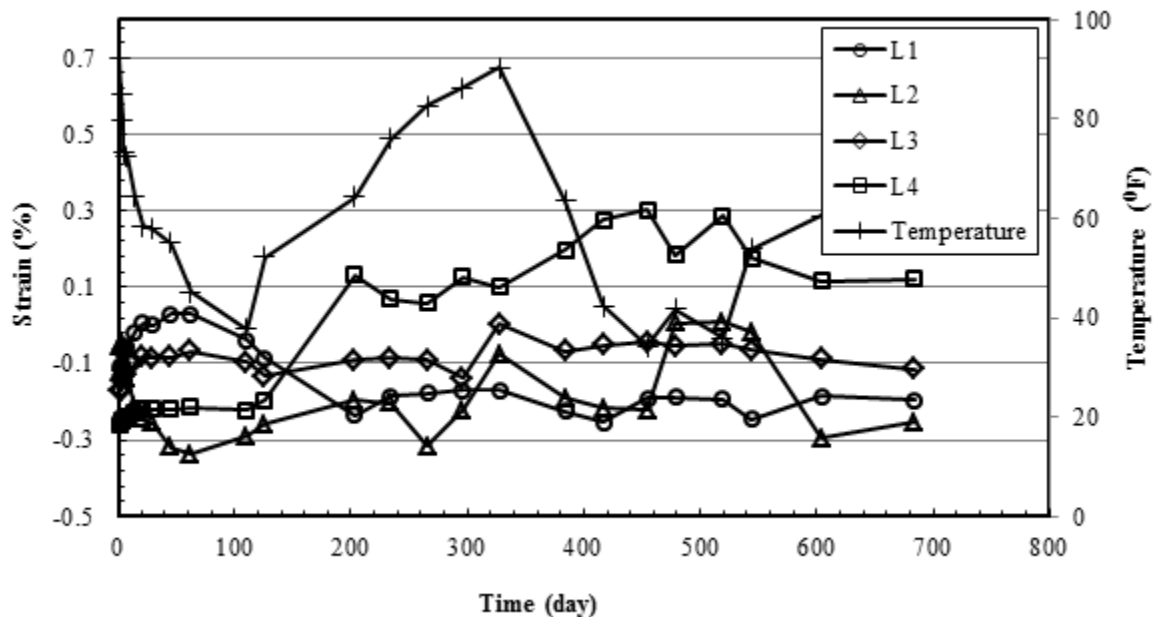


Figure 5.14: Longitudinal Strains on the Plastic Valley at the Pipe Crown in Section A

Figure 5.15 shows the longitudinal strains on the plastic valley at the pipe springline and the invert in Section A. The longitudinal strains at the springline and the invert were not influenced by the temperature. The strains at the pipe invert and the springline varied with the maximum value of -0.14% to -0.33%. The negative strains indicate that the plastic valley of the pipe in the longitudinal direction at the pipe springline and the pipe invert was under compression.

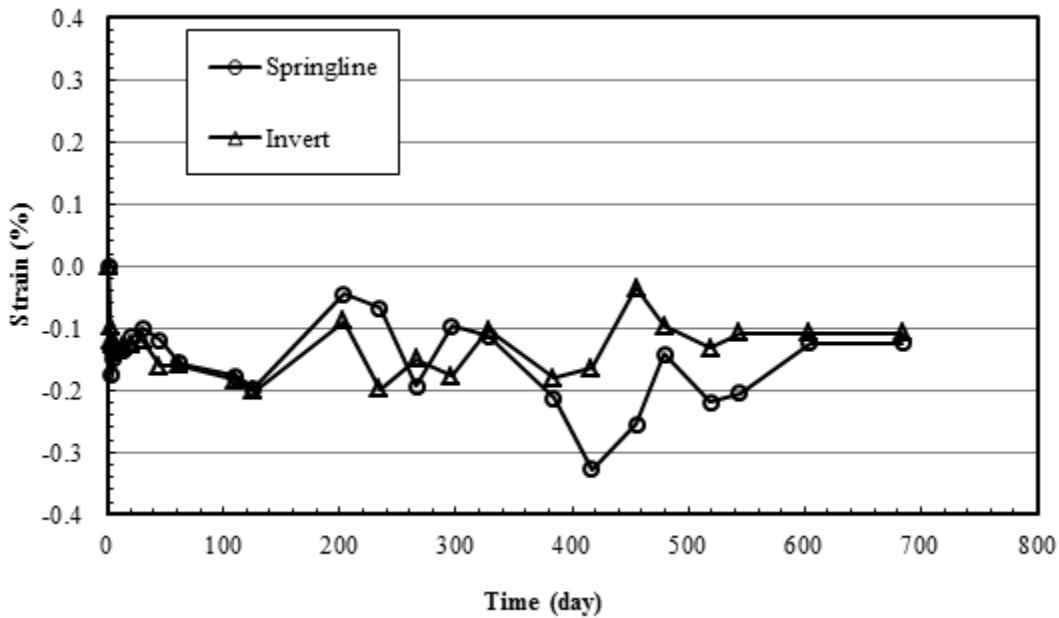


Figure 5.15: Longitudinal Strains on the Plastic Valley at the Pipe Springline and Invert in Section A

Figure 5.16 presents the circumferential strains of the plastic covers at the pipe crown, invert, and springline. The strains of the plastic cover varied with the temperature at all three locations. The maximum strain variation was 0.79% with a temperature change of 48.6°F (i.e., from 41°F to 89.6°F). The strains at the pipe crown changed more significantly than other two locations. The strains at the pipe invert were the lowest ones. The strains at the springline and the crown increased from negative to positive values. The strains at the pipe invert were always negative.

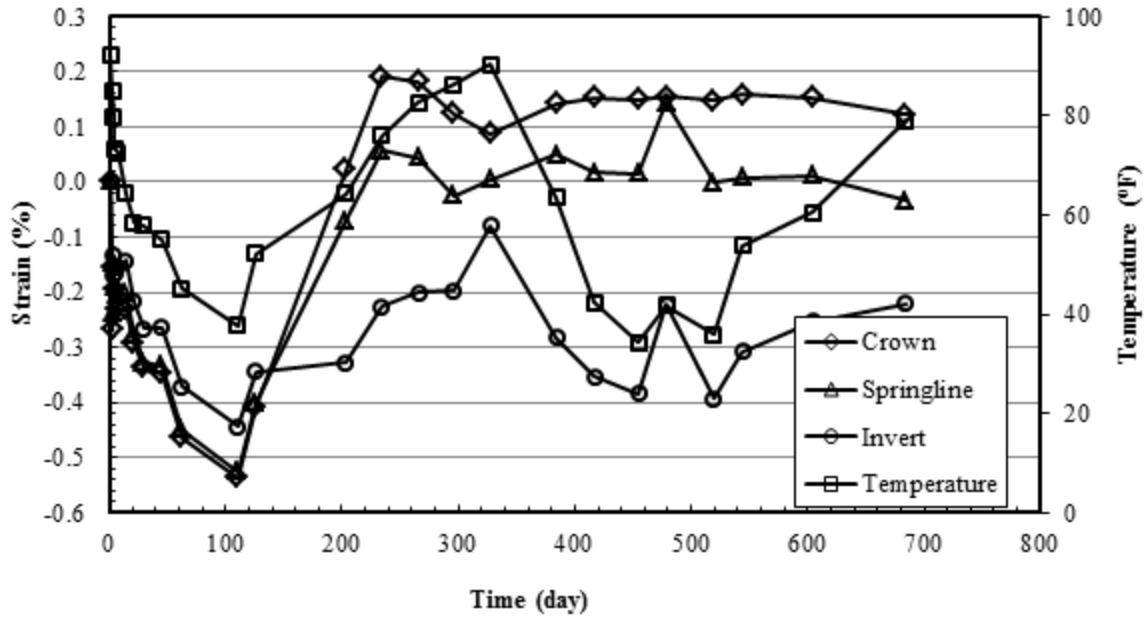


Figure 5.16: Circumferential Strains of the Plastic Cover in Section A

Figure 5.17 presents the circumferential strains of the steel ribs at the pipe crown and the springline in Section A. The measured strains were not affected by the temperature. The strains at both the pipe crown and the springline were negative, indicating that the steel ribs were under compression. The strains at the pipe springline generally increased with time to 400 days after construction and then decreased. The strains at the pipe crown increased with time. The maximum strain of the steel ribs in Section A was 0.17% at the pipe crown, which is less than the steel yield strain of 0.5%.

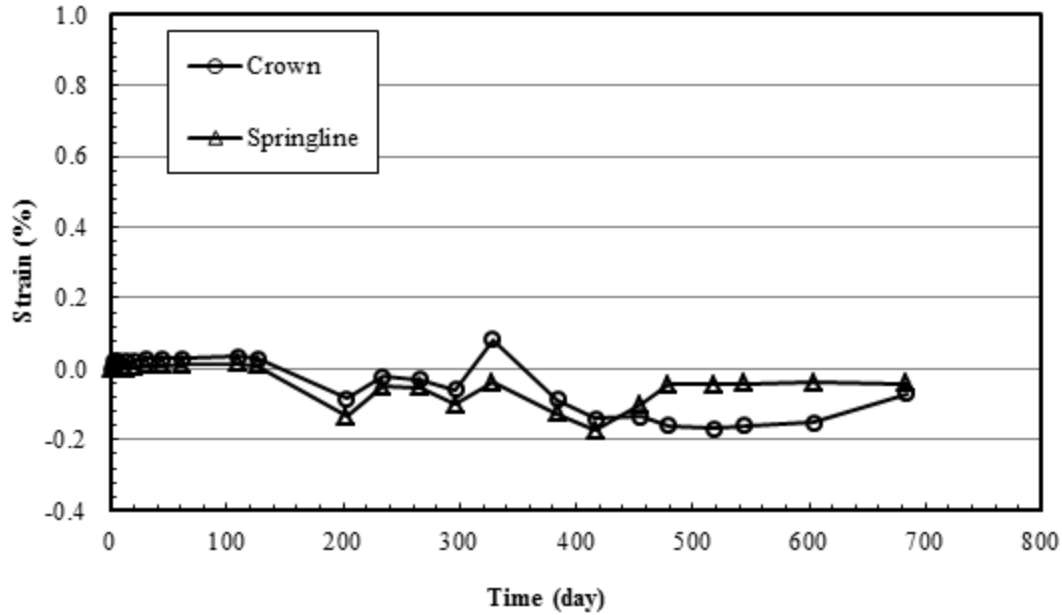


Figure 5.17: Circumferential Strains of Steel Ribs in Section A

5.3.3.2 Test Section B

Figure 5.18 shows the longitudinal strains at the pipe valley at the pipe crown in Section B. There are some variations of the measured strains but generally the strains on the plastic valley in the longitudinal direction were almost constant through the observation time. Strains at the plastic valley and the plastic cover in this section were also adjusted using a factor of 1.29 according to Brachman et al. (2008). The magnitudes of the strains decreased with an increase of the distance to the centerline, which was consistent with that in Section A. The maximum strain on the plastic valley in the longitudinal direction was approximately 0.35% at 9 inches from the roadway centerline, which is 1.3 times that in Section A.

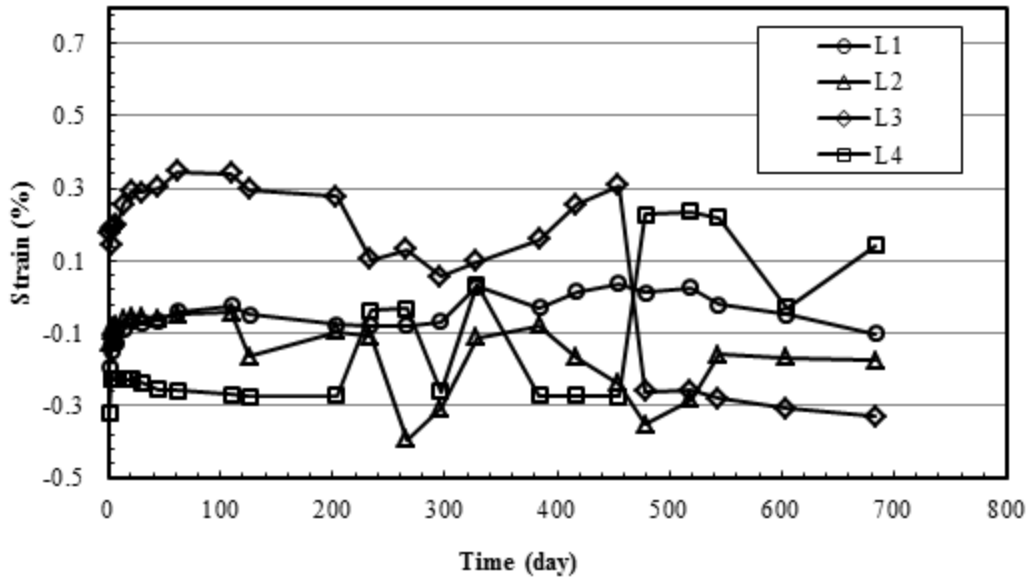


Figure 5.18: Longitudinal Strains on the Pipe Valley at the Pipe Crown in Section B

Figure 5.19 shows the longitudinal strains of the plastic valley at the pipe springline and invert in Section B. The longitudinal strains of the plastic valley at the springline and the pipe invert mostly varied within 0.2%.

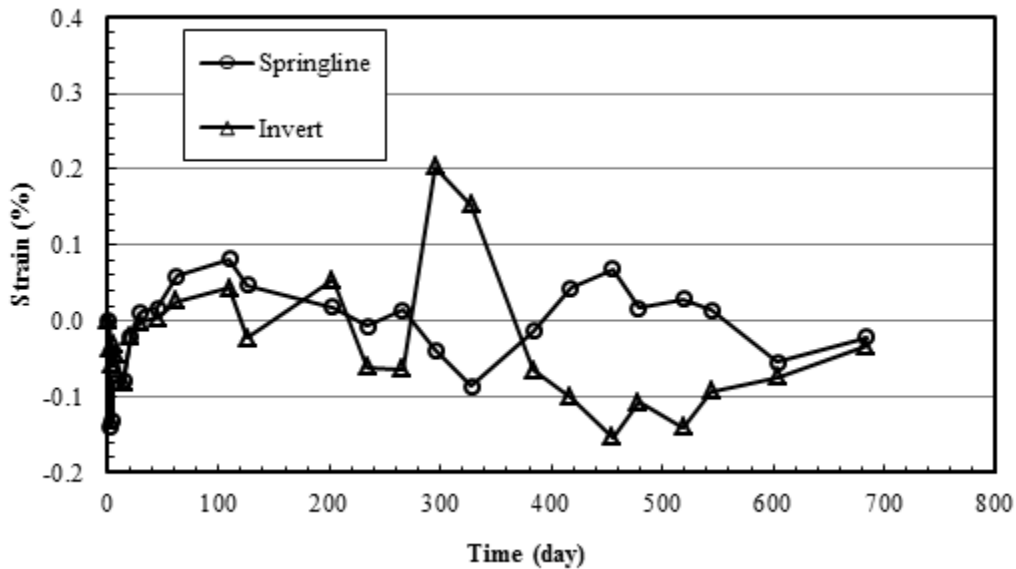


Figure 5.19: Longitudinal Strains on the Pipe Valley at the Pipe Springline and the Invert in Section B

Figure 5.20 presents the circumferential strains of the plastic covers at the pipe crown, invert, and springline. The strains of the plastic covers varied with the temperature at all three locations. The maximum strain variation was 0.57% with a temperature change of 48.6°F (i.e., from 41°F to 89.6°F). The strains at three locations were similar, and the strains at the pipe crown were slightly larger than strains at other locations. Their difference was approximately 0.1%. Most measured strains of the plastic covers were negative, indicating that the pipes in the circumferential direction in Section B were under compression.

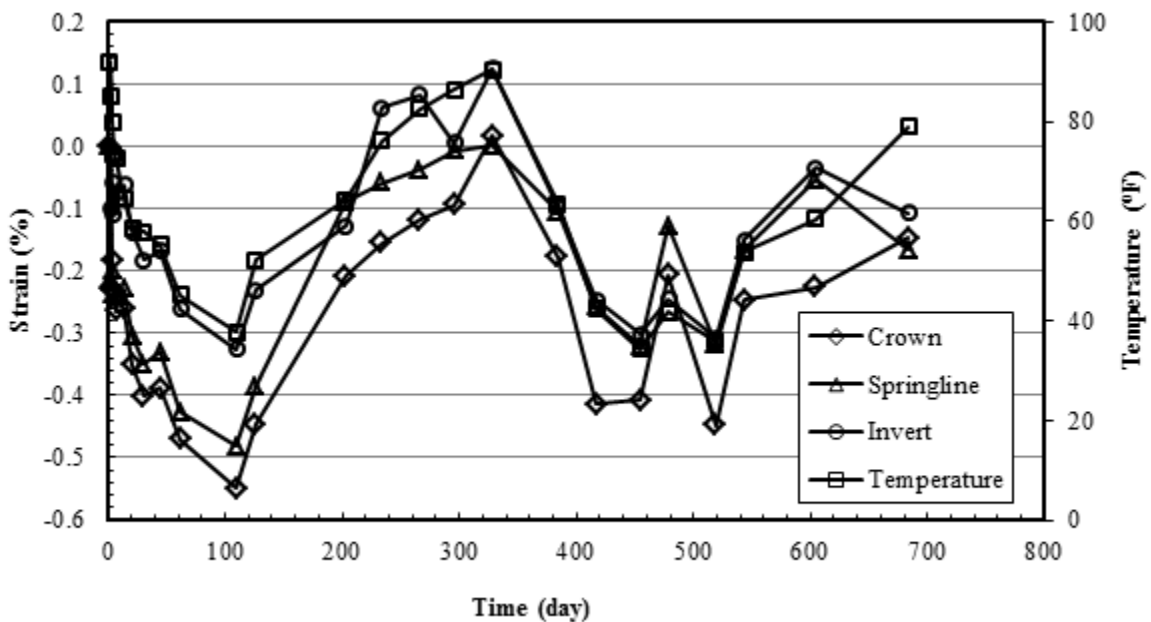


Figure 5.20: Circumferential Strains of the Pipe Covers in Section B

Figure 5.21 presents the circumferential strains of the steel ribs at the pipe crown and the springline. They were not affected by the temperature. The positive strains at the springline illustrated the steel rib at the pipe springline was under tension. The negative strains at the pipe crown demonstrated that the steel rib at the pipe crown was under compression. The strains of the steel ribs increased with the time. The maximum strain of the steel rib in Section B was 0.18%, which is lower than the steel yield strain of 0.5%.

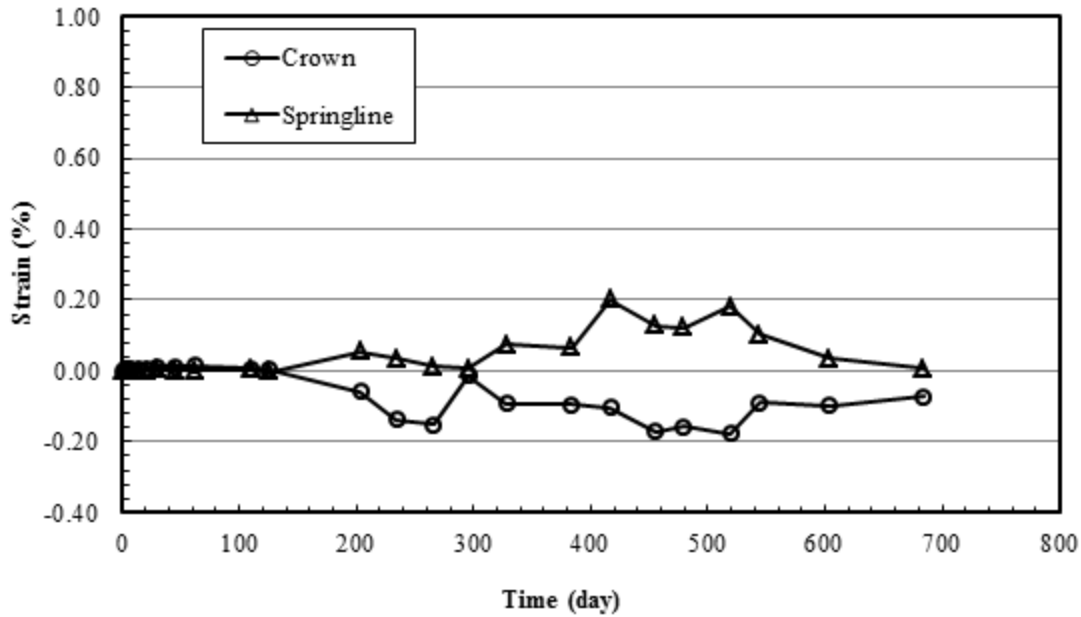


Figure 5.21: Circumferential Strains of Steel Ribs in Section B

5.4 Long-Term Empirical Correlations

The design service life of a pipeline system is typically 100 years. So far, no field test data is available to evaluate the SRHDPE pipe performance in its design service life. A typical way to evaluate long-term performance of pipes is to establish an empirical correlation with the time based on field data in a relative long time. This method was also adopted in the current study. Based on the literature review, two parameters are important for the evaluation of long-term performance of HDPE pipes: VAF and pipe stiffness. VAF is essential to calculate the load above the pipe in the design, which can be used to calculate pipe deflections and strains. Internal forces, deflections, and strains of pipes depend on pipe stiffness or relative stiffness between pipe and backfill material. The long-term stiffness of HDPE pipes has been investigated by several researchers (e.g., Hsuan & Zhang, 2005; Hsuan & McGrath, 2005). Creep and degradation of the HDPE material with time influence long-term stiffness of the HDPE pipes. However, the stiffness of the SRHDPE pipe is expected to be different from the HDPE pipe since the SRHDPE pipe includes steel reinforcements. Therefore, it is necessary to evaluate the SRHDPE pipe stiffness under a long-term condition.

5.4.1 Vertical Soil Arching Factor

Figure 5.22 shows the variation of the VAFs with the time in Sections A and B, which can be approximately expressed by a linear relationship as follows:

$$VAF = 0.11 \log(t) + 1.20 \text{ (AB3 aggregate)} \quad \text{Equation 5.3a}$$

$$VAF = 0.15 \log(t) + 1.53 \text{ (crushed stone)} \quad \text{Equation 5.3b}$$

Where:

VAF = the vertical soil arching factor at the pipe top

t = the time after the pipe installation (days)

Based on Equations 5.3a and 5.3b, the VAFs for 50 and 100 years in Section A (the AB3 aggregate section) are 1.67 and 1.70, respectively, while they are 2.17 and 2.21 in Section B (the crushed stone section).

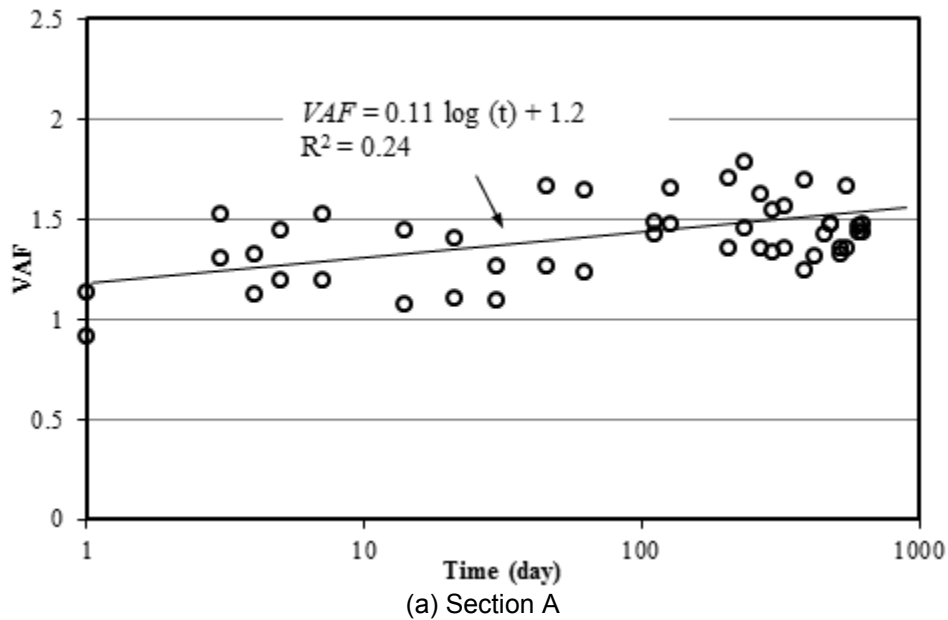


Figure 5.22: Variation of the VAFs With the Time

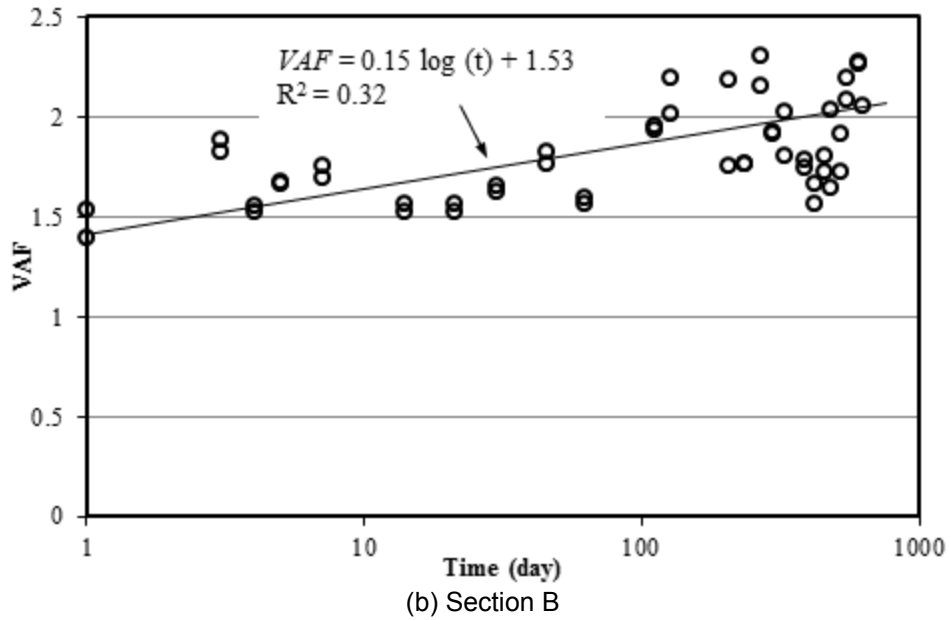


Figure 5.22: Variation of the VAFs With the Time (Continued)

5.4.2 Pipe Stiffness

Pipe creep tests can be used to determine the pipe stiffness under a long-term condition. Khatri (2012) conducted a creep test on the SRHDPE pipe in air using a loading frame in the laboratory for 700 hours. He back-calculated the time-dependent pipe stiffness factor (EI) based on the load and the pipe deflection within the test period using Equation 5.4:

$$EI = 0.149R^3PS = 0.149R^3 \frac{F}{\Delta y} \quad \text{Equation 5.4}$$

Where:

R = the pipe radius

PS = the pipe stiffness

F = the load on the pipe

Δy = the pipe deflection.

Khatri (2012) found the stiffness (EI) factor of the pipe decreased by 25% in 700 hours, which can significantly influence the pipe performance. Khatri pointed out that the stiffness

reduction with time should be less if the pipe is buried in soil. Therefore, it is important to develop a correlation of the pipe stiffness factor (EI) with time based on field data.

Figure 5.23 shows the variation of the pipe stiffness factor based on the field data calculated using Equation 5.4, which can be approximately expressed as follows:

$$EI = -1.9 \log(t) + 11.0 \text{ (AB3 aggregate)} \quad \text{Equation 5.5a}$$

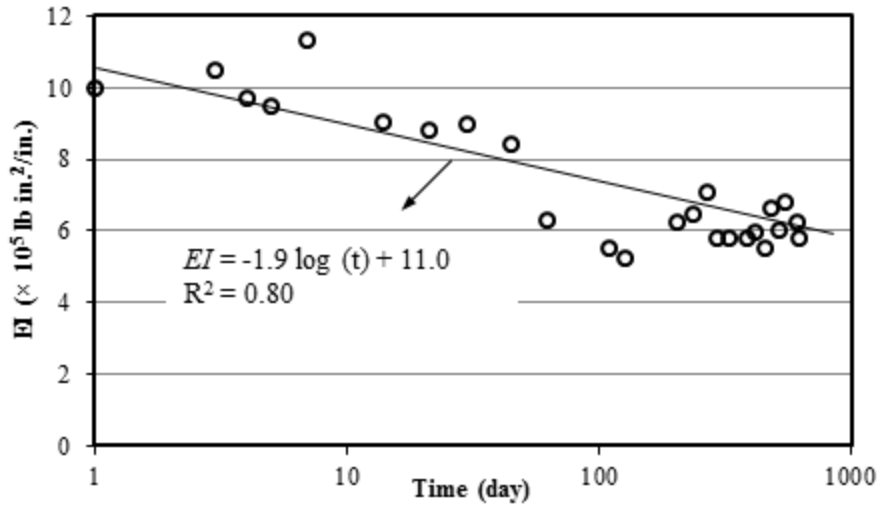
$$EI = -1.96 \log(t) + 10.8 \text{ (crushed stone)} \quad \text{Equation 5.5b}$$

Where:

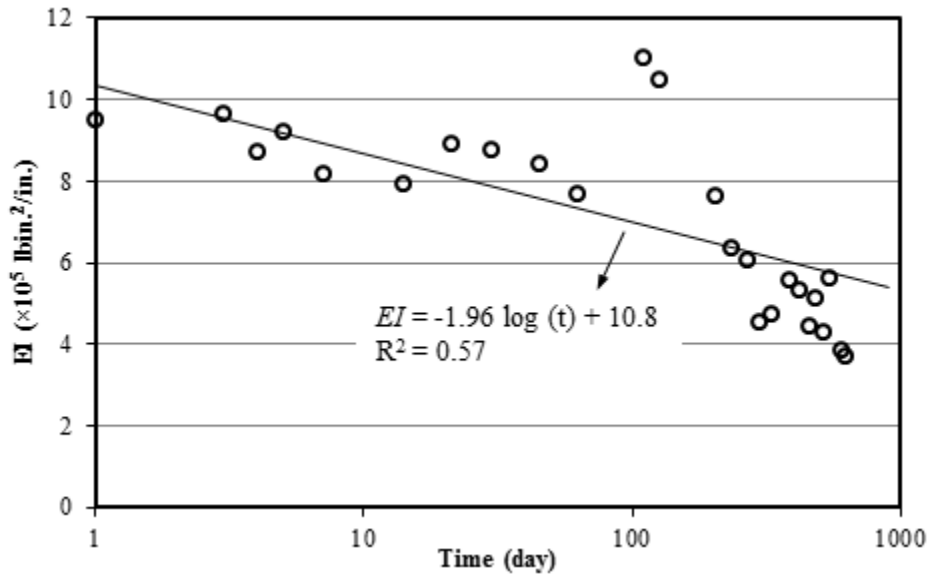
EI = pipe stiffness factor ($\times 10^5$ lb·in.²/in.)

t = the time after the pipe installation (days)

Based on Equations 5.5a and 5.5b, the pipe stiffness factors at 1 day, 50 years, and 100 years in the AB3 aggregate section are 1.13×10^6 , 2.90×10^5 , and 2.33×10^5 lb·in.²/in, respectively, while they are 1.08×10^6 , 2.45×10^5 , and 1.86×10^5 lb·in.²/in. in the crushed stone section at the same time periods. The pipe stiffness factor in the AB3 aggregate section was higher than that in the crushed stone section due to the higher soil reaction modulus of the AB3 aggregate as compared with the crushed stone. The pipe stiffness factors at 100 years decreased by 79% and 83% from the initial values at 1 day in the AB3 aggregate section and the crushed stone section, respectively.



(a) Section A



(b) Section B

Figure 5.23: Variation of the Pipe Stiffness Factor with Time for Sections A and B

5.5 Conclusions

The pipes in the Lawrence field test were monitored for 680 days after the construction. The variations of the earth pressures around the pipes, the deflections of the pipes, and the strains of the pipes with time were analyzed in this chapter. Long-term empirical correlations were developed for the vertical soil arching factor (VAF) and the pipe stiffness factor (EI) based on the field data. The following conclusions can be made from the analysis:

1. The earth pressures generally increased at all locations in both sections. The VAFs were 1.72 and 2.18 after 680 days of construction in the AB3 aggregate section and the crushed stone section, respectively. The lateral earth pressure coefficients next to the pipes were 0.75 and 1.38 in the AB3 aggregate section and the crushed stone section, respectively.
2. The deflections of the pipe generally increased with time in the vertical and horizontal directions. The pipe diameter change was insignificant at 45° from the pipe crown in both sections. The maximum deflections were 0.6% and 0.8% the pipe diameter in the AB3 aggregate section and the crushed stone section, respectively.
3. The strains of the pipes mostly increased with time at all locations in both sections. The maximum strains occurred on the plastic valley in the longitudinal direction at the pipe crown, which were 0.30% and 0.35% in the AB3 aggregate section and the crushed stone section, respectively.
4. Long-term empirical correlations were proposed based on the field data for vertical soil arching factor (VAF) and the pipe stiffness factor (EI). The VAFs would increase to 1.7 and 2.21 in the AB3 aggregate section and the crushed stone section in 100 years, respectively. The pipe stiffness factors in 100 years would decrease by 79% and 83% from the initial value at 1 day in the AB3 aggregate section and the crushed stone section, respectively.

Chapter 6: Design Procedures for SRHDPE Pipes

6.1 Introduction

As mentioned in Chapter 1, no widely accepted design procedure is available for SRHDPE pipes even though they combine the advantages of metal pipes and HDPE pipes. Since SRHDPE pipes include steel ribs, they can carry more load than HDPE pipes. Based on the laboratory and field tests in this study, vertical arching factors (VAF) for SRHDPE pipes in granular backfill were greater than 1, which implies SRHDPE pipe cross sections behave like metal pipes due to steel ribs. However, the measured peak strains on the plastic valley in field tests were the maximum strains, which were higher than the strains of the plastic cover; therefore, the strain of the plastic valley controls the strain limit design of plastic components in SRHDPE pipes. In other words, design of SRHDPE pipes should consider analysis of steel ribs and plastic valley (liner). AASHTO (2012) has recommended design methods for both metal pipes and HDPE pipes. In this chapter, these two design methods are summarized and modified for design of SRHDPE pipes.

6.2 AASHTO Design Methods

A load and resistance factor design (LRFD) method is adopted for design of the buried structures in the AASHTO (2012) standard. The factored resistance is calculated by:

$$R_r = \phi R_n \quad \text{Equation 6.1}$$

Where:

R_r = the factored resistance

ϕ = the resistance factor

R_n = the nominal resistance

The resistance factor for minimum wall area and buckling of metal pipes is 1. The resistance factor for thrust and flexure of HDPE pipes is 1, while those for soil stiffness and global buckling are 0.9 and 0.7, respectively.

6.2.1 Strength Limit State

The following strength limit states should be analyzed for design of metal pipes and HDPE pipes:

Metal pipe:

- Wall area
- Buckling
- Beam failure
- Flexibility limit for construction
- Flexure of box and deep corrugated structures

HDPE pipe:

- Wall area (including local buckling)
- Buckling
- Flexibility limit

6.2.2 Flexibility Factor Limit

Table 6.1 provides the flexibility factor limits of metal pipes and HDPE pipes. The flexibility factor of metal pipes depends on corrugation sizes while that of HDPE pipes is constant.

Table 6.1: Flexibility Factor Limits

Pipe type	Condition	Corrugation size (in.)	Flexibility factor (in./kip)
Steel pipe	-	0.25	43
	-	0.5	43
	-	1.0	33
Spiral rib metal pipe	Embankment	0.75×0.75×7.5	$217I^{1/3}$
	Embankment	0.75×1.0×11.5	$140I^{1/3}$
	Trench	0.75×0.75×7.5	$263I^{1/3}$
	Trench	0.75×1.0×11.5	$163I^{1/3}$
HDPE pipe	-	-	95

Note: I is the moment of inertia of the pipe (in.⁴/in.).

6.2.3 Soil Envelop

For a trench condition, the minimum trench width should not be less than the greater of the pipe outside diameter plus 16 inches or 1.5 times pipe outside diameter plus 12 inches. For an embankment condition, the minimum width of the soil envelop on each side of a pipe should be not less than the following values:

1. $D/12$ ft (D is the outside pipe diameter) when $D < 24$ inches;
2. 2.0 ft when $24 \text{ inches} < D < 144$ inches;
3. 5.0 ft when $D > 144$ inches.

6.2.4 Soil Cover Thickness

The minimum soil cover thickness for spiral metal pipes is the greater of $D/4$ (D is the outside diameter of the pipe) or 12 inches, while that for corrugated metal pipes is the greater of $D/8$ or 12 inches. The minimum soil cover thickness of HDPE pipes is the greater of $D_i/8$ (D_i is the inside diameter of the pipe) or 12 inches under an unpaved condition, while that under a paved condition is the greater of $D_i/2$ or 24 inches.

6.2.5 Pipe Spacing

The following requirements should be met for clear spacing of multiple pipe lines, S :

1. $S = 1$ ft when $D < 2.0$ ft;
2. $S = D/2$ when $2.0 \text{ ft} < D < 6.0$ ft;
3. $S = 3$ ft when $D > 6.0$ ft

6.2.6 Metal Pipe Design

Metal pipe design requires five key parameters:

6.2.6.1 Thrust

The factored thrust can be calculated as follows:

$$T_L = p_F \left(\frac{D}{24} \right) \quad \text{Equation 6.2}$$

Where:

T_L = the factored thrust per unit length (kip/ft)

D = the pipe diameter (in.), which is equal to the pipe outside diameter if the pipe is round

p_F = the factored vertical crown pressure due to earth and live loads (ksf)

6.2.6.2 Wall Resistance

The factored axial resistance, without considering buckling, can be calculated as follows:

$$R_n = \phi F_y A \quad \text{Equation 6.3}$$

Where:

R_n = the factored axial resistance

F_y = the yield strength of metal (ksi)

A = the wall area (in.²/ft)

ϕ = the resistance factor as described in Section 6.2.1

6.2.6.3 Resistance to Buckling

If $D < \left(\frac{r}{k} \right) \sqrt{\frac{24E_m}{F_u}}$, the critical buckling stress is:

$$f_{cr} = F_u - \frac{\left(\frac{F_u k D}{r} \right)^2}{48E_m} \quad \text{Equation 6.4a}$$

If $D > \left(\frac{r}{k} \right) \sqrt{\frac{24E_m}{F_u}}$, the critical buckling stress is:

$$f_{cr} = \frac{12E_m}{\left(\frac{kD}{r}\right)^2}$$

Equation 6.4b

Where:

D = the outside diameter of the pipe (in.)

E_m = the modulus of elasticity of metal (ksi)

F_u = the tensile strength of metal (ksi)

f_{cr} = the critical buckling stress (ksi)

r = the radius of gyration of corrugation (in.)

k = the soil stiffness factor (taken as 0.22)

6.2.6.4 Seam Resistance

For pipes with longitudinal seams, the factored seam resistance should be greater than the factored thrust in the pipe wall, T_L , as presented in Equation 6.2.

6.2.6.5 Handling and Installation Requirements

Handling flexibility as indicated by a flexibility factor can be determined as follows:

$$FF = \frac{D^2}{E_m I}$$

Equation 6.5

Where:

FF = the flexibility factor

D = the pipe outside diameter or span

E_m = the modulus of elasticity of metal

I = the moment of inertia of the pipe wall in unit length

6.2.7 HDPE Pipe Design

6.2.7.1 Deflection

The total deflection Δ_t should be smaller than the allowable deflection Δ_A (typically $5\%D$). The total deflection can be calculated using Spangler's formula combined with the circumferential shortening as follows:

$$\Delta_t = \frac{K_B(D_L P_{sp} + C_L P_L)D_0}{1000\left(\frac{E_P I_P}{R^3} + 0.061M_s\right)} + \varepsilon_{sc} D \quad \text{Equation 6.6}$$

In which:

$$\varepsilon_{sc} = \frac{T_s}{1000(A_{eff} E_P)} \quad \text{Equation 6.7}$$

$$T_s = P_s \left(\frac{D_0}{2}\right) \quad \text{Equation 6.8}$$

Where:

ε_{sc} = the service compressive strain due to thrust

T_s = the service thrust per unit length (lb./in.)

D_L = the deflection lag factor (typically 1.5)

K_B = the bedding coefficient (typically 0.1)

P_{sp} = the soil prism load at the pipe springline (psi)

C_L = the live load distribution coefficient

P_L = the design live load pressure including vehicle, dynamic load allowance, and multiple presence effect (psi)

D_0 = the outside diameter of pipe (in.)

E_P = the short or long-term modulus of pipe material (ksi)

I_P = the moment of inertia of the pipe profile per unit length of the pipe (in.⁴/in.)

R = the radius from the center of the pipe to the centroid of the pipe profile (in.)

D = the diameter to the centroid of the pipe profile

M_s = the secant constraint soil modulus as shown in Table 6.2

P_s = the design service load

A_{eff} = the effective area of the pipe wall per unit length of the pipe

6.2.7.2 Factored and Service Loads

The factored load P_u can be calculated as follows:

$$P_u = \eta_{EV} (\gamma_{EV} K_{\gamma E} K_2 VAF P_{sp} + \gamma_{WA} P_w) + \eta_{LL} \gamma_{LL} P_L C_L \quad \text{Equation 6.9}$$

The service load P_s can be taken as:

$$P_s = K_2 VAF P_{sp} + P_L C_L + P_w \quad \text{Equation 6.10}$$

In which:

$$VAF = 0.76 - 0.71 \left(\frac{S_H - 1.17}{S_H + 2.92} \right) \quad \text{Equation 6.11}$$

$$S_H = \frac{\phi_s M_s R}{E_p A_g} \quad \text{Equation 6.12}$$

$$C_L = \frac{L_w}{D_0} \leq 1.0 \quad \text{Equation 6.13}$$

$$L_w = L_0 + 12LLDF(H) \quad \text{Equation 6.14}$$

Where:

$K_{\gamma E}$ = the installation factor (taken as 1.5)

K_2 = the coefficient to account for the variation of the thrust around the circumference (1.0 at the springline and 0.6 at the crown)

VAF = the vertical arching factor

S_H = the hoop stiffness factor

P_w = the hydrostatic water pressure at the pipe springline (psi)

C_L = the live load distribution width in the circumferential direction at the elevation of the crown

H = the soil cover thickness (ft)

η_{EV} = the load modifier (taken as 1.0)

γ_{EV} = the load factor for the vertical pressure from the dead load of the earth fill
(the maximum value is 1.3 and the minimum one is 0.9)

P_{sp} = the soil prism pressure

γ_{WA} = the load factor for hydraulic pressure

η_{LL} = the load modifier (taken as 1.0)

γ_{LL} = the load factor for live load (taken as 1.75)

P_L = the live load pressure with the dynamic load allowance (psi)

ϕ_S = the resistance factor for soil stiffness

M_s = the secant constraint modulus of soil as shown in Table 6.2

R = the radius from the center of the pipe to the centroid of the pipe profile (in.)

E_p = the short or long-term modulus of pipe material (ksi)

A_g = the gross area of pipe wall per unit length of pipe (in.²/in.)

D_0 = the outside diameter of the pipe (in.)

$LLDF$ = the factor for live load distribution through earth fills

Table 6.2: Secant Constraint Modulus M_s of Backfill Based on Soil Type and Compaction Condition (Unit: ksi)

	P_{sp} stress level (psi)	100 % compaction	95 % compaction	90 % compaction	85 % compaction
Sand and gravel	1.0	2.350	2.000	1.275	0.470
	5.0	3.450	2.600	1.500	0.250
	10.0	4.200	3.000	1.625	0.570
	20.0	5.500	3.450	1.800	0.650
	40.0	7.500	4.250	2.100	0.825
	60.0	9.300	5.000	2.500	1.000
Silt	1.0		1.415	0.670	0.360
	5.0		1.670	0.740	0.390
	10.0		1.770	0.750	0.400
	20.0		1.880	0.790	0.430
	40.0		2.090	0.900	0.510
	60.0				
Clay	1.0		0.530	0.255	0.130
	5.0		0.625	0.320	0.175
	10.0		0.690	0.355	0.200
	20.0		0.740	0.395	0.230
	40.0		0.815	0.460	0.285
	60.0		0.895	0.525	0.345

Source: AASHTO (2012)

6.2.7.3 Soil Prism Load

The soil prism load P_{sp} can be calculated as follows:

If the water table is above the top of the pipe and at or above the ground surface:

$$P_{sp} = \frac{\left(H + 0.11 \frac{D_0}{12} \right) \gamma_b}{144} \quad \text{Equation 6.15}$$

If the water table is above the top of the pipe and below the ground surface:

$$P_{sp} = \frac{\left[\left(H_w - \frac{D_0}{24} \right) + 0.11 \frac{D_0}{12} \right] \gamma_b + \left[H - \left(H_w - \frac{D_0}{24} \right) \right] \gamma_s}{144} \quad \text{Equation 6.16}$$

If the water table is below the top of the pipe:

$$P_{sp} = \frac{\left(H + 0.11 \frac{D_0}{12} \right) \gamma_s}{144} \quad \text{Equation 6.17}$$

Where:

γ_s = the moist unit weight of the soil (pcf)

γ_b = the unit weight of the buoyant soil (pcf)

H_w = the depth of water table above the pipe springline (ft)

Definitions of other parameters are the same as those defined previously.

6.2.7.4 Hydrostatic Pressure

The pressure caused by the ground water can be calculated as follows:

$$P_w = \frac{H_w \gamma_w K_{wa}}{144} \quad \text{Equation 6.18}$$

Where:

P_w = the hydrostatic pressure

γ_w = the unit weight of water

K_{wa} = the factor for uncertainty in the level of the groundwater table (typically 1.0-1.3)

6.2.7.5 Live Load

The live load pressure can be calculated as follows:

$$P_L = \frac{P(1 + IM / 100)m}{\left[L_0 + (12H + K_1)LLDF \right] \left[W_0 + (12H + K_1)LLDF \right]} \quad \text{Equation 6.19}$$

Where:

P_L = the live load pressure on the pipe (psi)

P = the design wheel load (lbs)

IM = the dynamic load allowance (taken as 33%)

m = the multiple presence factor (1.2 for one lane road, 1.0 for two lanes road, 0.85 for three lanes road, and 0.65 for the road with the lane number greater than three)

L_0 = the length of the live load surface contact area parallel to the pipe diameter (for the AASHTO-H25 truck, use 10 in.)

$LLDF$ = the factor for the distribution of the live load through earth fills (typically 1.15)

W_0 = the width of the live load ground surface contact area parallel to the flow in the pipe (for the AASHTO-H25 truck, use 20 in.)

K_1 = the coefficient to consider the design location (0 for the pipe crown and $D_0/2$ for the springline)

H = the soil cover thickness (ft)

6.2.7.6 Effective Area

To determine buckling resistance, the profile wall pipe should be idealized as straight elements as shown in Figure 6.1.

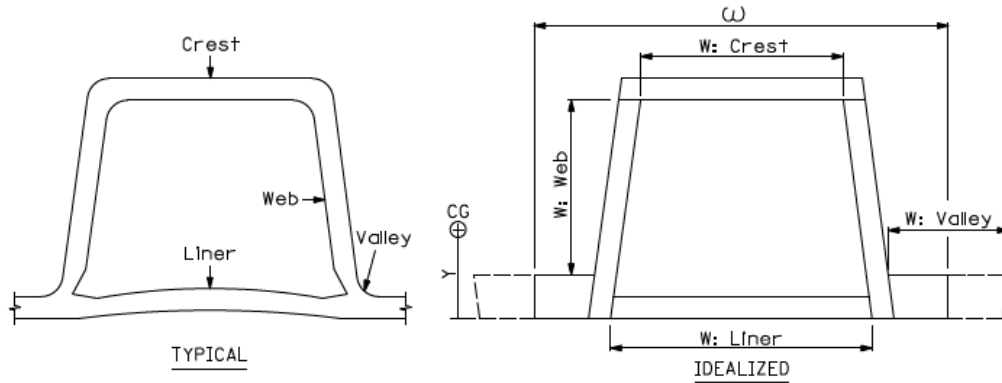


Figure 6.1: Typical and Idealized Cross Sections of a Profile Wall Pipe

Source: AASHTO (2012)

$$A_{eff} = A_g - \frac{\sum (w - b_e) t}{\omega} \quad \text{Equation 6.20}$$

In which:

$$b_e = \rho w \quad \text{Equation 6.21}$$

$$\rho = \frac{\left(1 - \frac{0.22}{\lambda}\right)}{\lambda} \quad \text{Equation 6.22}$$

$$\lambda = \left(\frac{w}{t}\right) \sqrt{\frac{\varepsilon_{yc}}{k}} \geq 0.673 \quad \text{Equation 6.23}$$

Where:

A_{eff} = the effective area of pipe wall per unit length of the pipe (in.²/in.)

b_e = the element effective width (in.)

ρ = the effective width factor

λ = the slenderness factor

ω = the spacing of corrugations (in.)

ε_{yc} = the factored compressive strain limit

A_g = the gross area of pipe wall per unit length of the pipe (in.²/in.)

t = the thickness of the element

w = the total clear width of the element between supporting elements (in.)

k = the plate buckling coefficient (taken as 4)

The effective area can also be determined using a stub compression test as follows:

$$A_{eff} = \frac{P_{st} K_t}{F_u} \leq A_g \quad \text{Equation 6.24}$$

Where:

P_{st} = the stub compression capacity (kip/in.)

K_t = the time factor (0.9 for initial, 0.3 for 50 years, and 0.25 for 75 years)

F_u = the material yield strength (ksi)

6.2.7.7 Compressive Strain

The factored compression strain due to the factored thrust and the service compression strain due to the service thrust are:

$$\varepsilon_{uc} = \frac{T_u}{1000 A_{eff} E_p} \quad \text{Equation 6.25}$$

$$\varepsilon_{sc} = \frac{T_s}{1000 A_{eff} E_p} \quad \text{Equation 6.26}$$

In which:

$$T_u = P_u \left(\frac{D_0}{2} \right) \quad \text{Equation 6.27}$$

Where:

ε_{uc} = the factored compressive strain due to the thrust

ε_{sc} = the service compressive strain due to the thrust

T_u = the factored thrust per unit length

T_s = the service thrust per unit length

6.2.7.8 Strain Limits

The factored compression strain due to the thrust should satisfy:

$$\varepsilon_{uc} \leq \phi_T \varepsilon_{yc} \quad \text{Equation 6.28}$$

Where:

ϕ_T = the resistance factor for thrust effects (taken as 1.0)

ε_{yc} = the factored compression strain limit (taken as 5%)

$$\varepsilon_{uc} \leq \phi_{bck} \varepsilon_{bck} \quad \text{Equation 6.29}$$

$$\varepsilon_{bck} = \frac{1.2C_n (E_p I_p)^{\frac{1}{3}}}{A_{eff} E_p} \left[\frac{\phi_s M_s (1-2\nu)}{(1-\nu)^2} \right]^{\frac{2}{3}} R_h \quad \text{Equation 6.30}$$

$$R_h = \frac{11.4}{11 + \frac{D}{12H}} \quad \text{Equation 6.31}$$

Where:

ϕ_{bck} = the resistance factor for global buckling (taken as 1.0)

ε_{bck} = the nominal strain capacity for general buckling

R_h = the correction factor for backfill soil geometry

C_n = the calibration factor to account for nonlinear effects

ϕ_s = the resistance factor for soil (taken as 0.9)

ν = Poisson's ratio of soil

D = the diameter to the centroid of the pipe profile (in.)

H = the depth of fill over the pipe top (ft)

6.2.7.9 Combined Strain Limit

The combination of the bending strain and the axial strain should satisfy:

$$\varepsilon_f - \varepsilon_{uc} < \phi_f \varepsilon_{yt} \quad (\text{tensile strain}) \quad \text{Equation 6.32}$$

$$\varepsilon_f + \varepsilon_{uc} < \phi_T 1.5 \varepsilon_{yc} \quad (\text{compressive strain}) \quad \text{Equation 6.33}$$

Where:

ε_f = the factored strain due to flexure

ε_{yt} = the service long-term tensile strain limit (taken as 4.1%)

ϕ_f = the resistance factor for flexure (taken as 1.0)

ϕ_T = the resistance factor for thrust (taken as 1.0)

$$\varepsilon_f = \gamma_{EV} D_f \left(\frac{c}{R} \right) \left(\frac{\Delta_f}{D} \right) \quad \text{Equation 6.34}$$

$$\Delta_f = \Delta_A - \varepsilon_{sc} D \quad \text{Equation 6.35}$$

Where:

Δ_f = the reduction of the vertical diameter due to flexure

D_f = the shape factor as shown in Table 6.3

c = the larger of the distance from the neutral axis of the profile to the extreme innermost or outermost fiber

R = the radius from the center of the pipe to the centroid of the pipe profile

D = the diameter to the centroid of the pipe profile

6.2.7.10 Handling and Installation Requirements

The flexibility factor can be taken as:

$$FF = \frac{D^2}{EI} \quad \text{Equation 6.36}$$

Where:

I = the moment of inertia

E = the initial modulus of elasticity of the pipe

D = the diameter of the pipe

Table 6.3: Shape Factors Based on Pipe Stiffness, Backfill, and Compaction Level

Pipe stiffness (ksi)	Backfill material and compaction level			
	Gravel		Sand	
	$D_r < 40\%$	$D_r > 40\%$	$D_r < 40\%$	$D_r > 40\%$
0.009	5.4	7.0	6.0	8.0
0.018	4.5	5.5	5.0	6.5
0.036	3.8	4.5	4.0	5.5
0.072	3.3	3.8	3.5	4.5

Note: D_r is the relative density of the backfill material.
Source: AASHTO (2012)

6.3 SRHDPE Pipe Design Considerations

Based on the field tests, the following considerations are suggested for design of an SRHDPE pipe in accordance with the AASHTO design methods for a metal pipe and an HDPE pipe:

1. Load: The load calculation is the basis of the SRHDPE pipe design to determine the strain and the pipe deflection, which are essential to evaluate the pipe responses. A VAF corresponding to an SRHDPE pipe should be used instead of that for an HDPE pipe in Equation 6.9. Based on the field test in this study, the short-term VAF for the SRHDPE pipe was 1.1 and the long-term VAF can be estimated by Equation 5.3.
2. Deflection: The laboratory and field tests showed that the SRHDPE pipe in granular backfill had a VAF greater than 1. This result implies that the pressure on the SRHDPE pipe is higher than the soil prism pressure. For the HDPE pipe design, the load on the pipe is treated as the soil prism load for conservation purposes. However, it will not be conservative if the soil prism load is still used for the SRHDPE pipe. Therefore, a VAF should be used to modify the soil prism load. Furthermore, the term $\varepsilon_{sc}D$ in Equation 6.6 is used to consider the circumferential shortening, which is only important for a very flexible pipe. For an SRHDPE pipe, this term can be dropped. The field monitoring showed the pipe stiffness factor $E_p I_p$ decreased with time. Therefore, when an SRHDPE pipe is used for long-

term applications, the initial pipe stiffness factor should be reduced by a percentage depending on the service time. For a 50-year service life, the pipe stiffness factor may be reduced by 73.6%, while for a 100-year service life, it may be reduced by 78.8%. As a result, the SRHDPE pipe deflection can be calculated as follows:

$$\Delta_t = \frac{K_B(D_L VAFP_{sp} + C_L P_L)D_0}{1000 \left(\frac{E_P I_P}{R^3} + 0.061 M_s \right)} \quad \text{Equation 6.37}$$

3. Strain: Based on the field test results, the strains of the plastic valley were much larger than those of the plastic cover. An SRHDPE pipe should be treated as an HDPE pipe first for the plastic strain limit check (i.e., Equations 6.28, 6.29, 6.32, and 6.33). The strain limits for plastic should be 5% for the compressive strain and 4.1% for the tensile strain. However, buckling of steel ribs also needs to be checked using Equation 6.4 to ensure the buckling stress of the steel rib is lower than the yield strength of steel. Nonlinear behavior of the pipe was not observed under the service loading; therefore, the calibration factor to account for nonlinear effects can be taken as 1.0 in Equation 6.30.
4. Flexibility Factor: The elastic modulus of pipe material is needed for the flexibility factor calculation for both metal and HDPE pipes (i.e., Equations 6.5 and 6.36). For an SRHDPE pipe flexibility factor calculation, the equivalent elastic modulus of the pipe should be used, which is based on the area weighted average of the moduli of steel and plastic.
5. Soil Envelop Width: The SRHDPE pipe is classified as a flexible pipe. Therefore, the soil envelop width for the metal pipe and the HDPE pipe presented in Section 6.2.4 should also be followed to determine the minimum soil envelop width for the SRHDPE pipe.

6. Soil Cover Thickness: The minimum soil cover thickness should be calculated based on the requirements for both steel and HDPE pipes in Section 6.2.5. The greater of the minimum soil cover thicknesses for both pipes should be used as the minimum soil cover thickness for the SRHDPE pipe.

6.4 Proposed SRHDPE Pipe Design Procedure

Based on the design considerations, the following design procedure is proposed for SRHDPE pipes:

1. Determine the soil envelop width based on Section 6.2.4;
2. Calculate the soil cover thickness in accordance with Section 6.2.5. The designer should calculate the minimum soil cover thicknesses for both the metal pipe and the HDPE pipe and then select the greater value as the minimum soil cover thickness for the SRHDPE pipe;
3. Calculate the external load using Equations from 6.15 to 6.19;
4. Calculate the total deflection of the SRHDPE pipe based on Equation 6.37 and ensure the total deflection is smaller than 5% pipe diameter;
5. Calculate the factored load based on Equation 6.9 using a VAF (typically 1.1) for a short-term condition and Equation 5.3 for a long-term condition;
6. Use Equations 6.28, 6.29, 6.32, and 6.33 to calculate plastic strains and check them against the strain limits;
7. Use Equations 6.2 to 6.4 to calculate pipe buckling, wall, and thrust resistance;
8. Use Equation 6.5 to check the flexibility of the pipe using the equivalent pipe modulus.

6.5 SRHDPE Pipe Design Example

6.5.1 Design Problem

An SRHDPE pipe with a nominal diameter of 36 inches is proposed as a culvert under a two-lane highway with a pavement. The outside diameter of the pipe is 37.25 inches, while the inside diameter is 35.35 inches. For the convenience of readers, the pipe cross section in Figure 4.9 was repeated here as Figure 6.2. The pipe stiffness is 33.4 psi, and the yield strength of the steel ribs of the SRHDPE pipe F_y is 33 ksi, while the tensile strength F_u is 45 ksi. The elastic modulus of the steel ribs E_m is 29,000 ksi. The stub compression capacity of the pipe is 40 kip/in., and the equivalent elastic modulus of the pipe of a 50-year service is 950 ksi. AASHTO H-25 loads are anticipated. Groundwater is below the pipe invert. Backfill material is crushed stone. The density of the crushed stone is 110 pcf and its minimum relative compaction is 95% based on the standard Proctor test maximum density. The design service life is 50 years. Design an SRHDPE pipe for this application.

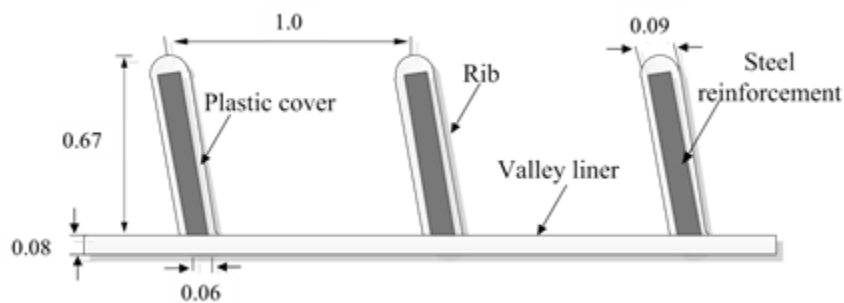


Figure 6.2: Schematic of Cross-Section of the Corrugated SRHDPE Pipe (Unit: Inches, Not to Scale)

6.5.2 Solution

Step 1: Soil Envelop Width Determination

The design pipe will be buried in an embankment condition and the pipe diameter is 36 inches. Based on the terms in Section 6.2.4, the minimum width of soil envelop on each side of the pipe should be 2 ft. Therefore, the total width of the soil envelop is:

$$B = 2 \times 12 \times 2 + 36 = 84 \text{ in.}$$

Equation 6.38

Step 2: Soil Cover Thickness Determination

For a metal pipe, the soil cover thickness should be the greater of $D/4$ or 12 inches, while for an HDPE pipe, the soil cover thickness is the greater of $D_i/8$ or 24 inches considering the paved condition in this design problem.

$D/4 = 9$ inches, take 12 inches for the metal pipe.

$D_i/8 = 35.35/8 = 4.4$ inches, take 24 inches for the HDPE pipe.

Therefore, the soil cover thickness should be 24 inches.

Step 3: External Load Calculation

Soil Prism Pressure. Since the water table is below the pipe top, using Equation 6.17:

$$P_{sp} = \frac{\left(H + 0.11 \frac{D_0}{12}\right) \gamma_s}{144} = \frac{\left(\frac{24}{12} + 0.11 \times \frac{36}{12}\right) \times 110}{144} = 1.8 \text{ psi} \quad \text{Equation 6.39}$$

Soil cover thickness $H = 24$ inches, the pipe diameter $D_0 = 36$ inches, and the unit weight of the backfill material $\gamma_s = 110$ pcf.

Hydrostatic Pressure. The water table is below the bottom of the pipe, therefore, the hydrostatic pressure in the pipe zone is zero.

Live Load. Equation 6.19 is used to estimate the live load:

$$P_L = \frac{P(1 + IM / 100)m}{\left[L_0 + (12H + K_1)LLDF\right]\left[W_0 + (12H + K_1)LLDF\right]} = \frac{16000 \times (1 + 0.33) \times 1.0}{(10 + 12 \times 2 \times 1.15) \times (20 + 12 \times 2 \times 1.15)} = 11.9 \text{ psi} \quad \text{Equation 6.40}$$

AASHTO-H25 truck, $P = 16$ kip, $IM = 33\%$, $m = 1.0$ (two-lane highway), $L_0 = 10$ inches, $W_0 = 20$ inches, $H = 2$ ft, $K_1 = 0$ for pipe crown, and $LLDF = 1.15$.

Step 4: Deflection Calculation

Since VAF increases with time and pipe stiffness decreases with time, the deflection at 50 years controls the design. Based on Equations 5.3 and 5.5, the VAF and EI for a 50-year service life are 2.17 and 2.45×10^5 lb·in.²/in, respectively. Equation 6.37 is used to calculate the total deflection of the pipe cross section at 50 years:

$$\Delta_t = \frac{K_B(D_L VAF P_{sp} + C_L P_L) D_0}{1000 \left(\frac{E_P I_P}{R^3} + 0.061 M_s \right)} = \frac{0.1 \times (1.5 \times 2.17 \times 1.8 + 1 \times 11.9) \times 37.25}{1000 \times \left(0.149 \times \frac{33.4}{1000} + 0.061 \times 2 \right)}$$

$$= 0.52 \text{ in.} < 5\% \times 36 = 1.8 \text{ in.} \quad \text{Ok}$$

Equation 6.41**Step 5: Factored Load Calculation (using Equation 6.37)**

Based on Equation 6.2, the VAF for a 50-year service life of the SRHDPE pipe buried in the crushed stone is 2.17. Equation 6.37 is used to calculate the factored load:

$$P_u = \eta_{EV} (\gamma_{EV} K_{\gamma E} K_2 VAF P_{sp} + \gamma_{WA} P_w) + \eta_{LL} \gamma_{LL} P_L C_L$$

$$= 1.0 \times (1.1 \times 1.5 \times 0.6 \times 2.17 \times 1.8) + 1.0 \times 1.75 \times 11.9 \times 1.0 = 24.7 \text{ psi}$$

Equation 6.42**Step 6: Strain Limit Check**

Effective area (Equation 6.24):

$$A_{eff} = \frac{P_{st} K_t}{F_u} = \frac{40 \times 0.3}{45} = 0.27 \text{ in}^2 < A_g = 0.16 \text{ in}^2$$

Equation 6.43

$K_t = 0.3$ for a 50-year service life

Taking $A_{eff} = 0.16 \text{ in}^2$

$$T_u = P_u \left(\frac{D_0}{2} \right) = 26.0 \times \frac{36}{2} = 468 \text{ lb / in.}$$

Equation 6.44

$$\varepsilon_{uc} = \frac{T_u}{1000A_{eff}E_p} = \frac{468}{1000 \times 0.16 \times 950} = 0.31\% \quad \text{Equation 6.45}$$

Compressive strain limit check:

$$\varepsilon_{uc} = 0.31\% \leq \phi_T \varepsilon_{yc} = 1.0 \times 5\% = 5\% \quad \text{OK.} \quad \text{Equation 6.46}$$

Buckling strain check:

$$R_h = \frac{11.4}{11 + \frac{D}{12H}} = \frac{11.4}{11 + \frac{36}{12 \times 2}} = 0.91 \quad \text{Equation 6.47}$$

$$\begin{aligned} \varepsilon_{bck} &= \frac{1.2C_n (E_p I_p)^{\frac{1}{3}}}{A_{eff} E_p} \left[\frac{\phi_s M_s (1-2\nu)}{(1-\nu)^2} \right]^{\frac{2}{3}} R_h \\ &= \frac{1.2 \times 1.0 \times (546)^{\frac{1}{3}}}{0.16 \times 950} \times \left[\frac{0.9 \times 2 \times (1-2 \times 0.3)}{(1-0.3)^2} \right]^{\frac{2}{3}} \times 0.91 = 7.5\% \end{aligned} \quad \text{Equation 6.48}$$

$$\varepsilon_{uc} = 0.31\% \leq \phi_{bck} \varepsilon_{bck} = 1.0 \times 7.5\% = 7.5\% \quad \text{Equation 6.49}$$

Combined strain limit check:

Since $\varepsilon_{sc} D = 0$ for the SRHDPE pipe,

$$\Delta_f = \Delta_A - \varepsilon_{sc} D = 0.59 \text{ in.} \quad \text{Equation 6.50}$$

Where:

c is half of the pipe thickness which is equal to $(37.25 - 35.35) / 2 = 0.95$ in.

Based on Table 6.3 and the pipe stiffness

$$D_f = 4.5$$

$$\varepsilon_f = \gamma_{EV} D_f \left(\frac{c}{R} \right) \left(\frac{\Delta_f}{D} \right) = 1.1 \times 4.5 \times \left(\frac{0.95}{18} \right) \times \left(\frac{0.59}{36} \right) = 0.43\% \quad \text{Equation 6.51}$$

$$\varepsilon_f - \varepsilon_{uc} = 0.12\% < \phi_f \varepsilon_{yt} = 1.0 \times 4.1\% = 4.1\% \quad (\text{Tensile strain}) \quad \text{OK.}$$

Equation 6.52

$$\varepsilon_f + \varepsilon_{uc} = 0.43\% + 0.31\% = 0.74\% < \phi_T 1.5 \varepsilon_{yc} = 1.0 \times 1.5 \times 5\% = 7.5\% \\ (\text{Compressive strain}) \quad \text{OK.}$$

Equation 6.53

Step 7: Metal Pipe Calculation

$$T_L = p_F \left(\frac{D}{24} \right) = 3.74 \times 1.5 = 5.61 \text{ kip / ft}$$

Equation 6.54

$$R_n = \phi F_y A = 1.0 \times 33 \times 0.48 = 15.8 \text{ ksi}$$

Equation 6.55

Based on Figure 6.2, the corrugation radius $r = 0.67$ inches. $k = 0.22$ as suggested in Equation 6.4. $E_m = 29,000$ ksi and $F_u = 45$ ksi.

$$D = 36 \text{ in.} < \left(\frac{r}{k} \right) \sqrt{\frac{24 E_m}{F_u}} = \left(\frac{0.67}{0.22} \right) \times \sqrt{\frac{24 \times 2.9 \times 10^4}{45}} = 378.7 \text{ in.}$$

Then the critical buckling stress is:

$$f_{cr} = F_u - \frac{\left(\frac{F_u k D}{r} \right)^2}{48 E_m} = 45 - \frac{\left(\frac{45 \times 0.22 \times 36}{0.67} \right)^2}{48 \times 2.9 \times 10^4} = 44.8 \text{ ksi}$$

Equation 6.56

Step 8: Flexibility Calculation

The flexibility factor limit for a metal pipe is 33 in./kip while that for an HDPE pipe is 95 in./kip (as shown in Table 6.1). Then the equivalent flexibility should be:

$$FF_r = \frac{A_{st} \times 33 + A_{pl} \times 95}{A_t} = \frac{0.04 \times 33 + 0.12 \times 95}{0.16} = 79.5 \text{ in. / kip} \quad \text{Equation 6.57}$$

Where:

FF_r = the required flexibility

A_{st} = the area of the steel ribs

A_{pl} = the area of the HDPE

A_t = the total area.

$$FF = \frac{D^2}{E_m I} = \frac{36^2}{0.149 \times 18^3 \times 33.4} \times 1000 = 44.7 \text{ in / kip} < 79.5 \text{ in / kip} \quad \text{OK.}$$

Equation 6.58

Chapter 7: Conclusions and Recommendations

7.1 Conclusions

This research has two phases. The first phase (i.e., Phase I), which is reported in Khatri, Han, Corey, et al. (2013), focused on laboratory tests of pipe material and steel-reinforced HDPE (SRHDPE) pipes buried in a test box at the University of Kansas. The second phase (i.e., Phase II, also this study) focused on two field tests conducted to investigate the SRHDPE pipe performance in the AB3 aggregate and the crushed stone during installation and static loading. Pipes in the first field test were monitored for 680 days after the field installation. Pipes in the second field test were exhumed to examine possible damage. Field measurements include earth pressures around pipes, pipe deflections, and strains at the plastic valley, the plastic cover, and the steel ribs. Field test data were reduced and analyzed. The following conclusions can be made based on this study:

1. The vertical arching factor (VAF) in both field tests during the installation was approximately 1.1, which indicated the SRHDPE pipe behaving like a metal pipe. The lateral earth pressure coefficient of the SRHDPE in the AB3 aggregate or the crushed stone was approximately 0.65. Peaking deflections were observed during pipe installation in both tests in a range of 0.25% to 1.80% pipe diameter. The maximum strain of the pipe occurred on the plastic valley in the longitudinal direction at the pipe crown, but it was much smaller than the strain limit of 5% suggested by AASHTO (2012).
2. The vertical pressure on the SRHDPE pipe induced by static loading on unpaved roads (i.e., during construction) can be calculated by the Giroud and Han (2004) method and the AASHTO (2012) method. When the base course had higher stiffness than the backfill above the pipe, the Giroud and Han method more accurately estimated the vertical pressure than the AASHTO method. The deflection of the SRHDPE pipe during the installation and the loading can both be calculated based on the Iowa Formula.

3. The earth pressures around the pipes generally increased with time at all locations in both field sections. The VAFs were 1.72 and 2.18 in the AB3 aggregate and the crushed stone, respectively, after 680 days of construction.
4. The vertical and horizontal deflections of the pipes generally increased with time and the maximum deflections were 0.6% and 0.8% pipe diameter in the AB3 aggregate and the crushed stone, respectively.
5. The measured strains generally increased with time at most locations in both field sections. The maximum strains which occurred on the plastic valley in the longitudinal direction at the pipe crown were 0.3% and 0.35% in the AB3 aggregate and the crushed stone, respectively, up to 680 days after pipe installation. The maximum strains of the steel ribs in both sections were lower than the strain corresponding to the steel yield strength.
6. Long-term empirical correlations were developed for the vertical soil arching factor (VAF) and the pipe stiffness factor (EI) with time based on the field data.
7. No obvious damage was observed after the installation of SRHDPE pipes in the field.
8. The SRHDPE pipe behaved like a metal pipe in the cross section direction but like an HDPE pipe in the longitudinal direction.

7.2 Recommendations

Based on the analysis of the field data in Phase II, in addition to the laboratory results in Phase I, a design procedure was proposed to modify the current AASHTO design methods by considering the behavior of SRHDPE pipes. A design example was presented to illustrate how the proposed design procedure can be used for design.

The authors would like to make the following recommendations based on this research:

1. SRHDPE pipes have apparent advantages of higher corrosion resistance than metal pipes and stiffer cross sectional response than HDPE pipes. Laboratory and field tests in this research demonstrated that SRHDPE pipes

performed well; therefore, they can be used to replace metal pipes and HDPE pipes for certain applications.

2. SRHDPE pipes can be designed using the methods for metal and HDPE pipes with some special considerations of the unique features of SRHDPE pipes.
3. This research was based on SRHDPE pipes with diameters of 2 and 3 ft. Pipe size may affect the behavior and performance of SRHDPE pipes. Further research is needed to verify the results and conclusions from this research for other pipe sizes.
4. This research adopted poorly-graded sand and crushed stone in the laboratory study and well-graded aggregate and crushed stone in the field study. All these materials are granular materials with no or low cohesion. Use of any backfill with cohesion that will change the behavior and performance of SRHDPE pipes deserves further research.
5. All pipes investigated in this research were installed above the groundwater table. Possible effects of groundwater on the behavior and performance of SRHDPE pipes were not investigated in this research and deserve further research.
6. The time effect on the behavior and performance of SRHDPE pipes was investigated in the field up to 680 days. Long-term behavior of the pipes should be verified with a longer time period.
7. SRHDPE pipes are made of a composite material (steel ribs and plastic), which has anisotropic behavior. However, the current design methods were developed based on isotropic pipe materials. A design method considering anisotropic pipe materials should be developed to better design SRHDPE pipes.

References

- American Association of State Highway and Transportation Officials (AASHTO). (1998). *AASHTO LRFD bridge construction specifications* (1st ed.). Washington, DC: Author.
- American Association of State Highway and Transportation Officials (AASHTO). (2010). *AASHTO LRFD bridge construction specifications* (3rd ed.). Washington, DC: Author.
- American Association of State Highway and Transportation Officials (AASHTO). (2012). *AASHTO LRFD bridge design specifications* (6th ed.). Washington, DC: Author.
- American Association of State Highway and Transportation Officials (AASHTO) M145. (2003). *Standard specification for classification of soils and soil-aggregate mixtures for highway construction purposes*. Washington, DC: AASHTO.
- American Concrete Pipe Association (ACPA). (2009). *Steel reinforced high density polyethylene pipe: An educational document from the American Concrete Pipe Association for users and specifiers*. Retrieved from <http://www.concretepipe.org/wp-content/uploads/2015/05/epipe003.pdf>
- Antaki, G.A. (1997). A review of methods for the analysis of buried pressure piping. *Welding Research Council Bulletin*, 425. New York, NY: Welding Research Council.
- Arockiasamy, M., Chaallal, O., & Limpeteprakarn, T. (2006). Full-scale field tests on flexible pipes under live load application. *Journal of performance of constructed facilities*, 20(1), 21-27.
- ASTM A798 / A798M-13. (2013). *Standard practice for installing factory-made corrugated steel pipe for sewers and other applications*. West Conshohocken, PA: ASTM International. DOI: 10.1520/A0798_A0798M, www.astm.org
- ASTM C1479-13. (2013). *Standard practice for installation of precast concrete sewer, storm drain, and culvert pipe using standard installations*. West Conshohocken, PA: ASTM International. DOI: 10.1520/C1479-13, www.astm.org
- ASTM D698-12. (2012). *Standard test methods for laboratory compaction characteristics of soil using standard effort*. West Conshohocken, PA: ASTM International. DOI: 10.1520/D0698-12, www.astm.org

- ASTM D1556-07. (2007). *Standard test method for density and unit weight of soil in place by the sand-cone method*. West Conshohocken, PA: ASTM International. DOI: 10.1520/D1556-07, www.astm.org
- ASTM D1557-12. (2012). *Standard test methods for laboratory compaction characteristics of soil using modified effort*. West Conshohocken, PA: ASTM International. DOI: 10.1520/D1557-12, www.astm.org
- ASTM D2321-14. (2014). *Standard practice for underground installation of thermoplastic pipe for sewers and other gravity-flow applications*. West Conshohocken, PA: ASTM International. DOI: 10.1520/D2321-14, www.astm.org
- ASTM D2412-11. (2011). *Standard test method for determination of external loading characteristics of plastic pipe by parallel-plate loading*. West Conshohocken, PA: ASTM International. DOI: 10.1520/D2412-11, www.astm.org
- ASTM D2487-11. (2011). *Standard practice for classification of soils for engineering purposes (Unified Soil Classification System)*. West Conshohocken, PA: ASTM International. DOI: 10.1520/D2487-11, www.astm.org
- ASTM D3080 / D3080M-11. (2011). *Standard test method for direct shear test of soils under consolidated drained conditions*. West Conshohocken, PA: ASTM International. DOI: 10.1520/D3080_D3080M-11, www.astm.org
- ASTM D4253-14. (2014). *Standard test methods for maximum index density and unit weight of soils using a vibratory table*. West Conshohocken, PA: ASTM International. DOI: 10.1520/D4253-14, www.astm.org
- ASTM D4254-14. (2014). *Standard test methods for minimum index density and unit weight of soils and calculation of relative density*. West Conshohocken, PA: ASTM International. DOI: 10.1520/D4254-14, www.astm.org
- ASTM D6951-03. (2003). *Standard test method for use of the dynamic cone penetrometer in shallow pavement applications*. West Conshohocken, PA: ASTM International. DOI: 10.1520/D6951-03, www.astm.org

- ASTM F2562 / F2562M-08. (2008). *Specification for steel reinforced thermoplastic ribbed pipe and fittings for non-pressure drainage and sewerage*. West Conshohocken, PA: ASTM International. DOI: 10.1520/F2562_F2562M-08, www.astm.org
- Brachman, R.W.I., Moore, I.D., & Munro, S.M. (2008). Compaction effects on strains within profiled thermoplastic pipes. *Geosynthetics International*, 15(2), 72-85.
- Cameron, D.A. (2006). *Analysis of buried pipes in granular backfill subjected to construction traffic* (Doctoral dissertation). The University of Sydney, Sydney, Australia.
- Centers for Disease Control and Prevention. (2013). *Fluoridation of drinking water and corrosion of pipes in distribution systems fact sheet*. Retrieved from <http://www.cdc.gov/fluoridation/factsheets/engineering/corrosion.htm>
- Chen, T.J., & Fang, Y.S. (2008). Earth pressure due to vibratory compaction. *Journal of Geotechnical and Geoenvironmental Engineering*, 134(4), 437-444.
- China Association for Engineering Construction Standardization (CECS). (2004). Technical specification for buried PE pipeline of sewer engineering. *China Architecture and Building Specifications*. Beijing, China: Author.
- Corey, R., Han, J., Khatri, D.K., & Parsons, R.L. (2014). Laboratory study on geosynthetic protection of buried steel-reinforced HDPE pipes from static loading. *Journal of Geotechnical and Geoenvironmental Engineering*, 140(6), 1-10.
- Duncan, J.M., & Seed, R.B. (1986). Compaction-induced earth pressures under K0-conditions. *Journal of Geotechnical Engineering*, 112(1), 1-22.
- Duncan, J.M., Williams, G.W., Sehn, A.L., & Seed, R.B. (1991). Estimation earth pressures due to compaction. *Journal of Geotechnical Engineering*, 117(12), 1833-1847.
- Elshimi, T.M., & Moore, I.D. (2013). Modeling the effects of backfilling and soil compaction beside shallow buried pipes. *Journal of Pipeline Systems Engineering and Practice*, 4(4), 1-7.
- Filz, G.M., & Duncan, J.M. (1996). Earth pressures due to compaction: Comparison of theory with laboratory and field behavior. *Transportation Research Record*, 1526, 28-37.

- Folkman, S.L., & Rowley, S. (2013). *Monitoring of DuroMaxx pipes installed on Manhead Road in Rich County, Utah* (Report No. UT-13.14). Salt Lake City, UT: Utah Department of Transportation.
- Foster, C.R., & Ahlvin, R.G. (1954). Stresses and deflections induced by a uniform circular load. *Highway Research Board Proceedings*, 33, 467-470.
- Geoken, Inc. (2011). *Instruction Manual: Models 4800, 4810, 4815, 4820 and 4830 VW Earth Pressure Cells*. Retrieved from http://www.geokon.com/content/manuals/4800_Earth_Pressure_Cells.pdf
- Giroud, J.P., & Han, J. (2004). Design method for geogrid-reinforced unpaved roads. I. Development of design method. *Journal of Geotechnical and Geoenvironmental Engineering*, 130(8), 775–786.
- Google. (n.d.). Google Earth. Retrieved from <http://www.google.com/earth/>
- Hall, W.J., & Newmark, N.M. (1977). Seismic design criteria for pipelines and facilities. In *The current state of knowledge of lifeline earthquake engineering* (pp. 18-34). New York, NY: American Society of Civil Engineers.
- Hardert, M.T. (2011). *Shape measurement of existing 120" diameter*. Contech Construction Products, Inc.
- Höeg, K. (1968). Stresses against underground structural cylinders. *Journal of Soil Mechanics and Foundations Division*, 94(4), 833-858.
- Howard, A. (1996). *Pipeline installation: A manual for construction of buried pipe*. Lakewood, CO: Relativity Publishing.
- Hsuan, Y.G., & McGrath, T.J. (2005). *Protocol for predicting long-term service of corrugated high density polyethylene pipes*. Tallahassee, FL: Florida Department of Transportation.
- Hsuan, Y.G., & Zhang, J.Y. (2005). Stress crack resistance of corrugated high-density polyethylene pipes in different test environments and temperatures. *Transportation Research Record*, 1928, 221-225.
- Kansas Department of Transportation (KDOT). (2007). Excavation and backfill for structures (Section 204). *Standard specifications for state road & bridge construction*. Topeka, KS: Author.

- Kansas Department of Transportation (KDOT). (2012). *State Transportation Improvement Program Fiscal Year 2013-2016*. Topeka, KS: Author.
- Katona, M.G. (1978). Analysis of long-span culverts by the finite element method. *Transportation Research Record*, 678, 59-66.
- Katona, M.G. (1988). *Minimum cover heights for HDPE corrugated plastic pipe under vehicular loading*. Corrugated Plastic Tubing Association.
- Katona, M.G. (2015a). Influence of soil models on performance of buried culverts. In *TRB 94th Annual Meeting compendium of papers*. Washington, DC: Transportation Research Board.
- Katona, M.G. (2015b). Modifying Duncan-Selig soil model for plasticlike behavior. *Transportation Research Record*, 2511, 53-62.
- Khatri, D.K. (2012). *Experimental evaluation of the behavior of steel-reinforced high density polyethylene (SRHDPE) pipes* (Master's thesis). The University of Kansas, Lawrence, KS.
- Khatri, D.K. (2014). *Laboratory and field performance of buried steel-reinforced high density polyethylene (SRHDPE) pipes in a ditch condition under a shallow cover* (Doctoral dissertation). The University of Kansas, Lawrence, KS.
- Khatri, D.K., Han, J., Corey, R., & Parsons, R.L. (2013). *Establishing a design procedure for buried steel-reinforced high density polyethylene (SRHDPE) pipes* (Report No. KU-11-6). Topeka, KS: Kansas Department of Transportation.
- Khatri, D.K., Han, J., Corey, R., Parsons, R.L., & Brennan, J.J. (2015). Laboratory evaluation of installation of a steel-reinforced high-density polyethylene pipe in soil. *Tunnelling and Underground Space Technology*, 49, 199-207.
- Khatri, D.K., Han, J., Parsons, R.L., Young, B., Brennan, J.J., & Corey, R. (2013). Laboratory evaluation of deformations of steel-reinforced high-density polyethylene pipes under static loads. *Journal of Materials in Civil Engineering*, 25(12), 1964-1969.
- Li, Y.G. (2009). *Study on unified calculation theory of earth pressure on top of trench-buried culverts and positive-buried culverts* (Doctoral dissertation). Taiyuan University of Technology, Taiyuan, China.

- Lischer, V.C. (1969). AWWA pipe standards in pipeline engineering. *Journal - American Water Works Association*, 61(9), 455-459.
- Mai, V.T., Hoult, N.A., & Moore, I.D. (2014). Effect of Deterioration on the Performance of Corrugated Steel Culverts. *Journal of Geotechnical and Geoenvironmental Engineering*, 140(2).
- Mamlouk, M.S., & Zaniewski, J.P. (2011). *Materials for Civil and Construction Engineers* (3rd ed.). Upper Saddle River, NJ: Pearson Prentice Hall.
- Marston, A. (1930). The theory of external loads on closed conduits in the light of the latest experiments. *Highway Research Board Proceedings*, 9, 138-170.
- Marston, A., & Anderson, A.O. (1913). *The theory of loads on pipes in ditches and tests of cement and clay drain tile and sewer pipe*. Ames, IA: Iowa State College of Agriculture and Mechanic Arts.
- Masada, T., & Sargand, S. (2007). Peaking deflections of flexible pipe during initial backfilling process. *Journal of Transportation Engineering*, 133(2), 105–111.
- Matyas, E.L. & Davis, J.B. (1983). Prediction of vertical earth loads on rigid pipes. *Journal of Geotechnical Engineering*, 109(2), 190-201.
- McAfee, R.P., & Valsangkar, A.J. (2008). Field performance, centrifuge testing, and numerical modelling of an induced trench installation. *Canadian Geotechnical Journal*, 45(1), 85-101.
- McGrath, T.J. (1998). Replacing E' with the constrained modulus in flexible pipe design. In *Pipelines in the Constructed Environment*. Reston, VA: American Society of Civil Engineers.
- McGrath, T.J., Selig, E.T., Webb, M.C., & Zoladz, G.V. (1999). *Pipe interaction with the backfill envelope* (FHWA-RD-98-191). McLean, VA: Federal Highway Administration.
- Meyerhof, G.G., & Adams, J.I. (1968). The ultimate uplift capacity of foundations. *Canadian Geotechnical Journal*, 5(4), 225-244.
- Meyerhof, G.G., & Baikie, L.D. (1963). Strength of steel culvert sheets bearing against compacted sand backfill. *Highway Research Record*, 30, 1-19.

- Molin, J. (1981). Flexible pipes in buried clay. In *Underground plastic pipe* (pp. 322-337). New York, NY: American Society of Civil Engineers.
- Moore, I.D. (2009). *DuroMaxx pipe assessment*. Contech Construction Products Inc.
- Moser, A.P., & Folkman, S. (2008). *Buried Pipe Design* (3rd ed.). New York, NY: McGraw-Hill Professional.
- Rogers, C.D.F., Fleming, P.R., Loeppky, M.W.J., & Faragher, E. (1995). The structural performance of profile-wall drainage pipe—Stiffness requirements contrasted with results of laboratory and field tests. *Transportation Research Record*, 1514, 83-92.
- Sargand, S.M., Hazen, G.A., Masada, T., Schehl, D.J., Moran, A., & Altarawneh, B. (2002). *Field verification of structural performance of thermoplastic pipe under deep backfill conditions* (Report No. FHWA/OH-2002/023). Columbus, OH: Ohio Department of Transportation.
- Sargand, S., Masada, T., & Hurd, J.O. (1996). Effect of rib spacing on deformation of profile-wall plastic pipes buried in coarse granular backfill. *Geotechnical Testing Journal*, 19(2), 217-222.
- Sargand, S.M., Masada, T., & Schehl, D.J. (2001). Soil pressure measured at various fill heights above deeply buried thermoplastic pipe. *Transportation Research Record*, 1770, 227-235.
- Sargand, S., Masada, T., Tarawneh, B., & Gruver, D. (2008). Deeply buried thermoplastic pipe field performance over five years. *Journal of Geotechnical and Geoenvironmental Engineering*, 134(8), 1181–1191.
- Schofield, A.N. (1980). Cambridge geotechnical centrifuge operations. *Geotechnique*, 30(3), 227-268.
- Seed, R.B., & Duncan, J.M. (1986). FE analyses: Compaction-induced stresses and deformations. *Journal of Geotechnical Engineering*, 112(1), 23–43.
- Spangler, M.G. (1941). *The structural design of flexible pipe culverts*. Ames, IA: Iowa State College of Agriculture and Mechanic Arts.
- Spangler, M.G. (1962). Culverts and conduits. In G.A. Leonards (Ed.), *Foundation Engineering* (pp. 965-999). New York, NY: McGraw Hill.

- Taleb, B., & Moore, I.D. (1999). Metal culvert response to earth loading: Performance of two-dimensional analysis. *Transportation Research Record*, 1656, 25-36.
- Wang, F., Han, J., Khatri, D.K., Parsons, R.L., Brennan, J.J., & Guo, J. (2015). Field installation effect on steel-reinforced high-density polyethylene pipes. *Journal of Pipeline Systems Engineering and Practice*. doi: 10.1061/(ASCE)PS.1949-1204.0000211
- Watkins, R.K., & Spangler, M.G. (1958). Some characteristics of the modulus of passive resistance of soil: A study in similitude. *Highway Research Board Proceedings*, 37, 576-583.
- Webb, M.C., McGrath, T.J., & Selig, E.T. (1996). Field tests of buried pipe installation procedures. *Transportation Research Record*, 1541, 97-106.
- Yang, X. (2010). *Numerical analyses of geocell-reinforced granular soils under static and repeated loads* (Doctoral dissertation). The University of Kansas, Lawrence, KS.
- Yang, X., Han, J., Leshchinsky, D., & Parsons, R.L. (2012). A three-dimensional mechanistic-empirical model for geocell-reinforced unpaved roads. *Acta Geotechnica*, 8(2), 201-213.

K-TRAN

KANSAS TRANSPORTATION RESEARCH AND NEW-DEVELOPMENT PROGRAM

